2013

Plasma Shape and Current Density Profile Control in Advanced Tokamak Operating Scenarios

Wenyu Shi
Lehigh University

Plasma Shape and Current Density Profile Control in Advanced Tokamak Operating Scenarios

by

Wenyu Shi

Presented to the Graduate and Research Committee

of Lehigh University

in Candidacy for the Degree of

Doctor of Philosophy

in

Mechanical Engineering

Lehigh University

May, 2013

Certificate of Approval

This thesis is accepted and approved in partial fulfillment of the requirements for the Doctor of Philosophy in Mechanical Engineering.

_____

Date

_____

Professor Eugenio Schuster

Dissertation Advisor

_____

Accepted Date

Committee Members:

_____

Professor Eugenio Schuster

Committee Chair

_____

Professor N. Duke Perreira

Committee Member

_____

Professor Mayuresh V. Kothare

Committee Member

_____

Professor Arnold Kritz

Committee Member

Acknowledgements

First of all, I would like to express my cordial gratitude to my advisor, Professor Eugenio Schuster, for introducing me to the exciting field of plasma physics and control, which will influence my career. I appreciate his patience and understanding, and always being available to give me advise and to answer my questions. With his great patience and kindness, my English capabilities, including both communication and writing skills, have improved significantly during my time at Lehigh.

I would like to thank the Plasma Control System (PCS) Group of the DIII-D National Fusion Facility at General Atomics. Without their help and support in the experiments, it would be impossible for me to accomplish my dissertation work. I would also like to express my sincere acknowledgement to Professor Arnold Kritz from the Department of Physics at Lehigh University for his help and technical support in learning the PTRANSP code.

I am so grateful to all the members and alumni of the Laboratory for Control of Complex Physical Systems at Lehigh University, especially Justin Barton, William Wehner, Dan Boyer, Dr. Yongsheng Ou and Dr. Chao Xu, for their instructive discussions, fruitful collaborations and priceless friendship. In addition, I would like to give my thanks to my friends at Lehigh University for their encouragement.

Finally and most of all, I would like to acknowledge my parents. I would like to thank them for supporting me in every way and sharing their lives through good and bad times. Without their love and support, I could not have finished my study at Lehigh University.

Contents

List of Tables

List of Figures

Abstract

The need for new sources of energy is expected to become a critical problem within the next few decades. Nuclear fusion has sufficient energy density to potentially supply the world population with its increasing energy demands. The tokamak is a magnetic confinement device used to achieve controlled fusion reactions. Experimental fusion technology has now reached a level where tokamaks are able to produce about as much energy as is expended in heating the fusion fuel. The next step towards the realization of a nuclear fusion tokamak power plant is ITER, which will be capable of exploring advanced tokamak (AT) modes, characterized by a high fusion gain and plasma stability. The extreme requirements of the advanced modes motivates researchers to improve the modeling of the plasma response as well as the design of feedback controllers. This dissertation focuses on several magnetic and kinetic control problems, including the plasma current, position and shape control, and data-driven and first-principles-driven modeling and control of plasma current density profile and the normalized plasma pressure ratio β_N.

The plasma is confined within the vacuum vessel by an external electromagnetic field, produced primarily by toroidal and poloidal field coils. The outermost closed plasma surface or plasma boundary is referred to as the shape of the plasma. A central characteristic of AT plasma regimes is an extreme elongated shape. The equilibrium among the electromagnetic forces acting on an elongated plasma is unstable. Moreover, the tokamak performance is improved if the plasma is located in close proximity to the torus wall, which guarantees an efficient use of available volume. As a consequence, feedback control of the plasma position and shape is necessary. In this dissertation, an H_∞-based, multi-input-multi-output (MIMO) controller for the

National Spherical Torus Experiment (NSTX) is developed, which is used to control the plasma position, shape, and X-point position.

Setting up a suitable toroidal current profile is related to both the stability and performance of the plasma. The requirements of ITER motivate the research on plasma current profile control. Currently, physics-based control-oriented modeling techniques of the current profile evolution can be separated into two major classes: data-driven and first-principles-driven. In this dissertation, a two-timescale linear dynamic data-driven model of the rotational transform ι profile and β_N is identified based on experimental data from the DIII-D tokamak. A mixed-sensitivity H_∞ controller is developed and tested during DIII-D high-confinement (H-mode) experiments by using the heating and current drive (H&CD) systems to regulate the plasma ι profile and β_N around particular target values close to the reference state used for system identification. The preliminary experimental results show good progress towards routine current profile control in DIII-D. As an alternative, a nonlinear dynamic first-principles-driven model is obtained by converting the physics-based model that describes the current profile evolution in H-mode DIII-D discharges into a form suitable for control design. The obtained control-oriented model is validated by comparing the model prediction to experimental data. An H_∞ control design problem is formulated to synthesize a stabilizing feedback controller, with the goal of developing a closed-loop controller to drive the current profile in DIII-D to a desirable target evolution. Simulations show that the controller is capable of regulating the system around the target ι profile in the presence of disturbances. When compared to a previously designed data-driven model-based controller, the proposed first-principles-driven model-based controller shows potential for improving the control performance.

Chapter 1

Introduction

1.1 What is a Tokamak?

The energy demand by humanity is continuously rising because of fast industrial development. Currently, about 80% of the energy comes from fossil fuels like oil, gas, and coal. However, fossil fuels are a limited resource. At the present rate of annual increase of energy use, experts predict that in about 30 years oil extraction will become uneconomical, whereas there should be about 200 years left for coal, and natural gas should last about 50 more years [1]. Besides being limited resources, fossil fuels cause serious problems in the environment, e.g., burning these fuels is the largest source of emission of carbon dioxide, which contributes to global warming. Therefore the need for new sources of energy to take the place of fossil fuels is becoming a critical problem for the future. Many alternative energy sources such as wind, hydro, solar, and biofuel seem to be attractive, but there is skepticism concerning the possibility of them replacing the fossil fuels around the world because of the limited energy density provided by these sources. For these reasons, a significant amount of research is being done to develop nuclear fusion.

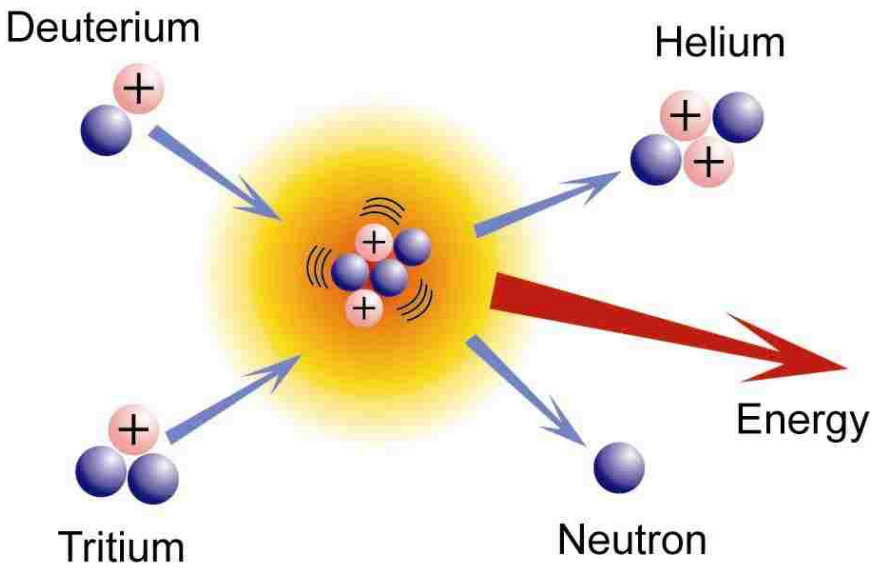

Figure 1.1: The D−T Fusion Reaction.

Nuclear fusion is a promising source of energy to support the increasing world demand. In fusion, two light nuclei (such as hydrogen isotopes deuterium D and tritium T) combine into one new nucleus (such as helium He) and release enormous energy in the process, which is shown in Figure 1.1. The most promising fusion reaction is

$$ {}^{2}_{1}D + {}^{3}_{1}T \longrightarrow {}^{4}_{2}He + {}^{1}_{0}n + 17.6MeV, \tag{1.1} $$

where n indicates a neutron. D occurs naturally in seawater, which makes it very abundant when compared to other energy resources. T does not occur naturally, but it can be produced in a conventional nuclear fission reactor, or in the present context, bred in a fusion reactor from lithium Li:

$$ {}^{7}_{3}Li + {}^{1}_{0}n \longrightarrow {}^{4}_{2}He + {}^{3}_{1}T + {}^{1}_{0}n + 2.5MeV, \quad {}^{6}_{3}Li + {}^{1}_{0}n \longrightarrow {}^{4}_{2}He + {}^{3}_{1}T + 4.8MeV. \tag{1.2} $$

Li is found in large quantities in the Earths crust. There is no air pollution or greenhouse gas produced because the major nuclear fusion production is helium.

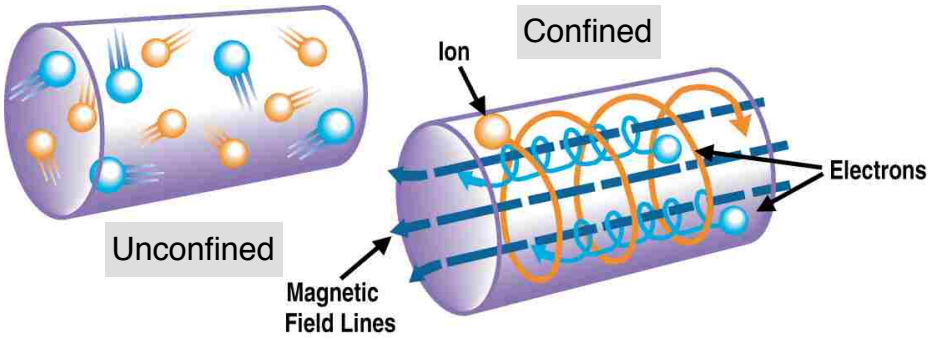

Figure 1.2: The Principle of Magnetic Confinement.

Minimal or no high level nuclear waste will be produced in fusion reactions.

To make fusion happen, it is necessary to bring two nuclei close enough to overcome the mutual repulsion due to their positive charges. The gas must be heated to temperatures around 100 million degrees. At that temperature, the electrons and nuclei separate, and the gas becomes a plasma, the fourth state of matter. The difficulty in producing fusion energy is the development of a device that can heat the fuel to a sufficiently high temperature and then confine it for a long time. There are three ways to confine the plasma: gravitational confinement, inertial confinement, and magnetic confinement. Magnetic confinement devices are the most promising devices for the development of a nuclear power plant, and therefore are the subject of intensive research.

In the plasma, since the electrons are stripped from the nuclei of the atoms, the individual charged particle can be confined by the magnetic fields. The ionized particles are tied to the magnetic field lines by the Lorentz force, limiting their motion to a helical path along the field lines, progressing linearly while gyrating in a circular orbit around the field lines. A magnetic field is thus capable of restricting the particle motion perpendicular to the field but does not prevent motion along the field lines, which is shown in Figure 1.2. To limit the confinement to a bounded volume, the common solution is to close the magnetic field lines in on themselves, forming a torus.

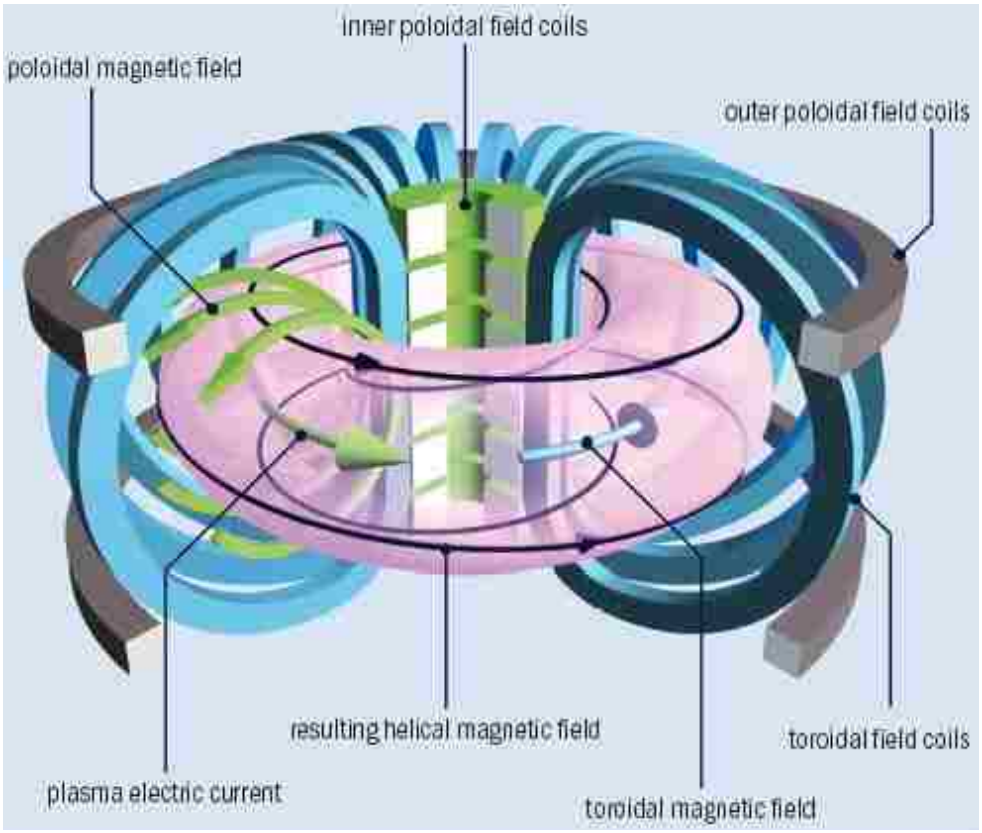

Figure 1.3: Tokamak. (Source: EFDA-JET)

There are several types of toroidal confinement systems, the most important being tokamaks (shown in Figure 1.3), stellarators and reversed field pinch (RFP) devices.

All existing tokamaks are pulsed machines, and the plasma is maintained within the tokamak for only a few seconds to several minutes. All tokamaks produce plasma pulses through approximately the same sequence of events. In each pulse the plasma is created, its current is ramped up to a constant flat-top value, and eventually the current is ramped down and the plasma is terminated. In most tokamak discharges, the plasma current is initiated and sustained by the ohmic heating (OH) coils, while the toroidal field (TF) coils and poloidal field (PF) coils provide the primary magnetic field to confine the plasma within a fixed volume (shown in Figure 1.3). Neutral beams (uncharged atoms of deuterium) are injected into the plasma at high velocity,

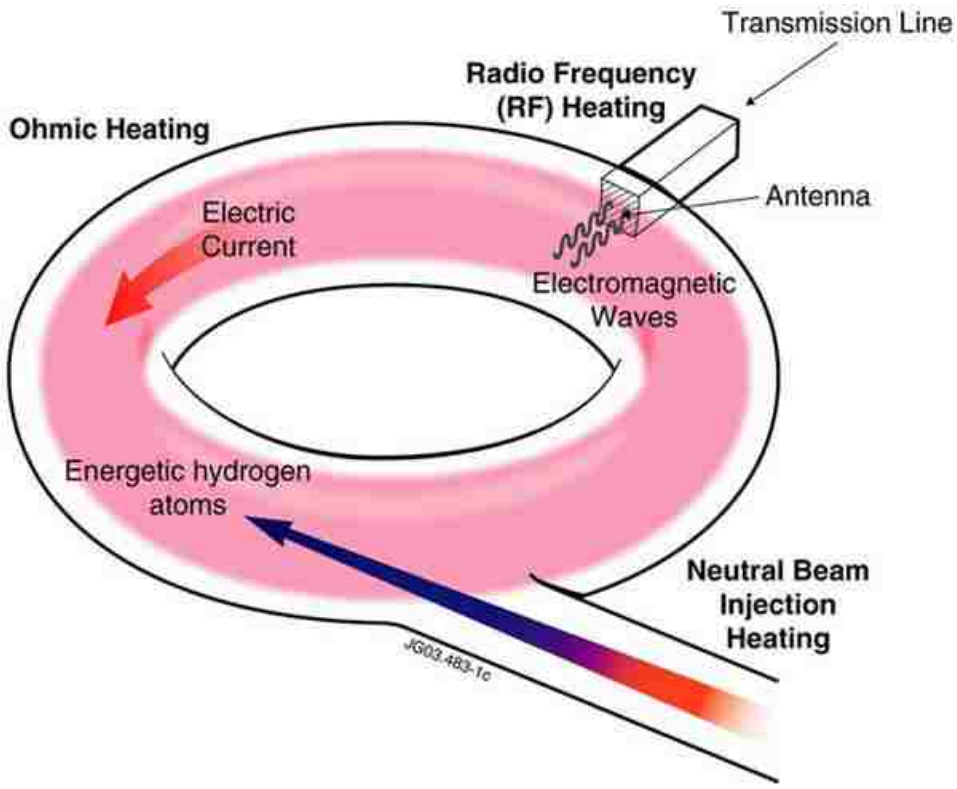

Figure 1.4: Typical Tokamak Heating Methods: Ohmic Heating, Radio-Frequency (RF) Heating and Neutral Beam Injection (NBI) Heating.

and these particles collide with particles in the plasma, thereby converting their momentum into current and further heating. Electromagnetic waves can be injected in the plasma with the same objectives (shown in Figure 1.4).

Experimental fusion technology has now reached a level where tokamaks are able to produce about as much energy as is expended in heating the plasma. The next step towards the realization of a commercial fusion reactor is the construction and operation of the ITER tokamak (see [1] and references therein), shown in Figure 1.5. The ITER tokamak goals are to demonstrate the physical understanding and some key technologies to maintain a burning plasma mode, a high ratio of fusion power to auxiliary power [2, 3]. The planned ITER reactor will be capable of exploring advanced tokamak (AT) modes of operation [4], characterized by high plasma pres-

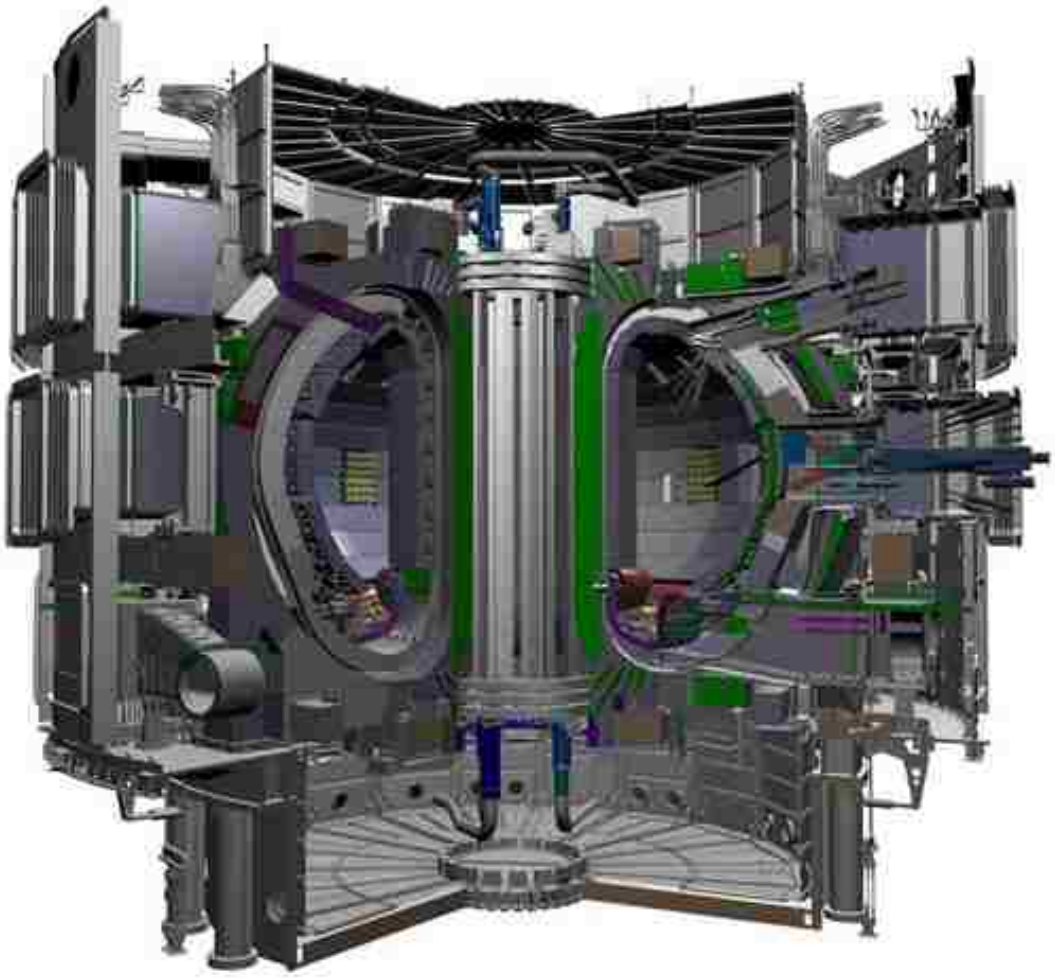

Figure 1.5: Schematic of the ITER tokamak

sure, long confinement times, and low levels of inductively driven plasma current, which allow for near steady-state operation. These advanced modes require active feedback control to maintain and develop high performance plasmas, and confinement to maintain sufficiently long plasma discharges.

1.2 Feedback Control in Tokamaks

The tokamak is a high order, distributed parameter, non-linear system with a large number of instabilities (such as resistive wall mode (RWM) [5, 6], neoclassical tearing mode (NTM) [7, 8], edge localized mode (ELM) [9], and sawtooch instabilities [10]), so there are many extremely challenging mathematical modeling and control problems, which must be solved before a fusion power plant becomes a viable entity. The tokamak control problem can be separated into two major classes: magnetic control and kinetic control. Magnetic control in tokamaks refers to controlling the magnetic fields, which maintain or change the plasma position, shape and current. This task is performed by a set of PF coils distributed around the vessel that contains the plasma. Highly shaped plasmas are required to operate at high plasma pressure and fusion efficiency. In addition, the achievement of certain types of plasma shapes can reduce the effect of instabilities induced by the high plasma pressure. Therefore, it is critical to meet shape requirements in a practical, highly-efficient tokamak. Kinetic control refers to controlling particle feed rates and heating to modify the plasma density, temperature, pressure, and current density. Due to the distributed parameter nature of tokamaks, it is important to control not only spatially averaged value of these parameters but also their spatial profiles. Stability properties, energy confinement, and the fraction of the self generated "bootstrap current" can be improved through control of the current profile and the normalized ratio between the internal kinetic pressure of the plasma and the external pressure of the magnetic field. In the following, we will present and discuss two of the most important control problems that need to be solved in tokamaks.

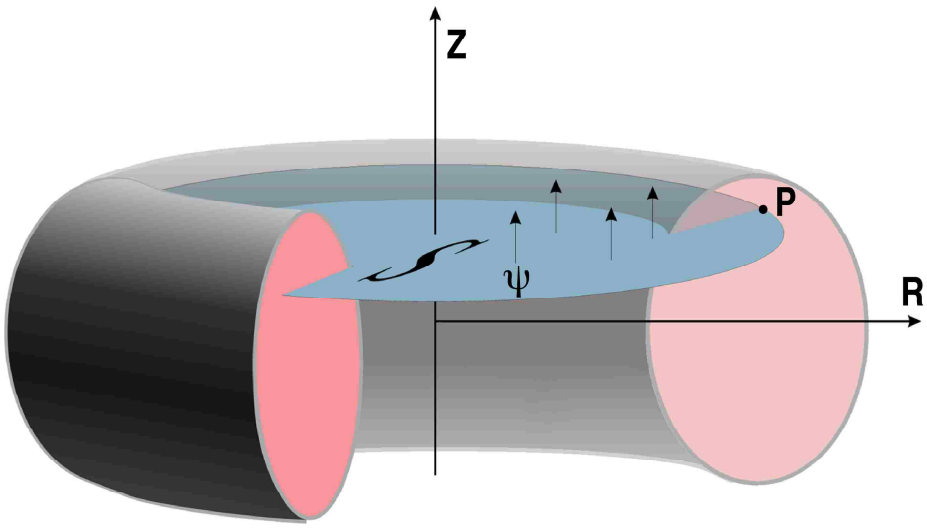

Figure 1.6: Definition of the Poloidal Flux in a Tokamak.

1.2.1 Plasma Shape and Position Control

The magnetic lines that guide the particles around the torus axis in the tokamak are helices, i.e., a combination of toroidal and poloidal magnetic fields. It is possible to use the poloidal component of the magnetic lines to define nested toroidal surfaces corresponding to constant values of the poloidal magnetic flux. As it is illustrated in Figure 1.6, the poloidal flux ψ at a point P is the total flux through the surface S bounded by the toroidal ring passing through P, i.e., $\psi = \frac{1}{2\pi}\int B_{pol} dS$, where B_{pol} is the poloidal magnetic field. As shown in Figure 1.7, the closed constant poloidal magnetic flux lines form a set of nested surfaces around the torus axis in the tokamak. The plasma boundary is the outermost closed flux surface entirely contained inside the vacuum vessel. It is the shape of this boundary that is generally referred to as plasma shape. The limiting magnetic surface, which approaches a single magnetic line, is called the magnetic axis. The parameter ρ is the mean effective minor radius of the flux surface, and the parameter ρ_b is the mean effective minor radius of the last closed magnetic flux surface. The total plasma current is the current flowing through

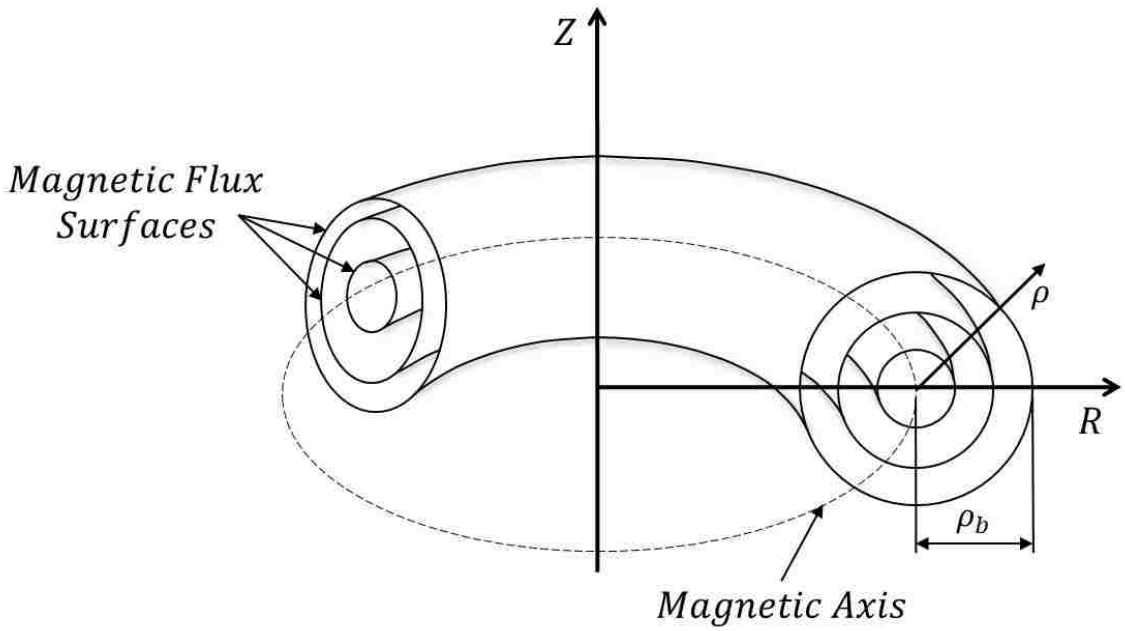

Figure 1.7: Poloidal Flux Surfaces in a Tokamak.

the poloidal plane in the plasma region. The horizontal and vertical coordinates of the plasma current centroid are defined as the plasma radial and vertical position respectively.

The plasma shape requirements in a practical, highly efficient tokamak are very stringent. The extreme shapes that must be achieved, intrinsic instability in the plasma vertical position (the more shaped the plasma, the more unstable), large number of control inputs (coil voltages) and control outputs (geometrical parameters and plasma current), and demanding regulation requirements make this problem very challenging. In order to improve plasma parameters, specifically to increase energy confinement time, a vertically elongated cross-section is used in many tokamaks. An active feedback control system is required to stabilize the plasma and confine the plasma in a fixed volume. Model-based control methods have been used in the past to design both vertical position [11, 12] and shape controllers [13, 14, 15, 16] during the

plasma-current flat-top phase of the discharge. A PII controller containing a parallel connection of proportional, integral, and double integral gains has been proposed for the ITER tokamak during the plasma current ramp-up phase [17]. The recent implementation of the real-time equilibrium reconstruction code rtEFIT [18] in the National Spherical Torus Experiment (NSTX) allows the plasma to be shaped by controlling the magnetic flux at the plasma boundary. A non-model-based, empirically-tuned, single-input-single-output (SISO), PID-based shape controller that exploits this capability has been recently proposed [19]. In this dissertation, this work is extended by proposing a model-based, multi-input-multi-output (MIMO) controller to be applied during both the ramp-up phase and the current flat-top phase in NSTX [20, 21].

1.2.2 Plasma Current Density Profile Control

The requirements of ITER for designing a "steady-state" fusion power plant motivate research in the high confinement mode (H-mode). One possible approach involves setting up a suitable toroidal current density profile in the machine that contributes to maintaining the bootstrap current, and many studies have shown the key influence of the plasma current profile on the development of a steady-state H-mode plasma. Therefore, real-time control of the current profile is of paramount importance. Most of the prior work has focused, however, on non-model-based control of scalar parameters characterizing the current profile such as the internal inductance l_i, the safety factor at the magnetic axis q_0, or the minimum value of the safety factor q_{min}. While the control of scalar parameters such as q_{min} is critical to mitigate plasma instabilities and improve confinement, the shaping of the entire q profile is necessary to maximize the fraction of bootstrap current and maintain stability in advanced scenarios. Therefore, techniques to actively control the evolution of the full q profile in closed loop during the discharge are of paramount importance to the success of ITER. The high

dimensionality of this problem, along with the strong coupling between the magnetic and kinetic profiles, motivate the use of model-based control synthesis that can accommodate this complexity by embedding physics-based dynamic models within the design.

Mathematical modeling of plasma transport phenomena with sufficient complexity to capture the dominant dynamics is therefore critical for plasma profile control design. There are two major modeling methods: data-driven modeling techniques and first-principles-driven modeling techniques. Transport theories (classical, neoclassical and anomalous), even under restrictive assumptions, produce strongly nonlinear models based on partial differential equations (PDEs). The complexity of these first-principles models needs to be reduced to facilitate design of compact and reliable control strategies. During this control-oriented model reduction process [22, 23, 24], there is always a trade-off between the simplicity of the model and both its physics accuracy and its range of validity. First-principles-driven modeling provides the freedom of arbitrarily handling this trade-off and deciding on the level of simplicity, accuracy and validity of the model. This features allows, for instance, for the derivation of models capturing the nonlinear response of the current profile to control actuation. Data-driven modeling techniques such as system identification [25] emerge as an alternative to first-principles-driven modeling and have the potential to obtain low-complexity dynamic models. This modeling approach lacks however the ability of arbitrarily deciding on the level of simplicity, accuracy and validity of the model since it directly produces linear models based on ordinary differential equations (ODEs). As the identified models are linear, they are only valid around the reference plasma state adopted during the system identification experiment. Therefore, the effectiveness of the controllers synthesized based on these models may be limited when the plasma state moves away from the reference state. Moreover, as these models are

device-specific, dedicated system identification experiments are needed in each device, and potentially for each control scenario, to develop model-based controllers. In spite of these limitations, data-driven control-oriented models can be useful for the design of local regulators around the reference state. In this dissertation, the data-driven modeling and first-principles-driven modeling approaches are discussed respectively, and these approaches are proposed for model-based feedback control design. Some of these controllers have been successfully experimentally tested in the DIII-D tokamak [26, 27, 28, 29].

Recent experiments in different tokamaks (JET [30, 31], Tore Supra [32, 33], JT-60U [34, 35], DIII-D [36]) have demonstrated significant progress in achieving current profile control by using data-driven modeling approach. In the JET tokamak, a two-timescale linear system has been used to describe the magnetic and kinetic profiles around certain quasi-steady-state trajectories, and the controller is composed of two composite feedback loops operating on the magnetic and kinetic time scales respectively [30, 31]. In discharges at the JT-60U tokamak, the momentum transport equation of the toroidal rotation profile has been estimated from transient data obtained by modulating the momentum source [32, 37]. Input/output(I/O) diagnostic data has been used by the author to model the current profile dynamics in the DIII-D tokamak [37]. The developed linear model of the plasma rotational transform ι profile was in turn used to design a full-profile feedback controller [26, 27, 28, 29, 38, 39], that was implemented and tested experimentally in DIII-D. These preliminary control experiments carried out at DIII-D suggest that regulation of the current profile around a reference state during the flat-top phase of the discharge, may be possible using a data-driven linear modeling and control approach if enough actuation is available. However, being able to control the current profile during the ramp-up and ramp-down phases, being able to regulate the current profile for different scenarios (around differ-

ent reference states), or being able to drive the current profile from one target profile to another will most likely require adaptive or nonlinear control approaches based on richer dynamic models obtained by a first-principles-driven modeling approach.

First-principles control-oriented models for low-confinement (L-mode) scenarios have been recently used to determine optimal open-loop (feedforward) actuator trajectories that achieve and sustain a desired q profile [40, 41, 42], and to design complementing closed-loop (feedback) control laws that add robustness against disturbances and model uncertainties. Several approaches have been recently proposed for first-principles current profile feedback control [43, 44, 45, 46, 47] and some of them have been experimentally tested in DIII-D [48, 49, 50, 51, 52]. In the dissertation, the author extended these previous work by developing first-principles-driven feedback controllers for current profile in high-confinement (H-mode) scenarios for on-axis and off-axis current drive scenarios respectively [53, 54]. When compared to a previously designed data-driven model-based controller, the proposed first-principles-driven model-based controller shows potential for improving the control performance, especially in the inner part of the current density profile.

1.3 Dissertation Outline

This dissertation is organized as follows.

Chapter 2

By leveraging the availability of real time EFIT, model-based, multi-input-multi-output (MIMO) magnetic controllers are proposed to provide current regulation, position stabilization, and shape control of the plasma during the current ramp-up phase and the current flat-top phase in the National Spherical Torus Experiment (NSTX).

The proposed controller is composed of three loops: the first loop is devoted to plasma current regulation, the second loop is dedicated to plasma radial and vertical position stabilization, and the third loop is used to control the plasma shape and X-point location. This control approach transforms the shape control problem into an output tracking problem. The goal is the minimization of a quadratic cost function that describes the tracking error in steady state. Computer simulations illustrate the performance of the robust, multi-model-based, shape controller, showing potential for improving the performance of present non-model-based controllers.

Chapter 3

System identification techniques have the potential of producing low-complexity, linear models that can capture the system dynamics around an equilibrium point. This chapter focuses on the modeling of the rotational transform ι profile and the normalized plasma pressure ratio β_N evolution in response to the heating and current drive (H&CD) systems and the total plasma current for on-axis and off-axis current drive scenarios respectively. Dedicated system-identification experiments without feedback control were carried out to generate data for the development of the identified models. The data-driven dynamic models, which are both device-specific and scenario-specific, represent the response of the ι profile and β_N to the electric field due to induction as well as to the H&CD systems during the current flat-top phase of an H-mode discharge in DIII-D. Note that Mr. William Wehner is mainly responsible for identifying the linear dynamic plasma models used by our research group [38, 39, 55]. The on-axis and off-axis identified models are employed for model-based current profile control design in Chapter 4 and Chapter 5, respectively.

Chapter 4

The control-oriented, two-timescale, linear, dynamic, response model of the rotational transform ι profile and the normalized beta β_N for the DIII-D tokamak introduced in Chapter 3 is employed in this chapter for model-based control design. The control goal is to use both induction and the H&CD systems to locally regulate the plasma ι profile and β_N around particular target values close to the reference state used for system identification. A singular value decomposition (SVD) of the plasma model at steady state is carried out to decouple the system and identify the most relevant control channels. A mixed-sensitivity robust control design problem is formulated based on the dynamic model to synthesize a stabilizing feedback controller without input constraints that minimizes the reference tracking error and rejects external disturbances with minimal control energy. The feedback controller is then augmented with an anti-windup compensator, which keeps the given controller well-behaved in the presence of magnitude constraints in the actuators and leaves the nominal closed-loop system unmodified when no saturation is present. The proposed controller represents one of the first feedback profile controllers integrating magnetic and kinetic variables ever implemented and experimentally tested in DIII-D. The preliminary experimental results presented in this work, although limited in number and constrained by actuator problems and design limitations, show good progress towards routine current profile control in DIII-D and leave valuable lessons for further advancements in the field.

Chapter 5

During the tokamak discharge, especially the ramp-up phase, the plasma state equilibrium continually evolves. As a consequence, the plasma response model should evolve as well. A linear plasma response model of the rotational transform ι profile and β_N is first identified around a desired equilibrium. Then, an uncertainty is in-

troduced to the identified model to partially account for the dynamic character of the plasma state equilibrium evolution. A robust controller is designed to stabilize this family of plasma models, which are reformulated into a nominal model plus a bounded uncertainty. The DK-iteration method, combining H_∞ synthesis and μ analysis, is applied to synthesize a closed-loop controller that minimizes the tracking error and input effort. The feedback controller is then augmented with an anti- windup compensator, which keeps the given profile controller well-behaved in the presence of magnitude constraints in the actuators and leaves the nominal closed-loop unmodified when no saturation is present. PTRANSP simulations and experimental results in DIII-D illustrate the performance of the model-based controller.

Chapter 6

In this chapter, a general control-oriented physics-based modeling approach is utilized, with emphasis on high performance operating scenarios, to convert the first-principles physics model that describes the current profile evolution in the DIII-D tokamak into a form suitable for control design, with the goal of developing closed-loop controllers to drive the current profile in the machine to a desirable target evolution. The PTRANSP advanced tokamak simulation code is then employed to tailor the first-principles-driven model to the DIII-D tokamak geometries for on-axis and off-axis current drive scenarios, respectively. The first-principles-driven models' prediction capabilities are demonstrated by comparing the prediction to experimental data from DIII-D. The tailored model is employed to design feedback control algorithms to control the current profile evolution in H-mode scenarios DIII-D, which is part of the next chapter. Closed-loop simulated results of the designed controller and the comparison with experimental results will be used to assess the true requirements for model accuracy.

Chapter 7

The first-principles-driven, control-oriented, nonlinear, partial-differential-equation model of the poloidal flux profile evolution introduced in Chapter 6 is utilized to design a feedback control algorithm to regulate the rotational transform profile in the DIII-D tokamak. The control goal is to regulate the rotational transform profile, which is related to the poloidal flux profile, around a particular target profile. The first-principles-driven plasma response model is validated first by comparing the model prediction to experimental data. After the model is validated, a singular value decomposition of the nominal plasma model at steady state is carried out to decouple the system and identify the most relevant control channels. A mixed sensitivity H_∞ control design problem is formulated to synthesize a stabilizing feedback controller to minimize the reference tracking error with minimal control energy. Simulations with the first-principles-driven model show that the H_∞ controller is capable of regulating the system around the target ι profile in the presence of disturbances. When compared to a previously designed data-driven model-based controller, the proposed first-principles-driven model-based controller shows potential for improving the control performance.

Chapter 8

In this chapter, the work included in this dissertation is summarized and future research work is discussed.

Chapter 2

Multivariable Model-based Shape Control System for the National Spherical Torus Experiment (NSTX)

2.1 Introduction

The recent implementation of the real-time equilibrium reconstruction code rtEFIT [18] in the National Spherical Torus Experiment (NSTX) allows the plasma to be shaped by controlling the magnetic flux at the plasma boundary. The strong coupling between the different geometrical parameters describing the shape of the plasma calls for a model-based, multivariable approach to obtain improvements in closed-loop performance.

The dynamics of the NSTX system, composed of the plasma, shaping coils, and passive structure, are described using circuit equations derived from Faraday's Law

and radial and vertical force balance relations for a particular magnetohydrodynamic (MHD) equilibrium [56]. In addition, the rigid radial and vertical displacements of the equilibrium current distribution are assumed, and a series of resistive plasma equations are specified. The result is a circuit equation describing the linearized response, around a particular plasma equilibrium, of the conductor-plasma system to voltages applied to the active conductors. However, the MHD equilibrium continually evolves during the ramp-up phase of the discharge. Different scenario points are chosen to describe the plasma equilibrium evolution, which represent the described reference trajectory of the system, during the plasma current ramp-up phase in NSTX. These models are reformulated into a nominal model with uncertainty.

Model-based MIMO magnetic controllers are proposed to account for disturbances and uncertainties in the plasma model in both the current ramp-up phase and the current flat-top phase. The control goal is to drive the system to the reference plasma current, vertical and radial position, and shape. The proposed controllers are composed of three loops: the first loop is devoted to plasma current regulation, the second loop is dedicated to radial and vertical position stabilization, and the third loop is used to control the plasma shape and X-point location. The design of independent current and position control loops transforms the shape control problem into an output tracking problem, and singular value decomposition (SVD) is used to decouple and identify the most relevant control channels [16]. The H_∞ technique is used to minimize the tracking errors and optimize input efforts in the current flat-top phase, and the DK-iteration, combining H_∞ synthesis and μ analysis, is applied to synthesize a closed-loop controller in the current ramp-up phase. The proposed controllers are successfully tested in computer simulations.

This chapter is organized as follows. In Section 2.2, the NSTX tokamak is briefly described and the linearized plasma model is presented. In Section 2.3 and 2.4, the

design of the plasma control algorithms is described and computer simulation results are presented. Section 2.5 states the conclusions.

2.2 Description of NSTX

2.2.1 NSTX Tokamak and Isoflux Control

The NSTX at the Princeton Plasma Physics Laboratory (PPPL) produces a plasma that is shaped like a sphere with a hole through its center, different from the other shaped plasmas of conventional tokamaks. NSTX has several advantages including plasma stability through improved confinement, but NSTX presents a unique control challenge relative to other tokamaks in that there are no shaping control coils on the inboard radius of the plasma. Therefore, it is not possible to independently control the inner gap and each point on the outer boundary. The problem is further complicated by the small number of poloidal field coils on the outboard major radius of the plasma.

Isoflux control exploits the capability of the real-time EFIT plasma shape reconstruction algorithm to calculate the magnetic flux at specified locations within the tokamak vacuum vessel. Figure 2.1 shows a typical isoflux control configuration in NSTX. The controlled parameters are the values of flux at the pre-specified control points along with the X-point r and z positions. By requiring that the flux at each control point be equal to the same value, the controller forces the same flux contour to pass through all of these control points. By choosing this value equal to the flux at the X-point, this flux contour must be the last closed flux surface, or separatrix. The desired separatrix location is specified by selecting one of a large number of control points along each of several control segments. An X-point control grid is used to assist in calculating the X-point location by providing detailed flux and field information

at a number of closely spaced points in the vicinity of the X-point.

At present, NSTX combines a relatively simple non-model-based PID position and current control (PCC) algorithm during the ramp-up phase of the discharge with a non-model-based PID rtEFIT/isoflux control algorithm [19]. The transition between algorithms has been implemented using fuzzy logic. During the rtEFIT/isoflux phase, the errors between the reference and control-point fluxes are used as the inputs to the PID controllers. In practice, the various coils are assigned to the control points on a one-to-one basis. The X-point is assumed to be inside a control region (Figure 2.1), and its location is found iteratively at each time step. The r and z locations of the X-point are controlled by requiring the poloidal field (PF) coils to adequately control the magnetic field of the X-point. If the X-point is located outside this region, the code extrapolates using gradients.

2.2.2 Plant Model

The system, which is composed of the plasma, shaping coils, and passive structure, is described using circuit equations derived from Faraday's Law and radial and vertical force balance relations for a particular plasma equilibrium. The result is a series of circuit equations describing the linearized response of the conductor-plasma system to voltages applied to the active conductors. The mapping from currents to outputs is expressed explicitly in terms of current deviations from the equilibrium values. The linearized model equations for the PF coil current, vessel current, and plasma current can be expressed as:

$$\begin{aligned} M^*_{cc}\dot{I}_c + R_c I_c + M^*_{cv}\dot{I}_v + M^*_{cp}\dot{I}_p &= V_c \\ M^*_{vv}\dot{I}_v + R_v I_v + M^*_{vc}\dot{I}_c + M^*_{vp}\dot{I}_p &= 0 \\ L^*_p\dot{I}_p + R_p I_p + M^*_{pc}\dot{I}_c + M^*_{pv}\dot{I}_v &= V_{no} \end{aligned} \tag{2.1}$$

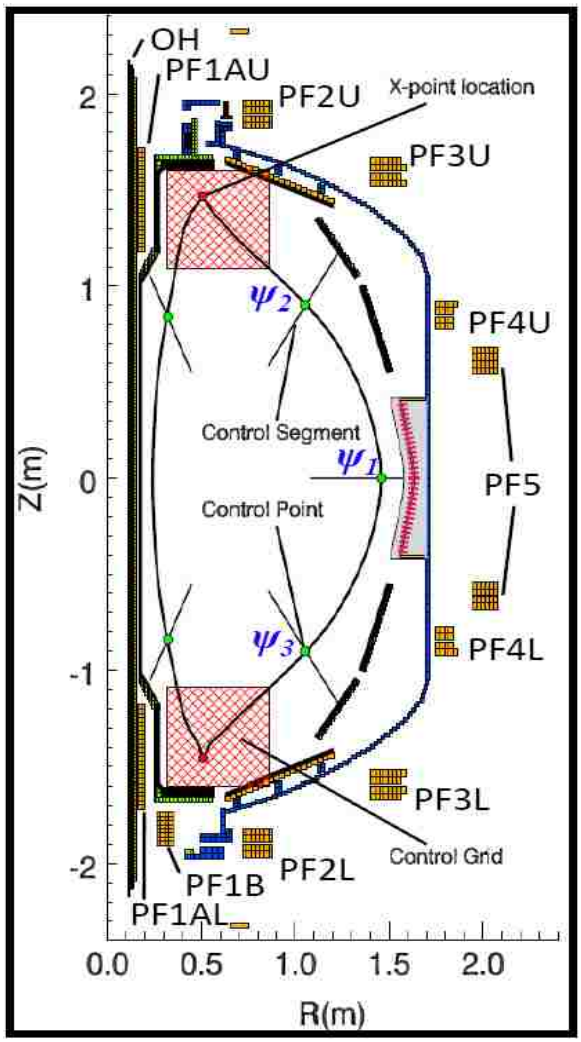

Figure 2.1: NSTX Isoflux Control Configuration

where I_c, I_v, and I_p represent the currents in the PF coils, vessel, and plasma respectively, R_c, R_v, and R_p represent the PF coils, vessel, and plasma resistances respectively, M^*_{ab} (with $L^*_p = M^*_{pp}$) represents the plasma-modified mutual inductance matrix where $a, b \in \{c, v, p\}$, V_c represents the vector of voltages applied to the PF coils, and V_{no} represents the effective voltage applied to drive plasma current by noninductive sources (no noninductive current source is considered in this work, i.e., $V_{no} = 0$).

For control design and simulation purposes, the linearized plasma response model

(2.1) is written in state space form [57]

$$\dot{x} = Ax + Bu, \qquad \delta y = C\delta x \tag{2.2}$$

where $x = [I_c^T \; I_v^T \; I_p^T]^T$ and $u = [V_c^T \; 0 \; V_{no}^T]^T$. We define $\delta y = y - y_{eq}$ and $\delta x = x - x_{eq}$ where y_{eq} and x_{eq} are the values of the equilibrium outputs and states from which the model is derived. The state vector $x \in \Re^n$ $(n = 45)$ represents the currents in the ohmic (OH) coil, PF coils, vessel and plasma. The input vector $u \in \Re^m$ $(m = 9)$ represents the PF coil voltages shown in Figure 2.1 (PF4U/L are not currently used for magnetic control). The output vector $y \in \Re^p$ $(p = 8)$ represents the fluxes ψ_1, ψ_2, ψ_3 at the control points, the magnetic field B_r and B_z at the desired X point location, the plasma radial and vertical positions R_p and Z_p, and the plasma current I_p.

2.3 Control System Design for the Current Flat-top Phase

2.3.1 Control System Structure

The proposed control architecture, shown in Figure 2.2, is composed of three loops. The first loop is devoted to plasma current regulation (proportional, integral and derivative (PID) controller), the second loop is dedicated to plasma radial and vertical position stabilization (PID controller), and the third loop is used to control the plasma shape and X-point location (multi-input-multi-output (MIMO) H_∞ controller).

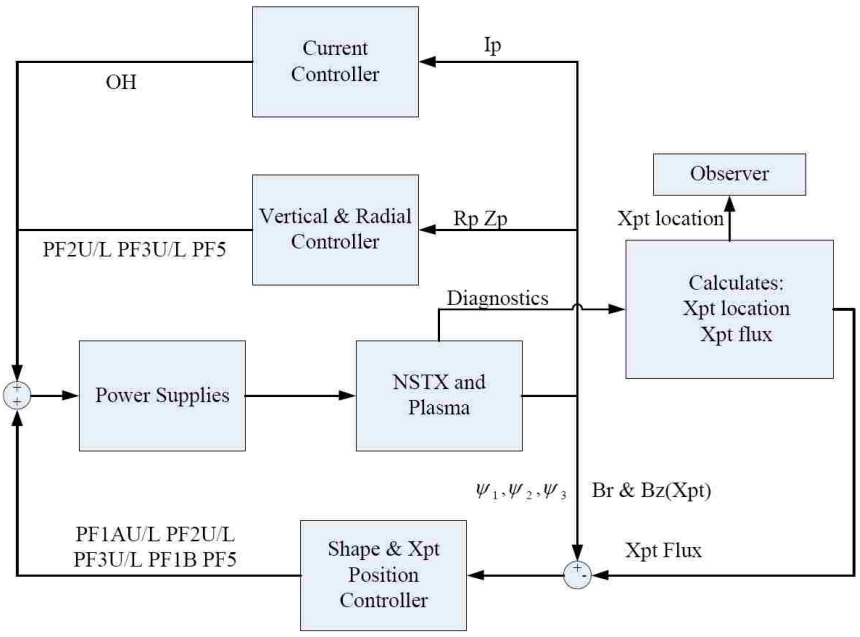

Figure 2.2: NSTX Control System Architecture

2.3.2 Plasma Current Controller

The ohmic (OH) coil is dedicated to plasma current regulation. The proposed plasma current controller is written as

$$V_{OH} = G_P^{I_p} \Delta I_p + G_I^{I_p} \int_0^t \Delta I_p dt + G_D^{I_p} \frac{d\Delta I_p}{dt}, \tag{2.3}$$

where $\Delta I_p = I_p - I_P^{ref}$ and I_P^{ref} denotes the reference plasma current. The parameters $G_P^{I_p}$, $G_I^{I_p}$, and $G_D^{I_p}$ are the plasma current PID error gains.

2.3.3 Plasma Position Controller

Since the plasma is elongated in NSTX, a servo system is required to stabilize the plasma position. Poloidal field coils PF2U/L, PF3U/L, and PF5 are used for plasma radial position control while poloidal field coils PF2U/L and PF3U/L are used for plasma vertical position control. The selection of these sets of actuators is the result

of a sensitivity study carried out for the steady-state transfer function.

The proposed radial position controller is written as

$$\Delta V_{PF2_R}^{U/L} = \Delta V_{PF3_R}^{U/L} = \Delta V_{PF5_R} = V_{R_p} \tag{2.4}$$

$$V_{R_p} = G_P^{R_p} \Delta R_P + G_I^{R_p} \int_0^t \Delta R_P dt + G_D^{R_p} \frac{d\Delta R_P}{dt} \tag{2.5}$$

where $\Delta R_p = R_p - R_P^{ref}$ with R_P^{ref} denoting the reference plasma radial position. The parameters $G_P^{R_p}$, $G_I^{R_p}$, and $G_D^{R_p}$ are the plasma current proportional, integral and derivative (PID) error gains.

The proposed vertical position controller is written as

$$\Delta V_{PF2_Z}^{j} = \Delta V_{PF3_Z}^{j} = V_{Z_p}(j) \tag{2.6}$$

$$V_{Z_p}(j) = (-1)^j \left(G_P^{Z_p} \Delta Z_P + G_I^{Z_p} \int_0^t \Delta Z_P + G_D^{Z_p} \frac{d\Delta Z_P}{dt} \right) \tag{2.7}$$

where the superscript $j = 0, 1$ refers to upper and lower PF coils respectively. The parameters $G_P^{Z_p}$, $G_I^{Z_p}$, and $G_D^{Z_p}$ are the PID error gains.

2.3.4 Plasma Shape and X point Location Controller

The separate design of the plasma current and position controllers transforms the shape control problem into an output tracking problem. The tracking error is defined as $e(t) = r(t) - y(t)$, where the system output $y(t)$ is defined as the magnetic flux at three control points and the magnetic field components at the desired X-point location, i.e., $y = [\psi_1 \ \psi_2 \ \psi_3 \ B_r \ B_z]^T$ and $r(t)$ is the desired reference trajectory. The system input is defined as $u = [V_{PF1U} \, V_{PF2U} \, V_{PF3U} \, V_{PF5} \, V_{PF3L} \, V_{PF2L} \, V_{PF1L} \, V_{PF1B}]^T$. The control goal is to guarantee closed-loop stability while minimizing a quadratic cost function that weights the tracking error.

A MIMO H_∞ controller is introduced in this section. The plasma shape and X-point location control algorithm is summarized by the following steps: (1) calculate ψ_1, ψ_2 and ψ_3 at the control points, and B_r and B_z at the desired X-point location; (2) estimate the actual X-point location and compute the flux at this point which is defined as ψ_{ref}; (3) make the flux at the control points track the flux ψ_{ref} and make B_r and B_z at the desired X-point location go to zero.

The relation between the inputs and the outputs is the linear model (2.2) which is expressed in terms of its transfer function $P(s)$, i.e.,

$$\frac{Y(s)}{U(s)} = P(s) = C(sI - A)^{-1}B \tag{2.8}$$

where s denotes the Laplace variable and $Y(s)$ and $U(s)$ denote the Laplace transform of output and input vectors respectively. Assuming a constant reference $\bar{r}$ and closed-loop stabilization, the system can be maintained at steady state around the equilibrium. Under these assumptions, the input-output relation in steady state is expressed as

$$\bar{y} = \bar{P}\bar{u} = -CA^{-1}B\bar{u} \tag{2.9}$$

where $\bar{y}$ is the steady state output, $\bar{u}$ is the steady state input, and $\bar{P}$ is the steady state transfer function (i.e. $s \to 0$). Therefore, the closed-loop system is specified by

$$\bar{y} = \bar{P}\bar{u} \qquad \bar{u} = \bar{\hat{K}}\bar{e} = \bar{\hat{K}}\left(\bar{r} - \bar{y}\right), \tag{2.10}$$

where $\hat{K}(s)$ represents the transfer function of the controller and $\bar{\hat{K}} = \hat{K}(0)$.

We consider the problem of minimizing a steady-state cost function given by

$$\bar{J} = \lim_{t\to\infty} e^T(t)Qe(t) = \bar{e}^T Q\bar{e} \tag{2.11}$$

where $Q \in \Re^{p \times p}$ is a symmetric positive definite weighting matrix and p is the number of outputs. In order to weight the control effort, another positive definite weighting matrix $R \in \Re^{m \times m}$ is also introduced where m is the number of inputs. We then define the "weighted" steady-state transfer function as

$$\tilde{P} = Q^{1/2} \bar{P} R^{-1/2}, \tag{2.12}$$

and write its singular value decomposition (SVD) as

$$\tilde{P} = USV^T, \tag{2.13}$$

where $S = \text{diag}(\sigma_1, \sigma_2, \cdots, \sigma_m) \in \Re^{m \times m}$, $U \in \Re^{p \times m}$ $(U^T U = I)$, and $V \in \Re^{m \times m}$ $(V^T V = VV^T = I)$. The steady-state input-output relation is now expressed as

$$\bar{y} = Q^{-1/2} \tilde{P} R^{1/2} \bar{u} = Q^{-1/2} USV^T R^{1/2} \bar{u}. \tag{2.14}$$

By invoking the properties of the SVD, we note that the columns of the matrix $Q^{-1/2}US$ define a basis for the subspace of obtainable steady-state output values. Therefore, we can always write

$$\bar{y} = Q^{-1/2} US \bar{y}^* \iff \bar{y}^* = S^{-1} U^T Q^{1/2} \bar{y} \tag{2.15}$$

where $\bar{y}^* \in \Re^m$. This implies that we will only be able to track the component of the reference vector $\bar{r}$ that lies in this subspace. We now write the reference vector as the sum of trackable components $\bar{r}_t$ and non-trackable components $\bar{r}_{nt}$, i.e., $\bar{r} = \bar{r}_t + \bar{r}_{nt}$, where

$$\bar{r}_t = Q^{-1/2} US \bar{r}^* \iff \bar{r}^* = S^{-1} U^T Q^{1/2} \bar{r} \tag{2.16}$$

with $\bar{r}^* \in \Re^m$ and $S^{-1}U^TQ^{1/2}\bar{r}_{nt} = 0$. By defining

$$\bar{u}^* = V^T R^{1/2} \bar{u}, \tag{2.17}$$

the relationship between $\bar{y}^*$ and $\bar{u}^*$ is obtained by using (2.14) as

$$\bar{y}^* = S^{-1}U^TQ^{1/2}\bar{y} = S^{-1}U^TQ^{1/2}Q^{-1/2}USV^TR^{1/2}\bar{u} = \bar{u}^* \tag{2.18}$$

and a one-to-one relationship between the inputs and outputs is obtained, and the new system is a square decoupled system. The steady state error is now written as

$$\bar{e} = \bar{r} - \bar{y} = Q^{-1/2}US(\bar{r}^* - \bar{y}^*). \tag{2.19}$$

Substituting this expression into (2.11), the performance index is expressed as

$$\bar{J} = (\bar{r}^* - \bar{y}^*)^T S^2 (\bar{r}^* - \bar{y}^*) = \sum_{i=1}^{m} \sigma_i^2 (\bar{r}_i^* - \bar{y}_i^*)^2. \tag{2.20}$$

The goal of the shape controller is to minimize the performance index $\bar{J}$. However, it is usually the case where $\sigma_1 > \cdots \sigma_k \gg \sigma_{k+1} > \cdots > \sigma_m > 0$. Note that the singular value σ_i, for $i = 1, \ldots, m$, is the weight parameter for the i^{th} component of the tracking error. Therefore, it is possible that with the intent of minimizing $\bar{J}$ in (2.20) we will spend a lot of control effort to minimize the i^{th} component of the tracking error, for $i > k$, which has a very small contribution to the overall value of the cost function. To avoid spending a lot of control effort for a marginal improvement of the cost function value, we partition the singular value set into significant singular

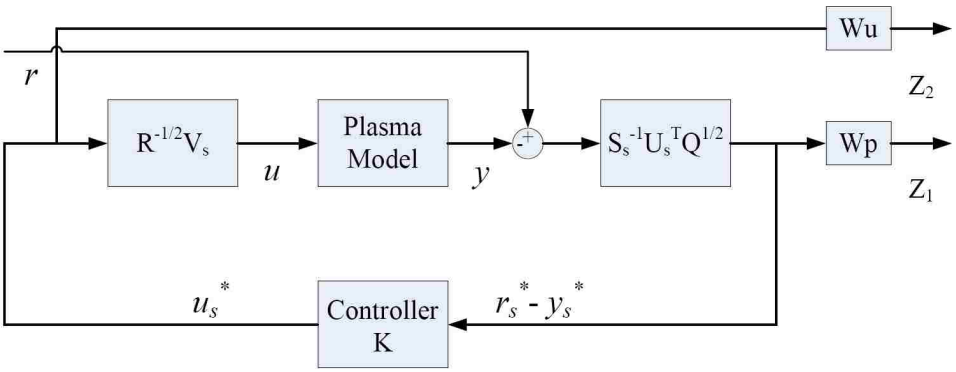

Figure 2.3: H_∞ Control Formulation

values S_s and negligible singular values S_n. We then write

$$U = \begin{bmatrix} U_s & U_n \end{bmatrix}, V = \begin{bmatrix} V_s & V_n \end{bmatrix}, S = \begin{bmatrix} S_s & 0 \\ 0 & S_n \end{bmatrix} \tag{2.21}$$

to obtain a reduced form of the cost function defined in (2.20)

$$\bar{J}_s = \sum_{i=1}^{k} \sigma_i^2 (\bar{r}_i^* - \bar{y}_i^*)^2 = (\bar{r}_s^* - \bar{y}_s^*)^T S_s^2 (\bar{r}_s^* - \bar{y}_s^*) \tag{2.22}$$

where

$$\bar{r}_s^* = S_s^{-1} U_s^T Q^{1/2} \bar{r}, \quad \bar{y}_s^* = S_s^{-1} U_s^T Q^{1/2} \bar{y}, \quad \bar{u}_s^* = V_s^T R^{1/2} \bar{u}. \tag{2.23}$$

2.3.5 Design of H_∞ MIMO Controller

The mixed sensitivity H_∞ method is used to design the shape and X-point location controller. The design is based on the reduced-order plasma model described above. The structure of the proposed controller is shown in the Figure 2.3 where two frequency-dependent weighting functions W_p and W_u are introduced. The signals of the general control configuration are defined as the control input $\tilde{u} = u_s^*$, the tracking error $\tilde{e} = r_s^* - y_s^*$, the exogenous reference $\tilde{r} = \bar{r}$ and the external performance signal

$\tilde{z}$.

Using the Laplace Transform we can obtain a frequency-domain representation of the overall system. The plant $G(s)$ is the transfer function from the exogenous reference $\tilde{r}$ to the performance output $\tilde{z} = \begin{bmatrix} \tilde{z}_1 & \tilde{z}_2 \end{bmatrix}^T$ and expressed as

$$\begin{bmatrix} \tilde{z} \\ \tilde{e} \end{bmatrix} = \begin{bmatrix} \tilde{z}_1 \\ \tilde{z}_2 \\ \tilde{e} \end{bmatrix} = G(s) \begin{bmatrix} \tilde{r} \\ \tilde{u} \end{bmatrix} = \begin{bmatrix} G_{11}(s) & G_{12}(s) \\ G_{21}(s) & G_{22}(s) \end{bmatrix} \begin{bmatrix} \tilde{r} \\ \tilde{u} \end{bmatrix}$$

$$\tilde{u} = K(s)\tilde{e}. \tag{2.24}$$

The closed-loop transfer function from $\tilde{r}$ to $\tilde{z}$ is given by the lower linear fractional transformation (LFT), i.e.,

$$T_{zr} = F_l(G, K) = G_{11} + G_{12}K(I - G_{22}K)^{-1}G_{21} \tag{2.25}$$

where

$$\begin{aligned} G_{11} &= \begin{bmatrix} W_p S_s^{-1} U_s^T Q^{1/2} \\ 0 \end{bmatrix} \\ G_{12} &= \begin{bmatrix} -W_p S_s^{-1} U_s^T Q^{1/2} P R^{-1/2} V_s \\ W_u \end{bmatrix} \\ G_{21} &= S_s^{-1} U_s^T Q^{1/2} \\ G_{22} &= -S_s^{-1} U_s^T Q^{1/2} P R^{-1/2} V_s. \end{aligned}$$

We define the transfer function M_s as

$$M_s = (I + S_s^{-1} U_s^T Q^{1/2} P R^{-1/2} V_s K)^{-1} S_s^{-1} U_s^T Q^{1/2}, \tag{2.26}$$

and write the closed-loop transfer function as

$$T_{zr} = F_l(G, K) = \begin{bmatrix} W_p M_s \\ W_u K M_s \end{bmatrix}. \tag{2.27}$$

We seek a controller $K(s)$ that stabilizes the system and minimizes the H_∞ norm of the transfer function $T_{zr}(G, K)$ between $\tilde{r}$ and $\tilde{z}$, i.e.,

$$\min_{K(s)} \|T_{zr}(G, K)\|_\infty = \min_{K(s)} (\sup_\omega \bar{\sigma}[T_{zr}(G, K)(j\omega)]) = \min_{K(s)} \left\| \begin{matrix} W_p M_s \\ W_u K M_s \end{matrix} \right\|_\infty ,$$

where $\bar{\sigma}$ represents the maximum singular value. This statement defines a mixed sensitivity H_∞ control problem, where the goal is to minimize both the error tracking ($W_p M_s$) and the control effort ($W_u K M_s$) at the same time. The weighting functions W_p and W_u are parameterized as

$$W_p(s) = \frac{\frac{s}{M_1} + w_{b1}}{s + w_{b1} A_1} K_p, \quad W_u(s) = \frac{s + w_{b2} A_2}{\frac{s}{M_2} + w_{b2}} K_u,$$

where the coefficients M_i, A_i, w_{bi}, for $i = 1, 2$, as well as K_p and K_u, are design parameters in the H_∞ control synthesis.

Finally, the overall plasma shape and X-point location controller can be written as

$$\hat{K}(s) = \frac{U(s)}{Y(s)} = R^{-1/2} V_s K(s) S_s^{-1} U_s^T Q^{1/2}. \tag{2.28}$$

2.3.6 Simulation Results

The H_∞ MIMO controller design is based on a linear plasma response model for shot ♯124616. The reference values for the radial position, vertical position, plasma current

Table 2.1: Current and Position Control Gains (Current Flat-top Phase)

Controller	G_p	G_i	G_d
Current Control	1	0.02	0.1
Radial Control	800	100	1
Vertical Control	200	0	10

Table 2.2: H_∞ Control Parameters

Weight Function	M_i	w_{bi}	A_i	K_i
W_p	100	0.01	7500	10^6
W_u	500	1	75	10^{-6}

and X-point location are those of the equilibrium around which the linearized model is obtained. The reference value for the flux at the control points is equal to that of the X-point, which is computed every 10 ms.

The PID parameters for the plasma current, vertical position and radial position loops are shown in the Table 2.1. The weight matrices Q and R are chosen to minimize the tracking error and optimize the control effort. Poloidal field coils PF3U/L and PF5 play the most significant role in shaping the plasma. Therefore, the matrices are set as $Q = \text{diag}\begin{bmatrix} 1 & 1 & 1 & 1 & 1 \end{bmatrix}$ and $R = \text{diag}\begin{bmatrix} 10 & 1.5 & 5 & 1 & 2.5 & 2.5 & 10 & 10 \end{bmatrix}$. The parameters for the H_∞ control synthesis are shown in Table 2.2. Only two significant singular values are retained during the control design procedure.

The plasma positions are controlled by the two independent PID control loops (2.4)–(2.5) and (2.6)–(2.7). The time responses for the plasma radial and vertical positions are shown in Figure 2.4 (a). The vertical position is stabilized by the controller and a steady-state values is quickly achieved. The plasma current is controlled by the PID control loop (2.3). Figure 2.4 (b) shows the time evolution for the plasma current and compare it with its reference. The tracking error is less than 0.5%. Figure 2.4 (c) shows both the flux at the X-point and the flux at the three control points (ψ_1, ψ_2,

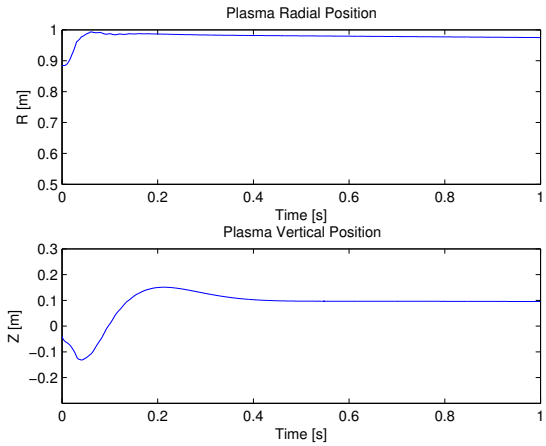

(a)

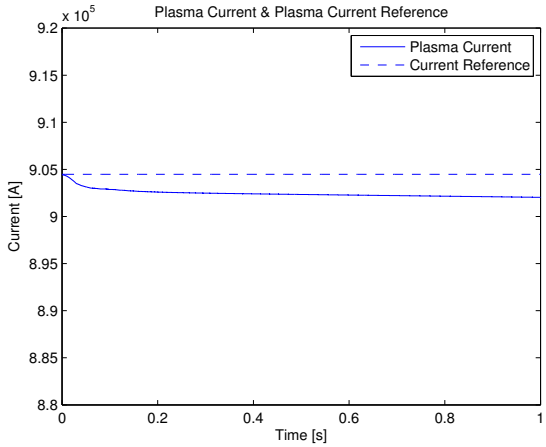

(b)

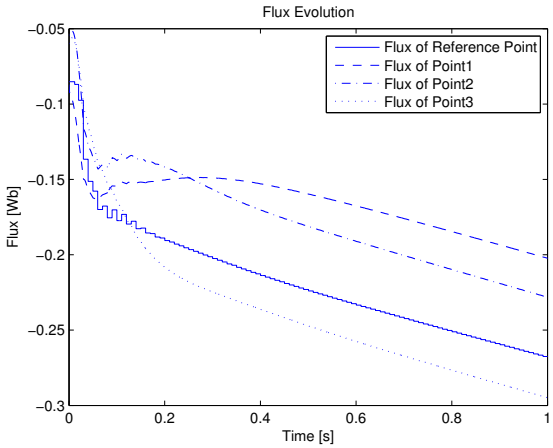

(c)

Figure 2.4: Closed-loop evolution: (a) Plasma radial and vertical position; (b) Plasma current; (c) Magnetic flux at the control points.

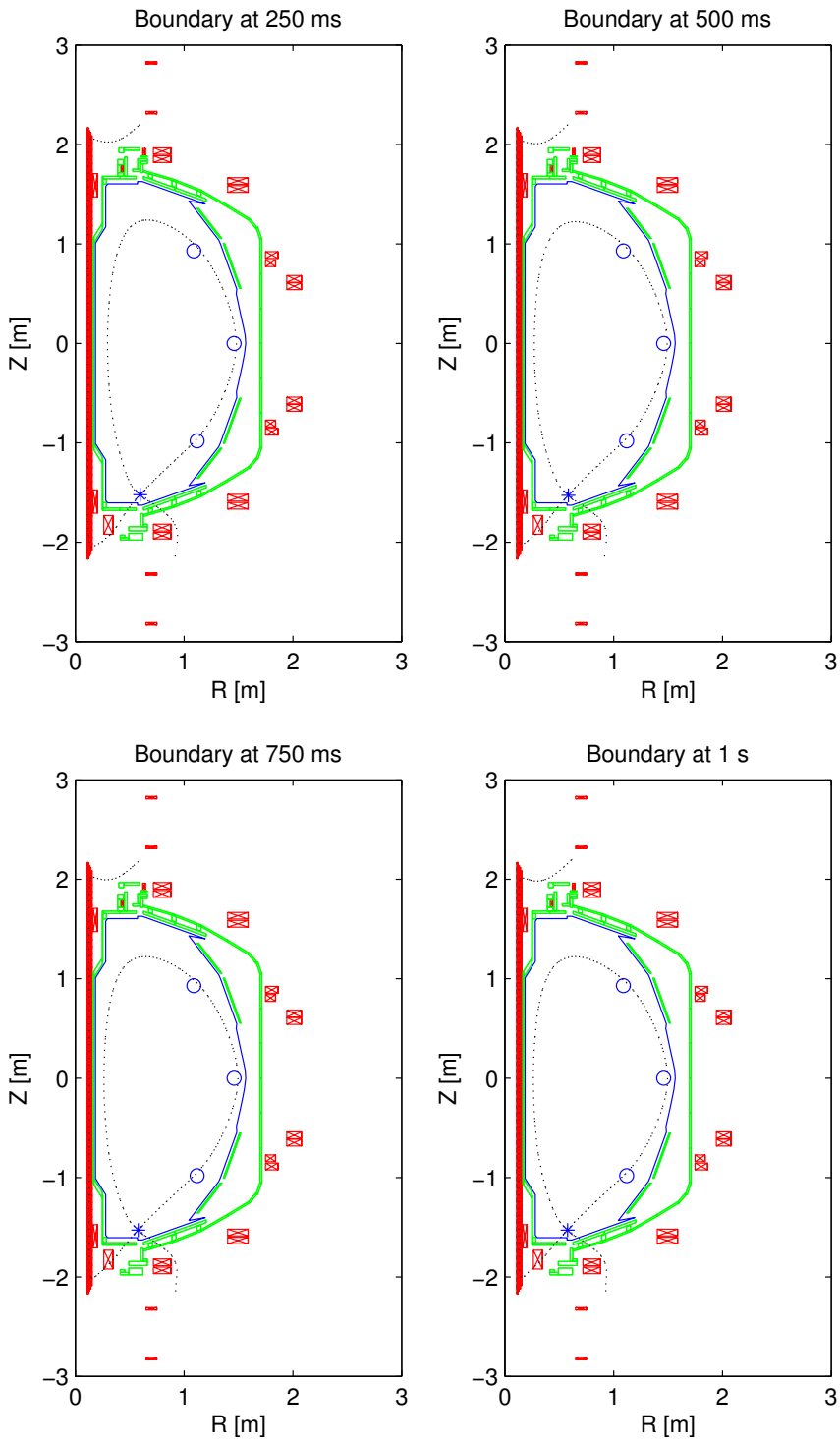

Figure 2.5: Plasma Boundary at 250 ms, 500 ms, 750 ms and 1 s

and ψ_3). The flux of at the control points track the flux at the X-point with a small constant tracking error. After about 400 ms, the system achieves steady-state tracking errors of less than 0.02 Wb. Simulations results confirm that coils PF3U/L and PF5 significantly influence the flux at the control points significantly. The value of the tracking error can be reduced by modifying relation between the weight matrices Q and R at the expense of a higher control effort.

The plasma boundary is defined as the outermost closed magnetic surface entirely contained in the vacuum vessel. The boundary flux value, which identifies the plasma boundary surface, is determined by the flux at X point. The goal of the controller is to keep the plasma boundary surface located inside the vacuum vessel and to achieve pre-specified shapes. A series of four plasma boundary shapes at different times during the simulated discharge is shown in the Figure 2.5. The blue circles represent the control points and the blue asterisk represents the actual location of the X point. The voltages of the PF coils are regulated according to the H_∞ control law (2.28) in order to keep the plasma boundary at the control points and to regulate the X-point location around the desired value.

Based on the simulation results above, the control scheme proves to be successful in stabilizing the plasma position while regulating the plasma current and keeping the plasma shape and X-point location as specified.

2.4 Control System Design for the Current Ramp-up Phase

During the plasma current ramp-up phase, the MHD equilibrium continually changes, and as a result, the plasma response model (2.2) changes. In this work, 26 scenario points from the experimental shot #124616 from 91 ms to 391 ms are chosen to

describe the plasma equilibrium evolution. The equilibrium plasma current, radial and vertical position, and shape of these 26 models represent the described reference trajectories of the system. Therefore, the control goal is to drive the system to these specified reference trajectories with as little control effort as possible.

2.4.1 Plasma Current Controller

The OH coil is dedicated to plasma current regulation, and the proposed plasma current controller in the current ramp-up phase is the same with (2.3).

2.4.2 Plasma Position Controller

Because the plasma response model (2.2) changes during the ramp-up phase, an adaptive PID controller is proposed to improve the tracking performance of the closed-loop system when compared with a static PID controller. In order to achieve this goal, an adjusted parameter k_c is introduced to the PID controller. The goal is to minimize the closed-loop cost function $J(k_c) = e(k_c)^2/2$. The error e is defined as $e(k_c, t) = r(t) - y(k_c, t)$, where $r(t)$ is the reference and $y(k_c, t)$ is the output defined as the actual radial and vertical position of plasma. In order to make J small, it is reasonable to change k_c in the direction of the negative gradient of J, which is defined as

$$\dot{k}_c = \frac{dk_c}{dt} = -\lambda \frac{\partial J}{\partial k_c} = -\lambda \frac{\partial J}{\partial e} \frac{\partial e}{\partial k_c} = \lambda e \frac{\partial y}{\partial k_c} \tag{2.29}$$

where λ is the step length, and $\partial y/\partial k_c$ is the sensitivity derivative. The output is expressed as $y = Pu$, where P is the transfer function of the plasma model (2.2), and the input u is defined as $u = k_c K_{PID} e$ where K_{PID} is a PID controller. The goal is to make $y(k_c, t) = r(t)$ by choosing the optimal value of the adjusted parameter k_c, which is denoted k_c^*. The optimal reference is assumed to be $r = P k_c^* K_{PID} e =$

$(k_c^*/k_c)Pk_cK_{PID}e = (k_c^*/k_c)y$ [58]. The adjusted parameter k_c is therefore expressed as

$$\dot{k}_c = \lambda e \frac{\partial y}{\partial k_c} = \lambda e \frac{\partial \frac{(rk_c)}{k_c^*}}{\partial k_c} = \frac{\lambda}{k_c^*} er = \nu er \tag{2.30}$$

where ν is the adaptive gain.

The proposed radial position controller is written as

$$\Delta V_{PF2_R}^{U/L} = \Delta V_{PF3_R}^{U/L} = \Delta V_{PF5_R} = V_{R_p}, \tag{2.31}$$

$$V_{R_p} = k_{cr}(G_P^{R_p} \Delta R_P + G_I^{R_p} \int_0^t \Delta R_P dt + G_D^{R_p} \frac{d\Delta R_P}{dt}), \tag{2.32}$$

where $\Delta R_p = R_p - R_P^{ref}$, R_P^{ref} denotes the reference plasma radial position, $\dot{k}_{cr} = \nu_r \Delta R_p R_P^{ref}$ denotes the radial adjusted parameter, and ν_r denotes the radial adaptive gain. The parameters $G_P^{R_p}$, $G_I^{R_p}$, and $G_D^{R_p}$ are the plasma radial position PID error gains.

The proposed vertical position controller is written as

$$\Delta V_{PF2_Z}^{j} = \Delta V_{PF3_Z}^{j} = V_{Z_p}(j), \tag{2.33}$$

$$V_{Z_p}(j) = (-1)^j k_{cz}(G_P^{Z_p} \Delta Z_P + G_I^{Z_p} \int_0^t \Delta Z_P + G_D^{Z_p} \frac{d\Delta Z_P}{dt}), \tag{2.34}$$

where $\Delta Z_p = Z_p - Z_P^{ref}$, Z_P^{ref} denotes the reference plasma vertical position, $\dot{k}_{cz} = \nu_z \Delta Z_p Z_P^{ref}$ denotes the vertical adjusted parameter, ν_z denotes the vertical adaptive gain, and the superscript $j \in 0, 1$ refers to upper and lower PF coils respectively. The parameters $G_P^{Z_p}$, $G_I^{Z_p}$, and $G_D^{Z_p}$ are the plasma vertical position PID error gains.

The voltage offsets $\Delta V_{PFi_R}^{j}$ and $\Delta V_{PFi_Z}^{j}$ are added to the voltage shape control requests.

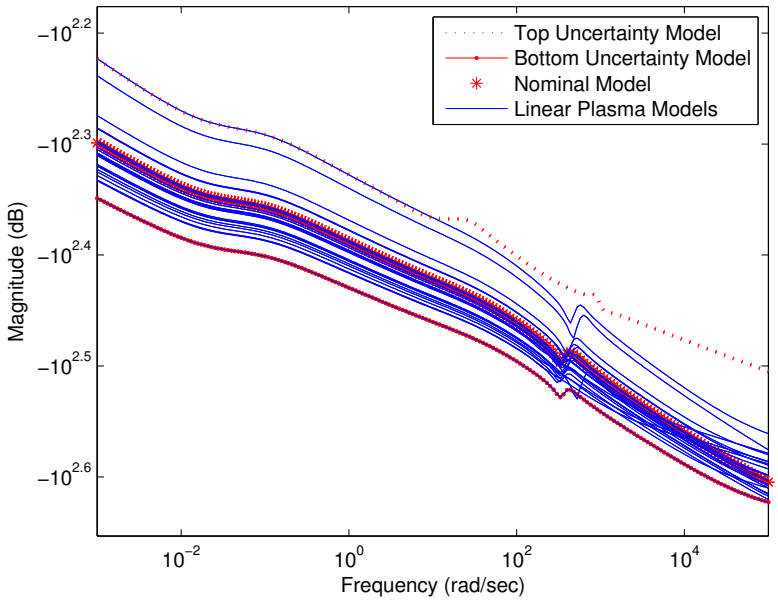

Figure 2.6: Frequency Study of Plasma Models

2.4.3 Plasma Shape and X-point Location Controller

A frequency study of the family of the decoupled plasma models discussed in section 2.3.4, which preserve the dynamic character of the MHD equilibrium evolution during the current ramp-up phase, shows that the models do not have a large magnitude difference, as shown in Figure 2.6. This suggests it is possible to develop a tracking control system with one robust controller. Based on this frequency study, the linear model at 115 ms, which is denoted as P_{top}, has the highest magnitude over the frequency range considered, and the model at 391 ms, which is denoted as P_{bot}, has the lowest magnitude. The model at 211 ms is chosen as the nominal model, which is denoted as P_0. The family of plasma models can be considered as one time varying state-space system, which is written as an uncertain state-space model and formulated into a robust control framework.

By defining the matrix

$$M = \begin{bmatrix} A & B \\ C & D \end{bmatrix}, \tag{2.35}$$

the transfer function of a linear system with state-space matrices A, B, C, and D can be written as a linear fractional transformation (LFT) as

$$P(s) = F_u\left(M, \frac{1}{s}I\right) = C(sI - A)^{-1}B + D. \tag{2.36}$$

By defining the matrices

$$M_0 = \begin{bmatrix} A_0 & B_0 \\ C_0 & D_0 \end{bmatrix}, \quad \Delta_i = \begin{bmatrix} \Delta A_i & \Delta B_i \\ \Delta C_i & \Delta D_i \end{bmatrix}, \tag{2.37}$$

where

$$\begin{aligned} \Delta A_i &= A_i - A_0, & \Delta B_i &= B_i - B_0, \\ \Delta C_i &= C_i - C_0, & \Delta D_i &= D_i - D_0, \end{aligned} \tag{2.38}$$

and $i \in 1, 2$ refers to the top and bottom uncertainty respectively, the state-space system matrices are now written as uncertain matrices as

$$\begin{aligned} A &= A_0 + \sum_{i=1}^{2} \delta_i \Delta A_i, \quad B = B_0 + \sum_{i=1}^{2} \delta_i \Delta B_i, \\ C &= C_0 + \sum_{i=1}^{2} \delta_i \Delta C_i, \quad D = D_0 + \sum_{i=1}^{2} \delta_i \Delta D_i, \end{aligned} \tag{2.39}$$

where $\delta_1 \in [0, 1]$ and $\delta_2 \in [0, 1]$. By conducting a frequency analysis of the uncertain model of the system (2.39), the uncertain model is proven to capture the behavior of the family of reduced order decoupled plasma models as shown in Figure 2.6.

The uncertainty can be formulated into a LFT by achieving the smallest possible number of repeated blocks by employing the method outlined in [59]. Thus, the matrix ΔM_i is formed as

$$\Delta M_i = \begin{bmatrix} \Delta A_i & \Delta B_i \\ \Delta C_i & \Delta D_i \end{bmatrix}. \tag{2.40}$$

By using singular value decomposition and grouping terms, the matrix ΔM_i is expressed as

$$\Delta M_i = U_i \Sigma_i V_i^T = (U_i \sqrt{\Sigma})(\sqrt{\Sigma} V_i^T) = \begin{bmatrix} L_i \\ W_i \end{bmatrix} \begin{bmatrix} R_i \\ Z_i \end{bmatrix}^T. \tag{2.41}$$

By employing (2.41), the uncertainty is written as

$$\delta_i \Delta M_i = \begin{bmatrix} L_i \\ W_i \end{bmatrix} \begin{bmatrix} \delta_i I_{q_i} \end{bmatrix} \begin{bmatrix} R_i \\ Z_i \end{bmatrix}^T, \tag{2.42}$$

where q_i is the rank of the matrix ΔM_i. The matrix M, defined in (2.35), is finally expressed as

$$M = M_0 + \sum_{i=1}^{2} \delta_i \Delta M_i = H_{11} + H_{12} \Delta H_{21}, \tag{2.43}$$

where

$$\begin{aligned} H_{11} &= \begin{bmatrix} A_0 & B_0 \\ C_0 & D_0 \end{bmatrix}, \qquad H_{12} = \begin{bmatrix} L_1 & L_2 \\ W_1 & W_2 \end{bmatrix}, \\ H_{21} &= \begin{bmatrix} R_1^T & Z_1^T \\ R_2^T & Z_2^T \end{bmatrix}, \qquad \Delta = \begin{bmatrix} \delta_1 I_{q_1} & 0 \\ 0 & \delta_2 I_{q_2} \end{bmatrix}. \end{aligned} \tag{2.44}$$

The representation of the matrix M, defined in (2.43), is equal to the lower LFT

$$M = F_l(H, \Delta) = H_{11} + H_{12} \Delta H_{21}, \tag{2.45}$$

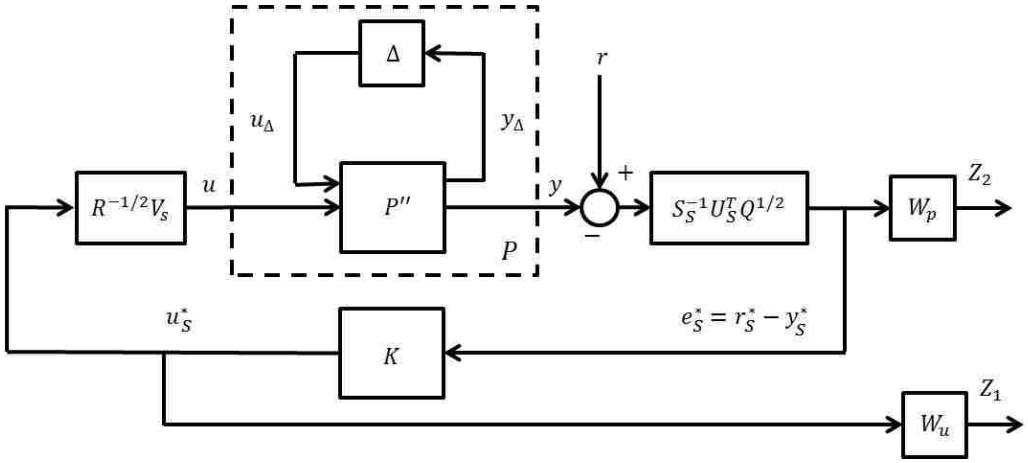

Figure 2.7: Shape Control System Design Structure

where

$$H = \begin{bmatrix} H_{11} & H_{12} \\ H_{21} & 0 \end{bmatrix}. \tag{2.46}$$

Using (2.36) and (2.45), the transfer function $P(s)$ between the output y and the input u is next expressed as

$$\begin{aligned} P(s) &= F_u\left(F_l(H,\Delta), \frac{1}{s}I\right) = F_l\left(F_u\left(H, \frac{1}{s}I\right), \Delta\right) \\ &= F_l(P', \Delta) = F_u(P'', \Delta), \end{aligned} \tag{2.47}$$

where $P' = \begin{bmatrix} P''_{22} & P''_{21} \\ P''_{12} & P''_{11} \end{bmatrix}$ and $P'' = \begin{bmatrix} P''_{11} & P''_{12} \\ P''_{21} & P''_{22} \end{bmatrix}$. Using the partition of the generalized plant P'', the input/output equations are

$$y_\Delta = P''_{11}u_\Delta + P''_{12}u, \quad y = P''_{21}u_\Delta + P''_{22}u.$$

The control goal is to design a $k \times k$ feedback controller K, where k is the number of significant singular values defined in (2.21), that can stabilize the system and keep the tracking error $e_s^* = r_s^* - y_s^*$ small. The corresponding block diagram of the system

is shown in Figure 2.7, where the weight functions $W_p(s)$ and $W_u(s)$ are parameterized as

$$W_p(s) = K_p \left(\frac{\frac{s}{M_1} + w_{b1}}{s + w_{b1} A_1} \right)^2, \; W_u(s) = K_u \left(\frac{s + w_{b2} A_2}{\frac{s}{M_2} + w_{b2}} \right)^2,$$

and the coefficients M_i, A_i, w_{bi}, for $i \in 1, 2$, as well as K_p and K_u, are design parameters.

The feedback system is now expressed in the conventional $\Delta - P^* - K$ robust control framework shown in Figure 2.8, where Δ is the uncertainty, P^* is the generalized plant, K is the feedback controller, $Z_1 = W_u u_s^*$, and $Z_2 = W_p e_s^*$. The input/output equations of the generalized plant P^* are expressed as

$$\begin{bmatrix} y_\Delta \\ Z_1 \\ Z_2 \\ e_s^* \end{bmatrix} = P^*(s) \begin{bmatrix} u_\Delta \\ r_s^* \\ u_s^* \end{bmatrix} = \begin{bmatrix} P_{11}^* & P_{12}^* & P_{13}^* \\ P_{21}^* & P_{22}^* & P_{23}^* \\ P_{31}^* & P_{32}^* & P_{33}^* \\ P_{41}^* & P_{42}^* & P_{43}^* \end{bmatrix} \begin{bmatrix} u_\Delta \\ r_s^* \\ u_s^* \end{bmatrix}, \tag{2.48}$$

where

$$\begin{aligned}
&P_{11}^* = P_{11}'', && P_{12}^* = 0, && P_{13}^* = P_{12}'', \\
&P_{21}^* = 0, && P_{22}^* = 0, && P_{23}^* = W_u, \\
&P_{31}^* = -W_p P_{21}'' S_s^{-1} U_s^T Q^{1/2}, && P_{32}^* = W_p S_s^{-1} U_s^T Q^{1/2}, && P_{33}^* = -W_p R^{-1/2} V_s P_{22}'' S_s^{-1} U_s^T Q^{1/2}, \\
&P_{41}^* = -P_{21}'' S_s^{-1} U_s^T Q^{1/2}, && P_{42}^* = S_s^{-1} U_s^T Q^{1/2}, && P_{43}^* = -R^{-1/2} V_s P_{22}'' S_s^{-1} U_s^T Q^{1/2}.
\end{aligned}$$

The closed-loop transfer function from the external input r_s^* to the external outputs $\begin{bmatrix} Z_1^T & Z_2^T \end{bmatrix}^T$ is defined as

$$T_{zr} = F_u(N, \Delta), \tag{2.49}$$

where $N = F_l(P^*, K)$. We seek a controller $K(s)$ that robustly stabilizes the system

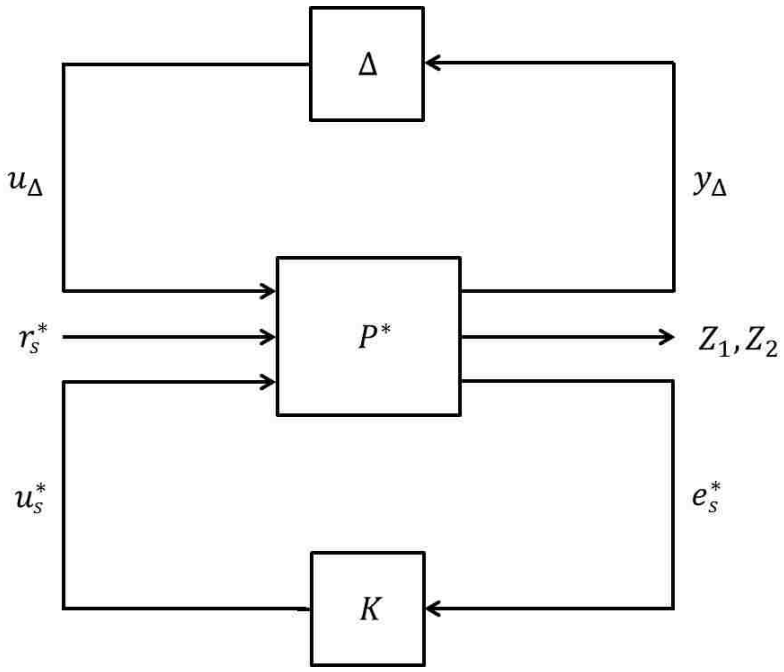

Figure 2.8: Model in $\Delta - P^* - K$ Robust Control Framework

and minimizes the H_∞ norm of the transfer function $T_{zr}(N, \Delta)$, i.e.,

$$\min_{K(s)} \|T_{zr}(N, \Delta)\|_\infty = \min_{K(s)} (\sup_\omega \bar{\sigma}[T_{zr}(N, \Delta)(j\omega)]), \tag{2.50}$$

where $\bar{\sigma}$ represents the maximum singular value. The control method employed in this work to achieve the control goal (2.50) is the μ synthesis design technique.

There is no direct method to synthesize a μ-optimal controller, however the DK-iteration method, which combines H_∞ synthesis and μ analysis, can be used to obtain an iterative solution. This method starts with an upper bound on μ in terms of the scaled singular value $\mu(N) \leq \min(\bar{\sigma}(DND^{-1})$. Then, we seek a controller that minimizes the peak value over frequency of this upper bound

$$\min_K (\min \left\| DN(K)D^{-1} \right\|_\infty).$$

The controller is designed by alternating between the two minimization problems until reasonable performance is achieved. The DK-iteration steps are summarized as follows: (1) K step: Synthesize an H_∞ controller for the scaled problem, $\min_K \|DN(K)D^{-1}\|_\infty$ with fixed $D(s)$. (2) D step: Find $D(j\omega)$ to minimize $\bar{\sigma}(DND^{-1}(j\omega))$ at each frequency with fixed N. (3) Fit the magnitude of each element of $D(j\omega)$ to a stable and minimum-phase transfer function $D(s)$ and go to step 1. The iteration continues until $\|DN(K)D^{-1}\|_\infty < 1$ or the H_∞ norm no longer decreases. The robust feedback controller K found by iteratively solving these minimization problems is written as

$$\begin{aligned} \dot{x}_c &= A_c x_c + B_c e_s^*, \\ u_s^* &= C_c x_c + D_c e_s^*, \end{aligned} \tag{2.51}$$

where A_c, B_c, C_c, and D_c are the controller system matrices, and x_c is the internal controller state.

To validate the designed controller, the robust stability of the closed-loop system is determined. The system is written in the $N-\Delta$ structure, and the robust stability is determined by evaluating the structured singular value

$$\mu(N_{11}(j\omega)) = \frac{1}{\min\{k_m | \det(I - k_m N_{11}\Delta) = 0\}} \tag{2.52}$$

where N_{11} is the transfer function from the input u_Δ to the output y_Δ. The closed-loop system is robustly stable for all allowable perturbations if and only if $\mu(N_{11}(j\omega)) < 1, \forall\omega$. Figure 2.9 shows a plot of the structed singular value μ versus frequency, and as can be seen $\mu < 1$ for all frequencies. Therefore, the closed-loop system is robustly stable. In other words, the controller stabilizes the whole family of models.

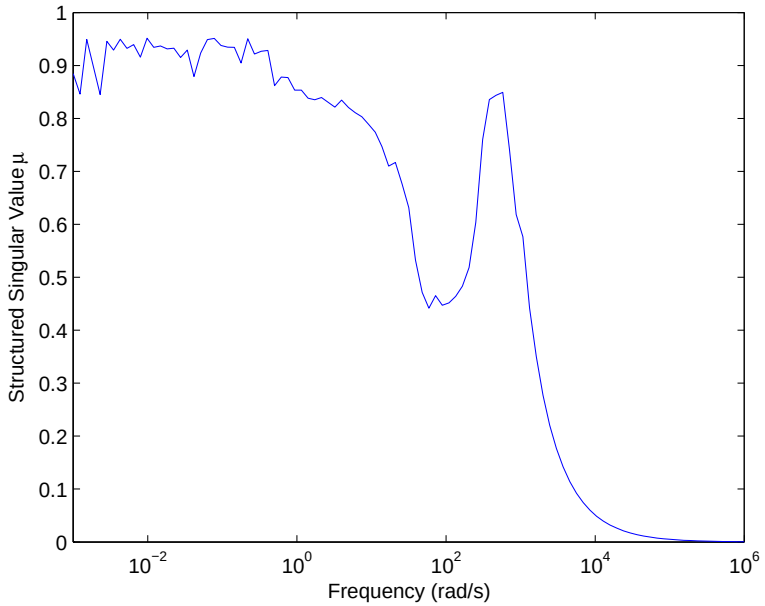

Figure 2.9: Structured Singular Value μ versus Frequency

Finally, the overall plasma shape and X-point location controller is written as

$$\hat{K}(s) = \frac{U(s)}{E(s)} = R^{-1/2} V_s K(s) S_s^{-1} U_s^T Q^{1/2} \tag{2.53}$$

where $E(s)$ denotes the Laplace transform of $e(t)$. The contribution to the coil voltages by the shape and X-point location controller is written as

$$\begin{aligned} V_{Shape} &= [\Delta V_{PF1A_s}^{U/L} \, \Delta V_{PF1B_s} \, \Delta V_{PF2_s}^{U/L} \, \Delta V_{PF3_s}^{U/L} \, \Delta V_{PF5_s}]^T \\ &= \mathcal{L}^{-1}\{\hat{K}(s)E(s)\} \end{aligned} \tag{2.54}$$

where $\mathcal{L}^{-1}$ denotes the inverse Laplace transform.

Table 2.3: Current and Position Control Gains (Current Ramp-up Phase)

Controller	G_p	G_i	G_d	ν_i
Current Control	1	0.02	0.1	
Radial Control	800	100	1	5
Vertical Control	200	0	10	-10

2.4.4 Simulation Results

The robust MIMO controller is designed based on linear plasma response models, which represent the MHD equilibrium evolution during the current ramp-up phase of shot #124616. The simulation model is updated every 12 ms, and the reference values for the radial position, vertical position, plasma current and X-point location are those of the equilibrium around which the linearized model is obtained. The reference value for the flux at the control points is equal to the flux at the X-point, which is computed every 4 ms.

The plasma current is controlled by the PID control loop (2.3), and the plasma position is controlled by the two independent adaptive PID control loops (2.31)–(2.32) and (2.33)–(2.34). In order to simplify the calculation, the adaptive gains ν_r and ν_z are assumed to be constant in the simulation. The parameters for the plasma current, vertical position and radial position loops are shown in Table 2.3. The weight matrices Q and R are chosen to minimize the tracking error and optimize the control effort. Poloidal field coils PF3U/L and PF5 play the most significant role in shaping the plasma; therefore, the matrices are set as $Q = \text{diag}\begin{bmatrix} 2 & 2 & 2 & 1 & 1 \end{bmatrix}$ and $R = \text{diag}\begin{bmatrix} 10 & 1.5 & 2.5 & 1 & 2.5 & 1.5 & 10 & 10 \end{bmatrix}$. The parameters for the μ synthesis are shown in Table 2.4.

The time responses for the plasma radial and vertical positions are shown in Figure 2.10 (a). The radial and vertical positions are stabilized by the controller and the reference values are quickly achieved. Figure 2.10 (b) (top) shows the time evolution

Table 2.4: μ Synthesis Control Parameters

Weight Function	M_i	w_{bi}	A_i	K_i
W_p	100	0.01	7500	10^3
W_u	500	1	75	10^{-3}

of the plasma current, and the tracking error is less than 0.5%. The components of magnetic field at the desired X-point are shown in the Figure 2.10 (b) (bottom), and the errors are less than 0.02 T. Figure 2.10 (c) (top) shows both the flux at the X-point and the flux at the three control points (ψ_1, ψ_2, and ψ_3), and the flux at the control points tracks the flux at the X-point. Figure 2.10 (c) (bottom) shows the tracking errors, which are less than 0.05 Wb. The value of the tracking error can be reduced by modifying the relation between the weight matrices Q and R at the expense of a higher control effort. Note that the flux reference ψ_{ref} is updated every 4 ms, and the control point locations are updated every 12 ms; therefore the results are not smooth curves, as shown in Figure 2.10 (c).

The plasma boundary is defined as the outermost closed magnetic surface entirely contained in the vacuum vessel. The boundary flux value, which identifies the plasma boundary surface, is determined by the flux at the X-point. The goal of the controller is to keep the plasma boundary surface located inside the vacuum vessel and to achieve a pre-specified shape. A series of four plasma boundary shapes at different times during the simulated ramp-up phase of the discharge are shown in the Figure 2.11. The blue circles represent the control points, the blue asterisk represents the actual location of the X-point, and the red asterisk represents the reference location of the X-point. The voltages of the PF coils are regulated according to the robust control law (2.53) in order to keep the plasma boundary at the control points and to regulate the X-point location around its desired value.

Based on the simulation, the control scheme proves to be successful in stabilizing

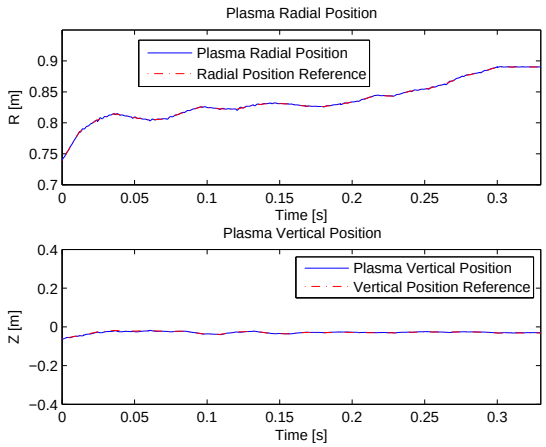

(a)

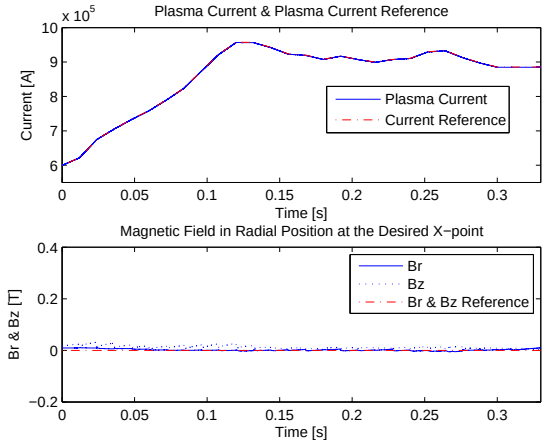

(b)

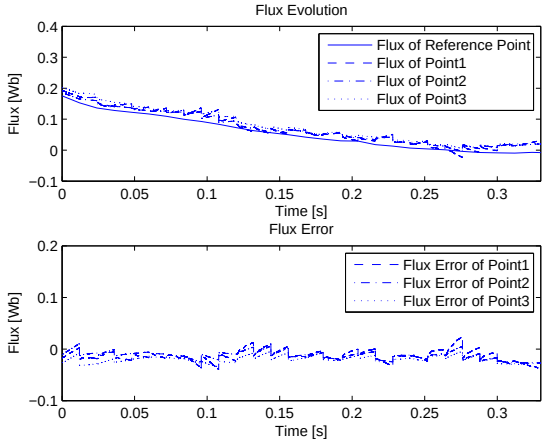

(c)

Figure 2.10: Closed-loop evolution: (a) Plasma radial & vertical position; (b) Plasma current and magnetic field; (c) Magnetic flux & flux error at the control points.

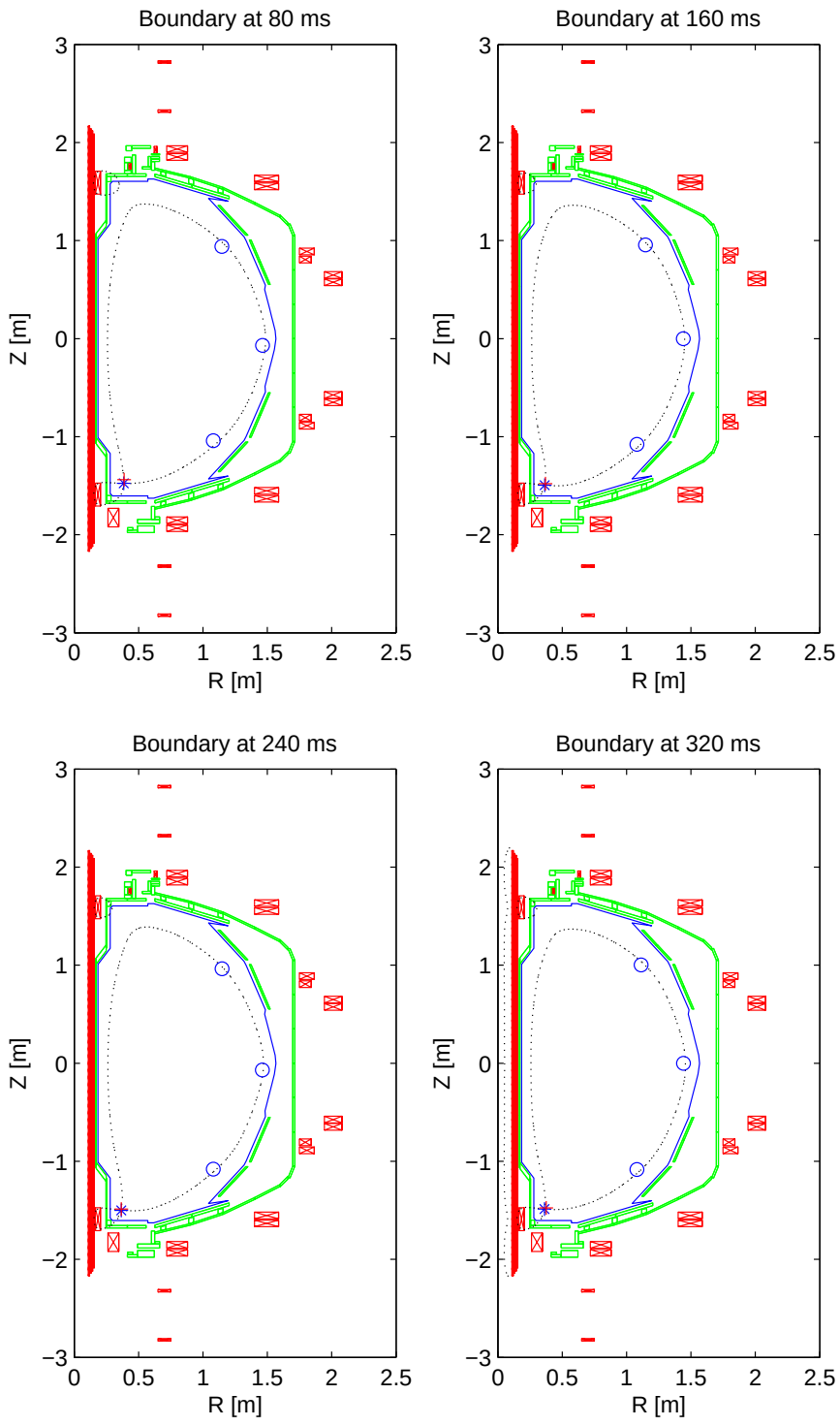

Figure 2.11: Plasma Boundary at 80 ms, 160 ms, 240 ms and 320 ms

the plasma position while regulating the plasma current and keeping the plasma shape and X-point location as specified. Because the controller forces the outputs to follow the desired reference trajectories, the MHD equilibrium evolves as specified during the ramp-up phase. In the simulation, the family of plasma models represents this equilibrium evolution, which validates our simulation condition of updating the plasma model every 12 ms.

2.5 Conclusion

Model-based MIMO controllers are designed for NSTX. The design is based on linearized plasma response models in both the current flat-top phase and the current ramp-up phase. The availability of independent current and position controllers transforms the shape control problem into an output tracking problem. Singular value decomposition (SVD) of the steady state transfer function is used to decouple the system and identify the most relevant control channels, and the shape controller is designed using this decoupled system.

The proposed model-based controllers, which are tested in simulations respectively, show potential for expanding present experimental control capabilities. A more exhaustive and realistic simulation study is part of our future work before experimental validation. Ideally this study should include free-boundary simulations, real-time boundary reconstruction, synthetic noise in the measurements and disturbances.

Chapter 3

Data-driven Modeling of Plasma Magnetic and Kinetic Responses for Advanced Tokamak Scenarios in DIII-D

3.1 Introduction

The shape of the toroidal current density profile as a function of the tokamaks minor radius is critical for the development and sustainment of self-generated non-inductive current, which in turn serves as an enabler for steady-state operation. The current density profile is intimately related to the rotational transform ι profile, which is defined as the inverse of the safety factor q profile, which in turn is defined as the ratio of the number of times a magnetic field line goes toroidally around the tokamak to the number of times it goes around poloidally. The parameter β_N , defined as the normalized ratio between the internal kinetic pressure of the plasma and the external

pressure of the magnetic field, is a key measure of performance used to gauge progress toward developing a power-producing fusion reactor. Therefore, real-time control of the ι profile and β_N is of paramount importance.

Mathematical modeling of plasma transport phenomena with sufficient complexity to capture the dominant dynamics is critical for plasma current profile control design. Data-driven modeling techniques such as system identification [25], have the potential to obtain low-complexity, linear, dynamic models useful for the design of local regulators around an equilibrium. In the past few years, system identification techniques have been successfully used to model plasma transport dynamics for active control design in various tokamaks (JET [30, 31], Tore Supra [32, 33], JT-60U [34, 35], DIII-D [36, 37]). A number of discharges in AT scenarios were run with identical ramp-up phase during the experimental campaign of 2009 in DIII-D [37]. The collected Input/Output(I/O) diagnostic data has been used to model the magnetic and kinetic parameters. In the Lehigh University Plasma Control Group, Mr. William Wehner has been responsible for identifying the linear dynamic plasma models [38, 39, 55], and the author has been responsible for using the identified models to develop the real-time feedback controllers for DIII-D [26, 27, 28, 29]. This chapter aims at briefly describing the input-output response models for the plasma rotation transform ι profile dynamics and normalized beta β_N during H-mode scenarios in DIII-D for on-axis and off-axis current drive scenarios respectively, which will be used in the following chapters.

This chapter is organized as follows. In Section 3.2, the system identification procedure carried out in the DIII-D tokamak is briefly described, and the dynamic linear models relating the rotational transform ι profile and β_N to the plasma current (I_p), neutral beam injection (NBI), and electron cyclotron (EC) heating and current drive (H&CD) are developed for on-axis and off-axis current drive scenarios, respectively.

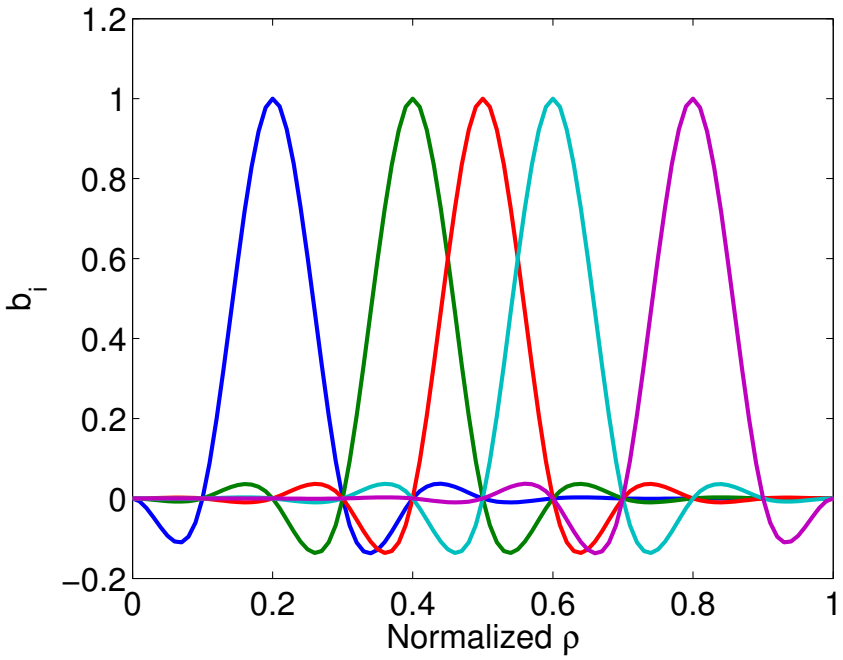

Figure 3.1: Cubic splines, b_i, used for the expansion of the ι profile.

Section 3.3 states the conclusions.

3.2 System Identification on DIII-D

3.2.1 Identified Model for On-axis Current Drive Scenarios

In order to use multivariable control theory for the synthesis of a controller capable of regulating the plasma ι-profile and β_N evolutions in advanced tokamak scenarios, system identification techniques are used to develop from measured data a control-oriented dynamic model for the linear response of these variables to the actuators. A Galerkin scheme [26, 30, 31, 37, 55] is used to convert the infinite-dimensional (PDE) transport equation for the ι-profile to a finite-dimensional (ODE) model in space. The Galerkin scheme assumes that by increasing the number of basis functions the identified ODE model will converge towards the PDE that best fits the data. The ι

profile in normalized radial coordinates is then approximated by the sum of a discrete number of spatial functions,

$$\iota(\hat{\rho}, t) \approx \sum_{i=1}^{N} G_i(t) b_i(\hat{\rho}), \tag{3.1}$$

where the expansion coefficients $G_i(t)$, $i = 1, \ldots, N$, are called Galerkin coefficients, and the spatial functions $b_i(\hat{\rho})$, $i = 1, \ldots, N$, are called Galerkin basis functions. In this work, system identification for the plasma rotational transform profile $\iota(\hat{\rho}, t)$ is carried out based on five cubic-splines Galerkin basis function centered around normalized radii $\hat{\rho} = 0.2, 0.4, 0.5, 0.6, 0.8$ as shown in Figure 3.1. The parameter $\hat{\rho}$ is the normalized effective minor radius, which can be denoted as $\hat{\rho} = \frac{\rho}{\rho_b}$, where ρ is the mean geometric minor radius of the flux surface, i.e., $\pi B_{\phi,0} \rho^2 = \Phi$. The parameter Φ is the toroidal magnetic flux, and $B_{\phi,0}$ is the magnetic field at the geometric major radius. The parameter ρ_b is the mean geometric minor radius of the last closed magnetic flux surface.

To collect the data for system identification a number of discharges were run with identical ramp-up phases and different flat-top phases characterized by varied actuator modulations schemes that excited the system around a predefined reference state. The reference plasma state was that of a 1.8 T, β_N-controlled AT scenario, with a center plasma density $n_{eo} \approx 5 \times 10^{19} m^{-3}$ and plasma current $I_p = 0.9$ MA. The scenario was developed to achieve non-inductive current fractions near unity, bootstrap current fractions larger than 65%, and a normalized confinement factor $H_{98(y,2)} \approx 1.5$ [37]. Actuator modulations were applied from $t = 2.5$ s, and the I_p and β_N controls were disabled to ensure no feedback response during data collection. The EC and NBI systems provided the non-inductive heating and current drive sources for these experiments. The EC system in DIII-D is composed by six gyrotrons with

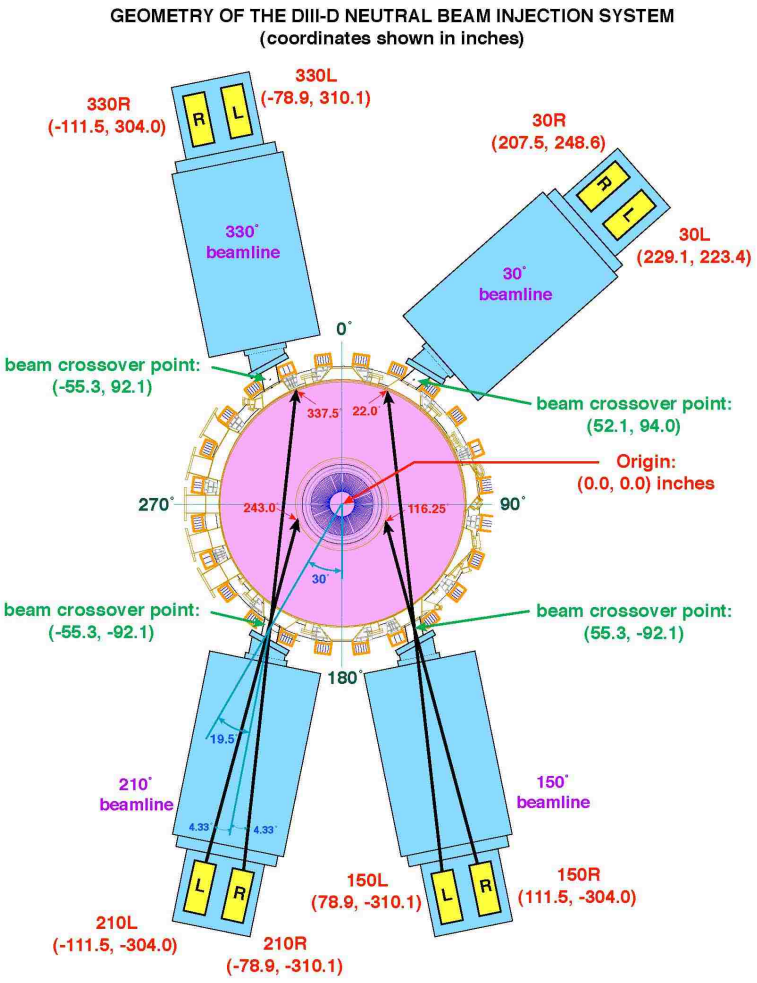

Figure 3.2: Plan view of four beamlines of NBI in DIII-D.

individual nominal power of around 1 MW at a central frequency of 110 GHz. The NBI system in DIII-D consists of four beam-lines, with each beam-line having two ion sources in parallel as shown in Figure 3.2. Each ion source produces an 80 keV deuterium beam and can inject a maximum of 2.5 MW of power into the plasma. Three of the beam-lines (30°, 150°, 330°) inject power in the same direction as the usual plasma current (counter-clockwise in the diagram in Figure 3.2). The 210° system is used for counter-injection, since its beam is injected in the opposite direction. Each beamline is aligned at an angle 19.5° from the radial through the injection port.

Available beam-lines and gyrotrons were grouped to form, together with I_p, five independent H&CD actuators: (i) plasma current I_p, (ii) co-current NBI power P_{CO} (150L and 330L), (iii) counter-current NBI power P_{CT} (210R), (iv) balanced NBI power P_{BL} (150R and 210L), and (v) total EC power from all gyrotrons P_{EC}. All actuators were modulated individually in open loop while the other actuators were held at their respective reference values. Several shots (#140076, 140077, 140093, 140106, and 140107) were used to identify the model. Shot 140107 performs modulation of I_p, shots 140076, 140077, and 140106 perform modulation of the neutral beam groups, and shot 140093 performs modulation of the total EC power. Typical ι profile, q profile, I_p and β_N at the beginning of the system identification experiment is given by shot #140090 in Figure 4.7 and Table 4.3. More details on the system identification experiments can be obtained from [37].

The relation between inputs and outputs for any shot can be assumed in the form of

$$y(t) = y_{FF} + \Delta y(t) = P_{FF}(u_{FF}) + P\Delta u(t), \tag{3.2}$$

where P_{FF} represents the relationship between the reference (feedforward) input u_{FF} and the reference (feedforward) output y_{FF}. The variable $\Delta y(t)$ denotes the deviation output defined as $\Delta y(t) = [\Delta\iota(t),\ \Delta\beta_N(t)] = y(t) - y_{FF}$, with $y(t) = [\iota(0.2,t)\ \iota(0.4,t)\ \iota(0.5,t)\ \iota(0.6,t)\ \iota(0.8,t),\ \beta_N(t)]^T$. The variable $\Delta u(t)$ denotes the deviation input defined as $\Delta u = u - u_{FF}$ with $u = [I_p,\ P_{CO},\ P_{CT},\ P_{BL},\ P_{EC}]$. By subtracting the feedforward value from our data set, we only consider the linear dynamics $\Delta y(t) = P\Delta u(t)$. The linear model P is identified from experimental data using the prediction error method (PEM) according to a least squares fit criterion [25]. By using a finite-dimensional approximation of the ι profile as proposed in (3.1) and neglecting the nonlinear dynamics, the structure of the to-be-identified model P is

derived from the transport equations and written as

$$\Delta i(t) = A_{11}\Delta\iota(t) + A_{12}\Delta\beta_N(t) + B_1\Delta u(t) \tag{3.3}$$

$$\varepsilon\Delta\dot{\beta}_N(t) = A_{21}\Delta\iota(t) + A_{22}\Delta\beta_N(t) + B_2\Delta u(t), \tag{3.4}$$

where the parameter $\varepsilon << 1$, representing the typical ratio between the energy confinement time and the characteristic resistive diffusion time, is used to indicate the existence of two timescales in the system. The magnetic variable is characterized by a slow dynamics with timescale given by t and the kinetic variable is characterized by a fast dynamics with timescale given by $\tau = t/\varepsilon$. The study of dynamic systems with two clear timescales has a long history in nonlinear control analysis, which is summarized by the theory of singular perturbations [60]. The modeling of the current profile dynamics as a two-timescale system indeed simplifies the associated control design. Therefore, the natural timescale separation observed in the system has been exploited in the past at the moment of developing a control-oriented model following both first-principles-driven [22] and data-driven [31] approaches. Following a similar approach in this work allows us to rewrite the model (3.3)-(3.4) as the combination of a slow model

$$\Delta i(t) = A_s\Delta\iota(t) + B_s\Delta u_s(t) \qquad \Delta\beta_{Ns} = C_s\Delta\iota + D_s\Delta u_s, \tag{3.5}$$

and a fast model

$$\Delta\dot{\beta}_{Nf}(t) = A_f\Delta\beta_{Nf}(t) + B_f\Delta u_f(t), \tag{3.6}$$

where $\Delta\beta_{Ns}$ and $\Delta\beta_{Nf}$ are the slow and fast components of $\Delta\beta_N$, and Δu_s and Δu_f are the slow and fast components of Δu. It is straightforward to show that the matrices to be identified in (3.5)-(3.6) are linked to the original model matrices

in (3.3)-(3.4) through the relations:

$$A_s = A_{11} - A_{12}A_{22}^{-1}A_{21}, \quad C_s = -A_{22}^{-1}A_{21}, \quad A_f = \varepsilon^{-1}A_{22},$$
$$B_s = B_1 - A_{12}A_{22}^{-1}B_2, \quad D_s = -A_{22}^{-1}B_2, \quad B_f = \varepsilon^{-1}B_2.$$

Because $\varepsilon << 1$ (denoting the natural timescale separation in the system), we usually have $A_{21}/\varepsilon, A_{22}/\varepsilon >> A_{11}, A_{12}$ and $B_2/\varepsilon >> B_1$. Therefore, identifying the system matrices in (3.5)-(3.6) instead of the system matrices in (3.3)-(3.4) avoids the risk of having seriously ill-conditioned system matrices and making the synthesis of a reliable control strategy even more challenging. Rewriting the model (3.3)-(3.4) as (3.5)-(3.6) requires the assumption that the ι profile dynamics has a limited bandwidth, which implies that its response to the control input Δu is identical to its response to the low-frequency-content control input Δu_s since the high-frequency-content control input Δu_f is filtered by the system itself. While this assumption is not restrictive at all and it is just a consequence of the slow dynamics exhibited by the magnetic variable, stating the two-timescale model structure as in equations (3.5)-(3.6) leaves the designer with another design choice to make, which is the value of the cutoff frequency separating the slow (low-frequency) content and the fast (high-frequency) content of the control input. Selecting a cutoff frequency too low in the effort of maximizing the separation between slow and fast dynamics may be indeed restrictive and may pose a risk to closed-loop performance due to the neglected dynamics. The cutoff frequency selection may become particularly challenging when the plasma current is used as a control input since in this case the outer part of the ι profile close to the plasma boundary (e.g., $\iota(0.8, t)$ in this work) may respond relatively fast to changes in the plasma current.

The slow model (3.5) and fast model (3.6) are finally combined with a first order low-pass filter to obtain the overall plant P. The first order low-pass filter is written

as

$$\dot{X}_{filter} = -2\pi X_{filter} + 2\pi\Delta u$$

$$\begin{bmatrix} \Delta u_s \\ \Delta u_f \end{bmatrix} = \begin{bmatrix} I \\ -I \end{bmatrix} X_{filter} + \begin{bmatrix} 0 \\ I \end{bmatrix} \Delta u, \tag{3.7}$$

where X_{filter} is the state, and I is the identity matrix. Substituting (3.7) into (3.5) and (3.6), the ι and β_N combined model can be obtained as

$$\begin{bmatrix} \Delta i \\ \Delta\dot{\beta}_{Nf} \\ \dot{X}_{filter} \end{bmatrix} = \begin{bmatrix} A_s & 0 & B_s \\ 0 & A_f & -B_f \\ 0 & 0 & -2\pi \end{bmatrix} \begin{bmatrix} \Delta\iota \\ \Delta\beta_{Nf} \\ X_{filter} \end{bmatrix} + \begin{bmatrix} 0 \\ B_f \\ 2\pi \end{bmatrix} \Delta u = A \begin{bmatrix} \Delta\iota \\ \Delta\beta_{Nf} \\ X_{filter} \end{bmatrix} + B\Delta u$$

$$\begin{bmatrix} \Delta\iota \\ \Delta\beta_N \end{bmatrix} = \begin{bmatrix} I & 0 & 0 \\ C_s & I & D_s \end{bmatrix} \begin{bmatrix} \Delta\iota \\ \Delta\beta_{Nf} \\ X_{filter} \end{bmatrix} = C \begin{bmatrix} \Delta\iota \\ \Delta\beta_{Nf} \\ X_{filter} \end{bmatrix}. \tag{3.8}$$

Embedding the low-pass filter in the model is a direct consequence of the assumption of a limited bandwidth for the ι profile response. As mentioned above, selecting a cutoff frequency for the low-pass filter which is too low may pose a risk to closed-loop performance. Nevertheless, it is important to emphasize that the source of this risk is the identification of the model based on input-output signals limited in bandwidth by the low-pass filter, and not the explicit inclusion of the low-pass filter in (3.8) by itself. In other words, the low-pass filter could be removed from (3.8) and the risk to closed-loop performance would persist due to the limited bandwidth of the slow-dynamics model. In this work, the lowest frequency at which the inputs used in the system identification experiment could be filtered while retaining a good fit of the unfiltered ι data by the slow model is found to be around 1 Hz. Therefore, the filter cutoff frequency has been chosen as 1 Hz to separate the slow and fast components

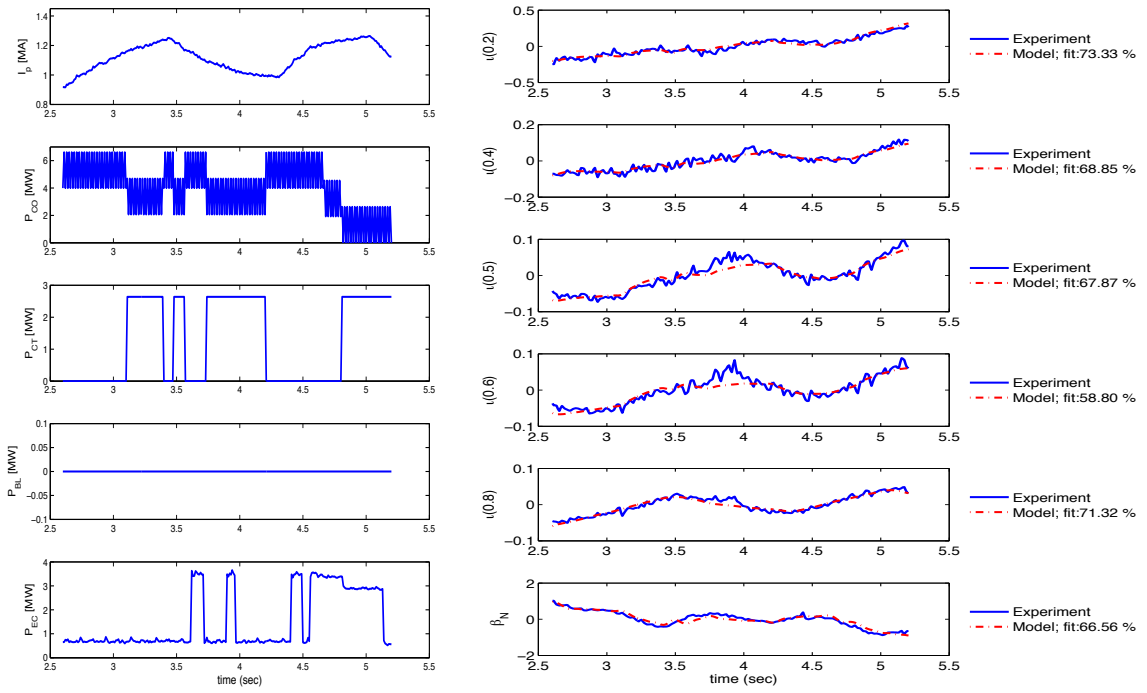

(a) (b)

Figure 3.3: Shot 140094: (a) Experimental actuator modulation; (b) Comparison between experimentally measured (blue solid line) and model-predicted (red dashed-dotted line) ι profile and β_N.

of the input data and β_N. It is important to note that this cutoff frequency is indeed related to the frequency content of the excitation (input) signals during the system identification experiment. If higher-frequency excitation signals had been used, a higher value for the cutoff frequency would have been most likely necessary.

A model validation procedure has been carried out by comparing the model prediction with experimental data from shots not used in the system identification procedure. This comparison includes both ι at $\hat{\rho} = 0.2, 0.4, 0.6, 0.8$ and β_N. Figure 3.3 and Figure 3.4 illustrate the cases of shots #140094 and #140109 as examples. While Figure 3.3 (a) and Figure 3.4 (a) display the experimental inputs, Figure 3.3 (b) and Figure 3.4 (b) compare predictions with experimental data. Fit functions f^i are introduced to quantify the relationship between the measured data y_m^i and the

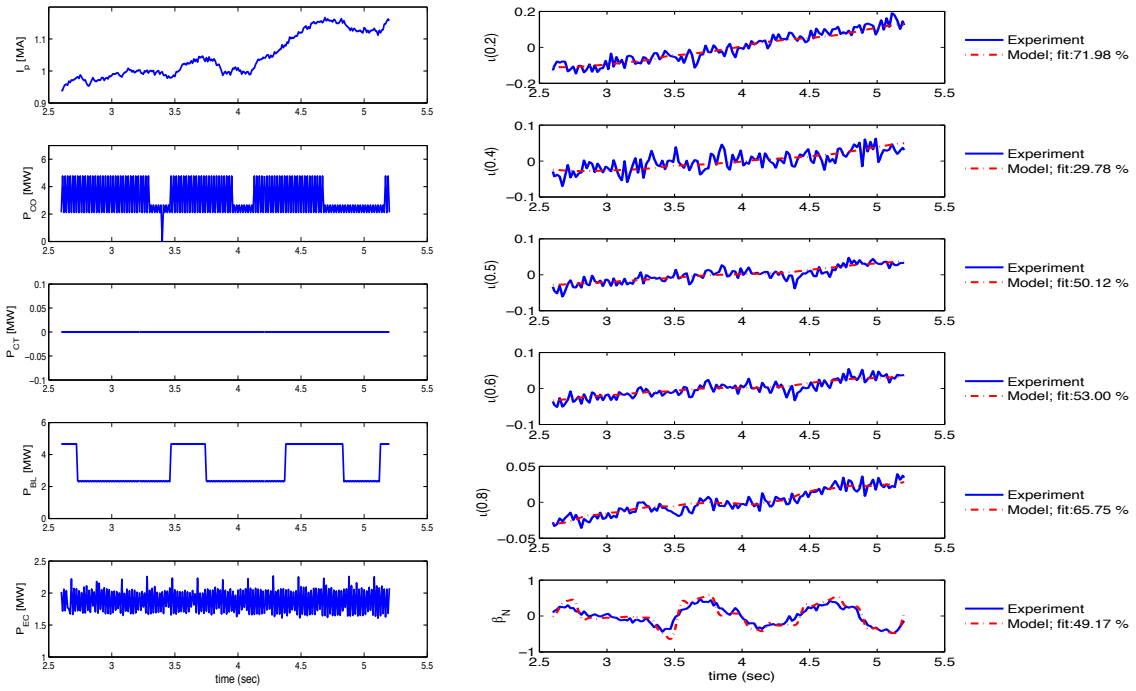

(a) (b)

Figure 3.4: Shot 140109: (a) Experimental actuator modulation; (b) Comparison between experimentally measured (blue solid line) and model-predicted (red dashed-dotted line) ι profile and β_N.

model-predicted data y^i, where the superindex denotes the i-th channel of the system output, i.e.,

$$f^i = 1 - \left[\frac{\sum_{k=1}^{N} [y_m^i(t_k) - y^i(t_k)]^2}{\sum_{k=1}^{N} [y_m^i(t_k) - < y_m^i >]^2} \right]^{1/2}, \tag{3.9}$$

where $f^i = 1$ is a perfect fit and $f^i = 0$ corresponds to a reconstructed data set identically equal to the mean of the measured data, $< y_m^i >$. Because the noise is included in the measured data from the experiment, the values of the fit functions are not sought to be 1 since that would mean that the identified model fits the noise perfectly, which is undesired. A "good" value, based on the definition of the fit functions, will therefore depend on the noise level present in the system and

the confidence bands assumed by the designer. Figure 3.3 (b) and Figure 3.4 (b) display the typical fit between measured and model-predicted data observed in the model validation procedure, which involved a larger number of shots and consistently showed the type of qualitatively agreement expected from a control-oriented model. Note that although the fit functions are far from 1, the control-oriented model seems to capture the trend of the system in response to the control actuation, which is the objective of the system identification procedure (not the perfect fit between predicted and experimental data). It is often not possible, however, to assess the true requirements for model accuracy until experimental tests of the model-based controller are performed. Therefore, an iterative process may be necessary.

3.2.2 Identified Model for Off-axis Current Drive Scenarios

High q_{min} scenario development at high β_N has been limited due to the overdrive of the central current by the on-axis NBI, which will be discussed in Section 4.3. Off-axis NBI can provide a broad current deposition at mid-radius without over-driving the current near the axis [61]. To achieve higher β_N and higher q_{min}, the beam-line optical axes of 150L and 150R were inclined up to 16.5° (shown in Figure 3.5), while the other beam-line optical axes were unchanged. The available beam-lines and gyrotrons were grouped to form, together with I_p, five independent H&CD actuators: (i) plasma current I_p, (ii) on-axis co-current NBI power P_{CO} (330L), (iii) off-axis co-current NBI power P_{OA} (150L and 150R), (iv) counter-current NBI power P_{CT} (210R), and (v) total EC power from all gyrotrons P_{EC}.

Several shots (#140076, 140077, 140093, 140106, and 140107)) [55] were used to identify the plasma response to the on-axis actuators. To collect the data for identifying the response of the off-axis beams (150L and 150R), a new shot #150082 with off-axis beams was run, while the other actuators were modulated around the

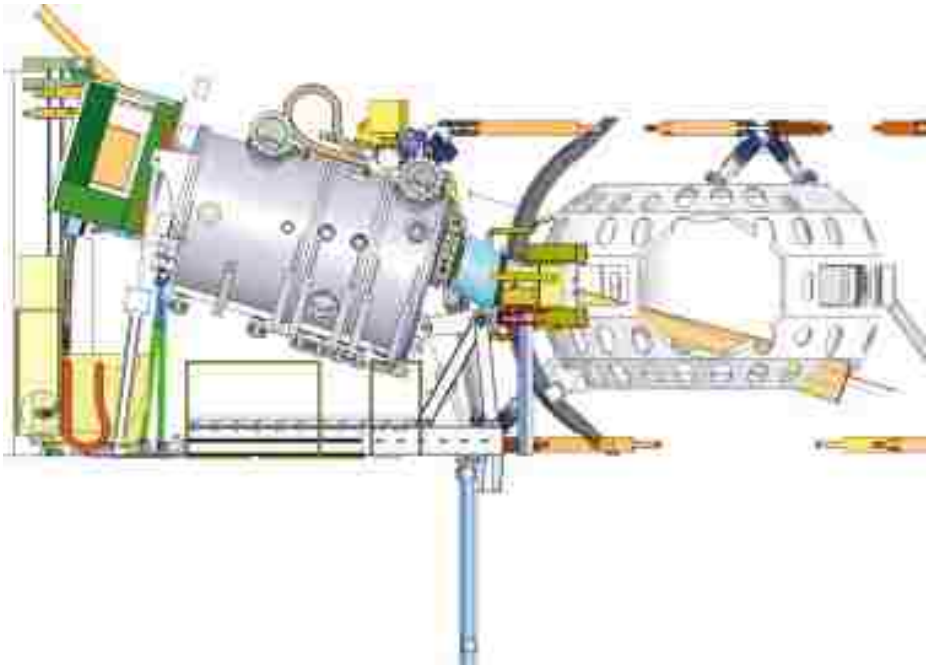

Figure 3.5: Off-axis NBI in DIII-D.

identical reference values as the previous shots. System identification for the plasma rotational transform profile $\iota(\hat{\rho})$ was carried out with 5 Galerkin coefficients computed at normalized radial coordinates $\hat{\rho} = 0.2, 0.4, 0.5, 0.6, 0.8$, starting at $t = 2.5s$.

The relation between inputs and outputs for any discharge is assumed in the same form as (3.2). The variable $\Delta u(t)$ in the off-axis current drive scenarios denotes the deviation input defined as $\Delta u = u - u_{FF}$ with $u = [I_p,\ P_{CO},\ P_{OA},\ P_{CT},\ P_{EC}]$, while the variable $\Delta y(t)$ denotes the deviation output defined as $\Delta y(t) = [\Delta\iota(t),\ \Delta\beta_N(t)] = y(t) - y_{FF}$, with $y(t) = [\iota(0.2,t)\ \ \iota(0.4,t)\ \ \iota(0.5,t)\ \ \iota(0.6,t)\ \ \iota(0.8,t),\ \ \beta_N(t)]^T$. By subtracting the feedforward value from our data set, we only consider the linear dynamics $\Delta y(t) = P\Delta u(t)$. The linear model P is identified from experimental data using the prediction error method (PEM) according to a least squares fit criterion [25], which has been discussed in Section 3.2.1. The identified feedback model P can be expressed

in the state space form

$$\dot{x} = A_{OA}x(t) + B_{OA}\Delta u(t), \qquad \Delta y(t) = C_{OA}x(t) \tag{3.10}$$

where the state $x(t)$ is defined as $x(t) = \Delta\iota(t) = \iota(t) - \iota_{FF}$.

3.3 Conclusion

Simplified linear models for the evolution of the plasma rotational transform ι profile as well as β_N in the DIII-D tokamak have been obtained based on the PEM system identification method. Reasonable model prediction of the magnetic profile evolution in response to modulations in the on-axis and off-axis neutral beam injector power, the total gyrotron power, and the plasma current are achieved. The identified models are employed to design feedback control algorithms to control the current profile evolution in on-axis and off-axis current drive scenarios, which will be discussed in the Chapter 4 and Chapter 5, respectively.

Chapter 4

H_∞ Control of the Plasma Rotational Transform Profile and Normalized Beta Dynamics for Advanced Tokamak Scenarios in DIII-D

4.1 Introduction

The planned ITER reactor [62] will be capable of exploring advanced tokamak (AT) modes of operation, characterized by high plasma pressure, long confinement times, and low levels of inductively driven plasma current, which allow for near steady-state operation. These advanced modes require active feedback control to maintain and develop high performance plasmas, good confinement, and long plasma discharges. In particular, the control of the plasma current profile, which is intimately related to

the safety factor profile q, or its inverse, the rotational transform ι profile, is critical for the development and sustainment of the self-generated, non-inductive, bootstrap current, which in turn serves as an enabler for steady-state operation. Previous work in the DIII-D tokamak towards closed-loop current profile control only includes non-model-based single-loop approaches [36] that led to oscillatory response.

A two-timescale dynamic model of the rotational transform ι profile and the normalized beta β_N has been identified from DIII-D data in Chapter 3. A model-based, multi-input-multi-output (MIMO) controller is synthesized based on the identified model for the simultaneous regulation of the ι profile and β_N during the current flat-top phase in H-mode discharges. A singular value decomposition (SVD) is used to decouple the combined system and identify the most relevant control channels. The mixed-sensitivity robust control method [63, 64] is applied to synthesize a closed-loop controller that minimizes the reference tracking error and rejects external disturbances with minimal control energy. The feedback controller is then augmented with an anti-windup compensator [65, 66, 67], which keeps the given ι profile and β_N controller well-behaved in the presence of actuator constraints and leaves the nominal closed-loop system unmodified when no saturation in the actuators is present. The proposed controller has been tested both in simulations and in a limited number of experiments on the DIII-D tokamak. These experiments mark the first time ever data-driven, model-based, current-profile controllers were implemented and tested in DIII-D. The experimental results, which are thoroughly analyzed in this work, are partially successful due to actuator constraints and design limitations. Nevertheless, these preliminary results represent an incremental step towards routine current profile control in DIII-D and provide valuable lessons regarding model identification, control design and controllability that will be exploited to achieve this goal.

This chapter is organized as follows. In Section 4.2, the design of the plasma

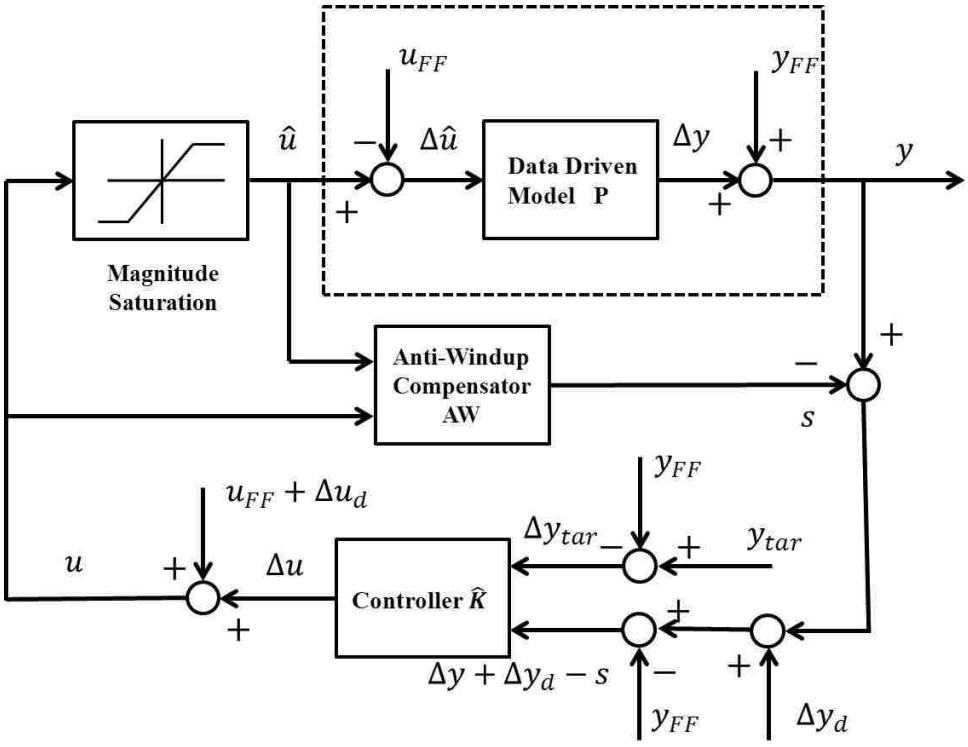

Figure 4.1: DIII-D ι-profile+β_N control system architecture.

control algorithm and the anti-windup compensator is introduced. Simulated and experimental results in DIII-D illustrating the performance of the controllers are presented in Section 4.3. Conclusions and future research directions are stated in Section 4.4.

4.2 Control System Design

4.2.1 Control System Structure

A multi-input-multi-output (MIMO) robust feedback controller based on the identified linear model (3.8) is proposed for the regulation of the evolution of the ι profile and β_N on DIII-D. In order to cope with the limitations on achievable values and rates for the actuators (plasma current, beam powers, gyrotron powers) we follow an

a posteriori design approach where the MIMO robust feedback controller is modified by an anti-windup compensator. The control design procedure is summarized by the following steps: (1) decouple the system and identify the most relevant control channels, (2) design an H_∞ controller $\hat{K}$ ignoring control input saturation, (3) add an anti-windup compensator AW to minimize the adverse effect of any control input saturation on the closed loop performance. The overall control system including the MIMO H_∞ controller and the anti-windup compensator is shown in Figure 4.1. By subtracting the reference (feedforward) output values y_{FF} from the measured output values y, the deviation output $\Delta y = y - y_{FF}$ is generated and used as the input to the feedback controller. The objective of the feedback controller is to make the deviation output $\Delta y = y - y_{FF}$ follow the target output $\Delta y_{tar} = y_{tar} - y_{FF}$ under the influence of input (Δu_d) and output (Δy_d) disturbances, i.e., to drive the tracking error $e(t) = \Delta y_{tar}(t) - \Delta y(t)$ close to zero. The target output y_{tar} represents the desired values for β_N and the ι profile at $\hat{\rho} = 0.2, 0.4, 0.5, 0.6, 0.8$. The output of the feedback controller Δu is added to the reference (feedforward) input values u_{FF} to generate the overall input values u requested to the actuators. The differences between requested (u) and achieved ($\hat{u}$) input values drive the anti-windup compensator that eventually modifies the measured output values y through the signal s when any of the actuators saturate.

4.2.2 Decoupling and Identification of Most Relevant Control Channels

The relation between the inputs and the outputs of the linear model (3.8) can be expressed in terms of its transfer function $P(s)$, i.e.,

$$\frac{\Delta Y(s)}{\Delta U(s)} = P(s) = C(sI - A)^{-1}B, \tag{4.1}$$

where s denotes the Laplace variable and $\Delta Y(s)$ and $\Delta U(s)$ denote the Laplace transforms of the output Δy and the input Δu respectively. Assuming a constant target $\Delta\bar{y}_{tar}$ and closed-loop stabilization, the system will reach steady state as $t \to \infty$. It is possible to define

$$\Delta\bar{y} = \lim_{t\to\infty} \Delta y(t), \quad \Delta\bar{u} = \lim_{t\to\infty} \Delta u(t), \quad \bar{e} = \lim_{t\to\infty} e(t) = \Delta\bar{y}_{tar} - \Delta\bar{y}, \tag{4.2}$$

where $e = \Delta y_{tar} - \Delta y$ denotes the tracking error. Under these assumptions, the closed-loop system is specified by

$$\Delta\bar{y} = \bar{P}\Delta\bar{u} = -CA^{-1}B\Delta\bar{u}, \tag{4.3}$$

$$\Delta\bar{u} = \bar{\hat{K}}\bar{e} = \bar{\hat{K}}\left(\Delta\bar{y}_{tar} - \Delta\bar{y}\right), \tag{4.4}$$

where $\bar{P} = P(0)$ is the steady state transfer function, $\hat{K}(s)$ is the transfer function of the to-be-designed controller and $\bar{\hat{K}} = \hat{K}(0)$. The steady state gains of the identified model for the ι profile are shown in Figure 4.2, where the steady-state response $\Delta\bar{\iota}$ to unitary changes in the various inputs is plotted. The plasma current is the most capable actuator in adjusting the magnetic profile in absolute terms. The co-injection and counter-injection beams are also very powerful, affecting the profile in different

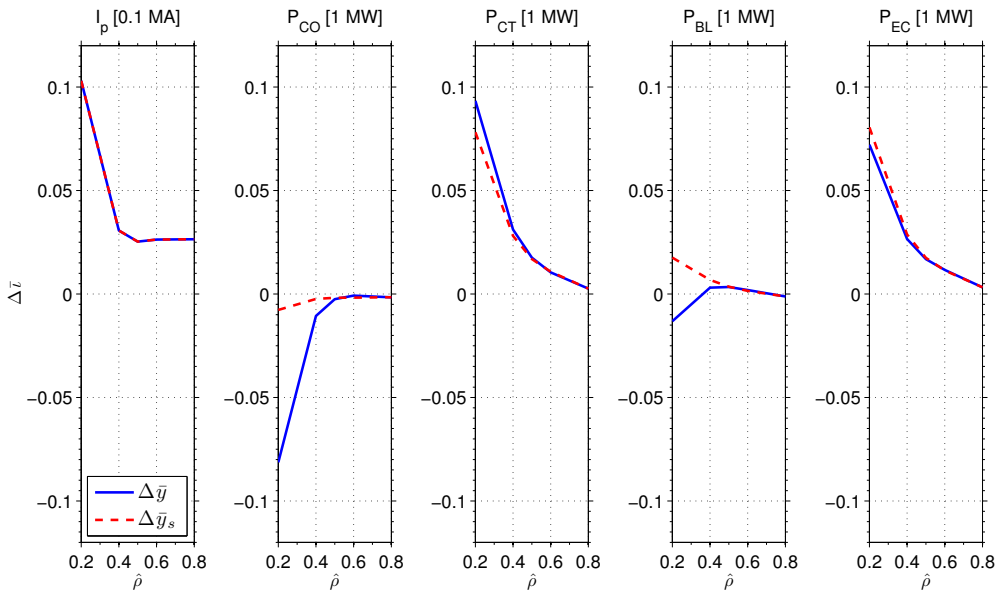

Figure 4.2: Steady-state gains for the ι-profile response. The steady-state output $\Delta\bar{y}$ (solid blue) is compared with the significant steady-state output $\Delta\bar{y}_s$ (dashed red) for $k = 2$. The powers are expressed in MW and the current in units of 0.1 MA. The weight matrices are chosen in this case as $R = \text{diag}([0.01,\ 0.25,\ 1000,\ 0.5,\ 0.25])$ and $Q = \text{diag}([1,\ 1,\ 1,\ 1,\ 1,\ 1])$.

directions in agreement with prior experiments. The EC power leads to an increase in the $\Delta\iota$ profile, and the balanced-injection beams nearly do not have influences in the magnetic flux profile.

Singular value decomposition (SVD) is employed to decouple the system and determine the most significant input-output channels for tracking based on the steady state transfer function $\bar{P}$. Symmetric positive definite matrices $Q \in \Re^{p\times p}$, where $p = 6$ is the number of outputs, and $R \in \Re^{m\times m}$, where $m = 5$ is the number of inputs, are introduced to weigh the tracking error and control effort, respectively. The singular value decomposition of the "weighted" steady-state transfer function is given by

$$\tilde{P} = Q^{1/2}\bar{P}R^{-1/2} = USV^T, \tag{4.5}$$

where $S = \text{diag}(\sigma_1, \sigma_2, \cdots, \sigma_m) \in \Re^{m \times m}$ since $m < p$, $U \in \Re^{p \times m}$, $V \in \Re^{m \times m}$. The matrices U and V are unitary, i.e., $U^T U = I$, $V^T V = V V^T = I$. The steady-state input-output relation can now be expressed as

$$\Delta \bar{y} = Q^{-1/2} \tilde{P} R^{1/2} \Delta \bar{u} = Q^{-1/2} U S V^T R^{1/2} \Delta \bar{u}. \tag{4.6}$$

By invoking the properties of the SVD, the columns of the matrix $Q^{-1/2}US$ define a basis for the subspace of obtainable steady-state output values. Therefore, it is always possible to write

$$\Delta \bar{y} = Q^{-1/2} U S \Delta \bar{y}^* \iff \Delta \bar{y}^* = S^{-1} U^T Q^{1/2} \Delta \bar{y}, \tag{4.7}$$

where $\Delta \bar{y}^* \in \Re^m$ denotes the basis coefficients of the component of the output signal that is indeed achievable. This implies that only the component of the reference vector $\Delta \bar{y}_{tar}$ that lies in this subspace will be trackable. The reference vector is now written as the sum of a trackable component $\Delta \bar{y}_{tar_t}$ and a non-trackable component $\Delta \bar{y}_{tar_{nt}}$, i.e., $\Delta \bar{y}_{tar} = \Delta \bar{y}_{tar_t} + \Delta \bar{y}_{tar_{nt}}$, where

$$\Delta \bar{y}_{tar_t} = Q^{-1/2} U S \Delta \bar{y}^*_{tar} \iff \Delta \bar{y}^*_{tar} = S^{-1} U^T Q^{1/2} \Delta \bar{y}_{tar}, \tag{4.8}$$

with $\Delta \bar{y}^*_{tar} \in \Re^m$ representing the basis coefficients of the component of the target signal that is indeed trackable and $S^{-1} U^T Q^{1/2} \Delta \bar{y}_{tar_{nt}} = 0$. By defining

$$\Delta \bar{u}^* = V^T R^{1/2} \Delta \bar{u}, \tag{4.9}$$

where $\Delta \bar{u}^* \in \Re^m$, the relationship between $\Delta \bar{y}^*$ and $\Delta \bar{u}^*$ is obtained by using (4.6),

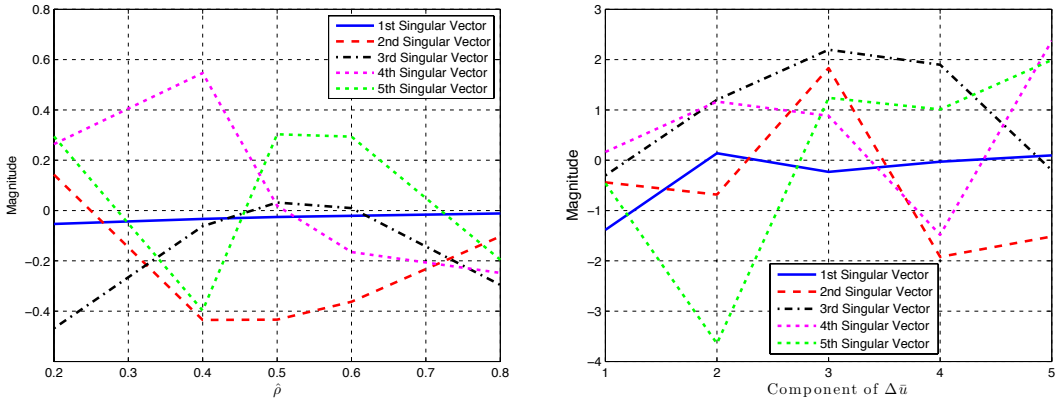

(a) (b)

Figure 4.3: (a) Output singular vectors $Q^{-1/2}U$, (b) Input singular vectors $V^T R^{1/2}$ from the SVD analysis ($\sigma_1 = 106.2544$, $\sigma_2 = 0.2697$, $\sigma_3 = 0.0624$, $\sigma_4 = 0.0077$, and $\sigma_5 = 0.0009$).

(4.7), (4.9) as

$$\Delta\bar{y}^* = S^{-1}U^T Q^{1/2}\Delta\bar{y} = S^{-1}U^T Q^{1/2}Q^{-1/2}USV^T R^{1/2}\Delta\bar{u} = \Delta\bar{u}^*. \tag{4.10}$$

This defines a one-to-one relationship between the inputs and outputs, i.e., $\Delta\bar{y}^* = \Delta\bar{u}^*$, which leads to a square and decoupled system.

The bases obtained through the singular value decomposition of the steady-state response predicted by the model are shown in Figure 4.3. The singular output vectors given by the columns of $Q^{-1/2}U$, which define the subspace of obtainable steady state output values and therefore the trackable component of the reference vector, are shown in Figure 4.3 (a). The corresponding input singular vectors given by the rows of $V^T R^{1/2}$, which define the associated steady-state input values, are shown in Figure 4.3 (b). As evidenced by the magnitude of the first singular value relative to the others, the first output singular vector is the dominant shape of an achievable steady state profile according to the model. In order to generate this profile shape, the feedback controller must actuate in the direction associated with the first input

singular vector. As the value of the singular value decreases, a larger amount of control effort is needed along the direction of the associated input singular vector to produce a significant contribution to the steady state profile in the direction of the associated output singular vector.

To quantify the tracking performance in steady state, a performance index can be defined as

$$\bar{J} = \lim_{t\to\infty} e^T(t)Qe(t) = \bar{e}^T Q\bar{e}, \tag{4.11}$$

where the steady-state tracking error $\bar{e}$ can now be rewritten as

$$\bar{e} = \Delta\bar{y}_{tar} - \Delta\bar{y} = Q^{-1/2}US(\Delta\bar{y}^*_{tar} - \Delta\bar{y}^*). \tag{4.12}$$

By substituting this expression into (4.11), the performance index is expressed as

$$\bar{J} = (\Delta\bar{y}^*_{tar} - \Delta\bar{y}^*)^T S^2(\Delta\bar{y}^*_{tar} - \Delta\bar{y}^*) = \sum_{i=1}^{m} \sigma_i^2(\Delta\bar{y}^*_{tar_i} - \Delta\bar{y}^*_i)^2. \tag{4.13}$$

The goal of the controller to be introduced in the next subsection is to minimize the tracking error by driving Δy^*_i towards $\Delta y^*_{tar_i}$, for $i = 1, \ldots, m$, both during dynamic transients and in steady state. It is easy to note that the singular value σ_i, for $i = 1, \ldots, m$, is the weight parameter for the i^{th} component of the tracking error in steady state. Since it is usually the case where $\sigma_1 > \cdots \sigma_k \gg \sigma_{k+1} > \cdots > \sigma_m > 0$, the input-output channels associated with the largest singular values are the most significant when minimizing $\bar{J}$ in (4.13). Therefore, it is possible that with the intent of minimizing $\bar{J}$ a lot of control effort will be spent to minimize the i^{th} component of the tracking error, for $i > k$, which has a very small contribution to the overall value of the cost function. To avoid spending a lot of control effort for a marginal improvement of the cost function value, the singular value set is partitioned into

significant singular values S_s and negligible singular values S_n, i.e.,

$$U = \begin{bmatrix} U_s & U_n \end{bmatrix}, V = \begin{bmatrix} V_s & V_n \end{bmatrix}, S = \begin{bmatrix} S_s & 0 \\ 0 & S_n \end{bmatrix} \approx \begin{bmatrix} S_s & 0 \\ 0 & 0 \end{bmatrix},$$

$$\Delta\bar{u}^* = \begin{bmatrix} \Delta\bar{u}_s^* \\ \Delta\bar{u}_n^* \end{bmatrix}, \Delta\bar{y}^* = \begin{bmatrix} \Delta\bar{y}_s^* \\ \Delta\bar{y}_n^* \end{bmatrix}. \tag{4.14}$$

The performance index defined in (4.13) can then be approximated as

$$\bar{J} \approx \bar{J}_s = \sum_{i=1}^{k} \sigma_i^2 (\Delta\bar{y}_{tar_i}^* - \Delta\bar{y}_i^*)^2 = (\Delta\bar{y}_{tar_s}^* - \Delta\bar{y}_s^*)^T S_s^2 (\Delta\bar{y}_{tar_s}^* - \Delta\bar{y}_s^*) \tag{4.15}$$

where

$$\Delta\bar{y} = Q^{-1/2} U S \Delta\bar{y}^* \approx Q^{-1/2} U_s S_s \Delta\bar{y}_s^* \iff \Delta\bar{y}_s^* = S_s^{-1} U_s^T Q^{1/2} \Delta\bar{y}, \tag{4.16}$$

$$\Delta\bar{y}_{tar} = Q^{-1/2} U S \Delta\bar{y}_{tar}^* \approx Q^{-1/2} U_s S_s \Delta\bar{y}_{tar_s}^* \iff \Delta\bar{y}_{tar_s}^* = S_s^{-1} U_s^T Q^{1/2} \Delta\bar{y}_{tar}, \tag{4.17}$$

$$\Delta\bar{u} = R^{-1/2} V \Delta\bar{u}^* = R^{-1/2} V_s \Delta\bar{u}_s^* + R^{-1/2} V_n \Delta\bar{u}_n^* \iff \Delta\bar{u}_s^* = V_s^T R^{1/2} \Delta\bar{u}, \tag{4.18}$$

$$\bar{e}_s^* = \Delta\bar{y}_{tar_s}^* - \Delta\bar{y}_s^*. \tag{4.19}$$

4.2.3 Design of H_∞ MIMO Controller

The SVD output and input bases reduce to $Q^{-1/2} U_s S_s$ and $R^{-1/2} V_s$, respectively. By defining

$$\Delta y_s^* = S_s^{-1} U_s^T Q^{1/2} \Delta y, \tag{4.20}$$

$$\Delta u_s^* = V_s^T R^{1/2} \Delta u, \tag{4.21}$$

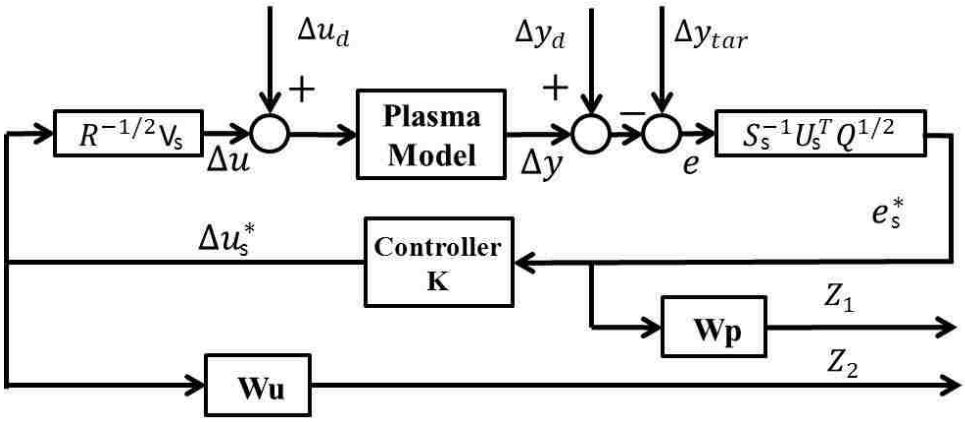

Figure 4.4: H_∞ control formulation. Note that W_p and W_u are used only in the design of the controller K to specify the performance criteria (they do not become part of the controller).

and using (4.1), we can write

$$\frac{\Delta Y_s^*(s)}{\Delta U_s^*(s)} = P_{DC} = S_s^{-1}U_s^TQ^{1/2}PR^{-1/2}V_s, \tag{4.22}$$

where $\Delta Y_s^*(s)$ and $\Delta U_s^*(s)$ represent the Laplace transforms of the output Δy_s^* and the input Δu_s^*, respectively. The transfer function P_{DC} reduces in steady state (i.e., $s = 0$) to a fully decoupled system in which there is a one-to-one relationship between the inputs Δu_s^* and the outputs Δy_s^*. The plasma controller is synthesized based on this one-to-one relationship. The structure of the proposed controller is shown in Figure 4.4, where two frequency-dependent functions, W_p and W_u, are introduced to weight the tracking error and the control effort. The signals defined within the proposed controller structure are the control input Δu_s^*, the system output Δy_s^*, the tracking error $e_s^* = \Delta y_{tar_s}^* - \Delta y_s^*$, the target $\Delta y_{tar_s}^* = S_s^{-1}U_s^TQ^{1/2}\Delta y_{tar}$, the input disturbance $\Delta u_{d_s}^* = V_s^TR^{1/2}\Delta u_d$, the output disturbance $\Delta y_{d_s}^* = S_s^{-1}U_s^TQ^{1/2}\Delta y_d$, and the weighted performance signal $[Z_1^T,\ Z_2^T]^T = [(W_pe_s^*)^T,\ (W_u\Delta u_s^*)^T]^T$.

The feedback system in Figure 4.4 can be expressed in the conventional $P^* - K$

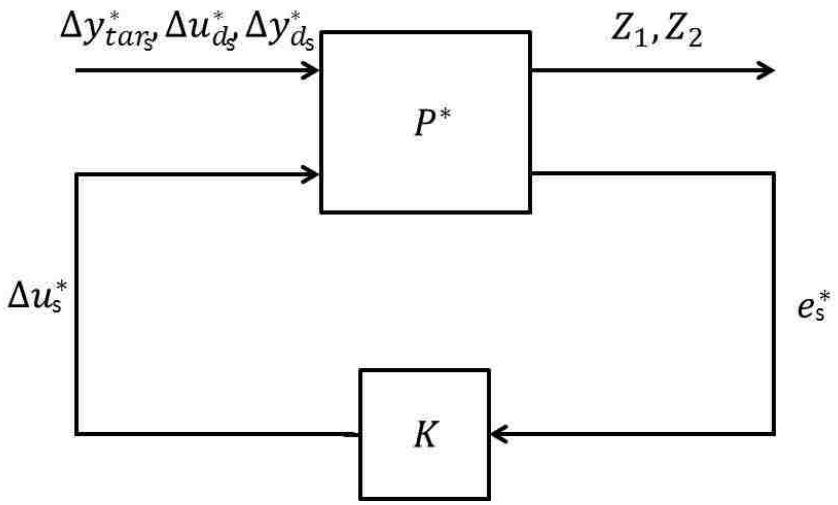

Figure 4.5: Model in $P^* - K$ control framework.

robust control design framework shown in Figure 4.5. The generalized open-loop plant P^* is partitioned first as

$$P^* = \begin{bmatrix} \tilde{P}_{11} & \tilde{P}_{12} \\ \tilde{P}_{21} & \tilde{P}_{22} \end{bmatrix}, \tag{4.23}$$

where

$$\begin{bmatrix} \begin{bmatrix} Z_1 \\ Z_2 \end{bmatrix} \\ e^*_s \end{bmatrix} = P^* \begin{bmatrix} \begin{bmatrix} \Delta y^*_{tar_s} \\ \Delta u^*_{d_s} \\ \Delta y^*_{d_s} \end{bmatrix} \\ \Delta u^*_s \end{bmatrix} = \begin{bmatrix} \tilde{P}_{11} & \tilde{P}_{12} \\ \tilde{P}_{21} & \tilde{P}_{22} \end{bmatrix} \begin{bmatrix} \begin{bmatrix} \Delta y^*_{tar_s} \\ \Delta u^*_{d_s} \\ \Delta y^*_{d_s} \end{bmatrix} \\ \Delta u^*_s \end{bmatrix}, \tag{4.24}$$

Then, the closed-loop transfer function T_{zw} from the input signal $w = [\Delta y^{*T}_{tar_s},\ \Delta u^{*T}_{d_s},\ \Delta y^{*T}_{d_s}]^T$ to the output signal $z = [Z_1^T,\ Z_2^T]^T$ can be computed by the lower linear fractional transformation (LFT), i.e.,

$$T_{zw} = F_l(P^*, K) = \tilde{P}_{11} + \tilde{P}_{12}K(I - \tilde{P}_{22}K)^{-1}\tilde{P}_{21}, \tag{4.25}$$

where

$$\begin{aligned}
\tilde{P}_{11} &= \begin{bmatrix} W_p & -W_p P_{DC} & -W_p \\ 0 & 0 & 0 \end{bmatrix} \\
\tilde{P}_{12} &= \begin{bmatrix} -W_p P_{DC} \\ W_u \end{bmatrix} \\
\tilde{P}_{21} &= [I \quad -P_{DC} \quad -I] \\
\tilde{P}_{22} &= -P_{DC}.
\end{aligned}$$

We define the transfer function M_s as

$$M_s = (I + P_{DC}K)^{-1}, \tag{4.26}$$

and write the closed-loop transfer function as

$$T_{zw} = F_l(P^*, K) = \begin{bmatrix} W_p M_s & -W_p M_s P_{DC} & -W_p M_s \\ W_u K M_s & -W_u K M_s P_{DC} & -W_u K M_s \end{bmatrix}. \tag{4.27}$$

The transfer function $W_p M_s$ ($-W_p M_s$) represents the response of the weighted tracking error to the target (output disturbance), while the transfer function $-W_p M_s P_{DC}$ denotes the response of the weighted tracking error to the input disturbance. The transfer function $W_u K M_s$ ($-W_u K M_s$) represents the response of the weighted control effort to the target (output disturbance), while the transfer function $-W_u K M_s P_{DC}$ denotes the response of the weighted control effort to the input disturbance.

A controller $K(s) = \Delta U_s^*(s)/E_s^*(s)$, where $E_s^*(s)$ denotes the Laplace transform of e_s^*, is sought to stabilize the closed-loop system and minimize the H_∞ norm of the

transfer function T_{zw}, denoted as $\|T_{zw}\|_\infty$, i.e.,

$$\min_{K(s)} \|T_{zw}\|_\infty. \tag{4.28}$$

The H_∞ norm of the transfer function T_{zw} is defined as the supremum over the frequency ω of the maximum singular value $\bar{\sigma}$ of the transfer function, i.e.,

$$\|T_{zw}(s)\|_\infty \triangleq \sup_\omega \bar{\sigma}[T_{zw}(j\omega)]. \tag{4.29}$$

The H_∞ norm represents the maximum energy amplification between input and output. Therefore, by minimizing $\|T_{zw}(s)\|_\infty$ while stabilizing the closed-loop system, the effect of the input signal (reference, input disturbance, output disturbance) on the energy of the output signal (frequency-weighted tracking error, frequency-weighted control effort) is also minimized. This is of critical importance because the objective is to keep the frequency-weighted tracking error $Z_1 = W_p e_s^*$ and control effort $Z_2 = W_u \Delta u_s^*$ small regardless of the characteristics of the reference $\Delta y_{tar_s}^*$, input disturbance $\Delta u_{d_s}^*$ and output disturbance $\Delta y_{d_s}^*$. Statement (4.28) defines what is called a mixed sensitivity H_∞ control problem since the goal is twofold: reduction of the tracking error (minimization of Z_1) while using as little feedback control effort as possible (minimization of Z_2). The H_∞ control synthesis technique is part of what is referred to as robust control theory [64] because by setting an upper bound for the H_∞ norm of the closed-loop transfer function, the controller is able to guarantee stability and a level of performance regardless of changes in the plant dynamics within a predefined set.

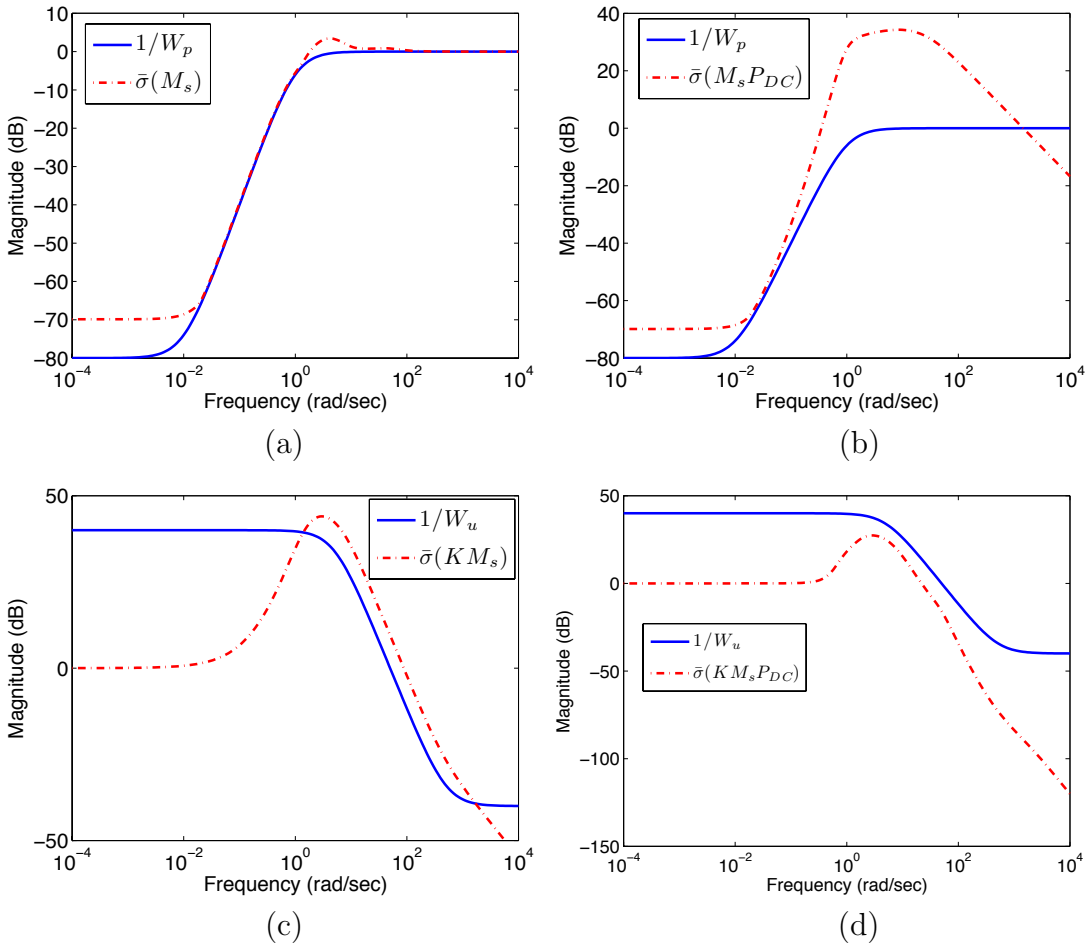

Figure 4.6: Inverse of performance weight W_p and maximum singular values of transfer function M_s (a) and M_sP_{DC} (b). Inverse of performance weight W_u and maximum singular values of transfer function KM_s (c) and KM_sP_{DC} (d).

Table 4.1: The H_∞ Control Parameters

Weight Function	M_i	w_{bi}	A_i	K_i
W_p	1	0.1	0.5	1
W_u	100	10	0.01	1

The weighting functions W_p and W_u, which can be parameterized as [63]

$$W_p(s) = \left(\frac{\frac{s}{M_1} + w_{b1}}{s + w_{b1}A_1}\right)^2 K_p, \quad W_u(s) = \left(\frac{s + w_{b2}A_2}{\frac{s}{M_2} + w_{b2}}\right)^2 K_u,$$

are used to shape in the frequency domain the responses of the tracking error and control effort. The coefficients M_1 and M_2 are related to the high frequency behaviors, the parameters A_1 and A_2 are related to the low frequency behaviors, and w_{b1} and w_{b2} are related to the bandwidths of the transfer functions. The design parameters in the H_∞ control synthesis as well as K_p and K_u are shown in Table 4.1. The parameters are chosen to shape the frequency responses $1/|W_p(j\omega)|$ and $1/|W_u(j\omega)|$, which in turn serve as the desired upper bounds for the maximum singular values of the closed-loop transfer functions for the tracking error and control effort. Typically, references and disturbances are low frequency signals; therefore, for good reference tracking, the magnitude of M_s should approach zero at low frequency. In order to prevent amplification of high frequency noise, the peak magnitude of M_s needs to be suppressed and its magnitude should approach one at high frequency. Accordingly, for tight control the magnitude of KM_s should be larger than one at low frequency, and should be attenuated below one at high frequency to avoid noise amplification by the feedback controller. Finally, the frequency range over which the feedback controller can actuate the system is specified by placing upper and lower limits on the bandwidth of the closed-loop system. Figure 4.6 compares the frequency responses of the upper bounds $1/W_p$ and $1/W_u$ with the maximum singular values of the closed-loop transfer functions M_s, M_sP_{DC}, KM_s and KM_sP_{DC}, achieved with the synthesized feedback controller K (see transfer function (4.27)) for $R = \text{diag}([0.01,\ 0.25,\ 1000,\ 0.5,\ 0.25])$ and $Q = \text{diag}([0.05,\ 0.1,\ 1,\ 1,\ 1,\ 1])$. As can be seen from Figure 4.6 (a)-(d), the frequency responses of the magnitudes of the maximum singular values of the closed-loop transfer functions are very close to their respective upper bounds, achieving in this way the pursued tracking goal. From Figure 4.6 (b), it is possible to note however that the controller cannot reject input disturbances in all frequencies. This is indeed expectable since it is not feasible to shape independently all the possible transfer

functions in a closed loop system due to intrinsic sensitivity constraints [63, 64] and lack of degrees of freedom (note that that the transfer function between the target signal (or output disturbance) and the weighted tracking error in Figure 4.6 (a) and the transfer function between the input disturbance and the weighted tracking error in Figure 4.6 (b) share the same free parameter, which is the controller K through the sensitivity function M_s, and are sought to be bounded by the same weight function $1/W_p$). Importantly, the controller guarantees good tracking and effective rejection of input disturbances, which are constant in this work, at low frequencies, and no amplification of the output disturbance, which is usually noise, at high frequencies.

By solving the minimization problem (4.28), we can synthesize a controller K that guarantees tracking while using as little control effort as possible. This is achieved both during the transients and in steady state, minimizing in turn (4.13). In practice, the control input and measured output of the original system P are Δu and Δy, respectively. The measured output is in turn used to compute the tracking error $e = \Delta y_{tar} - \Delta y$. As shown in Figure 4.4, the overall ι-profile and β_N controller for system P can be computed as

$$\hat{K}(s) = \frac{\Delta U(s)}{E(s)} = R^{-1/2} V_s K(s) S_s^{-1} U_s^T Q^{1/2}, \tag{4.30}$$

where $\Delta U(s)$ and $E(s)$ denotes the Laplace transforms of Δu and e, respectively, and where the definition of $K(s)$ and the relationships $e_s^* = S_s^{-1} U_s^T Q^{1/2} e$, $\Delta u = R^{-1/2} V_s \Delta u_s^*$ have been used. For implementation in the DIII-D PCS, the controller (4.30) is expressed in state space form, i.e.,

$$\begin{aligned} \dot{x}_c &= A_c x_c + B_c(\Delta y_{tar} - \Delta y) \\ \Delta u &= C_c x_c + D_c(\Delta y_{tar} - \Delta y), \end{aligned} \tag{4.31}$$

where x_c and (A_c, B_c, C_c, D_c) denote the controller state vector and system matrices.

4.2.4 Control Objectives, Expectations and Limitations

The significant component of the tracking error e_s^* introduced in the previous section and shown in Figure 4.4 plays a crucial role both in understanding the objectives of the controller and in judging its performance. The significant component of the tracking error e_s^*, representing the difference between the significant components of the target $\Delta y_{tar_s}^*$ and the significant components of the output Δy_s^*, can be written as

$$\begin{aligned} e_s^* &= \Delta y_{tar_s}^* - \Delta y_s^* = S_s^{-1} U_s^T Q^{1/2} (\Delta y_{tar} - \Delta y) \\ &= S_s^{-1} U_s^T Q^{1/2} (y_{tar} - y) = S_s^{-1} U_s^T Q^{1/2} e, \end{aligned} \tag{4.32}$$

where $e = \Delta y_{tar} - \Delta y = y_{tar} - y$ denotes the tracking error. It is critical to realize at this point that the dynamic component of the controller introduced in Section 4.2.3 is designed to reduce not the tracking error e but the significant components of the tracking error e_s^* as decided by the static component of the controller designed in Section 4.2.2, which takes care of the decoupling of the system and the selection of the significant control channels based on the significant basis given by the columns of $Q^{-1/2} U_s S_s$. The cost function

$$\begin{aligned} J_s &= (e_s^*)^T S_s^2 (e_s^*) = (\Delta y_{tar_s}^* - \Delta y_s^*)^T S_s^2 (\Delta y_{tar_s}^* - \Delta y_s^*) \\ &= \sum_{i=1}^{k} \sigma_i^2 (\Delta y_{tar_i}^* - \Delta y_i^*)^2 \triangleq \sum_{i=1}^{k} J_{s_i}, \end{aligned} \tag{4.33}$$

which reduces to the the cost function (4.15) as $t \to \infty$, could therefore be used to evaluate the performance of the controller.

In other words, the objective of the controller is only to drive the component of the output Δy lying in the subspace generated by the significant basis close to the component of the target Δy_{tar} lying in the same subspace. The difference between these two components is indeed the part of the tracking error e that can be driven to zero or removed by the controller if enough actuation is available. The tracking error can then be written as $e = e_{rm} + e_{nrm}$, where e_{rm} is the removable tracking error and e_{nrm} is the unremovable tracking error, which has no projection on the subspace generated by the significant basis, i.e. $S_s^{-1}U_s^T Q^{1/2} e_{nrm} = 0$. The removable tracking error can be written as

$$\begin{aligned} e_{rm} = Q^{-1/2}U_s S_s e_s^* &= Q^{-1/2}U_s S_s [S_s^{-1}U_s^T Q^{1/2} e] \\ &= Q^{-1/2}U_s S_s [S_s^{-1}U_s^T Q^{1/2}(\Delta y_{tar} - \Delta y)] \\ &= Q^{-1/2}U_s U_s^T Q^{1/2}\Delta y_{tar} - Q^{-1/2}U_s U_s^T Q^{1/2}\Delta y \\ &= (Q^{-1/2}U_s U_s^T Q^{1/2}\Delta y_{tar} + y_{FF}) - (Q^{-1/2}U_s U_s^T Q^{1/2}\Delta y + y_{FF}). \end{aligned} \tag{4.34}$$

The controller is then designed to reduce e_{rm}, or equivalently, to drive the significant output $\Delta y_s = Q^{-1/2}U_s U_s^T Q^{1/2}\Delta y$ close to the significant target $\Delta y_{tar_s} = Q^{-1/2}U_s U_s^T Q^{1/2}\Delta y_{tar}$.

It is important to realize that, regardless of the number of significant singular vectors used for control design, the objective of the MIMO controller is not to achieve tight regulation for a finite number of components of the significant output but to reduce a removable tracking error that includes all the components of the output. The proposed controller is designed to drive the outputs as close as possible to their target values in order to minimize the overall weighted tracking error, which sometimes may result for instance in increasing the tracking error for some components of the output if this leads to a decrease of the tracking error for some other components

that produces a net reduction of the overall weighted tracking error. It is therefore not expected individual and independent control of a finite number of points on the profile but a consistent reduction of the overall weighted tracking error. As the overall weighted tracking error is driven to zero, tight regulation of all the components of the output is achieved (in the subspace generated by the basis of significant singular vectors). However, it is unrealistic to expect no tracking error. As long as the control effort is limited by physical (actuation saturation) or design (actuation penalization) constraints, there will be some unreachable target output. Besides the saturation of the actuators, which is inherent to any physical system, in this work we penalize the control effort during both the static controller design (weighting matrix R) and the dynamic controller design (weighting function W_u). Therefore, neither the cost function (4.33) nor the removable error (4.35) will be driven to zero by the controller since its goal is not the pure elimination of tracking error but the combined minimization of tracking error and control effort.

It is also critical to understand that the controller is designed for a limited bandwidth. The weighting functions W_p and W_u, which are functions of the frequency, not only impose relative weights on the tracking error and the control effort but also define the bandwidth over which the weights are imposed. In this way, the closed-loop transfer functions are shaped in the frequency domain with a particular bandwidth that will of course affect the response of the system. This can be appreciated from Figure 4.6 (a), which shows the frequency response of the sensitivity function M_s that relates the target signal with the tracking error. It is possible to note that for frequencies below 1 Hz, the tracking error is attenuated, while for frequencies above 1 Hz, it is not. This implies that the closed-loop system will be able to track only targets with frequency content below 1 Hz. The bandwidth of the closed-loop system is directly correlated with the bandwidth of the open loop system, which is assumed

Table 4.2: Actuator Limits in DIII-D (some limits are due to practical constraints on operating the actuators while others (e.g., I_p) are defined as administrative limits)

Channel	Actuator	Min	Max	Units
1	Ip	0.3	1.5	MA
2	Co-beam Power	0	12.5	MW
3	Ct-beam Power	0	5	MW
4	Blanced-beam Power	0	2.5	MW
5	Total EC Power	0.3	3	MW

during the modeling procedure by choosing the frequency content of the excitation (input) signals during the system identification experiment and the cutoff frequency of the low-pass filter (3.7).

Finally, it is always important to remember that the plasma response models used for control design in this work are linear and valid only around the reference state used during the system identification experiment. The linearity of the model limits the controller to applications where the control objective is just the regulation of the system around the reference state. Moreover, attempting just regulation around a reference state different from that used for system identification may limit the closed-loop performance.

4.2.5 Design of Anti-windup Compensator

The DIII-D tokamak is a nonlinear complex system, which is subject to actuator saturations as shown in Table 4.2. At the moment of designing the mixed-sensitivity H_∞ MIMO controller (4.31), the actuator saturations were not considered, i.e., $\hat{u} = u$ and $\Delta\hat{u} = \Delta u$. As a result of saturation, the actual plant input may be different from the output of the controller. In this case the controller output does not drive the plant input and, as a consequence, the states of the controller may wind up because the plant does not respond as expected, which can cause the behavior of the system

to deteriorate dramatically or even become unstable. To cope with the negative effects of saturation, the goal is not to redesign the proposed MIMO controller but to design an anti-windup compensator that keeps the controller well-behaved and avoid undesirable oscillations when saturation is present. The anti-windup compensator must in addition leave the nominal closed-loop unmodified when no saturation is present. The anti-windup augmentation is written as

$$\begin{aligned} \dot{x}_{aw} &= A_{aw}x_{aw} + B_{aw}(\hat{u} - u) + \gamma(u, \hat{u})\lambda \\ s &= C_{aw}x_{aw} \\ \lambda &= -cx_{aw} - A_{aw}x_{aw} - B_{aw}(\hat{u} - u) \end{aligned} \quad , \tag{4.35}$$

where $\hat{u}$ denotes the output of the saturation function defined as

$$\hat{u}_i = sat_{u_i^{min}}^{u_i^{max}}(u_i) = \begin{cases} u_i^{max} & \text{if } u_i^{max} < u_i \\ u_i & \text{if } u_i^{min} < u_i < u_i^{max} \\ u_i^{min} & \text{if } u_i < u_i^{min} \end{cases} \quad , \tag{4.36}$$

where u_i^{max} and u_i^{min} are the maximum and minimum saturation limits for i^{th} input channel, for $i = 1, \ldots, m$, $\gamma(u, \hat{u}) = 1$ if $u = \hat{u}$ and 0 otherwise, and c is a positive constant. The system matrices (A_{aw}, B_{aw}, C_{aw}) of the anti-windup compensator are chosen identical to the system matrices (A, B, C) of the plant P in (3.8) [65, 66, 67].

When $\hat{u} \neq u$ (saturation), the anti-windup compensator should keep the controller well-behaved and avoid undesirable oscillations. To achieve this goal, the output of the anti-windup compensator s must modify the nominal closed-loop system as shown in Figure 4.1. In this case, $\gamma \equiv 0$ and the anti-windup compensator (4.35) reduces to

$$\begin{aligned} \dot{x}_{aw} &= A_{aw}x_{aw} + B_{aw}(\hat{u} - u) \\ s &= C_{aw}x_{aw} \end{aligned} \quad . \tag{4.37}$$

The relation between input and output of the linear model (4.37) can be expressed in terms of its transfer function $AW(s)$, i.e.,

$$\frac{\Delta S(s)}{\Delta \hat{U}(s) - \Delta U(s)} = AW(s) = C_{aw}(sI - A_{aw})^{-1}B_{aw}, \tag{4.38}$$

where s denotes the Laplace variable and $\Delta S(s)$ and $\Delta \hat{U}(s) - \Delta U(s)$ denote the Laplace transforms of the output s and the input $\hat{u} - u$ respectively. It is possible to note from Figure 4.1 that the input to the controller will be in this case equal to

$$\Delta Y(s) - \Delta S(s) = P(s)\Delta \hat{U}(s) - AW(s)(\Delta \hat{U}(s) - \Delta U(s)), \tag{4.39}$$

where both (3.8) and (4.38) have been used. By choosing the system matrices (A_{aw}, B_{aw}, C_{aw}) of the anti-windup compensator identical to the system matrices (A, B, C) of the plant model, the transfer functions $P(s)$ and $AW(s)$ are also identical. Therefore, the input to the controller reduces to

$$\Delta Y(s) - \Delta S(s) = P(s)\Delta U(s), \tag{4.40}$$

which represents the response of the system to the unsaturated control input $\Delta U(s)$ requested by the controller. The anti-windup compensator hides the saturation from the nominal controller [65, 66, 67] and guarantees in this way that the controller remains well behaved.

When $\hat{u} = u$ (no saturation), the anti-windup compensator should leave the nominal closed-loop unmodified. To achieve this goal, the output of the anti-windup compensator s, and therefore its state x_{aw}, must be forced to zero. In this case, $\gamma \equiv 1$

and the anti-windup compensator (4.35) reduces to

$$\begin{aligned} \dot{x}_{aw} &= -cx_{aw} \\ s &= C_{aw}x_{aw} \end{aligned} . \tag{4.41}$$

With the freedom of choosing the positive constant c, the state x_{aw} will converge to zero arbitrarily fast and so will the output s.

4.2.6 Control Algorithm Implementation in the DIII-D PCS

The controller was implemented as a discrete-time state-space system with a sampling time of 20 milliseconds. This sampling time was set based on the modulation of the motional Stark effect (MSE) beam used to obtain q profile measurements in real-time, which was modulated on for 10 milliseconds then off for 10 milliseconds. The measurements provided to the PCS by rtEFIT, are β_N, the plasma current I_p, the poloidal stream function at the magnetic axis ψ_{axis} and at the plasma boundary ψ_{bdry}, and the safety factor q on a normalized flux spatial domain $\psi_n = \frac{\psi - \psi_{axis}}{\psi_{bdry} - \psi_{axis}}$. The safety factor $q(\psi_n^{rt})$ is provided by rtEFIT at 64 evenly spaced points $\psi_{n_k}^{rt} = 0, 1/64, 2/64, \ldots, 63/64$. By using the relationship between the toroidal flux and the mean effective minor radius, a coordinate transformation algorithm (see [51], Appendix D) has been implemented in the PCS as part of this work to construct the to-be-controlled magnetic profile (q, ι, $\Psi = 2\pi\psi$, or $\theta \triangleq \partial\psi/\partial\hat{\rho}$) as a function of $\hat{\rho}$ from the data provided by the rtEFIT algorithm ($q(\psi_n^{rt})$, ψ_{axis}, ψ_{bdry}, and I_p).

Table 4.3: Initial Conditions

Shot	Identification	Reference	Dist. I	Dist. II	Dist. III
I_p	0.9045 MA	0.9013 MA	0.8997 MA	0.8957 MA	0.8972 MA
β_N	1.8840	2.3897	2.3122	2.4097	2.3763

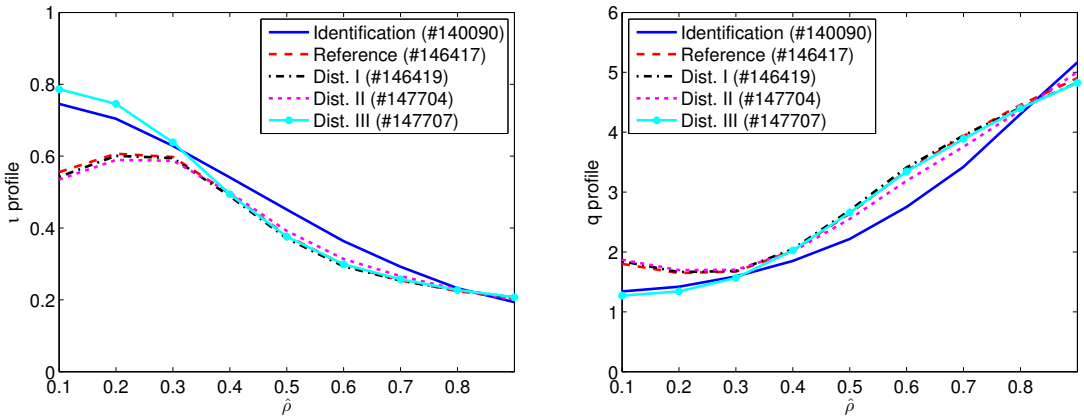

(a) (b)

Figure 4.7: Rotational transform ι profile (a) and safety factor q profile (b) for shots #140090, #146417, #146419, #147704 and #147707 at $t = 2.5$ s.

4.3 Closed-loop Simulated and Experimental Results

Simulated and experimental results are presented in this section to illustrate the performance of the proposed feedforward + feedback control scheme. The whole control system, which combines the MIMO controller and the anti-windup compensator, is shown in Figure 4.1. A reference (feedforward) control shot #146417 for the control experiment was run first without feedback control in order to reproduce flat-top conditions of the system identification experiment. Figure 4.7 compares ι and q at $t = 2.5$ s for the typical system identification shot #140090 and the reference control shot #146417, and Table 4.3 provides the values of I_p and β_N at $t = 2.5$ s for both shots. Both the figure and the table show that the reproduction is not completely

Table 4.4: Input Disturbances

Number	ΔI_{p_d}	ΔP_{CO_d}	ΔP_{CT_d}	ΔP_{BL_d}	ΔP_{EC_d}
Disturbance I	0.02 MA	-0.25 MW	0 MW	-0.25 MW	-0.1 MW
Disturbance II	0.1 MA	0 MW	0 MW	0 MW	0 MW
Disturbance III	0.1 MA	0.1 MW	0 MW	-0.1 MW	0MW

successful, neither in terms of the q or ι profiles, nor in terms of β_N, which can impact the closed-loop performance due to the questionable validity of the linear model. The feedforward inputs (after $t = 2.5$ s), denoted as u_{FF}, for the reference control shot #146417, which are represented by red dashed lines in the figures in this section, are $I_p = 0.9$ MA, $P_{CO} = 1.9838$ MW, $P_{CT} = 0$ MW, $P_{BL} = 2$ MW, and $P_{EC} = 1.4415$ MW. The feedforward inputs are rather different from those used during the system identification experiment, which are given by $I_p = 0.85$ MA, $P_{CO} = 3.2681$ MW, $P_{CT} = 0$ MW, $P_{BL} = 0$ MW, and $P_{EC} = 1.4431$ MW (after $t = 2.5$ s). This choice was driven by the decision of: i- moving the feedforward input values away from the saturation values and providing more headroom for the feedback controller while approximately preserving the total NBI power; ii- creating a to-be-tracked target profile slightly different from the system-identification reference profile (assuming good reproduction of system-identification conditions at $t = 2.5$ s). The ι profile and β_N resulting from these reference (feedforward) inputs in shot #146417, denoted as y_{FF}, are used as targets in the control experiments and represented by red dashed lines in the figures in this section.

The goal for both simulations and experiments was to demonstrate that the proposed controller is capable of regulating the system around target ι profile and β_N even in the presence of disturbances. Note that since the control goal is regulation, $\Delta y_{tar} \equiv 0 \iff y_{tar} = y_{FF}$ in all the control experiments. As discussed in Section 4.2.4, this implies that $\Delta y_{tar_s} = \Delta y_{tar} \equiv 0$ and $e_{rm} = y_{FF} - (\Delta y_s + y_{FF})$. Since

the goal of the controller is to drive e_{rm} close to zero while minimizing the control effort, it is therefore of interest to compare $\Delta y_s + y_{FF}$ with $y_{tar}(= y_{FF})$, which are represented by black dashed-dotted lines and red dashed lines, respectively, in the figures in this section. Three sets of input disturbances (shown in Table 4.4) were created for this purpose. The input disturbances of the plasma current and H&CD powers can be expressed as $\Delta u_d = [\Delta I_{p_d}^T,\ \Delta P_{CO_d}^T,\ \Delta P_{CT_d}^T,\ \Delta P_{BL_d}^T,\ \Delta P_{EC_d}^T]^T$ (see Figure 4.1 or Figure 4.4 for disturbance injection point). Disturbance I, representing relatively large disturbances in the neutral beam powers and a small disturbance in the plasma current, is introduced at $t = 3.5$ s to test ι profile control. Disturbance II, representing a relatively large disturbance in the plasma current, is introduced at $t = 3$ s to test ι profile control. Disturbance III, representing relatively large disturbances in both the plasma current and the neutral beam powers, is introduced at $t = 3$ s to test simultaneous ι profile and β_N control.

The decision of not smoothening the target signal $y_{tar}(= y_{FF})$ obtained as a direct measurement from the reference (feedforward) control shot #146417, although not optimal and leading to a more complicated analysis of the results, responds to the convenience of minimizing operations between discharges to avoid implementation mistakes and to maximize the experimental time. The objective is however by no means the tracking of the measurement noise. The high-frequency noise cannot be indeed tracked by the closed-loop system due to its limited bandwidth (see Figure 4.6 (a)). It is therefore expected that most of the noisy component of the target be filtered by the closed-loop system itself and approximately the same closed-loop response be obtained regardless of using a noisy or a smoothened target signal.

During the control experiments, the counter-injection beam was not available and the gryotrons were either poorly controlled or unavailable. The unavailability of the counter-injection beam was known right before the experiment, allowing for the

redesign of the controllers in preparation for this condition by setting a high value for the associated weight in the R matrix. Associating a high weight to an unavailable actuator instead of removing it from the model, which would indeed be a better solution, allows for the redesign of the controller without modifying its number of outputs, reducing in this way the risk of controller implementation problems when the actuator is lost right before the experiment. The gyrotrons were lost during the experiment, not allowing for the redesign of the controller. Note that the controller does not request counter-injection beam power but it does request gyrotron power.

The proposed controllers were tested in the flat-top phase of the discharge, from $t_i = 2.5$ s to $t_f = 6$ s in both simulations and experiments. To allow for comparison between simulations and experiments, the experimental situations are replicated in the simulation studies.

4.3.1 Case 1: Rotational Transform ι Profile Control under Disturbance I

When the objective is the control of just the ι profile, only the state equation of the slow model (3.5) is used for control design (model (3.8) is reduced by eliminating the second rows in both the state and output equations). All singular values are kept during the controller design ($k = m = 5$) in this case. The plasma current I_p plays a significant role in controlling the ι profile at the plasma boundary, and the counter-injection beam was not available in the experiment; therefore, the matrix is set as $R = \text{diag}([0.1,\ \ 0.25,\ \ 1000,\ \ 0.5,\ \ 0.25])$. Equal weight is put on each tracking error component, i.e., $Q = \text{diag}([1,\ \ 1,\ \ 1,\ \ 1,\ \ 1])$.

Figure 4.8 shows simulation results. The simulated closed-loop-controlled inputs (solid blue lines) are shown in Figure 4.8 (a) and compared with the refer-

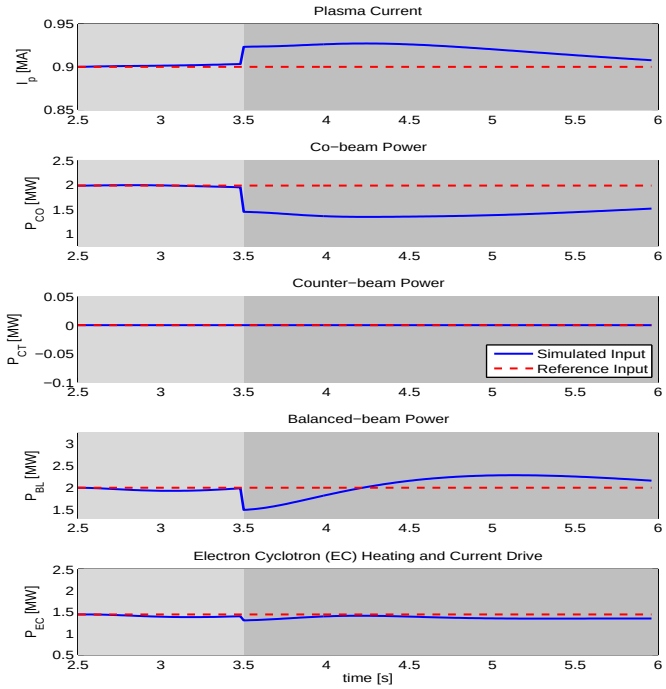

(a)

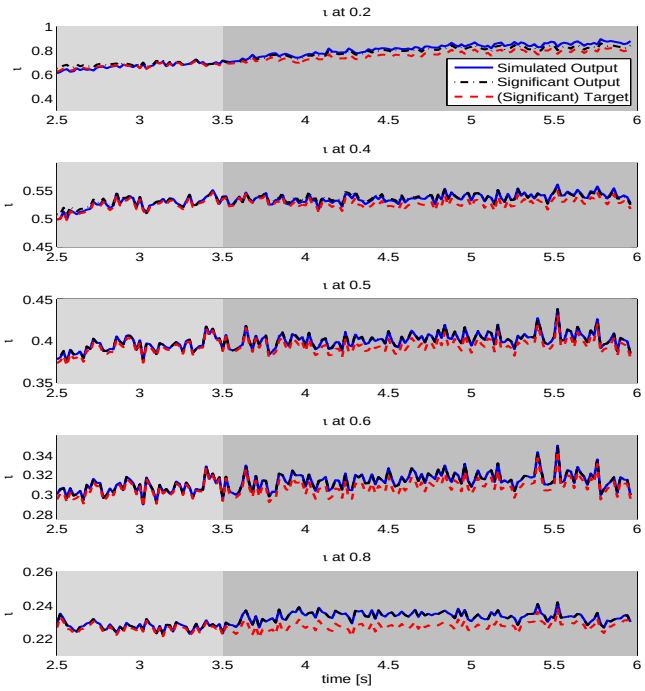

(b)

Figure 4.8: Rotational transform ι profile closed-loop-controlled simulation (shot #146419): (a) Inputs, (b) Outputs. Disturbance I. Light-gray background: feedback on - disturbance off, dark-gray background: feedback on - disturbance on.

ence open-loop inputs (red dashed lines). The controller rejects the disturbance in the plasma current I_p rather slowly, and I_p nearly stays constant during the simulation, as shown in Figure 4.8 (a.1). Beam and gyrotron powers, shown in Figure 4.8 (a.2)-(a.5), are modulated by the feedback controller away from their reference values without hitting saturation limits. The simulated closed-loop-controlled ι profile at $\hat{\rho} = 0.2, 0.4, 0.5, 0.6, 0.8$ (solid blue lines) is shown in Figure 4.8 (b). Moreover, the significant output (dashed-dotted black lines) is compared with the (significant) target (red dashed lines) in the same figure. In the first second of the simulation, from $t = 2.5$ s to $t = 3.5$ s, the controller regulates ι around the target; afterwords the controller strives to reject the disturbance injected at $t = 3.5$ s, keeping the tracking error under 10%.

Figure 4.9 shows the experimental results obtained from shot #146419. The experimental closed-loop-controlled inputs are shown in Figure 4.9 (a) and compared with the reference open-loop inputs (red dashed lines). Both the values requested by the ι-profile controller (magenta dashed-dotted lines) and the values achieved by the dedicated plasma current, beam power and gyrotron power dedicated controllers (blue solid lines) are illustrated in the figure. Note that while the plasma current and beam power controllers successfully deliver the values requested by the ι-profile controller, the EC power control is very poor during this discharge, which can be interpreted as an additional input disturbance. The trends of all experimental inputs (Figure 4.9 (a)) are very similar to those obtained in simulations (Figure 4.8 (a)), which suggests that the data-driven linear model successfully approximates the ι profile response around the reference profile. The experimental closed-loop-controlled ι profile at $\hat{\rho} = 0.2, 0.4, 0.5, 0.6, 0.8$ (solid blue lines) are shown in Figure 4.9 (b). In addition, the significant output (dashed-dotted black lines) is compared with the (significant) target (red dashed lines) in the same figure. From $t = 2.5$ s to $t = 3.5$ s, there are

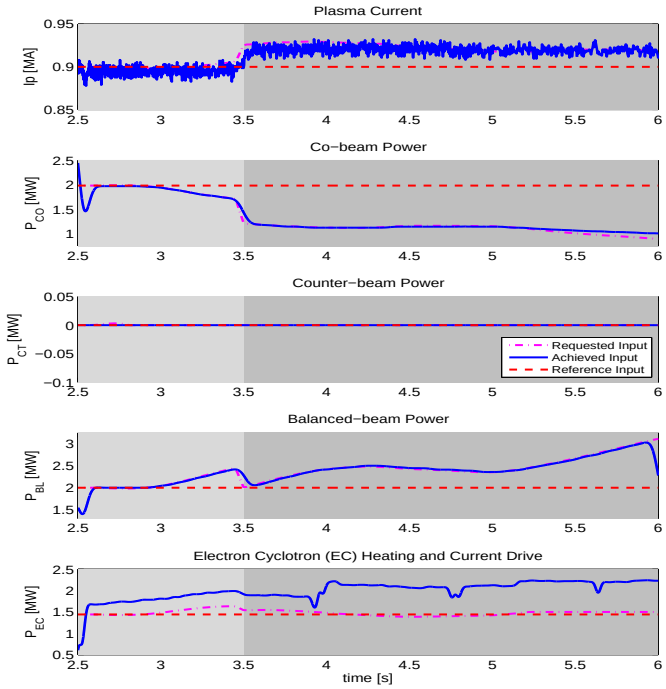

(a)

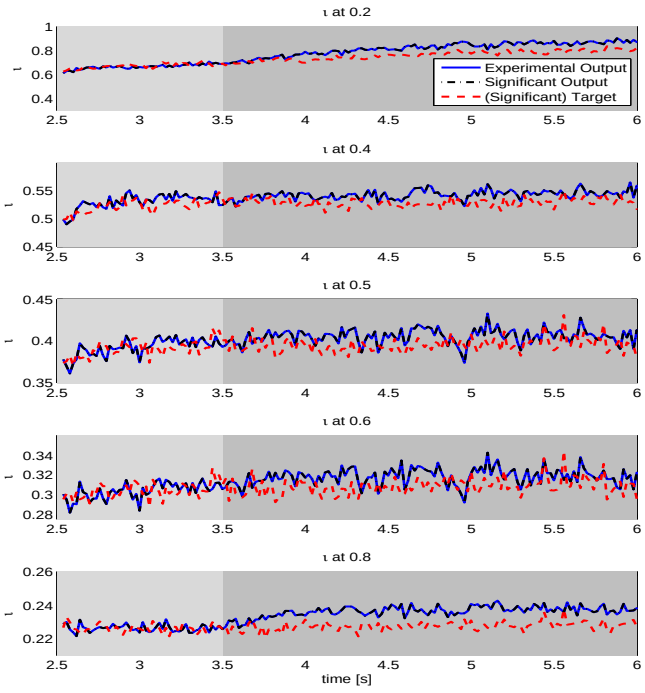

(b)

Figure 4.9: Rotational transform ι profile closed-loop-controlled experiment (shot #146419): (a) Inputs, (b) Outputs. Disturbance I. Light-gray background: feedback on - disturbance off, dark-gray background: feedback on - disturbance on.

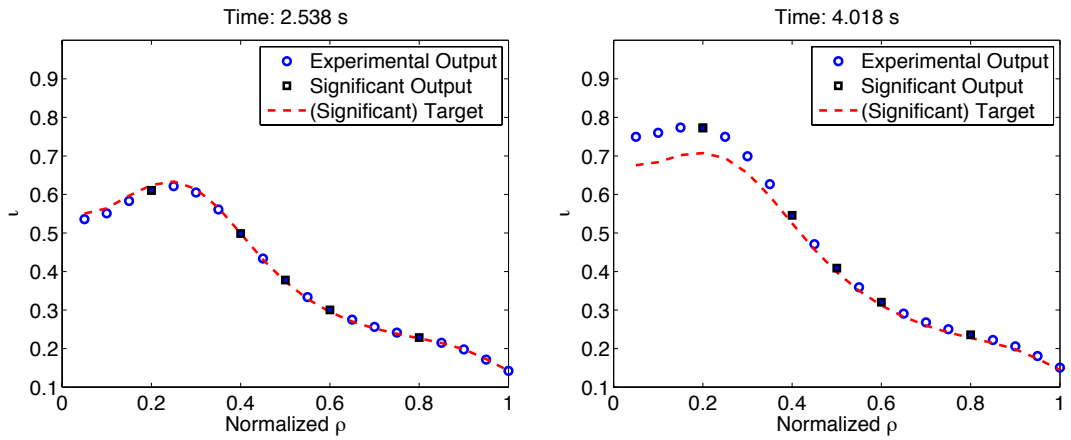

(a) Feedback ON, Disturbance OFF

(b) Feedback ON, Disturbance ON

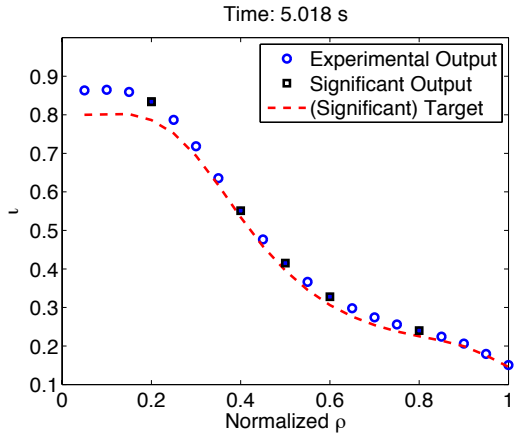

(c) Feedback ON, Disturbance ON

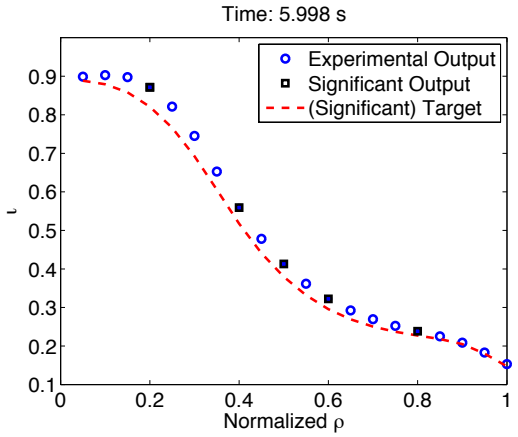

(d) Feedback ON, Disturbance ON

Figure 4.10: Plasma $\iota(\hat{\rho})$ profile at time t= 2.538, 4.018, 5.018, 5.998 s (shot # 146419).

no input disturbances, and the tracking errors are less than 0.5%. Disturbance I is injected at $t = 3.5$ s and its effect is very clear from Figure 4.9 (a). The tracking quality clearly deteriorates after $t = 3.5$ s but the controller manages to drive the system within a 10% margins around the target profile. As in the simulation study, the plasma current I_p nearly keeps a constant value and shows a rather sluggish behavior. In addition, the available actuation does not seem to be fully used.

A series of four plasma ι profiles at different times during the experiment are shown in Figure 4.10. The red dashed line denotes the (significant) target profile,

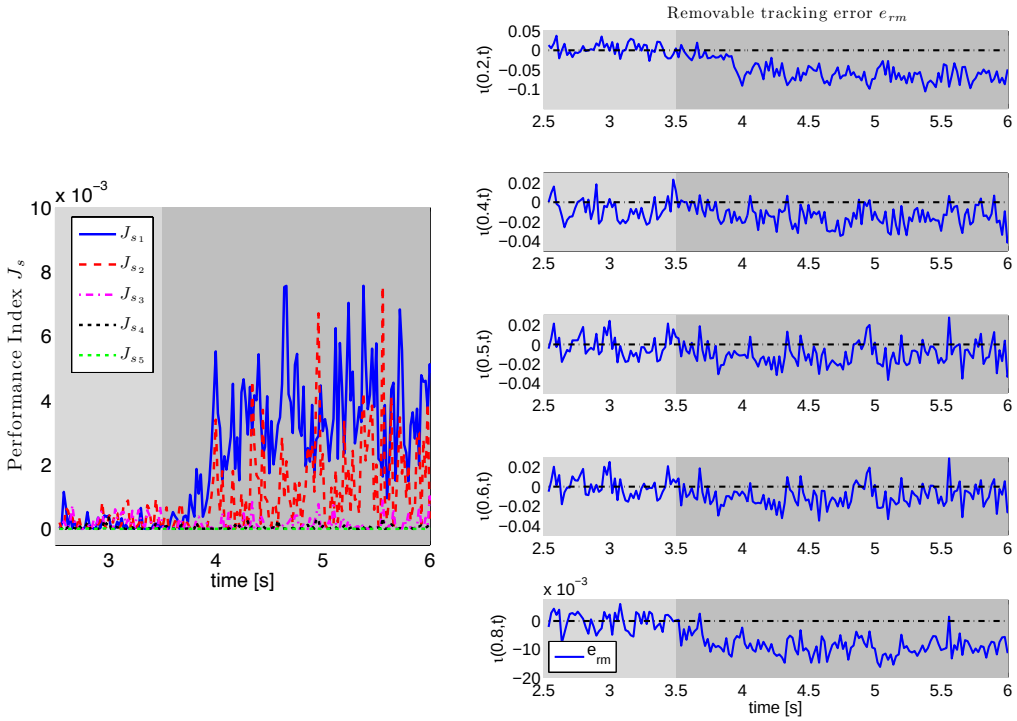

(a) (b)

Figure 4.11: Control performance metrics (shot #146419 - Disturbance I): (a) Cost function, (b) Removable tracking error for ι profile at $\hat{\rho} = 0.2, 0.4, 0.5, 0.6, 0.8$. Light-gray background: feedback on - disturbance off, dark-gray background: feedback on - disturbance on.

the black squares represent the significant output, and the blue circles represent the measured ι profile at different locations (the solid circles denote the control points). As can be seen from Figure 4.10 (a), the initial profile is very close to the target, which implies that the conditions of shot #146417 have been successfully reproduced at $t = 2.5$ s. After the input disturbances are injected into the system, the tracking errors become larger. As the time goes on, the controller rejects the disturbance, and the errors become smaller, which is shown in Figure 4.10 (b), (c), (d).

Figure 4.11 illustrates some metrics related to the performance of the controller. On the left, Figure 4.11 (a) shows the performance index J_s (4.33), while on the right,

Figure 4.11 (b) shows the removable tracking error e_{rm} (4.35). Since $k = m = p = 5$ in this case, all outputs and targets live in the subspace generated by the significant singular vectors. In other words, $\Delta y_s = \Delta y$, $\Delta y_{tar_s} = \Delta y_{tar}$, and all the tracking error is removable ($e = e_{rm}$). This explains the fact that blue solid lines and dashed-dotted black lines are coincident in Figure 4.8 and Figure 4.9, and blue circles and black squares are coincident in Figure 4.10. Under these conditions, the controller could in principle drive the output to the target. This is not shown, however, in any of the figures. Instead, the controller seems to drive the tracking error to a small (note scale in Figure 4.11 (a)) but non-zero steady value both in the experiment and in the simulation. As discussed in Section 4.2.4, this could be explained by the controller trying to minimize control effort at the expense of a larger tracking error. This would be consistent with the observed actuator behavior (weak and sluggish actuation) and would indicate the need to reduce the weight R in comparison with the weight Q. There is, however, another reason for this behavior, which is the lack of two actuators (P_{CT} and P_{EC}). Since $m = 3$ in practice, the controller is able to independently actuate the system only in three different directions (input singular vectors). This implies that only three different output singular vectors are indeed available for the generation of the system output in a space of dimension $p = 5$, which makes Δy_s (Δy_{tar_s}) indeed different from Δy (Δy_{tar}) and the tracking error not completely removable.

4.3.2 Case 2: Rotational Transform ι Profile Control under Disturbance II

To improve the tracking performance while avoiding spending a lot of control effort for a marginal improvement of the cost function value, the control weight matrix is

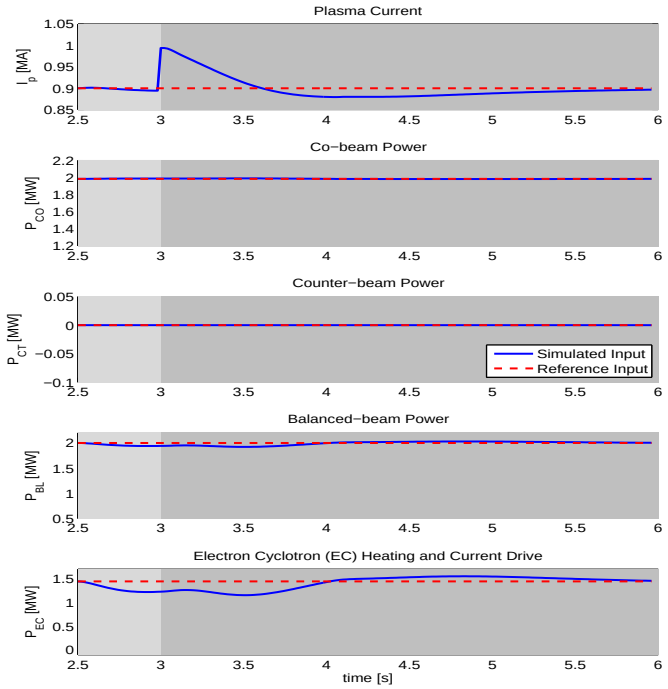

(a)

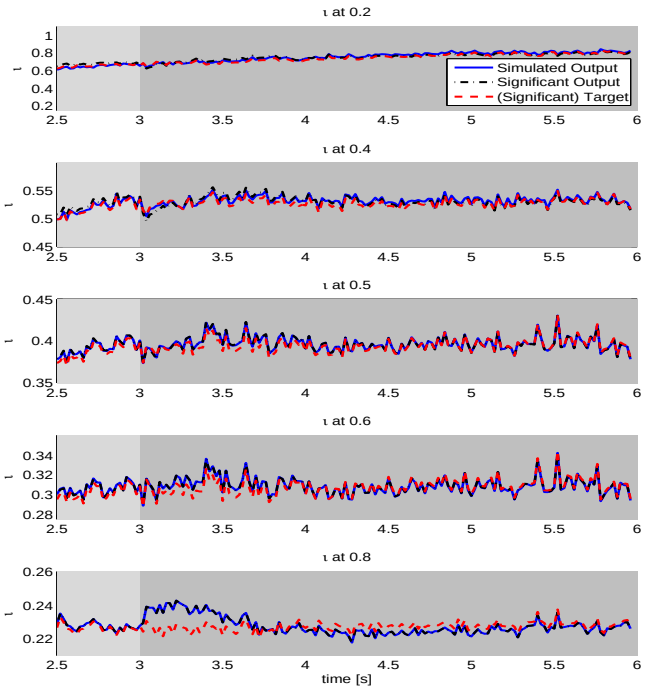

(b)

Figure 4.12: Rotational transform ι profile closed-loop-controlled simulation (shot #147704): (a) Inputs, (b) Outputs. Disturbance II. Light-gray background: feedback on - disturbance off, dark-gray background: feedback on - disturbance on.

redefined as $R = \text{diag}([0.01,\ 0.25,\ 1000,\ 0.5,\ 0.25])$ and only the two most significant singular values ($k = 2$) are preserved in this case study. In this way more I_p regulation is allowed and the effort by the controller is focused on reducing the two most significant contributions to the cost function value (see the contributions by the different singular values in Figure 4.11 (a) as an example). Note that this decision is rather conservative because up to $k = 3$ singular values could have been kept according to the number of available actuators (I_p, P_{CO}, P_{BL}). Equal weight is put on each tracking error component, i.e., $Q = \text{diag}([1,\ 1,\ 1,\ 1,\ 1])$.

Figure 4.12 shows simulation results. The controller now rejects the disturbance in the plasma current I_p more quickly and drives the I_p close to the constant reference (feedforward) value, as shown in Figure 4.12 (a.1). Beam and gyrotron powers, shown in Figure 4.12 (a.2)-(a.5), are weakly modulated by the feedback controller within the saturation limits and are driven towards to their reference (feedforward) values by the end of the discharge. In the first 0.5 second of the simulation, from $t = 2.5$ s to $t = 3$ s, the regulation results for the undisturbed plant are satisfactory for all control points ($\hat{\rho} = 0.2, 0.4, 0.5, 0.6, 0.8$) as shown in Figure 4.12 (b). Once the disturbance in the plasma current is injected at $t = 3$ s, its effect on the outer ι profile becomes clearly notable from Figure 4.12 (b.5), where it is shown that the ι value at $\hat{\rho} = 0.8$ ramps up. The robust controller rejects the disturbances and reduces the tracking errors in less than one second, keeping them below 5% for the rest of the discharge.

Figure 4.13 shows the experimental results obtained from shot #147704. As shown in Figure 4.13 (a.1), the ι-profile controller rejects the plasma current disturbance rather fast and the dedicated I_p controller delivers the requested current very closely. The working beams successfully follow the values requested by the ι-profile controller but the EC H&CD system is not available during the discharge and does not deliver the requested value, which introduces an additional disturbance into the closed-loop

system that the controller must overcome. Both the EC H&CD system and the counter-injection beam have important effects on the plasma resistivity and toroidal current density in the center of the plasma. This can be appreciated by examining the steady-state gains of the system in Figure 4.2, where both P_{CT} and P_{EC} strongly affect the inner part of the steady-state ι profile. The lack of EC H&CD power regulation, added to the unavailability of the counter-injection beam, makes the control of the inner ι profile very challenging as observed clearly from Figure 4.13 (b.1)-(b.2). Since the plasma current disturbance is quickly rejected after $t = 3$ s, the outer profile tracking errors are kept small. There are nearly no tracking errors after $t = 4$ s for ι at $\hat{\rho} = 0.5, 0.6, 0.8$ as noted from Figure 4.13 (b.3)-(b.5). During the experiment, the requested EC and balanced-beam powers reach saturation and activate the anti-windup compensator, which causes the difference observed between simulation (Figure 4.12) and experiment (Figure 4.13).

A series of four plasma ι profiles at different times during the experiment are shown in Figure 4.14. As can be seen from Figure 4.14 (a), the initial profile is very close to the target, which implies that the conditions of shot # 146417 have been successfully reproduced at $t = 2.5$ s. After the input disturbances is injected into the system, the tracking performance deteriorates, particularly in the inner region of the plasma as shown in Figure 4.14 (b). As time goes on, the controller rejects the disturbance and forces the tracking errors at $\hat{\rho} = 0.5, 0.6, 0.8$ to become smaller as shown in Figure 4.14 (c)-(d). Due to the unavailability of both the EC H&CD and the counter-injection NBI systems in this experiment, the tracking performance at $\hat{\rho} = 0.2, 0.4$ remains rather poor during the whole discharge.

Since $(k = 2) < (m = p = 5)$ in this case, not all the outputs live in the subspace generated by the significant singular vectors. In other words, $\Delta y_s \neq \Delta y$ and not all the tracking error is removable ($e = e_{rm} + e_{nrm}$). This explains the fact that blue

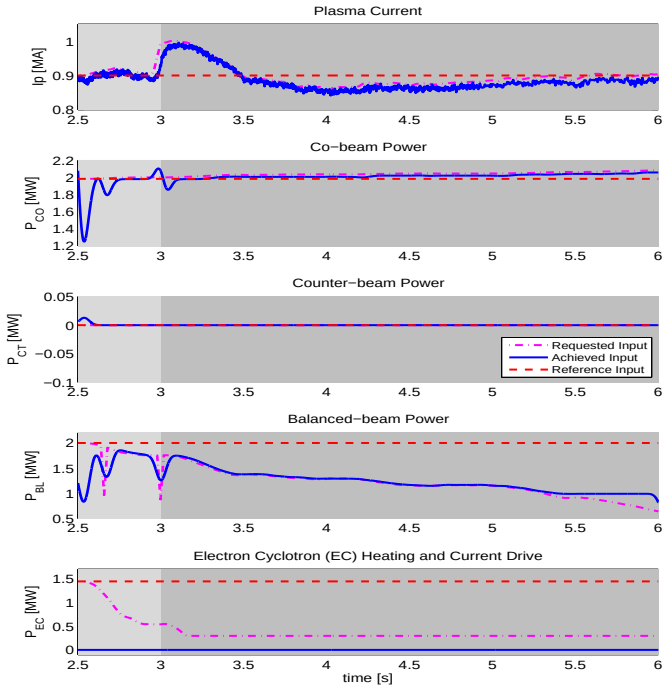

(a)

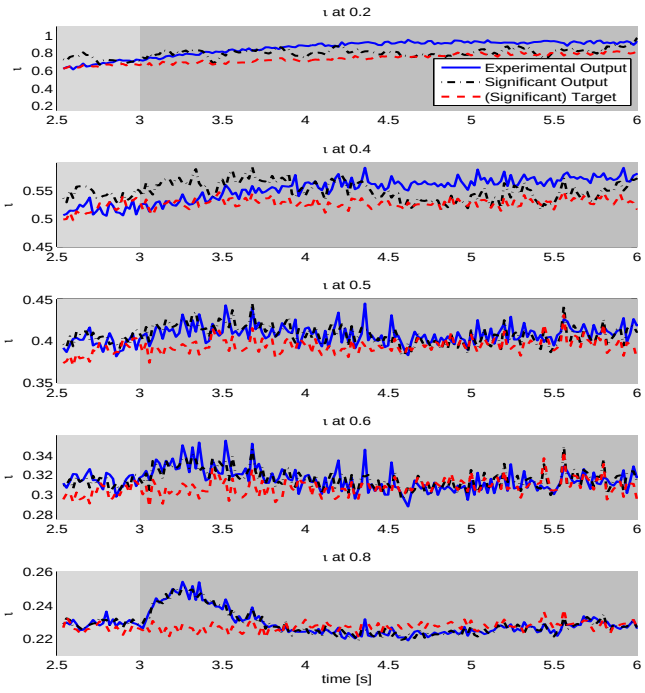

(b)

Figure 4.13: Rotational transform ι profile closed-loop-controlled experiment (shot #147704): (a) Inputs, (b) Outputs. Disturbance II. Light-gray background: feedback on - disturbance off, dark-gray background: feedback on - disturbance on.

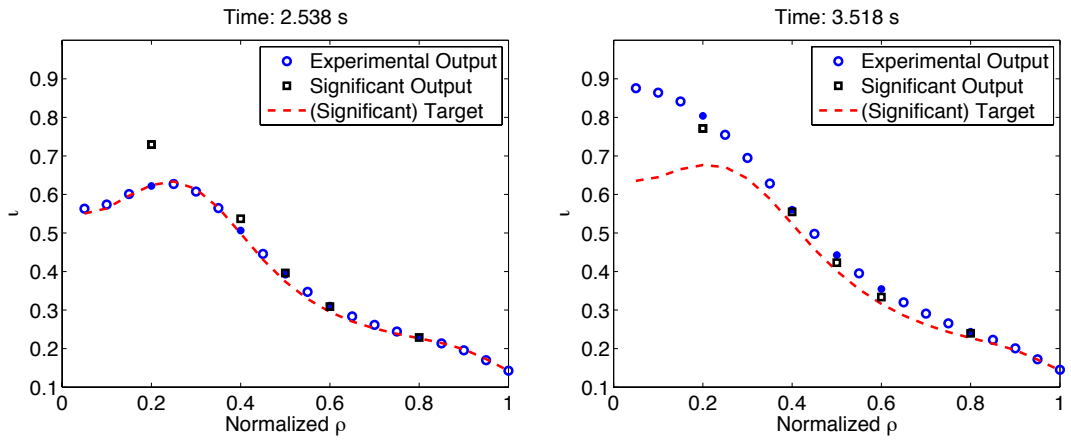

(a) Feedback ON, Disturbance OFF

(b) Feedback ON, Disturbance ON

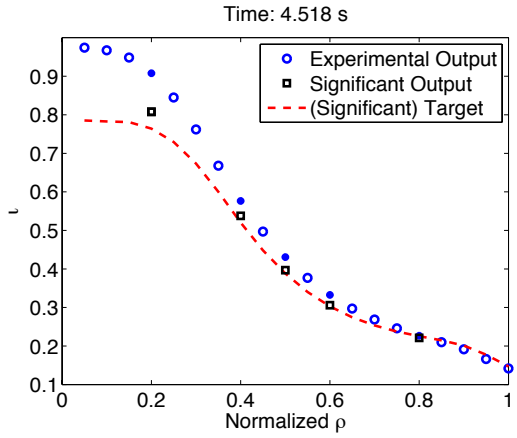

(c) Feedback ON, Disturbance ON

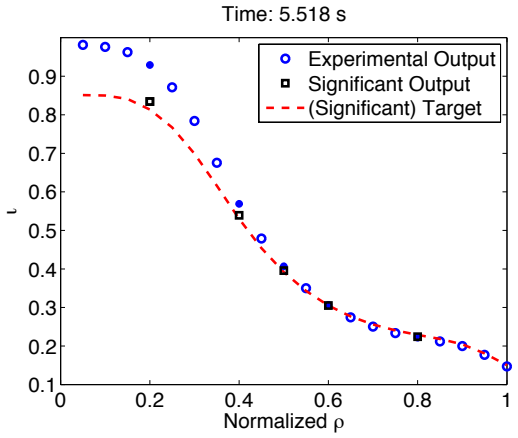

(d) Feedback ON, Disturbance ON

Figure 4.14: Plasma $\iota(\hat{\rho})$ profile at time t= 2.538, 3.518, 4.518, 5.518 s (shot # 147704). Target (red dashed line), significant ι (black squares) and experimental ι (blue circles) profiles.

solid lines and dashed-dotted black lines are not coincident in Figure 4.13, and blue circles and black squares are not coincident in Figure 4.14. It is however possible to note from these figures that the two dominant output singular vectors can indeed reproduce quite well the outer part of the profile, i.e., $\Delta y_s \approx \Delta y$ in the outer region. This is not the case in the in inner region, where there is a marked difference between Δy_s and Δy, and therefore a significant unremovable tracking error. This can be explained by examining the steady-state gains of the system in Figure 4.2, where the

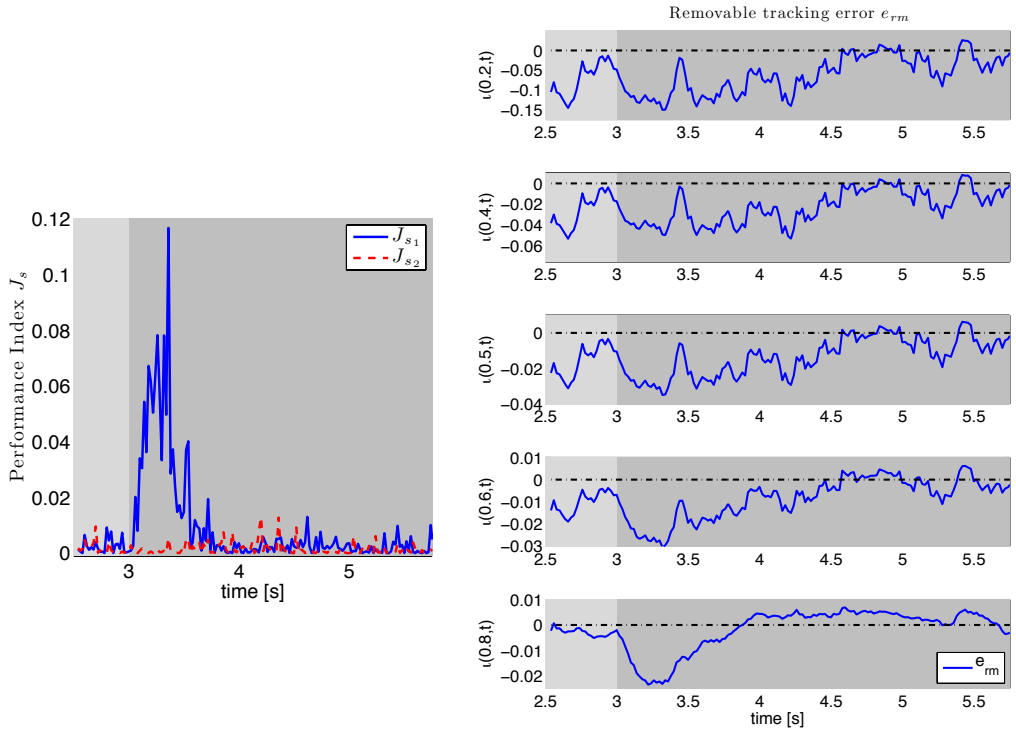

(a) (b)

Figure 4.15: Control performance metrics (shot #147704 - Disturbance II): (a) Cost function, (b) Removable tracking error for ι profile at $\hat{\rho} = 0.2, 0.4, 0.5, 0.6, 0.8$. Light-gray background: feedback on - disturbance off, dark-gray background: feedback on - disturbance on.

responses of the system to both P_{CO} and P_{BL}, the only beam groups available in this experiment, show a marked difference between $\Delta\bar{y}_s$ and $\Delta\bar{y}$ in the inner region and a good match in the outer region. Therefore, it is not only the unavailability of P_{EC} and P_{CT} but also the inability of P_{CO} and P_{BL} to make $\Delta y_s \approx \Delta y$ in the inner region the reasons for a poor tracking performance at $\hat{\rho} = 0.2, 0.4$ as shown in Figure 4.13 and Figure 4.14. However, what is important from the point of view of the controller performance is its ability to drive Δy_s close to zero, or $\Delta y_s + y_{FF}$ (dashed-dotted black lines) close to $y_{tar} = y_{FF}$ (red dashed lines), as shown in Figure 4.13 for all the points of the ι profile, including those in the inner region ($\hat{\rho} = 0.2$ and $\hat{\rho} = 0.4$).

This can also be appreciated from Figure 4.14, where the significant output profile $\Delta y_s + y_{FF}$ (black squares) is driven close to the target profile $y_{tar} = y_{FF}$ (red dashed lines). The time evolution of the significant components of the cost function J_s (4.33) in Figure 4.15 (a) shows the effectiveness of the controller in rejecting the disturbance within the subspace generated by the dominant singular vectors. Note that the effect of the disturbance is mainly captured by the most dominant output singular vector. This can be explained by noting that Disturbance II (see Table 4.4) heavily affect the most dominant input singular vector (see Figure 4.3 (b)). Figure 4.15 (b) shows that all the removable tracking error e_{rm} (4.35) components are driven close to zero.

4.3.3 Case 3: Rotational Transform ι Profile and β_N Control under Disturbance III

Due to the large difference in plasma resistivity between the center and the edge, the current density rapidly equilibrates at the edge, and evolves slowly in the center. This, combined with the actuation limitations discussed in Section 4.3.2, makes the control of the inner ι profile very challenging. Recognizing the lack of capability for controlling the inner part of the profile, and to prevent the controller from spending a large amount of control effort through the available actuators trying to reduce the tracking error in the inner region without any significant improvement in overall performance, the state weight matrix is chosen as $Q = \text{diag}([0.05,\ 0.1,\ 1,\ 1,\ 1,\ 1])$ (the weights of the tracking errors associated with $\iota(0.2, t)$ and $\iota(0.4, t)$ are reduced). The main control effort is therefore applied to $\iota(0.5, t)$, $\iota(0.6, t)$, $\iota(0.8, t)$, and $\beta_N(t)$. Moreover, in order to be able to evaluate the controller effectiveness in regulating the ι profile and $\beta_N(t)$ within the limited controllable region defined by the available actuators, only the two most important singular values ($k = 2$) are preserved in this

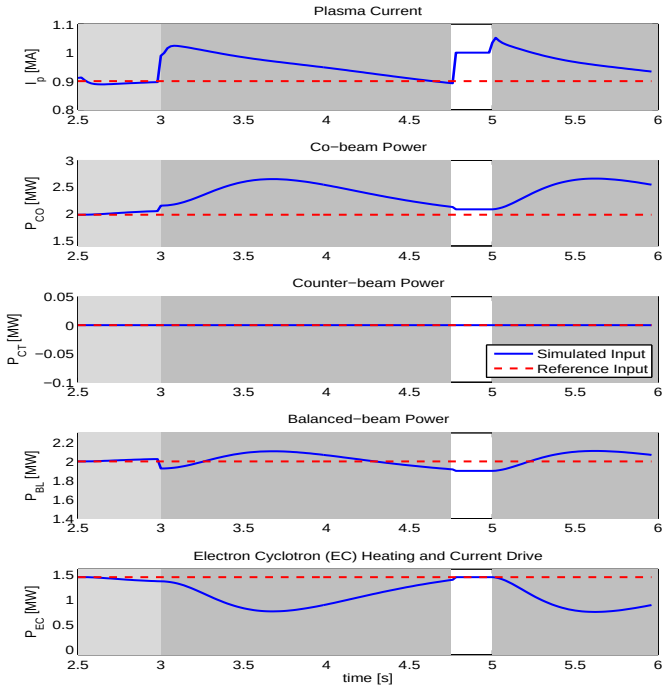

(a)

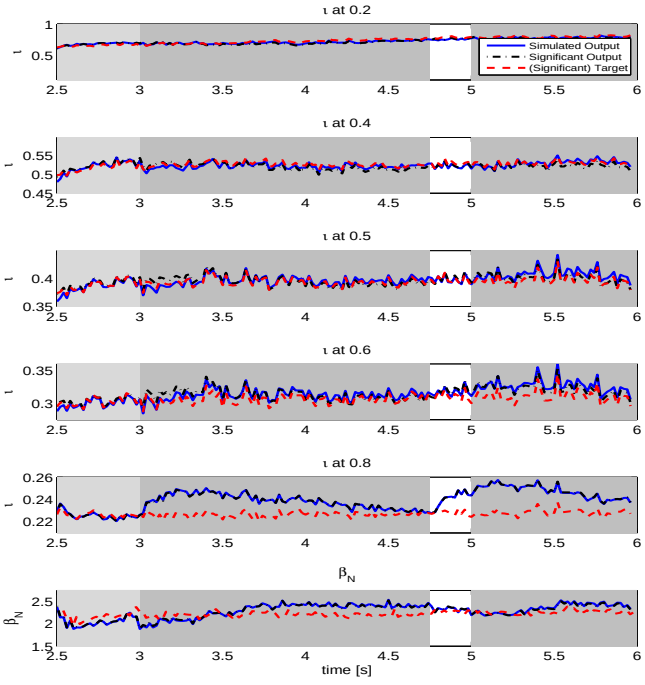

(b)

Figure 4.16: Closed-loop simulation (shot #147707): (a) Inputs, (b) Outputs. Disturbance III. Light-gray background: feedback on-disturbance off, dark-gray background: feedback on-disturbance on, white background: feedback off-disturbance on.

case study. Note that this decision, as in the previous case, is rather conservative because up to $k = 3$ singular values could have been preserved. The expectation is that the three available actuators will provide the capability of actuating in these two most dominant directions. The other control parameters are the same as in Section 4.3.2. The feedback controller is turned on and off throughout the discharge, i.e., OFF for 0 to 2.5 s, ON for 2.5 to 4.75 s, OFF for 4.75 to 5 s, and ON for 5 to 6 s.

Figure 4.16 shows simulation results. In the first 0.5 second of the simulation, from $t = 2.5$ s to $t = 3$ s, the controller regulates ι and β_N around the target values. When the disturbance is initially introduced into the system at $t = 3$ s, the outer ι profile moves away from the target value immediately. As shown in Figure 4.16 (a.1), the disturbance in the plasma current is rejected by the controller and the reference (feedforward) value is recovered after the transient. Beam and gyrotron powers, shown in Figure 4.16 (a.2)-(a.5), are modulated by the feedback controller away from their reference values without hitting saturation limits. Due to the increased level of beam power, β_N also moves away from its target value. The feedback controller finally rejects the effects of the input disturbance after around 1.75 s, and both the target ι profile and β_N evolutions are once again effectively tracked. Then the controller is turned off for 0.25 second from $t = 4.75$ s to $t = 5$ s, and the tracking errors become larger. In the final second of the simulation, from $t = 5$ s to $t = 6$ s, the controller is turned back on and it rejects nearly all the effects of the disturbance by repeating the control actions already observed during the first on-period from $t = 3$ s to $t = 4.75$ s. Based on the results from Figure 4.16, we can note that the outer ι profile is strongly affected by the plasma current and β_N is strongly affected by the beam and gyrotron powers. The controller tries to recover the target ι profile without producing large β_N excursions. Once the disturbance is rejected, the ι profile and β_N are driven to the target values.

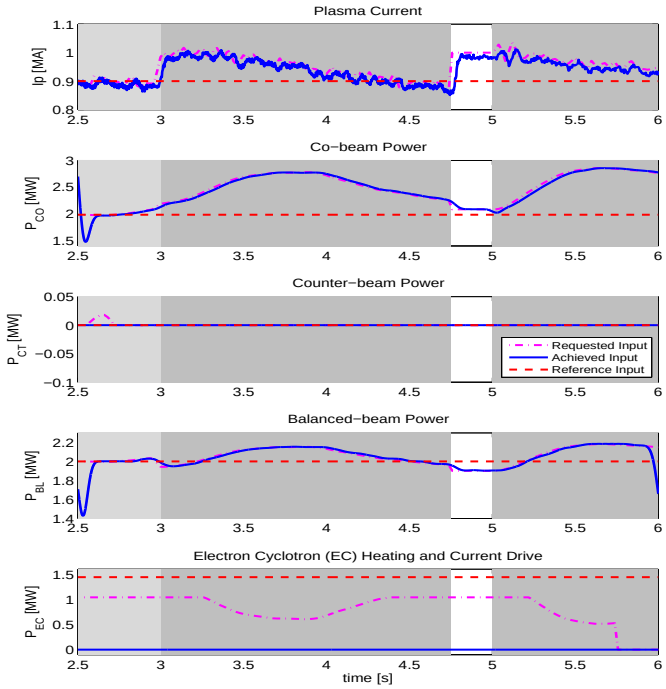

(a)

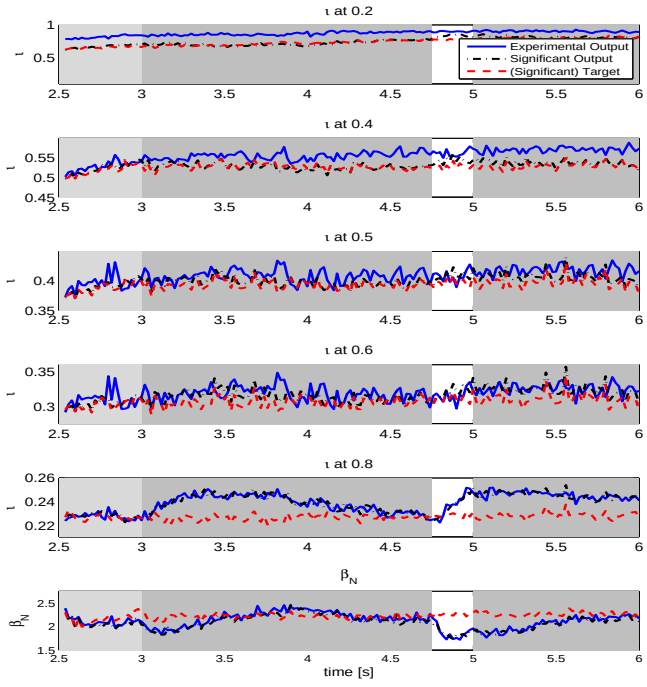

(b)

Figure 4.17: Experiment (shot #147707): (a) Inputs, (b) Outputs. Disturbance III. Light-gray background: feedback on - disturbance off, dark-gray background: feedback on - disturbance on, white background: feedback off - disturbance on.

Figure 4.17 shows the experimental results obtained from shot #147707. The plasma current (Figure 4.17 (a.1)) and the beams (Figure 4.17 (a.2)-(a.4)) successfully follow the requested values without exhibiting any saturation. The EC (Figure 4.17 (a.5)), used for plasma heating and current drive, is off during the experiment. The difference between achieved and requested values of P_{EC} (Figure 4.17 (a.5)) can be interpreted as an additional disturbance because, as explained before, the controller has not been redesigned to avoid using the EC H&CD system and still requests a P_{EC} value. It can be noted from Figure 4.18 (a) that it is indeed not possible to reproduce the target profile in the center of the plasma (ι at $\hat{\rho} = 0.2$) at the beginning of the closed-loop control experiment ($t = 2.5$ s), i.e., the conditions of the reference control shot #146417 at $t = 2.5$ s have not been successfully reproduced in this case. This is also reflected in the initial condition of the time trace for ι at $\hat{\rho} = 0.2$ in Figure 4.17 (b). It may be important to appreciate from Figure 4.7 that the initial profile is closer in this case to that achieved in the system identification shot #140090 at $t = 2.5$. From $t = 3$ s to $t = 4.75$ s, the controller rejects the input disturbance very effectively. Note from Figure 4.17 (b) how both the ι profile and β_N recover their target values after the transient produced by the injection of disturbances at $t = 3$ s. This is in part due to the fact that the achieved control inputs follow the requested values very well for the working actuators. When the controller is turned off at $t = 4.75$ s, the actuator values drift away from the feedforward values immediately and a tracking error becomes noticeable particularly for β_N and the outer ι profile. Finally, the feedback controller is turned on at $t = 5$ s and it drives back the ι profile and β_N to their target values, rejecting once again the effects of the input disturbance. When the experimental input and output signals in Figure 4.17 are compared with those in Figure 4.16, which are predicted by the identified model in closed-loop simulations, it is possible to observe a remarkable similarity. Since the input signals (Figure 4.16

(a) and Figure 4.17 (a)) are determined exclusively by the controller based on the measurements provided by the diagnostics, the observed similarity is another proof of the capability of the identified model to capture the plasma dynamics.

A series of six plasma profiles at different times of the shot #147707 are shown in Figure 4.18. Due to the design of the weight matrix Q, the control effort is mainly applied to $\iota(0.5,t)$, $\iota(0.6,t)$, $\iota(0.8,t)$ and β_N. The ι tracking errors in the center of the plasma are larger than the ι tracking errors at the edge of plasma. This is in part explained by the fact that, as shown in Figure 4.18 (a), the target profile is not reproduced at the initial time probably due to the loss of critical actuators (counter-injection NBI and EC powers). After the input disturbances are injected into the system, these tracking errors become larger, as shown in Figure 4.18 (b). As time goes on in shot #147707, the tracking errors become smaller as shown in Figure 4.18 (c), (d) thanks to the action of the feedback controller. When the feedback controller is turned off, the tracking errors increase once again as shown in Figure 4.18 (e) before recovering after the controller is turned back on as shown in Figure 4.18 (f).

Since $(k = 2) < (m = 5), (p = 6)$ in this case, not all the outputs live in the subspace generated by the significant singular vectors. Therefore, as in the previous case, $\Delta y_s \neq \Delta y$ and not all the tracking error is removable ($e = e_{rm} + e_{nrm}$). This explains the fact that blue solid lines and dashed-dotted black lines are not coincident in Figure 4.17, and blue circles and black squares are not coincident in Figure 4.18. Similarly to the previous case, the two dominant output singular vectors can indeed reproduce quite well the outer part of the profile, i.e., $\Delta y_s \approx \Delta y$ in the outer region. This is not the case in the in inner region, where there is a marked difference between Δy_s and Δy, and therefore a significant unremovable tracking error. What is important from the point of view of the controller performance is its ability to drive Δy_s close to zero, or $\Delta y_s + y_{FF}$ (dashed-dotted black lines) close to $y_{tar} = y_{FF}$ (red dashed

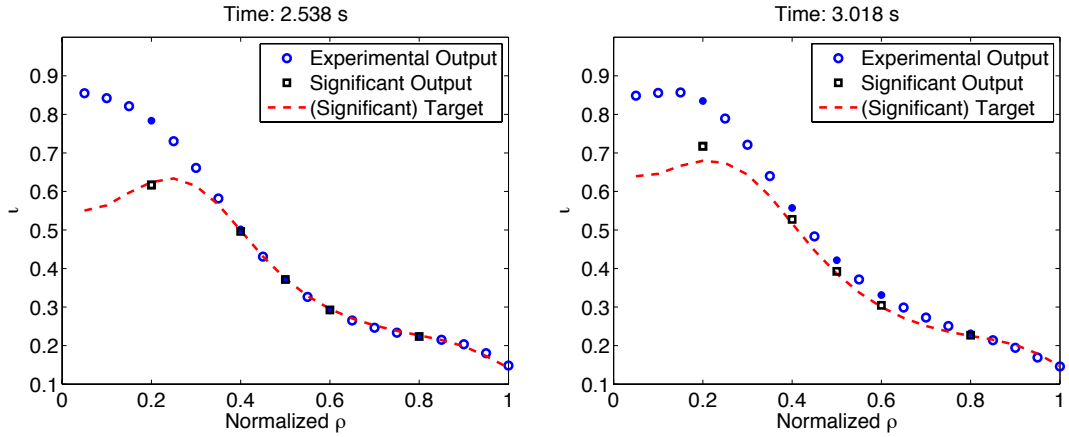

(a) Feedback ON, Disturbance OFF

(b) Feedback ON, Disturbance OFF

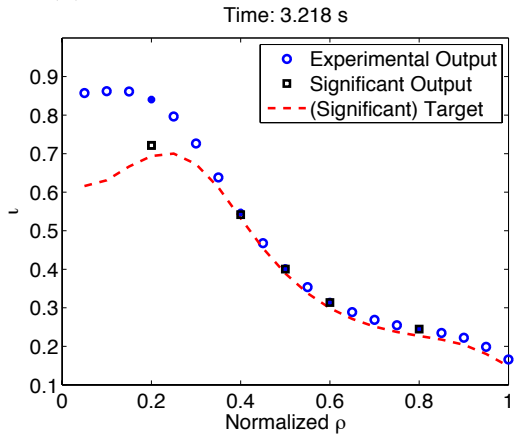

(c) Feedback ON, Disturbance ON

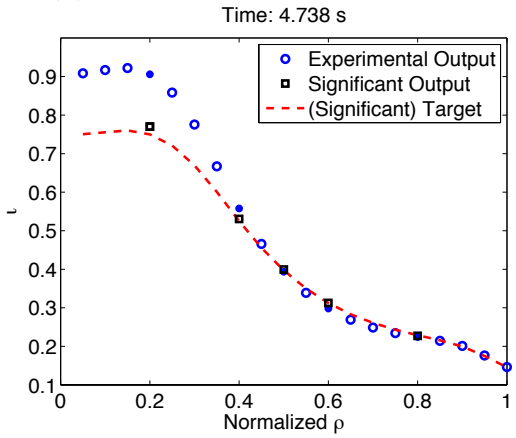

(d) Feedback ON, Disturbance ON

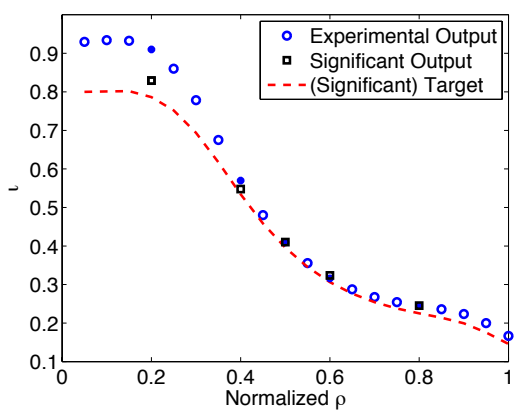

(e) Feedback ON, Disturbance ON

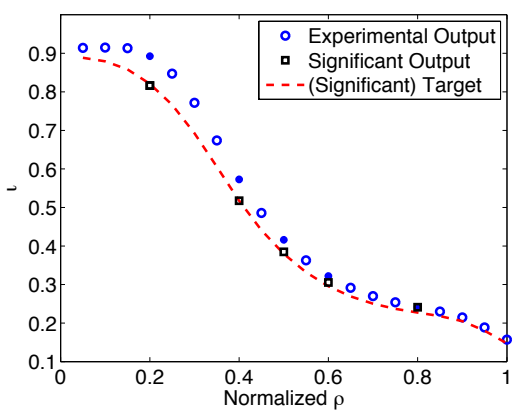

(f) Feedback ON, Disturbance ON

Figure 4.18: Plasma $\iota(\hat{\rho})$ profile at time t= 2.538, 3.018, 3.218, 4.738, 5.018, 5.998 s (shot # 147707). Target (red dashed line), significant ι (black squares) and experimental ι (blue circles) profiles.

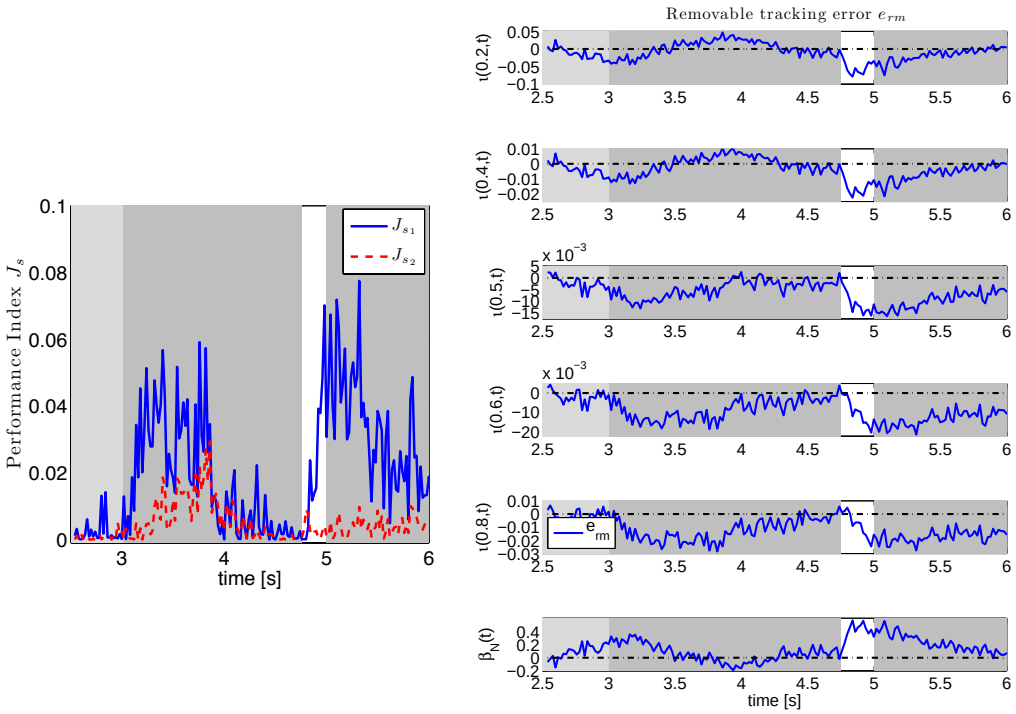

(a) (b)

Figure 4.19: Control performance metrics (shot #147707 - Disturbance III): (a) Cost function, (b) Removable tracking error for ι profile at $\hat{\rho} = 0.2, 0.4, 0.5, 0.6, 0.8$ and β_N. Light-gray background: feedback on - disturbance off, dark-gray background: feedback on - disturbance on, white background: feedback off - disturbance on.

lines), as shown in Figure 4.17 for all the points of the ι profile. This can also be appreciated from Figure 4.18, where the significant output profile $\Delta y_s + y_{FF}$ (black squares) is driven close to the target profile $y_{tar} = y_{FF}$ (red dashed lines). Note, as a difference from the previous case, that the removable component of the error is relatively small during all the discharge in the inner region ($\hat{\rho} = 0.2$ and $\hat{\rho} = 0.4$), i.e., $\Delta y_s + y_{FF} \approx y_{tar} = y_{FF}$ for $\hat{\rho} = 0.2$ and $\hat{\rho} = 0.4$. This may be related to the selection made for the components of the matrix Q associated with these outputs, which makes almost the entirety of the error unremovable freeing the controller from the responsibility of tightly regulating the ι profile at these points. The time evolu-

tion of the significant components of the cost function J_s (4.33) in Figure 4.19 (a) shows the effectiveness of the controller in rejecting the disturbance within the subspace generated by the dominant singular vectors. Note that in this case the effect of the disturbance is captured by the two most dominant output singular vectors since Disturbance III (see Table 4.4) projects not only on the first but also on the second most dominant input singular vector (see Figure 4.3 (b)). Figure 4.19 (b) shows that all the removable tracking error e_{rm} (4.35) components are driven close to zero.

4.4 Conclusion

A robust, model-based, MIMO, ι-profile and β_N controller has been designed for the flat-top phase of DIII-D H-mode discharges. The design is based on a two-timescale linear, dynamic, plasma-response model, which has been identified around a reference profile during the current flat-top phase. The feedback controller is designed based on this model to regulate the system around a target, which is assumed to be close to the reference profile around which the model has been identified, even in the presence of various disturbances. Singular value decomposition of the steady state transfer function is used to decouple the system and identify the most relevant control channels. The mixed sensitivity H_∞ technique is used to minimize the tracking error and to optimize control effort ignoring the saturation. Then the closed-loop system is augmented with an anti-windup compensator in order to minimize the effects of any control input constraint. The proposed controller represents one of the first profile controllers integrating magnetic and kinetic variables ever implemented and experimentally tested in DIII-D.

The preliminary experimental results presented in this work, although limited in number and constrained by actuators problems, show good progress towards routine

current profile control in DIII-D and leaves valuable lessons for control redesign. The controller has been proven effective at reducing the removable component of the tracking error, which has been defined as the part of the tracking error that can be driven to zero based on the control authority given by the number of significant singular values retained during the selection of the most relevant control channels. The number of significant singular values should be no greater than the number of available actuators. Demonstration of full profile control is still pending and will require the availability of all the actuators and the use of all the control channels.

Some rather sluggish and weak actuation observed in the closed-loop experiment may not be related to the inability of the controller to actuate in some directions because of limited actuation or neglected control channels but to the limited bandwidth of the closed-loop system. More aggressive controllers could be designed in this case by increasing the frequency content of the excitation (input) signals during the system identification experiment, by increasing the cutoff frequency, or even better, by eliminating the need to choose a cutoff frequency associated with the slow dynamics of the system during the identification of the data-driven model, by increasing the weight Q and decreasing the weight R (tighter control at the expense of more control effort) during the design of the static component of the controller, and by selecting weights W_p and W_u leading to an increase of the closed-loop response bandwidth during the design of the dynamic component of the controller. The anti-windup compensator would be an indispensable companion of these more aggressive controllers. In addition, it would be critical to simultaneously control β_N while controlling the ι profile to prevent the controller from triggering MHD instabilities in its aggressive effort to achieve the desired target profile. The risk of triggering MHD instabilities in our search for a faster response is however not reserved to an aggressive feedback control action. As we introduce more vigorous excitations in order to increase

the bandwidth of the data-driven response model, we also increase the likelihood of triggering MHD instabilities during the open-loop system identification experiment, which clearly represents another challenge associated with the design of data-driven controllers.

More experimental tests are needed to assess the appropriateness of using data-driven linear models for current profile control. Being able to control the current profile during the ramp-up and ramp-down phases, being able to regulate the current profile for different scenarios (around different reference states), or being able to drive the current profile from one target profile to another will most likely require adaptive or nonlinear control approaches based on richer dynamic models obtained by a first-principles-driven modeling approach. However, the preliminary control experiments carried out at DIII-D suggest that regulation of the current profile around a reference state during the flat-top phase of the discharge, as is the objective of this work, may be possible using a data-driven linear modeling and control approach if enough actuation is available. However, a serious study on the performance of the regulator as the target state moves away from the reference state around which the linear model has been identified is still pending. In relation to the control approach proposed in this work, the sensitivity of the static component of the controller, which decides the most relevant control channels by a SVD approach, to un-modeled or mis-modeled plasma response and its impact on performance need further analysis.

Chapter 5

PTRANSP Simulation and Experimental Test of a Robust Current Profile and Normalized Beta Controller for Off-axis Current Drive Scenarios in DIII-D

5.1 Introduction

In this chapter, we extend the work presented in Chapter 4 in many important areas. Firstly, the off-axis current drive is introduced to the experiments, which could provide more heating in the mid-radius of the tokamak that would not be possible with only on-axis current drive. This capability should greatly increase the parameter space available for AT scenario development [61]. Secondly, the start time of the control phase is moved backward from the current flat-top phase to the current ramp-up

phase. The plasma equilibrium continually evolves during the ramp-up phase, but the identified model describes the linearized response around a particular equilibrium in the flat-top phase. In order to increase the validity range of the identified model, we increase/decrease the singular values of the identified model to form a series of models to cover a neighborhood of the desired equilibria. DK-iteration, combining H_∞ synthesis and μ analysis, is applied to synthesize a closed-loop controller that minimizes the control error and optimizes input effort. Then, the robust controller is successfully tested in the PTRANSP code [68], a tokamak transport analysis code, before experiments to evaluate the influence of the off-axis current drive system in DIII-D. Finally, a profile control experiment integrating magnetic and kinetic variables on DIII-D illustrates the performance of the proposed controller.

This chapter is organized as follows. In Section 5.2, the designs of the plasma control algorithm and the anti-windup compensator are described. Closed-loop PTRANSP simulated results with off-axis current drive (CD) are presented in Section 5.3, and experimental results from the DIII-D tokamak are presented in Section 5.4. Section 5.5 states the conclusions.

5.2 Control System Design

5.2.1 Singular Value Decomposition

The relation between the inputs and the outputs in the linear dynamic off-axis model (3.10) can be expressed in terms of its transfer function $P(s)$, i.e., $\frac{\Delta Y(s)}{\Delta U(s)} = P(s) = C_{OA}(sI - A_{OA})^{-1}B_{OA}$, where s denotes the Laplace variable and $\Delta Y(s)$ and $\Delta U(s)$ denote the Laplace transforms of the output Δy and the input Δu respectively. Assuming a constant target $\Delta\bar{y}_{tar}$ and closed-loop stabilization, the system will reach steady state as $t \to \infty$. It is possible to define $\Delta\bar{y} = \lim_{t\to\infty} \Delta y(t)$, $\Delta\bar{u} = \lim_{t\to\infty} \Delta u(t)$, and

$\bar{e} = \lim_{t\to\infty} e(t) = \Delta\bar{y}_{tar} - \Delta\bar{y}$. Therefore, under these assumptions the closed-loop system is specified by

$$\Delta\bar{y} = \bar{P}\Delta\bar{u} = -C_{OA}A_{OA}^{-1}B_{OA}\Delta\bar{u}, \quad \Delta\bar{u} = \bar{\hat{K}}\bar{e}, \tag{5.1}$$

where $\hat{K}(s)$ represents the transfer function of the to-be-designed controller and $\bar{\hat{K}} = \hat{K}(0)$.

In order to weight the control effort and tracking error, two positive definite weighting matrices $R \in \Re^{m\times m}$ and $Q \in \Re^{p\times p}$ are introduced to the system, where $p = 6$ is the number of outputs and $m = 5$ is the number of inputs. We then define the "weighted" steady-state transfer function, and its singular value decomposition (SVD) as $\tilde{P} = Q^{1/2}\bar{P}R^{-1/2} = USV^T$, where $S = \text{diag}(\sigma_1, \sigma_2, \cdots, \sigma_m) \in \Re^{m\times m}$, $U \in \Re^{p\times m}$ ($U^TU = I$), and $V \in \Re^{m\times m}$ ($V^TV = VV^T = I$). By invoking the properties of the SVD, the matrix $Q^{-1/2}US$ defines a basis of the steady-state output values, and the matrix $R^{-1/2}V$ defines a basis of the steady-state input values. By defining $\Delta\bar{y}^* = S^{-1}U^TQ^{1/2}\Delta\bar{y}$, $\Delta\bar{y}^*_{tar} = S^{-1}U^TQ^{1/2}\Delta\bar{y}_{tar}$, and $\Delta\bar{u}^* = V^TR^{1/2}\Delta\bar{u}$, a square decoupled system is obtained:

$$\Delta\bar{y}^* = S^{-1}U^TQ^{1/2}\Delta\bar{y} = S^{-1}U^TQ^{1/2}Q^{-1/2}USV^TR^{1/2}\Delta\bar{u} = \Delta\bar{u}^*.$$

Substituting these expressions into the performance index $\bar{J} = \bar{e}Q\bar{e}^T$, we can obtain the steady state cost function:

$$\bar{J} = (\Delta\bar{y}^*_{tar} - \Delta\bar{y}^*)^TS^2(\Delta\bar{y}^*_{tar} - \Delta\bar{y}^*) = \sum_{i=1}^{m}\sigma_i^2(\Delta\bar{y}^*_{tar_i} - \Delta\bar{y}^*_i)^2.$$

It is usually the case where $\sigma_1 > \cdots \sigma_k \gg \sigma_{k+1} > \cdots > \sigma_m > 0$. To avoid spending a lot of control effort for a marginal improvement of the cost function value, we

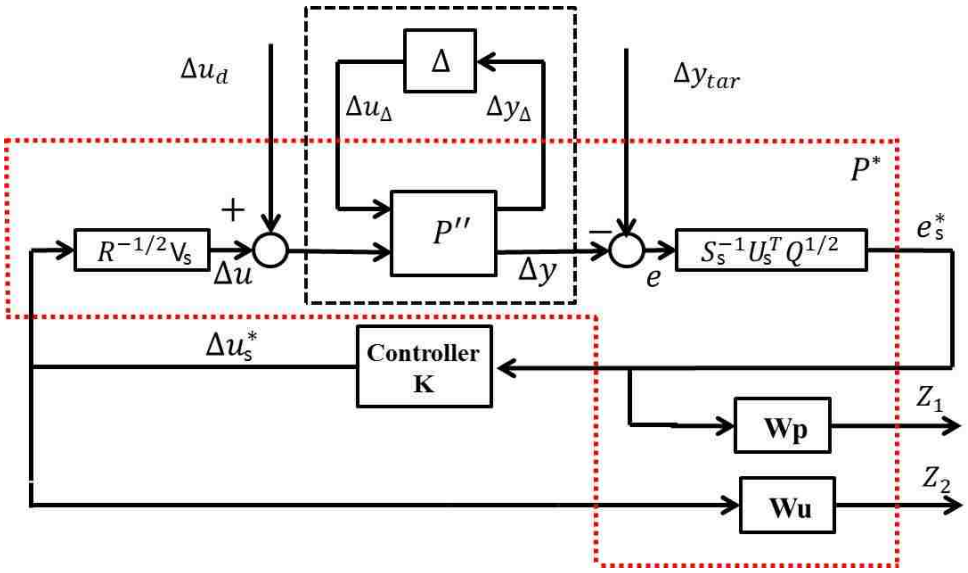

Figure 5.1: Mixed-sensitivity H_∞ control problem.

partition the singular value set into significant singular values S_s and negligible singular values S_n. We can write $U = \begin{bmatrix} U_s & U_n \end{bmatrix}$, $V = \begin{bmatrix} V_s & V_n \end{bmatrix}$, $S = \text{diag}(S_s, \ S_n)$, and approximate the cost function $\bar{J}$ by

$$\bar{J}_s = \sum_{i=1}^{k} \sigma_i^2 (\Delta\bar{y}^*_{tar_i} - \Delta\bar{y}^*_i)^2 = (\Delta\bar{y}^*_{tar_s} - \Delta\bar{y}^*_s)^T S_s^2 (\Delta\bar{y}^*_{tar_s} - \Delta\bar{y}^*_s),$$

where $\Delta\bar{y}^*_{tar_s} = S_s^{-1}U_s^TQ^{1/2}\Delta\bar{y}_{tar}$, $\Delta\bar{y}^*_s = S_s^{-1}U_s^TQ^{1/2}\Delta\bar{y}$, $\bar{e}^*_s = \Delta\bar{y}^*_{tar_s} - \Delta\bar{y}^*_s$ and $\Delta\bar{u}^*_s = V_s^TR^{1/2}\Delta\bar{u}$. The matrix bases reduce to $Q^{-1/2}U_sS_s$ and $R^{-1/2}V_s$, and the decoupled system,

$$P_{DC} = S_s^{-1}U_s^TQ^{1/2}PR^{-1/2}V_s, \tag{5.2}$$

represents a one-to-one relationship between the inputs $\Delta\bar{u}^*_s$ and the outputs $\Delta\bar{y}^*_s$. More details of SVD can be obtained from the Section 4.2.2.

5.2.2 Design of μ Synthesis Controller

It is important to recall that the model P (3.10) was identified using only data after 2.5s during the current flat-top phase. The start time of the control phase in the experiment was moved backward from 2.5 s to 1 s, i.e., during the current ramp-up phase. The plasma state continually changes during the plasma current ramp-up phase, and as a result, the plasma response model (3.10) should change. In order to partially account for this, we define the decoupled identified model P_{DC} (5.2) as the nominal model, and assume the singular values of the system P_{DC} can increase/decrease to form a broad frequency range covering a neighborhood of plasma states, which define a range of uncertainty ΔP. The new plasma model can be considered as the sum of P_{DC} with uncertainty ΔP, which is formulated into a robust control framework. There is always a trade-off between the performance of the controller and the robustness properties of the closed-loop system. The maximum increasing/decreasing magnitude of the singular values represents the desired robustness level of the closed-loop system. In this work, the singular values S_s are assumed to increase and decrease 20% to attempt to capture the dynamic character of the plasma state equilibrium evolution during the current ramp-up phase.

The decoupled system P_{DC} (5.2) based on P (3.10) is chosen as the nominal model, which is denoted as P_0. The singular values S_s decrease 20% to obtain a new system $P_{DC_t} = (0.8S_s^{-1})U_s^T Q^{1/2} P R^{-1/2} V_s$, which is denoted as P_{top}, and has the highest magnitude over the frequency range considered. The singular values S_s increase 20% to obtain another new system $P_{DC_b} = (1.2S_s^{-1})U_s^T Q^{1/2} P R^{-1/2} V_s$, which is denoted as P_{bot}, and has the lowest magnitude. The top and bottom uncertainty can be expressed in state-space form as:

$$\Delta A_i = A_i - A_0 \qquad \Delta B_i = B_i - B_0$$
$$\Delta C_i = C_i - C_0 \qquad \Delta D_i = D_i - D_0$$

where the subscript $i \in 1, 2$ refers to the top and bottom respectively. The state-space system matrices are now written as uncertain matrices as

$$\begin{aligned} A &= A_0 + \sum_{i=1}^{2} \delta_i \Delta A_i \quad B = B_0 + \sum_{i=1}^{2} \delta_i \Delta B_i \\ C &= C_0 + \sum_{i=1}^{2} \delta_i \Delta C_i \quad D = D_0 + \sum_{i=1}^{2} \delta_i \Delta D_i \end{aligned} \tag{5.3}$$

where $\delta_1 \in [0, 1]$ and $\delta_2 \in [0, 1]$. By conducting a frequency analysis of the uncertain model of the system (5.3), the uncertain model is shown to capture the behavior of the family of decoupled plasma models.

By exploiting the structure of the state matrices (5.3) and using singular value decomposition, the system can be expressed in the conventional $P'' - \Delta$ control framework (black dashed block in Figure 5.1), by employing the method outlined in [59]. See Section 2.4 for an example of this technique. Using the partition of the generalized plant $P'' = \begin{bmatrix} P''_{11} & P''_{12} \\ P''_{21} & P''_{22} \end{bmatrix}$, the input/output equations are

$$\Delta y_\Delta = P''_{11} \Delta u_\Delta + P''_{12} (\Delta u^*_s + \Delta u^*_{d_s}),$$
$$\Delta y = P''_{21} \Delta u_\Delta + P''_{22} (\Delta u^*_s + \Delta u^*_{d_s}),$$

where $\Delta u^*_s = V_s^T R^{1/2} \Delta u$, $\Delta u^*_{d_s} = V_s^T R^{1/2} \Delta u_d$, and Δu_d is the input disturbance.

The control goal is to design a $k \times k$ feedback controller K, where k is the number of significant singular values. The corresponding block diagram of the system is shown

in Figure 5.1 where the weight functions $W_p(s)$ and $W_u(s)$ are parameterized as

$$W_p(s) = K_p \left(\frac{\frac{s}{M_1} + w_{b1}}{s + w_{b1}A_1} \right)^2, \quad W_u(s) = K_u \left(\frac{s + w_{b2}A_2}{\frac{s}{M_2} + w_{b2}} \right)^2$$

and the coefficients $M_i,\ A_i,\ w_{bi}$, for $i \in 1, 2$, as well as K_p and K_u, are design parameters.

The feedback system can now be expressed in the conventional $\Delta - P^* - K$ robust control framework, shown in Figure 5.2, where Δ is the uncertainty, P^* is the generalized plant (red dotted block in Figure 5.1) , K is the feedback controller, and $[Z_1^T,\ Z_2^T]^T = [(W_p e_s^*)^T,\ (W_u \Delta u_s^*)^T]^T$ is the weighted performance signal. The closed-loop transfer function from the input $[\Delta y_{tar_s}^{*T},\ \Delta u_{d_s}^{*T}]^T$ to the output $\begin{bmatrix} Z_1^T & Z_2^T \end{bmatrix}^T$ is defined as

$$T_{zr} = F_u(N, \Delta), \tag{5.4}$$

where $\Delta y_{tar_s}^* = S_s^{-1} U_s^T Q^{1/2} \Delta y_{tar}$, $\Delta y_s^* = S_s^{-1} U_s^T Q^{1/2} \Delta y$, $e_s^* = \Delta y_{tar_s}^* - \Delta y_s^*$, and the subsystem

$$N = F_l(P^*, K) = \begin{bmatrix} W_p M_s & -W_p M_s P_{22}'' \\ W_u K M_s & -W_u K M_s \end{bmatrix}. \tag{5.5}$$

The sensitivity transfer function M_s is defined as $M_s = (I + P_{22}'' K)^{-1}$. We seek a controller $K(s)$ that robustly stabilizes the system and minimizes the H_∞ norm of the transfer function $T_{zr}(N, \Delta)$, i.e.,

$$\min_{K(s)} \|T_{zr}(N, \Delta)\|_\infty = \min_{K(s)} (\sup_\omega \bar{\sigma}[T_{zr}(N, \Delta)(j\omega)]), \tag{5.6}$$

where $\bar{\sigma}$ represents the maximum singular value. The control method employed in this work to achieve the control goal (5.6) is the μ synthesis design technique.

There is no direct method to synthesize a μ-optimal controller, however the DK-

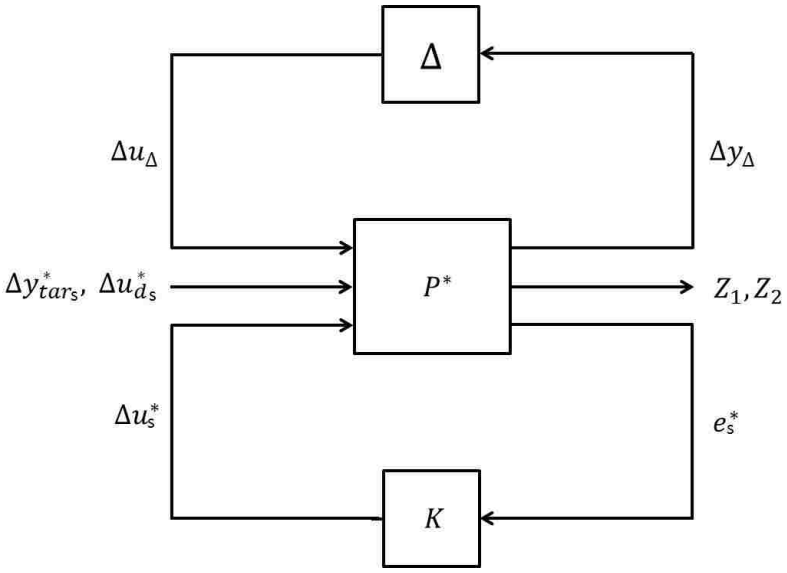

Figure 5.2: Model in $\Delta - P^* - K$ Robust Control Framework

iteration method [59], which combines H_∞ synthesis and μ analysis, can be used to obtain an iterative solution. This method starts with an upper bound on μ in terms of the scaled singular value $\mu(N) \leq \min(\bar{\sigma}(DND^{-1})$. Then, we seek a controller that minimizes the peak value over frequency of this upper bound

$$\min_K(\min \left\| DN(K)D^{-1} \right\|_\infty).$$

To validate the designed controller, the robust stability of the closed-loop system is determined. The system is written in the $N - \Delta$ structure, and the robust stability is determined by evaluating the structured singular value

$$\mu(N_{11}(j\omega)) = \frac{1}{\min\{k_m | \det(I - k_m N_{11}\Delta) = 0\}} \tag{5.7}$$

where N_{11} is the transfer function from the input Δu_Δ to the output Δy_Δ. The closed-loop system is robustly stable for all allowable perturbations if and only if $\mu(N_{11}(j\omega)) < 1, \forall\omega$. Figure 5.3 shows a plot of the structured singular value μ versus

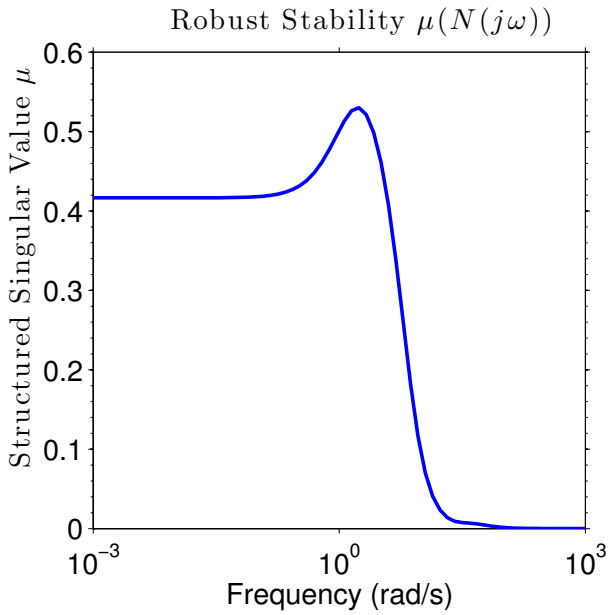

Figure 5.3: Structured Singular Value μ versus Frequency

frequency, and as can be seen $\mu < 1$ for all frequencies. Therefore, the closed-loop system is robustly stable. In other words, the controller stabilizes the whole family of models.

In practice, the control input and measured output of the original system P are Δu and Δy, respectively. The measured output is in turn used to compute the tracking error $e = \Delta y_{tar} - \Delta y$. As shown in Figure 5.1, the overall ι-profile and β_N controller for system P can be computed as

$$\hat{K}(s) = \frac{\Delta U(s)}{E(s)} = R^{-1/2} V_s K(s) S_s^{-1} U_s^T Q^{1/2} \tag{5.8}$$

where $\Delta U(s)$ and $E(s)$ denotes the Laplace transforms of Δu and e, respectively, and where the relationships $e_s^* = S_s^{-1} U_s^T Q^{1/2} e$, $\Delta u = R^{-1/2} V_s \Delta u_s^*$ have been used.

5.2.3 Design of the Anti-windup Compensator

The DIII-D tokamak is a nonlinear complex system, which is subject to actuator saturations as shown in Table 4.2. At the moment of designing the robust MIMO controller (5.8), the actuator saturations were not considered. As a result of saturation, the actual plant input may be different from the output of the controller. In this case the controller output does not drive the plant input and, as a consequence, the states of the controller may wind up because the plant does not respond as expected, which can cause the behavior of the system to deteriorate dramatically or even become unstable. The goal is not to redesign the proposed MIMO controller but to design an anti-windup compensator that keeps the controller well-behaved and avoid undesirable oscillations when saturation is present. The anti-windup compensator must in addition leave the nominal closed-loop unmodified when no saturation is present. Details of the anti-windup compensation can be obtained from the Section 4.2.5.

5.3 Closed-loop PTRANSP Simulations

PTRANSP is a time dependent tokamak transport analysis code developed at the Princeton Plasma Physics Laboratory (PPPL) [68]. The code provides a means to invert data from tokamak experiments, to provide a picture of the processes which account for the confinement and heating in tokamak plasmas. The code incorporates a wealth of physics modeling for neutral beam heating, neutral transport, diagnostic simulations, etc. Some quantities, for instance the current density profile and neutral density profile, can be predicted by models to supplement the measured data in the simulation. The advantage is that the interpretation of the data is more direct and comparison with theoretical models is straightforward.

PTRANSP reads diagnostic data from tokamak experiments, and after extensive

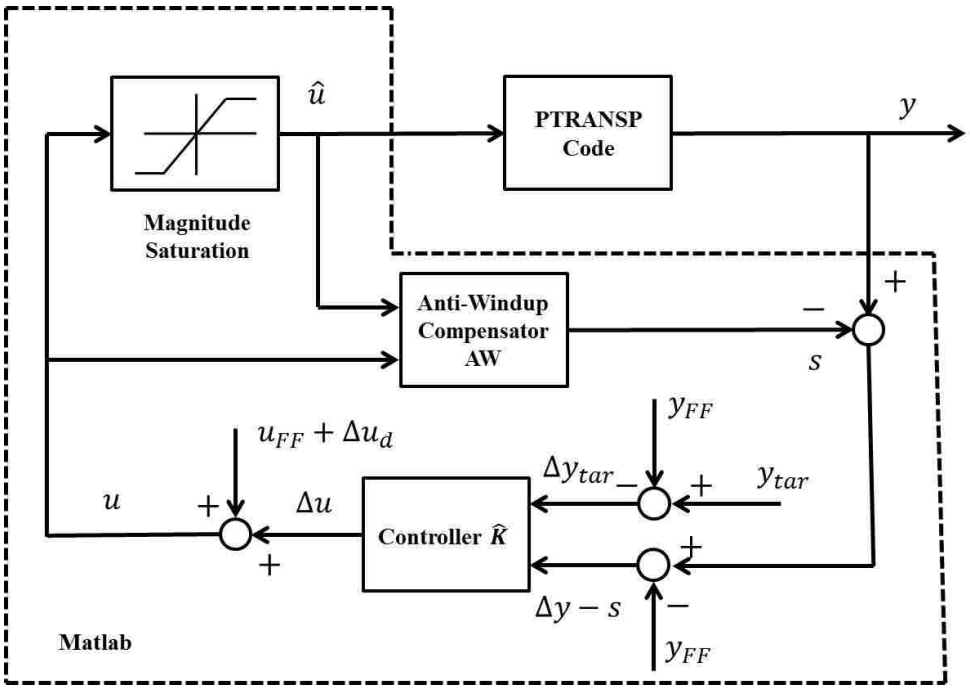

Figure 5.4: The architecture of the closed-loop PTRANSP simulation.

computational modeling, creates over 150 scalar functions and 300 profile functions of time describing the plasma. These functions represent parameters, measured or calculated, which together describe the evolution of an experimental tokamak system. The inputs to the code include the plasma current I_p, the surface voltage V_{sur}, the NBI and EC powers, and the spectroscopic measurements of hydrogen and impurity confinement times τ_p in addition to profile measurements of electron density n_e, electron temperature T_e, and ion temperature T_i. On the basis of the experimental measurements, PTRANSP solves the magnetic field diffusion equation for the poloidal magnetic field B_θ in order to evaluate the current density profile j. From these quantities the ohmic input power P_{OH}, the electron energy confinement time τ_{Ee}, and the safety factor q are calculated [68]. The ι profile, which is our control variable, is defined as the inverse of the safety factor q profile. The parameter β_N is a measured input in PTRANSP, so we cannot control it.

In PTRANSP, experimental data is used directly to calculate the plasma state evolution without feedback. In order to form the closed-loop simulation, we combined the PTRANSP code with Matlab. A general framework for closed-loop feedback control implemented in PTRANSP is shown in Figure 5.4. The PTRANSP solver is set to evolve in time only the ι profile based on the updated I_p, beam powers (P_{CO}, P_{OA}, and P_{CT}), and EC power P_{EC} output by the feedback controller. The feedback portion of the controller was implemented as a discrete time state-space controller with a sampling time of 20 milliseconds, because the controller implemented in DIII-D PCS has a sampling time of 20 milliseconds. The PTRANSP calculation stops every 20 milliseconds, and sends the calculated output y to Matlab. Based on the tracking error, Matlab calculates the next step input $\hat{u}$, and sends it back to PTRANSP. Then the PTRANSP code calculates the plasma state evolution for the next 20 milliseconds. This configuration provides us the ability to test the feedback controller in reference tracking and disturbance rejection simulations before experiments.

In our case, the closed-loop simulation is based on the robust controller (5.8), and the anti-windup compensator is added to minimize the effects of any control input saturation. The reference shot for PTRANSP is shot #147626, which is a shot with off-axis neutral beam injection, and the feedforward inputs and target ι profiles are shown in Figure 5.5 (red dashed line). The feedback controller is turned on at $t = 2.5$ s, and the disturbance is introduced at $t = 3$ s, which are $\delta I_p = 0.1$ MA, $\delta P_{CO} = -0.1$ MW, $\delta P_{OA} = 0$ MW, $\delta P_{CT} = 0$ MW, and $\delta P_{EC} = -0.3$ MW. A good control performance on the boundary of ι profile and β_N was observed in the Section 4.3. An important goal of the model-based current profile controller is to regulate ι profile in the center precisely, since this affects confinement and stability for advanced scenarios. In order to reach this goal, we take $Q = \text{diag}([5,\ 2.5,\ 1.5,\ 1.5,\ 1.5,\ 0.5])$ to increase the weights of the tracking errors associated with $\iota(0.2, t)$ and $\iota(0.4, t)$, and the control

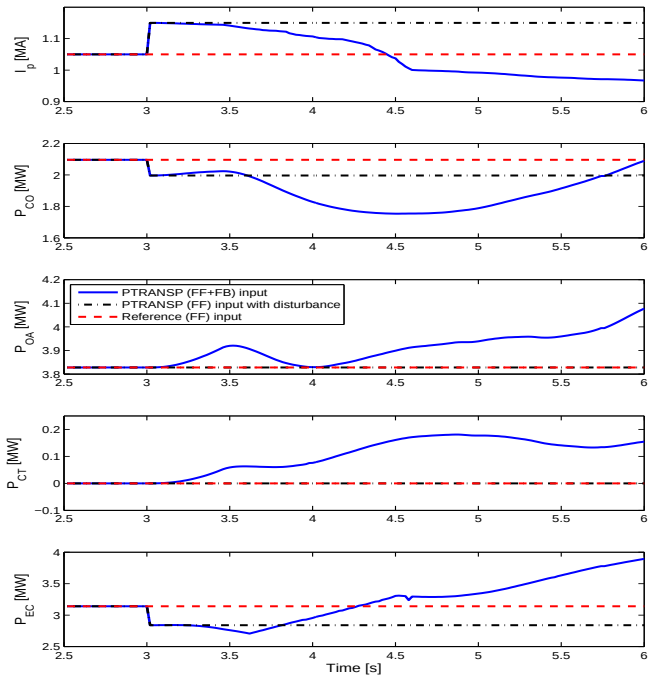

(a)

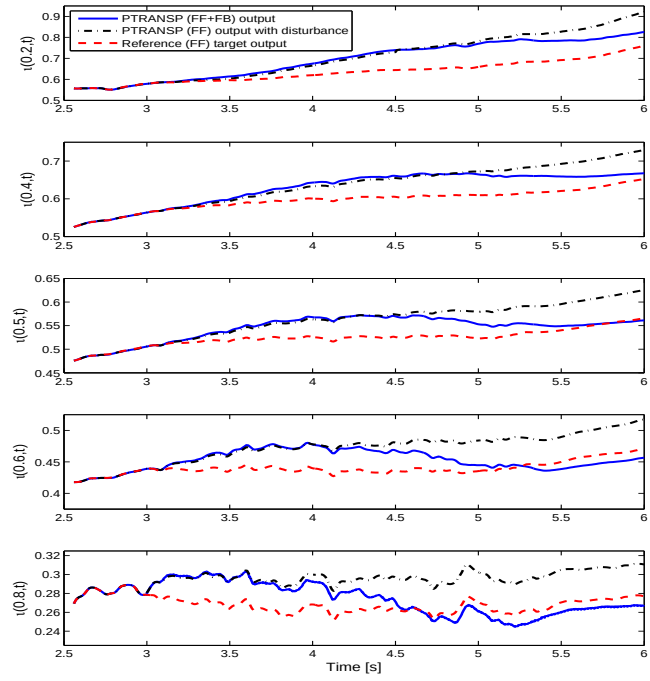

(b)

Figure 5.5: PTRANSP simulation with off-axis NBI: (a) Feedforward (FF) inputs, FF inputs with disturbance and feedforward+feedback (FF+FB) control inputs; (b) Reference target ι profile, FF with disturbance ι profile and FF+FB ι profile.

weight matrix is redefined as $R = \text{diag}([0.5,\ 0.1,\ 0.1,\ 0.1,\ 0.05])$. The parameter c for the anti-windup compensator is set as 0.1.

The simulated closed-loop-controlled inputs (solid blue lines) are shown in Figure 5.5 (a) and compared with the reference open-loop inputs (red dashed lines) and another feedforward open-loop inputs with disturbance (dot-dash line). The simulated closed-loop-controlled ι profile at $\hat{\rho} = 0.2, 0.4, 0.5, 0.6, 0.8$ (solid blue lines) are shown in Figure 5.5 (b) and compared with the target values (red dashed lines) and the feedforward open-loop outputs with disturbance (dot-dash line). By examining Figure 5.5 (b) , we see that with feedforward control only the target profile is not achieved in the presence of the disturbance. In the first 0.5 second of the closed-loop simulation, from $t = 2.5$ s to $t = 3$ s, the controller works well, and the ι profile is regulated around the target values. Then the disturbance is introduced into the system at $t = 3$ s, and the plasma current, beam and gyrotron powers are modulated around their reference values without saturation by the feedback controller. Due to the design of the weight matrix Q, the control effort is mainly applied to $\iota(0.2, t)$ and $\iota(0.4, t)$, and the controller increases P_{OA} and the total EC power P_{EC} and requests the I_p to decrease to drive the system towards the desired inner ι profile. Note that the inner ι profile response is much slower than the boundary ι profile response, and the effect of the control effort on the inner ι profile is shown with a time delay. This is due to the high temperature and slow diffusivity in the core relative to the boundary. Improved performance can be observed from the comparison between the controlled results (solid blue line) and uncontrolled results (dotted-dashed line).

5.4 Experimental Results on DIII-D

The chosen reference plasma state was that of a 1.65 T, β_N-controlled AT scenario, at a central plasma density, $n_{eo} \approx 3.5 \times 10^{19} m^{-3}$ and plasma current, $I_p = 1.05$ MA. In order to compare relevant experimental results with PTRANSP simulation, the same controller was applied and the same input disturbances were introduced in the experiment. The target ι profile and β_N obtained from shot #147634 with these discharge parameters are shown in Figure 5.6 (red dashed line). The disturbance was introduced at $t = 4.5$ s, and the feedback controller was turned on and off throughout the discharge according to

$$\Delta u = \begin{cases} \text{0 to 1 second} & \text{OFF} \\ \text{1 to 5.8 second} & \text{ON} \\ \text{5.8 to 6.3 second} & \text{OFF} \end{cases} . \tag{5.9}$$

The inputs prescribed by the feedforward+feedback controller represent the reference values to the dedicated physical control loops on the DIII-D tokamak. Figure 5.6 (a) shows the reference (red dashed lines), requested feedforward+feedback inputs (solid blue lines) and achieved inputs (dotted-dashed lines) during the experiment (shot #150749). As shown in Figure 5.6 (a.1)-(a.4), the plasma current and the beam powers successfully follow the requested values. During the shot, the total EC power is limited to around 2 MW, but the requested value goes up to 6 MW (Figure 5.6 (a.5)). The difference between achieved and requested values of EC power can be interpreted as a large disturbance that the controller must try to overcome. After $t \approx 2.5$ s, the P_{CO} reaches saturation, which activates the anti-windup compensator in an attempt to keep the states of the feedback controller from winding up. The experimental closed-loop-controlled ι profile at $\hat{\rho} = 0.2, 0.4, 0.5, 0.6, 0.8$ and β_N

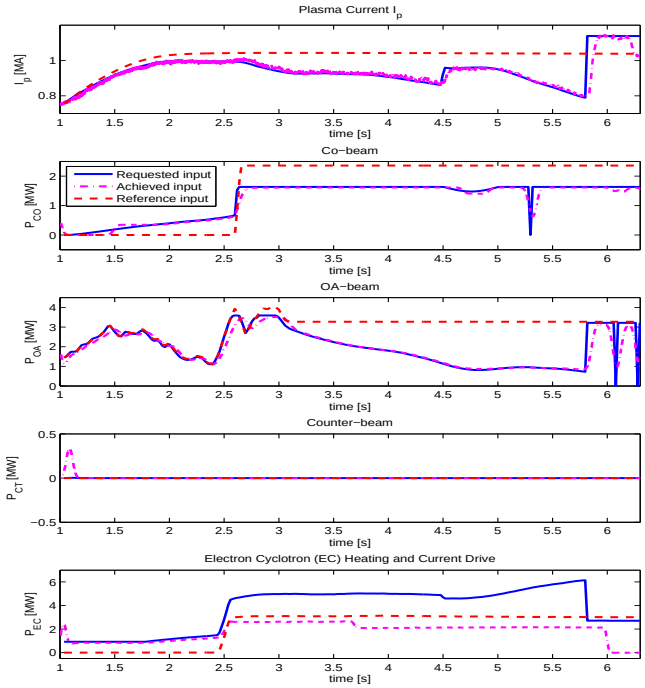

(a)

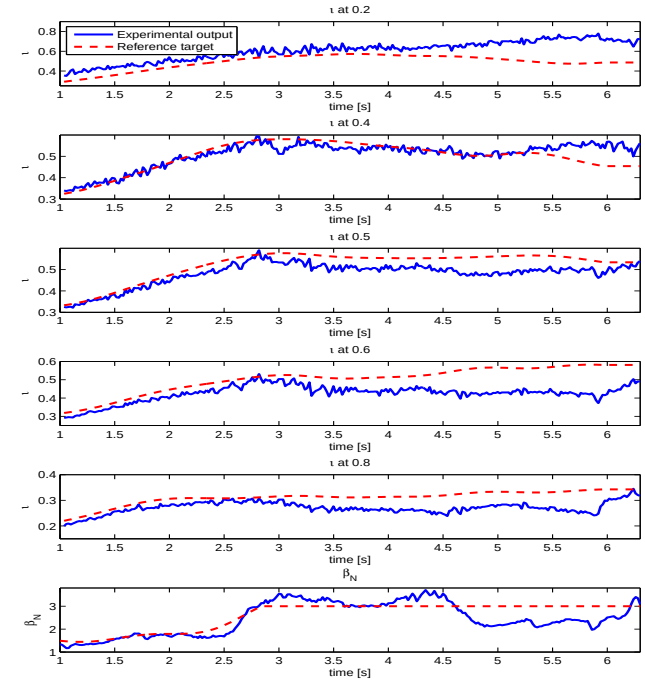

(b)

Figure 5.6: Experiment (shot #150749) with off-axis NBI: (a) FF inputs, requested FF+FB control inputs and achieved control inputs; (b) Reference target ι profile and β_N and experimental closed-loop-controlled ι profile and β_N.

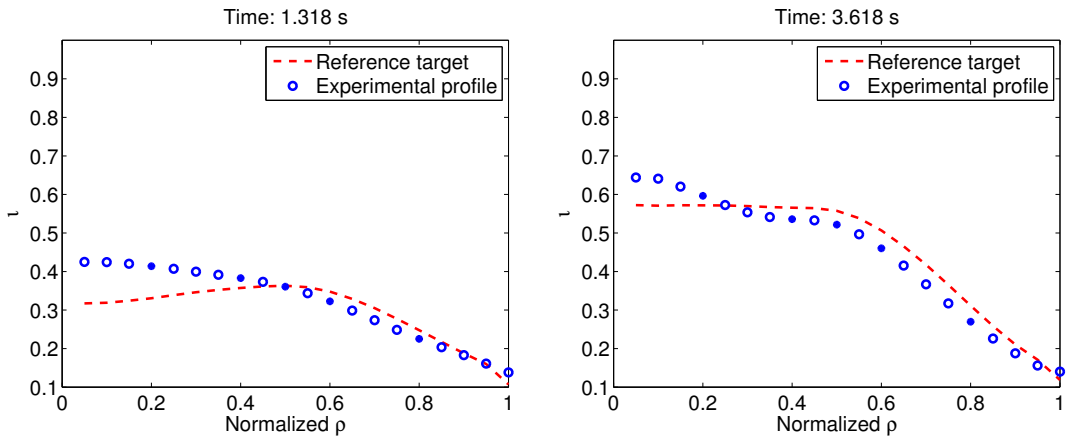

(a) Feedback ON, Disturbance OFF

(b) Feedback ON, Disturbance OFF

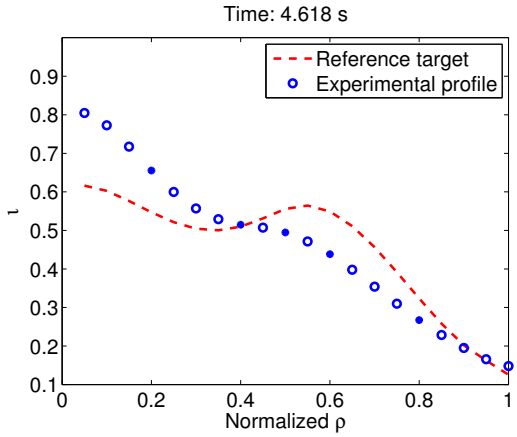

(c) Feedback ON, Disturbance ON

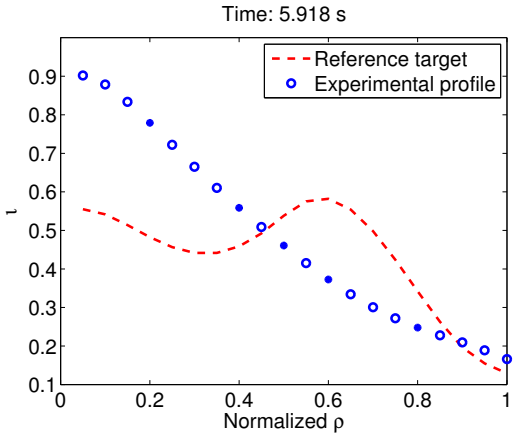

(d) Feedback OFF, Disturbance ON

Figure 5.7: Plasma $\iota(\hat{\rho})$ profile at time t= 1.318, 3.618, 4.618, 5.918 seconds from shot #150749 on DIII-D.

(solid blue lines) are shown in Figure 5.6 (b) and compared with the target values (red dashed lines). The controller regulates the ι profile close to the target profile until the disturbance is introduced, even in the current ramp-up phase. The total EC power could not follow the requested value, making the control of the inner ι profile and β_N more challenging. The controller drives some of the beams into saturation and requests the plasma current to decrease, which increases the tracking error in the outer part of the ι profile, in order to try to reduce the tracking error in the inner part of the ι profile. When the controller is turned off at $t = 5.8$ s, the actuator values

drift away from the feedforward+feedback values immediately. Because the outer ι profile is more quickly influenced by I_p, the tracking errors at $\hat{\rho} = 0.5$, 0.6, and 0.8 become smaller with the increasing of I_p.

The introduction of the off-axis NBI into the experiment placed the plasma in a different operating state with respect to the reference state around which the model was identified. As a result, the validity of the linear plasma model may limit the performance of the model-based controller in this operating scenario. During the closed-loop experiment, the EC power request was not achieved, therefore, the feedback controller output was no longer driving the plant, and as a result, the states of the controller were incorrectly updated. Finally, the actuator saturation during the experiment limited the ability of the feedback controller to manipulate the profile evolution. In order to evaluate the whole ι profile, a series of four plasma profiles at different times during shot #150749 are shown in Figure 5.7. Although the model was identified using only data after 2.5 s, the model-based controller performs reasonably well in the current ramp-up phase, which is shown in Figure 5.7 (a). Before $t = 4.2$ s, the controller regulates the ι profile close to the target profile (Figure 5.7 (b)). After this time, the tracking errors become larger. The input disturbances are injected into the system at $t = 4.5$ s, and the controller decreases the I_p to decrease the ι profile near the plasma boundary in order to attempt to track the desired inner ι profile as shown in Figure 5.7 (c). However, the tracking errors increase further as shown in Figure 5.7 (d).

5.5 Conclusion

A robust, model-based, MIMO, ι profile and β_N controller was designed for DIII-D. The design was based on a linear, identified model for H-mode discharges, includ-

ing uncertainty. The proposed controller was simulated in PTRANSP, and then the controller was experimentally tested in DIII-D. More experimental tests are needed to assess the appropriateness of using data-driven linear models for current profile control. The sensitivity of the static component of the controller to un-modeled or mis-modeled plasma response and its impact on performance need further analysis. Being able to control the current profile during the ramp-up and ramp-down phases, and being able to regulate the current profile for different scenarios will most likely require robust or nonlinear control approaches based on richer dynamic models obtained by a first-principles-driven modeling approach. The author will discuss this problem in the following chapter.

Chapter 6

Physics-based Control-oriented Modeling of the Poloidal Flux Profile Evolution in Advanced Tokamak Scenarios in DIII-D

6.1 Introduction

The tokamak is a high order, distributed parameter, nonlinear system with a large number of instabilities, and even under restrictive assumptions the poloidal flux profile, or equivalently current profile, models are highly nonlinear and based on partial differential equations (PDEs). The complexity of these first-principles models needs to be reduced to facilitate design of compact and reliable control strategies. During the model simplification process, there is always a trade-off between the simplicity of the model and both its physics accuracy and range of validity. First-principles-driven modeling provides the freedom of arbitrarily handling this trade-off and deciding on

the level of simplicity, accuracy and validity of the model. Several first-principles-driven, control-oriented, PDE models have been recently proposed for current profile control [22, 23, 24]. The model developed for DIII-D [22] is valid for low-confinement (L-mode) discharges, and has been used to determine optimal feedforward actuator trajectories that achieve and sustain a desired current profile [41]. The model has also been used to design complementing feedback controllers that add robustness against disturbances and model uncertainties, which have been experimentally tested in DIII-D [49, 50, 51].

In this work, the author converts the first-principles physics model of the evolution of the poloidal magnetic flux profile in DIII-D, which is related to the current profile evolution, into a form suitable for control design by combining it with simplified control-oriented versions of physics-based models of the electron density and temperature profiles, the plasma resistivity, and the non-inductive current-drives, with emphasis on high performance, H-mode, operating scenarios, thereby obtaining a first-principles-driven model. This model is developed with the goal of extending the control strategy employed in [49, 50, 51] to high performance H-mode scenarios, characterized by particle and energy transport barriers near the plasma boundary, which improve the plasma performance and result in the formation of large gradients in both the plasma density and temperature profiles that increase the complexity of the coupling between the magnetic and kinetic plasma parameters via the increase of the plasma self-generated "bootstrap current" [69].

The objective in developing the simplified physics-based models of the plasma parameters is to capture the dominant physics that describe how the control actuators affect the plasma parameters, and hence the current profile evolution, in H-mode scenarios. Progress towards physics-based modeling of the plasma profile evolutions has been recently reported in [22, 23, 24]. The first-principles-driven model of the

current profile evolution is extended from L-mode to H-mode, by modeling the self-generated "bootstrap current". Additionally, to utilize the full capabilities of the heating and current drive (H&CD) system, the effects of the actuators are modeled independently, instead of lumping them into a single input, to exploit the full capabilities of a given machines H&CD system [53]. The advanced tokamak simulation code, PTRANSP [68], which employs complex physics models to predict the plasma state evolution in the tokamak through exhaustive consumption of computational resources, is employed to obtain simulated data of the plasma state evolution to tailor the first-principles-driven models to the DIII-D tokamak. The tailored models are employed to design feedback control algorithms to control the current profile evolution in H-mode scenarios in DIII-D in Chapter 7 [54].

This chapter is organized as follows. In Section 6.2, the physics model of the poloidal flux profile evolution is introduced, and the actuators in the tokamak are discussed. The simplified physics-based models of the electron density and temperature profiles, plasma resistivity, and non-inductive current-drives are described in Section 6.3. In Section 6.4, the physics-based control-oriented model of the poloidal flux profile evolution is presented. In Section 6.5 and 6.6, the author tailors the models for on-axis and off-axis current drive scenarios, respectively, and compares the control-oriented model prediction to experimental data from DIII-D. Section 6.7 states the conclusions.

6.2 Current Profile Evolution Model

The evolution of the poloidal magnetic flux is given by the magnetic diffusion equation [70, 71]:

$$\frac{\partial \psi}{\partial t} = \frac{\eta(T_e)}{\mu_0 \rho_b^2 \hat{F}^2} \frac{1}{\hat{\rho}} \frac{\partial}{\partial \hat{\rho}} (\hat{\rho} \hat{F} \hat{G} \hat{H} \frac{\partial \psi}{\partial \hat{\rho}}) + R_0 \hat{H} \eta(T_e) \frac{< \bar{j}_{NI} \cdot \bar{B} >}{B_{\phi,0}}, \tag{6.1}$$

where ψ is the poloidal stream function which is related to the poloidal flux Ψ, i.e. $\Psi = 2\pi\psi$, η is the plasma resistivity, T_e is the electron temperature, μ_0 is the vacuum permeability, $\bar{j}_{NI}$ is any external source of non-inductive current density (EC, NBI, bootstrap current), $\bar{B}$ is the magnetic field, $B_{\phi,0}$ is the magnetic field at the geometric major radius R_0, the parameter ρ_b is the effective minor radius of the last closed magnetic flux surface and <> denotes a flux-surface average. The parameters $\hat{F}$, $\hat{G}$ and $\hat{H}$ are geometric factors pertaining to the magnetic configuration of a particular plasma equilibrium, and are defined as,

$$\hat{F}(\hat{\rho}) = \frac{R_0 B_{\phi,0}}{R B_\phi(R,Z)}, \quad \hat{G}(\hat{\rho}) =< \frac{R_0^2}{R^2} |\Delta\rho|^2 >, \quad \hat{H}(\hat{\rho}) = \frac{\hat{F}}{< R_0^2/R^2 >},$$

where B_ϕ is the toroidal magnetic field at the spatial location, and R is the major radius of the flux surfaces. The boundary conditions are given by

$$\frac{\partial \psi}{\partial \hat{\rho}}|_{\hat{\rho}=0} = 0, \qquad \frac{\partial \psi}{\partial \hat{\rho}}|_{\hat{\rho}=1} = -\frac{\mu_0}{2\pi} \frac{R_0}{\hat{G}|_{\hat{\rho}=1} \hat{H}|_{\hat{\rho}=1}} I_p(t), \tag{6.2}$$

where $I_p(t)$ is the plasma current.

There are several actuators that can manipulate the current profile evolution in DIII-D. The first actuator is the total plasma current I_p. The second actuator is the neutral beam injection (NBI) system. Injecting beams of highly energetic neu-

tral particles into the plasma provides a source of non-inductive current as well as plasma heating through collisions. The beams in the clockwise direction in Figure 3.2 (30L/R, 150L/R, 210L/R, and 330L/R) are referred to as $nbi_1, nbi_2, \cdots, nbi_8$ in this dissertation. The third actuator is the electron cyclotron (EC) heating and current drive system. The frequency of the radio waves, which are injected into the plasma through electron cyclotron (gyrotron) launchers, can be tuned to excite the electrons. There are six gyrotrons in DIII-D (Gyrotron 1, 2, $\cdots$, 6), which are referred to as $ec_1, ec_2, \cdots, ec_6$ in this dissertation. The final actuator is the electron density, which is controlled by gas-feeding and pellet launchers.

6.3 Simplified Physics-based Models of Plasma Parameters

The objective in developing the simplified physics-based models of the plasma parameters is to capture the dominant physics that describe how the control actuators affect the plasma parameters, and hence the current profile evolution. The simplified models are developed with particular care being taken to ensure their applicability to H-mode scenarios [53].

Electron Density Modeling

The control action employed to regulate the electron density is assumed to weakly affect the radial distribution of the electrons. Therefore, the electron density $n_e(\hat{\rho}, t)$ is modeled as

$$n_e(\hat{\rho}, t) = n_e^{prof}(\hat{\rho}, t_r) u_n(t), \tag{6.3}$$

where t_r is a reference time, $n_e^{prof}(\hat{\rho}, t_r)$ is a reference electron density profile and $u_n(t)$ regulates time evolution of the electron density.

Electron Temperature Modeling

The slowly evolving electron temperature profile evolution is modeled as

$$T_e(\hat{\rho}, t) = k_{T_e}(\hat{\rho}, t_r) \frac{T_e^{prof}(\hat{\rho}, t_r)}{n_e^{prof}(\hat{\rho}, t_r)} \frac{I_p(t)\sqrt{P_{tot}(t)}}{u_n(t)}, \tag{6.4}$$

where $T_e^{prof}(\hat{\rho}, t_r)$ is a reference electron temperature profile at a reference time t_r, and $P_{tot}(t)$ is the total power injected into the plasma. The constant $k_{T_e}(\hat{\rho}, t_r)$ is expressed as

$$k_{T_e}(\hat{\rho}, t_r) = \frac{n_e(\hat{\rho}, t_r)}{I_p(t_r)\sqrt{P_{tot}(t_r)}}.$$

Plasma Resistivity Modeling

The plasma resistivity $\eta(T_e)$ scales with the electron temperature as

$$\eta(\hat{\rho}, t) = \frac{k_{sp}(\hat{\rho}, t_r) Z_{eff}}{T_e(\hat{\rho}, t)^{3/2}}, \tag{6.5}$$

where Z_{eff} is the effective average charge of the ions in the plasma. The constant $k_{sp}(\hat{\rho}, t_r)$ is expressed as

$$k_{sp}(\hat{\rho}, t_r) = \frac{\eta(\hat{\rho}, t_r) T_e(\hat{\rho}, t_r)^{3/2}}{Z_{eff}}.$$

Non-inductive Current Drive Modeling

The total non-inductive current drive is produced by EC, NBI and the bootstrap current and is expressed as

$$\frac{<\bar{j}_{NI}\cdot\bar{B}>}{B_{\phi,0}}=\sum_{i=1}^{6}\frac{<\bar{j}_{ec_i}\cdot\bar{B}>}{B_{\phi,0}}+\sum_{i=1}^{8}\frac{<\bar{j}_{nbi_i}\cdot\bar{B}>}{B_{\phi,0}}+\frac{<\bar{j}_{bs}\cdot\bar{B}>}{B_{\phi,0}}, \tag{6.6}$$

where $\bar{j}_{ec_i}$ is the non-inductive current generated by the i^{th} gyrotron launcher in EC system, $\bar{j}_{nbi_i}$is the non-inductive current generated by the i^{th} NBI and $\bar{j}_{bs}$ is the non-inductive current generated by the bootstrap effect.

The non-inductive toroidal current density provided by each gyrotron launcher is modeled as

$$\frac{<\bar{j}_{ec_i}\cdot\bar{B}>}{B_{\phi,0}}=k_{ec_i}(\hat{\rho},t_r)j_{ec_i}(\hat{\rho},t_r)\frac{T_e(\hat{\rho},t)}{n_e(\hat{\rho},t)}P_{ec_i}(t), \tag{6.7}$$

where $j_{ec_i}(\hat{\rho},t_r)$ is a reference deposition profile for each respective current drive source, the term $T_e(\hat{\rho},t)/n_e(\hat{\rho},t)$ represents the current-drive efficiency [72], and the normalizing gyrotron constant k_{ec_i} is expressed as

$$k_{ec_i}(\hat{\rho},t_r)=\frac{n_e(\hat{\rho},t_r)}{T_e(\hat{\rho},t_r)P_{ec_i}(t_r)}.$$

Therefore, the normalized gyrotron deposition profile at the reference time t_r is expressed as

$$j_{ec_i}^{norm}(\hat{\rho},t_r)=\frac{j_{ec_i}(\hat{\rho},t_r)}{P_{ec_i}(t_r)(\frac{T_e(\hat{\rho},t_r)}{n_e(\hat{\rho},t_r)})}=\frac{j_{ec_i}(\hat{\rho},t_r)n_e(\hat{\rho},t_r)}{P_{ec_i}(t_r)T_e(\hat{\rho},t_r)}=j_{ec_i}(\hat{\rho},t_r)k_{ec_i}(\hat{\rho},t_r).$$

The non-inductive toroidal current density provided by each NBI is modeled as

$$\frac{<\bar{j}_{nbi_i}\cdot\bar{B}>}{B_{\phi,0}}=k_{nbi_i}(\hat{\rho},t_r)j_{nbi_i}(\hat{\rho},t_r)\frac{T_e(\hat{\rho},t)}{n_e(\hat{\rho},t)}P_{nbi_i}(t), \tag{6.8}$$

where $j_{nbi_i}(\hat{\rho}, t_r)$ is a reference deposition profile, and the normalizing NBI constant k_{nbi_i} is expressed as

$$k_{nbi_i}(\hat{\rho}, t_r) = \frac{n_e(\hat{\rho}, t_r)}{T_e(\hat{\rho}, t_r) P_{nbi_i}(t_r)}.$$

The normalized NBI deposition profile is expressed as

$$j^{norm}_{nbi_i}(\hat{\rho}, t_r) = \frac{j_{nbi_i}(\hat{\rho}, t_r)}{P_{nbi_i}(t_r)(\frac{T_e(\hat{\rho}, t_r)}{n_e(\hat{\rho}, t_r)})} = \frac{j_{nbi_i}(\hat{\rho}, t_r) n_e(\hat{\rho}, t_r)}{P_{nbi_i}(t_r) T_e(\hat{\rho}, t_r)} = j_{nbi_i}(\hat{\rho}, t_r) k_{nbi_i}(\hat{\rho}, t_r).$$

Based on the assumption of tight coupling between the electron and ion species in the plasma, the bootstrap current is modeled as [73]

$$\frac{< \bar{j}_{bs} \cdot \bar{B} >}{B_{\phi,0}} = \frac{R_0}{\hat{F}(\hat{\rho})} \frac{1}{\partial \psi / \partial \hat{\rho}} [2\mathcal{L}_{31} T_e \frac{\partial n_e}{\partial \hat{\rho}} + (2\mathcal{L}_{31} + \mathcal{L}_{32} + \alpha \mathcal{L}_{34}) n_e \frac{\partial T_e}{\partial \hat{\rho}}], \tag{6.9}$$

where $\mathcal{L}_{31}$, $\mathcal{L}_{32}$, $\mathcal{L}_{34}$ and α depend on the reference plasma magnetic equilibrium and on particle collisionality in the plasma.

6.4 Physics-based Control-oriented Model of Poloidal Magnetic Flux Evolution

By combining the control-oriented models (6.3)-(6.9) with the magnetic diffusion equation (6.1), the desired first-principles-driven, control-oriented model of the poloidal magnetic flux profile evolution is obtained. The first term is expressed as:

$$\frac{\eta(T_e)}{\mu_0 \rho_b^2 \hat{F}^2}(\hat{\rho}, t) = f_1(\hat{\rho}) u_1(t), \tag{6.10}$$

where

$$f_1 = \frac{k_{sp} Z_{eff}}{\mu_0 \rho_b^2 \hat{F}^2 (k_{T_e} \frac{T_e^{prof}}{n_e^{prof}})^{3/2}}, \quad u_1 = \frac{u_n^{3/2}}{(I_p \sqrt{P_{tot}})^{3/2}}.$$

The terms for the six gyrotrons in the EC system are expressed as:

$$R_0\hat{H}\eta(T_e)\frac{<\bar{j}_{ec_i}\cdot\bar{B}>}{B_{\phi,0}} = f_{i+1}(\hat{\rho})u_{i+1}(t), \tag{6.11}$$

where $i \in \{1,2,3,4,5,6\}$, and

$$f_{i+1} = \frac{R_0\hat{H}k_{sp}Z_{eff}k_{ec_i}j_{ec_i}^{dep}}{(k_{T_e}T_e^{prof}n_e^{prof})^{1/2}}, \quad u_{i+1} = \frac{P_{ec_i}}{(I_p\sqrt{P_{tot}})^{1/2}u_n^{1/2}}.$$

The terms for the eight beams in the NBI system are expressed as:

$$R_0\hat{H}\eta(T_e)\frac{<\bar{j}_{nbi_i}\cdot\bar{B}>}{B_{\phi,0}} = f_{i+7}(\hat{\rho})u_{i+7}(t), \tag{6.12}$$

where $i \in \{1,2,3,4,5,6,7,8\}$, and

$$f_{i+7} = \frac{R_0\hat{H}k_{sp}Z_{eff}k_{nbi_i}j_{nbi_i}^{dep}}{(k_{T_e}T_e^{prof}n_e^{prof})^{1/2}}, \quad u_{i+7} = \frac{P_{nbi_i}}{(I_p\sqrt{P_{tot}})^{1/2}u_n^{1/2}}.$$

The bootstrap current term is expressed as:

$$R_0\hat{H}\eta(T_e)\frac{<\bar{j}_{bs}\cdot\bar{B}>}{B_{\phi,0}} = (\frac{\partial\psi}{\partial\hat{\rho}})^{-1}f_{16}(\hat{\rho})u_{16}(t), \tag{6.13}$$

where

$$u_{16} = \frac{u_n^{3/2}}{(I_p\sqrt{P_{tot}})^{1/2}},$$

$$f_{16} = \frac{k_{Jev}R_0^2\hat{H}k_{sp}Z_{eff}}{\hat{F}(k_{T_e}\frac{T_e^{prof}}{n_e^{prof}})^{3/2}}[k_{T_e}(2\mathcal{L}_{31}+\mathcal{L}_{32}+\alpha\mathcal{L}_{34})\frac{dT_e^{prof}}{d\hat{\rho}} + 2\mathcal{L}_{31}k_{T_e}\frac{T_e^{prof}}{n_e^{prof}}\frac{dn_e^{prof}}{d\hat{\rho}}].$$

By using the models (6.10)-(6.13), the developed first-principles-driven, control-oriented model of the poloidal magnetic flux profile evolution is expressed as

$$\frac{\partial \psi}{\partial t} = \frac{f_1 u_1}{\hat{\rho}} \frac{\partial}{\partial \hat{\rho}} (\hat{\rho} D_\psi \frac{\partial \psi}{\partial \hat{\rho}}) + \sum_{i=2}^{15} f_i u_i + (\frac{\partial \psi}{\partial \hat{\rho}})^{-1} f_{16} u_{16}(t), \tag{6.14}$$

with boundary conditions:

$$\frac{\partial \psi}{\partial \hat{\rho}}|_{\hat{\rho}=0} = 0, \quad \frac{\partial \psi}{\partial \hat{\rho}}|_{\hat{\rho}=1} = -k_{17} u_{17}(t),$$

where

$$D_\psi = \hat{F}\hat{G}\hat{H}, \quad k_{17} = \frac{\mu_0}{2\pi} \frac{R_0}{\hat{G}|_{\hat{\rho}=1} \hat{H}|_{\hat{\rho}=1}}, \quad u_{17}(t) = I_p(t).$$

6.5 Model Tailored for On-axis Current Drive Scenarios

We now employ on-axis current drive experimental data (shot #146419) and simulated data from the PTRANSP advanced tokamak simulation code [68] configured to the DIII-D geometry to tailor the first-principles-driven model to an on-axis current drive, H-mode, scenario in DIII-D that has energy and particle transport barriers near the plasma boundary. The auxiliary H&CD actuators on DIII-D are 6 independently configurable gyrotron launchers and 8 neutral beam launchers, where 6 are co-current-injection and 2 are counter-current-injection. The parameters related to the magnetic configuration of the plasma equilibrium are shown in Figure 6.1 (a) and (b), the reference profiles for the various models are shown in Figure 6.1 (d), (e) and (h), the normalizing constants are shown in Figure 6.1 (c), (f) and (i), and the normalized auxiliary current deposition profiles are shown in Figure 6.1 (g) and (j).

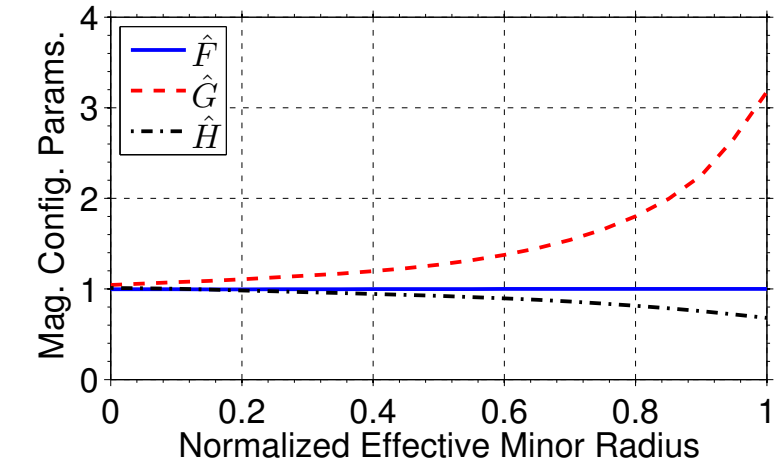
Mag. Config. Params.
$\hat{F}$
$\hat{G}$
$\hat{H}$
0
1
2
3
4
0
0.2
0.4
0.6
0.8
1
Normalized Effective Minor Radius

(a)

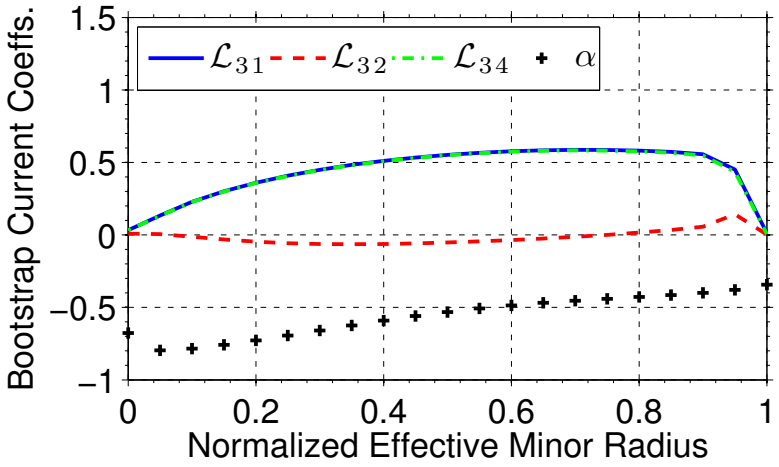
Bootstrap Current Coeffs.
$\mathcal{L}_{31}$
$\mathcal{L}_{32}$
$\mathcal{L}_{34}$
α
1.5
1
0.5
0
−0.5
−1
0
0.2
0.4
0.6
0.8
1
Normalized Effective Minor Radius

(b)

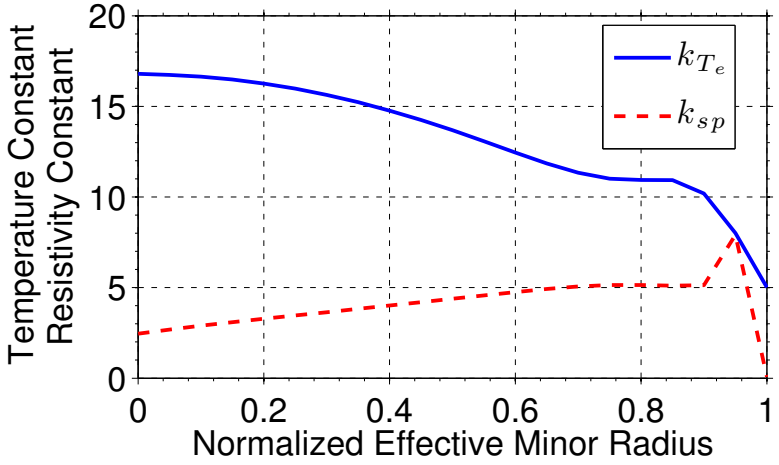
Temperature Constant
Resistivity Constant
k_{T_e}
k_{sp}
20
15
10
5
0
0
0.2
0.4
0.6
0.8
1
Normalized Effective Minor Radius

(c)

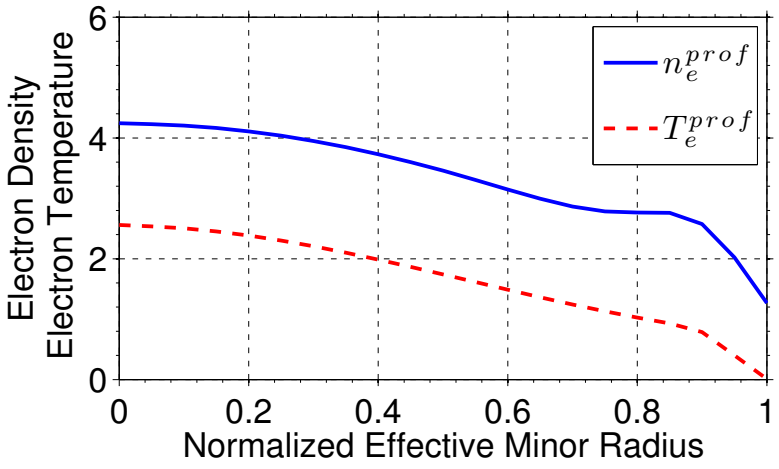
Electron Density
Electron Temperature
n_e^{prof}
T_e^{prof}
Normalized Effective Minor Radius

(d)

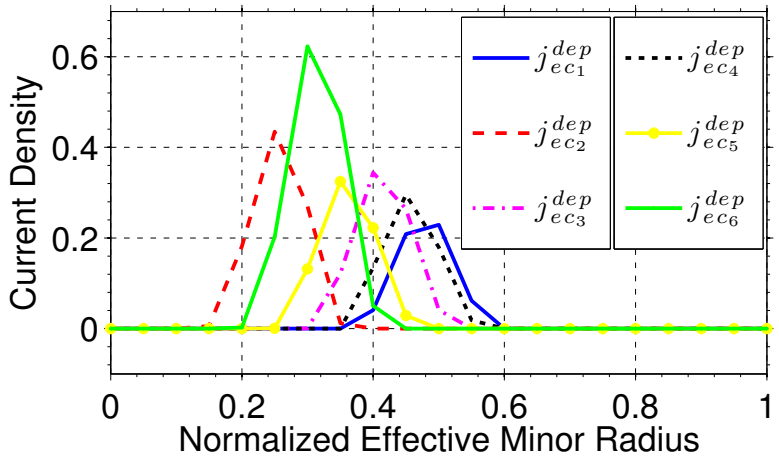
Current Density
$j_{ec_1}^{dep}$
$j_{ec_2}^{dep}$
$j_{ec_3}^{dep}$
$j_{ec_4}^{dep}$
$j_{ec_5}^{dep}$
$j_{ec_6}^{dep}$
Normalized Effective Minor Radius

(e)

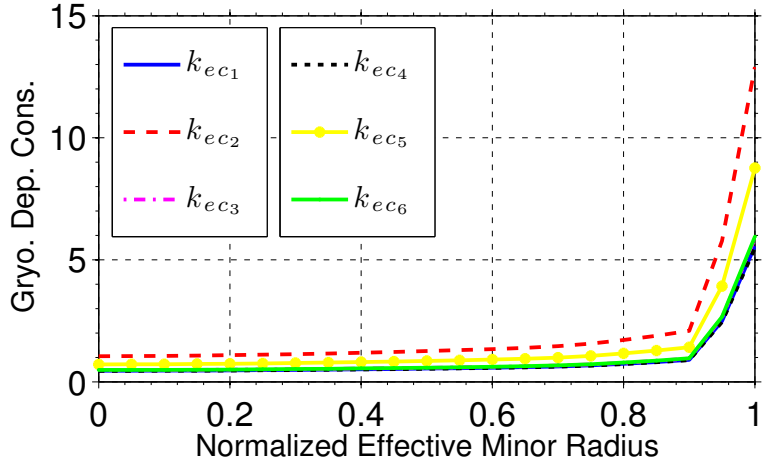
Gryo. Dep. Cons.
k_{ec_1}
k_{ec_2}
k_{ec_3}
k_{ec_4}
k_{ec_5}
k_{ec_6}
Normalized Effective Minor Radius

(f)

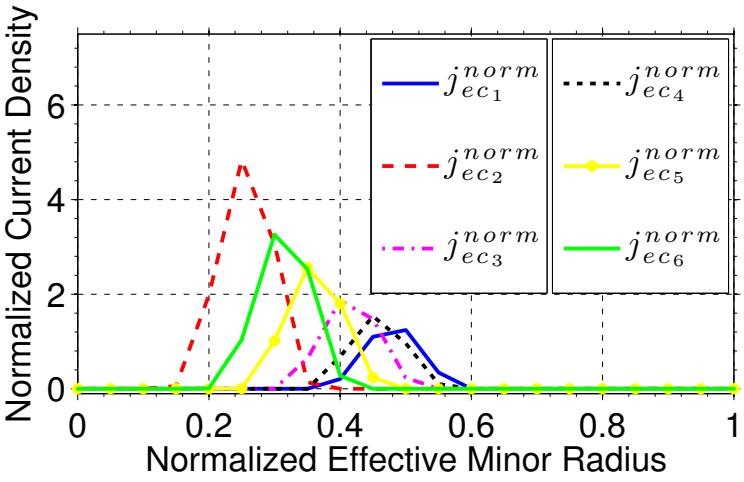
Normalized Current Density
Normalized Effective Minor Radius
$j_{ec_1}^{norm}$
$j_{ec_2}^{norm}$
$j_{ec_3}^{norm}$
$j_{ec_4}^{norm}$
$j_{ec_5}^{norm}$
$j_{ec_6}^{norm}$

(g)

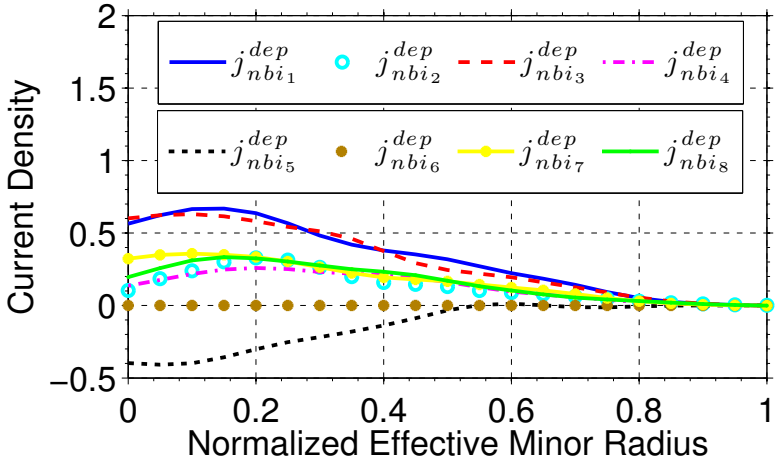
Current Density
Normalized Effective Minor Radius
$j_{nbi_1}^{dep}$
$j_{nbi_2}^{dep}$
$j_{nbi_3}^{dep}$
$j_{nbi_4}^{dep}$
$j_{nbi_5}^{dep}$
$j_{nbi_6}^{dep}$
$j_{nbi_7}^{dep}$
$j_{nbi_8}^{dep}$

(h)

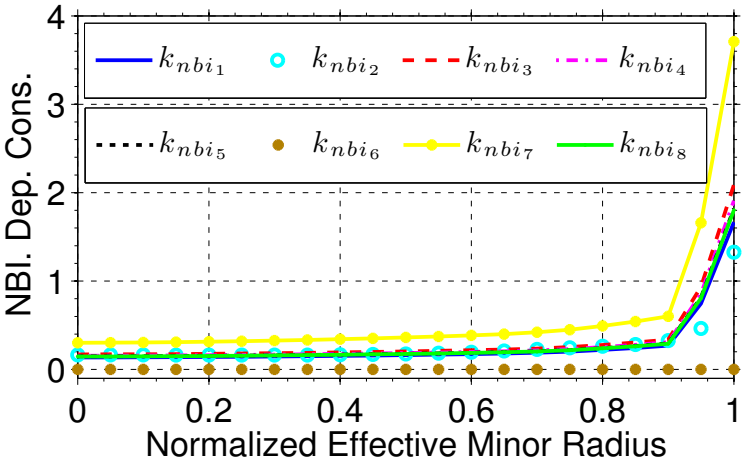
NBI. Dep. Cons.
Normalized Effective Minor Radius
k_{nbi_1}
k_{nbi_2}
k_{nbi_3}
k_{nbi_4}
k_{nbi_5}
k_{nbi_6}
k_{nbi_7}
k_{nbi_8}

(i)

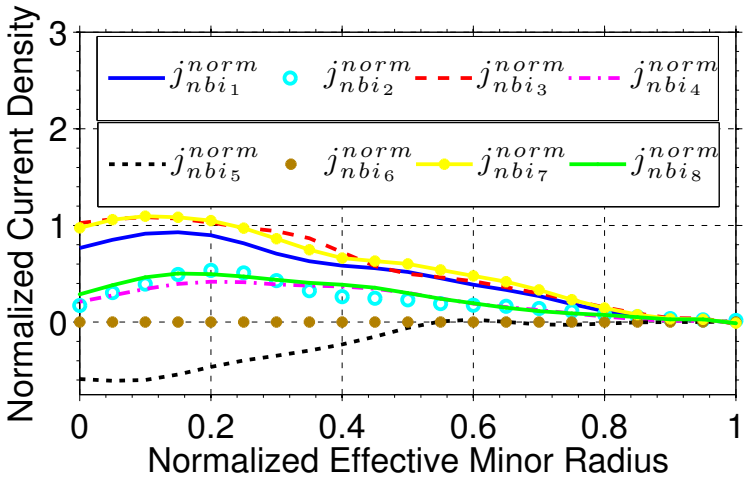

(j)

Figure 6.1: On-axis Current Drive Scenarios: (a) Magnetic Configuration Parameters, (b) Bootstrap Current Coefficients, (c) Temperature Coefficient k_{T_e} $(10^9 m^{-3}A^{-1}W^{-1/2})$ & Resistivity Coefficient k_{sp} $(10^{-8}\Omega m keV^{3/2})$, (d) Electron Density Profile n_e^{prof} (m^{-3}) & Electron Temperature Profile T_e^{prof} (keV), (e) Reference Gyrotron Current Deposition Profiles $j_{ec_i}^{dep}$ $(10^5 Am^{-2})$, (f) Gyrotron Model Coefficients k_{ec_i} $(10^{14}m^{-3}keV^{-1}W^{-1})$, (g) Normalized Gyrotron Deposition Profile $j_{ec_i}^{norm}$ $(10^{18}Am^{-5}keV^{-1}W^{-1})$, (h) Reference NBI Current Deposition Profiles $j_{nbi_i}^{dep}$ $(10^4 Am^{-2})$, (i) NBI Model Coefficients k_{nbi_i} $(10^{14}m^{-3}keV^{-1}W^{-1})$, (j) Normalized NBI Deposition Profile $j_{nbi_i}^{norm}$ $(10^{18}Am^{-5}keV^{-1}W^{-1})$.

The other model constants are $B_{\phi,0}$=1.68 T, R_0=1.76 m, ρ_b=0.80 m, and Z_{eff}=1.75.

The steady state gains of the on-axis first-principles-driven model for the ι profile are shown in Figure 6.2. In the figure, the steady state response $\Delta\bar{\iota}$ to unitary changes in the various inputs is plotted, where the dimensionless parameter Δu_n is given by 0.1, ΔP_{ec_i} and ΔP_{nbi_j} are given by 1 MW (co-injection is "+" and counter injection is "-") and ΔI_p is given by 0.1 MA, where $i \in \{1, 2, \cdots, 6\}$ and $j \in \{1, 2, \cdots, 8\}$. The plasma current I_p is the most capable actuator in adjusting the magnetic profile in absolute terms (shown in Figure 6.2 (a.1)), and the time evolution of the electron density u_n leads to the smallest change in the magnetic profile (shown in Figure 6.2 (a.2)). The EC powers lead to changes in the $\Delta\bar{\iota}$ profile, which are based on the injection positions of the gyrotrons. Based on Figure 6.1 (e) and (g), we can observe

that the injection positions of Gyrotron 1, 3 and 4 are close, and therefore the steady-state responses $\Delta\bar{\iota}$ to these three gyrotrons are very similar (shown in Figure 6.2 (a.3), (a.4), and (b.1)). The co-injection (30L/R, 150L/R, and 330L/R) and counter-injection (210L/R) beams are also very powerful, affecting the profile in different directions in agreement with prior experiments.

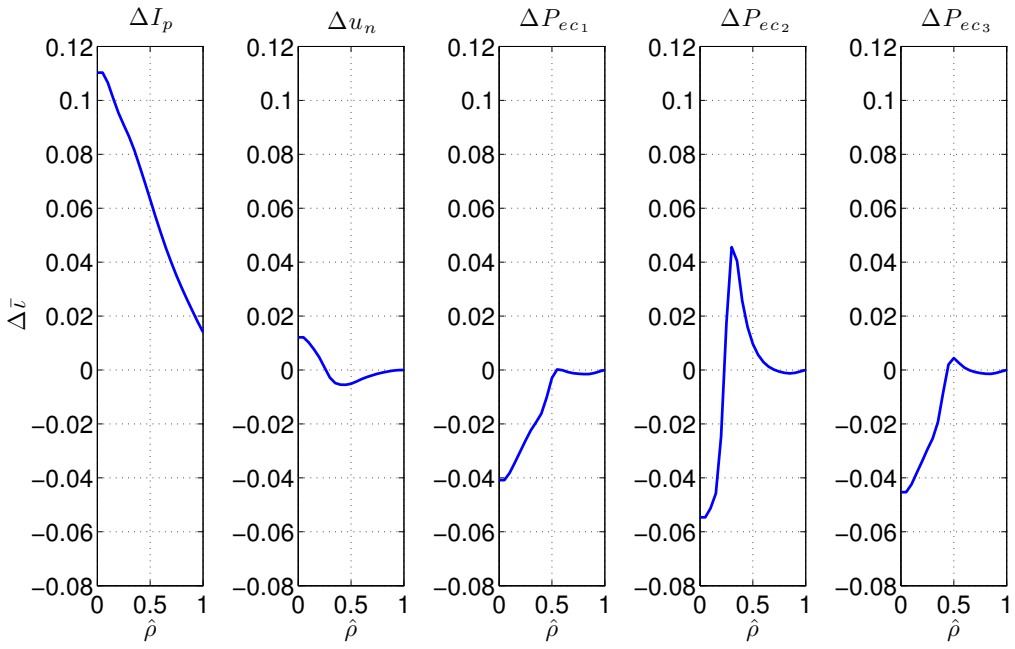

(a)

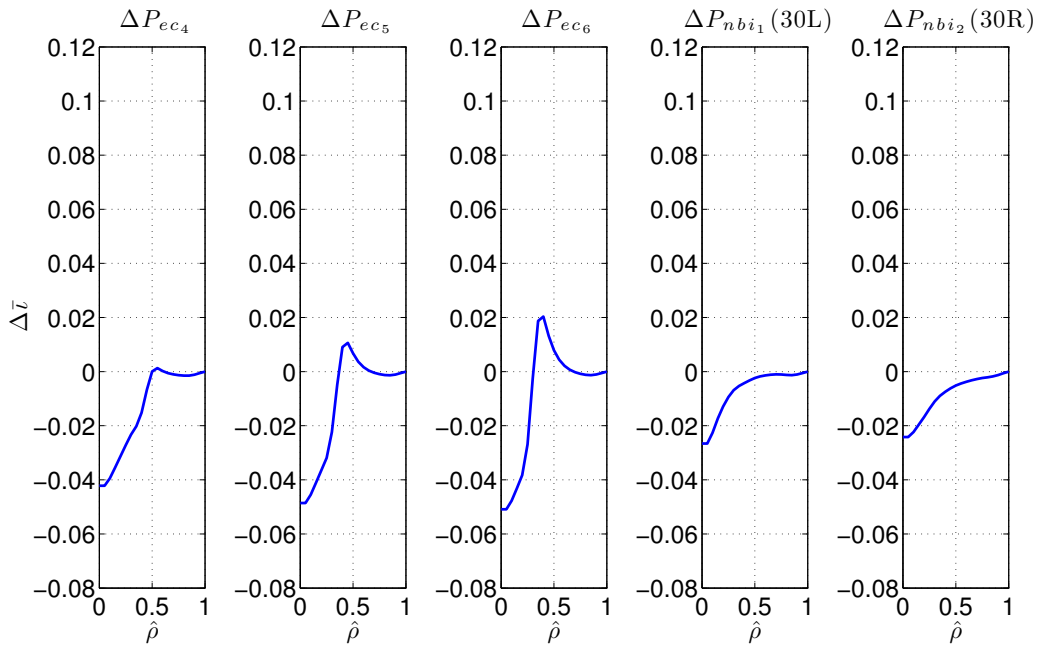

(b)

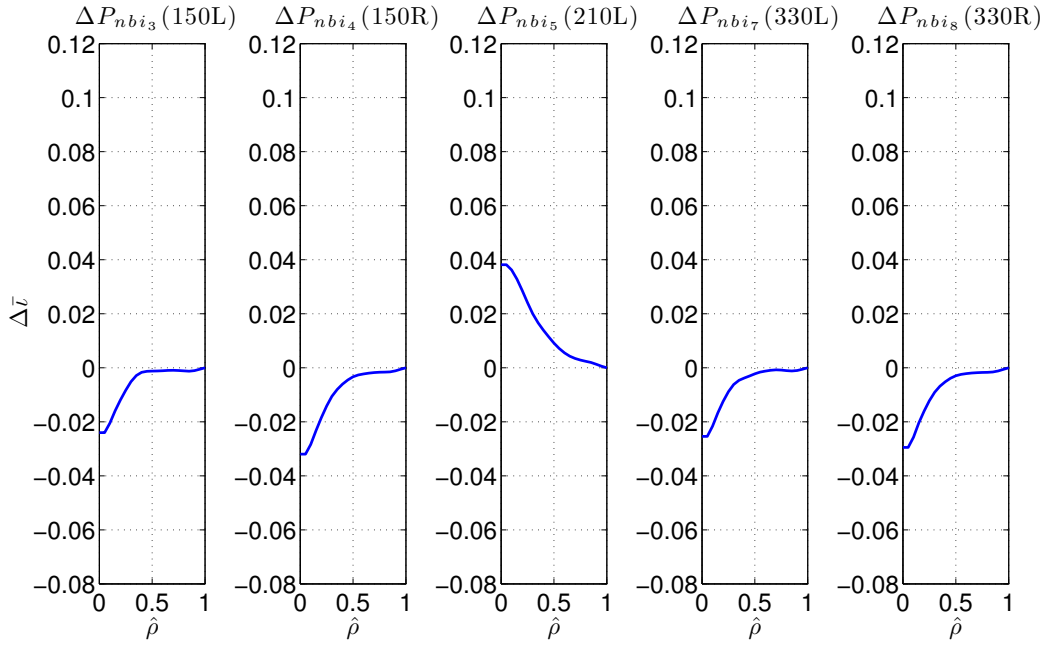

(c)

Figure 6.2: Steady state gains for the ι profile response for on-axis current drive scenarios. Note: the inputs are ΔP_{ec_i} (1 MW), ΔP_{nbi_j} (1 MW), Δu_n (0.1), and ΔI_p (0.1 MA), where $i \in \{1, 2, \cdots, 6\}$ and $j \in \{1, 2, \cdots, 8\}$.

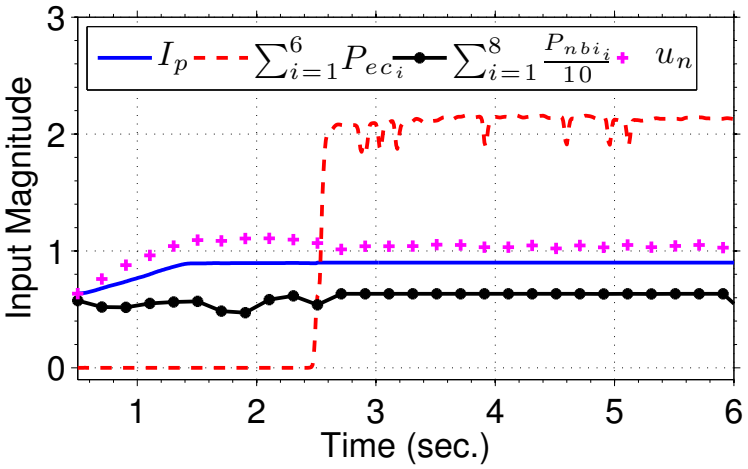

Figure 6.3: Control inputs applied during first-principles-driven model simulation and DIII-D shot #146417 (current in MA and power in MW).

6.5.1 Comparison between First-principles-driven Model Prediction and Experimental Data

We now describe a study that compares the evolution of the plasma parameters predicted by the first-principles-driven (FPD) model to the experimentally achieved plasma parameters in DIII-D on-axis shot #146417. The inputs (total plasma current I_p, total gyrotron launcher powers $\sum_{i=1}^{6} P_{ec_i}$, total neutral beam injection powers $\sum_{i=1}^{8} P_{nbi_i}$, and density regulation u_n) applied during both the simulation and the experiment are shown in Figure 6.3, time traces of ψ at various normalized effective minor radii are shown in Figure 6.4, and a comparison of the first-principles-driven model predicted and the experimentally achieved ψ and q profiles at various time instances is shown in Figure 6.5 (a)-(d) and Figure 6.5 (e)-(h), respectively. As shown in the figures, the trends of the first-principles-driven model predicted plasma parameters show good agreement with the experimental results.

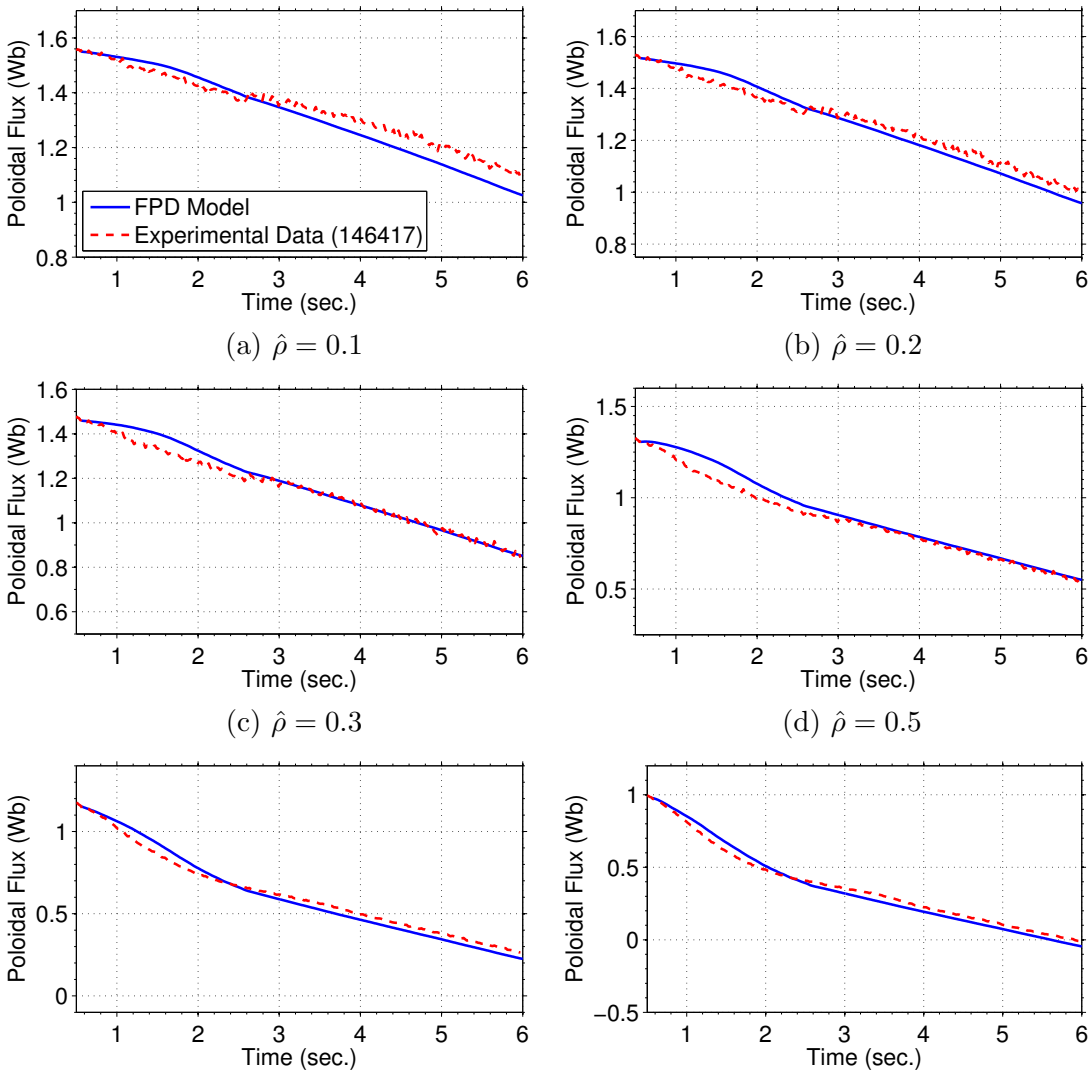

(a) $\hat{\rho} = 0.1$ (b) $\hat{\rho} = 0.2$

(c) $\hat{\rho} = 0.3$ (d) $\hat{\rho} = 0.5$

(e) $\hat{\rho} = 0.7$ (f) $\hat{\rho} = 0.9$

Figure 6.4: Time trace of poloidal magnetic flux ψ at various spatial locations. Note: first-principles-driven model (solid) and experimentally achieved (dash).

6.6 Model Tailored for Off-axis Current Drive Scenarios

We now employ off-axis current drive experimental data (shot #147626) and analyzed results for the same shot from the PTRANSP code configured to the DIII-D geometry to tailor the first-principles-driven model to an off-axis current drive, H-mode,

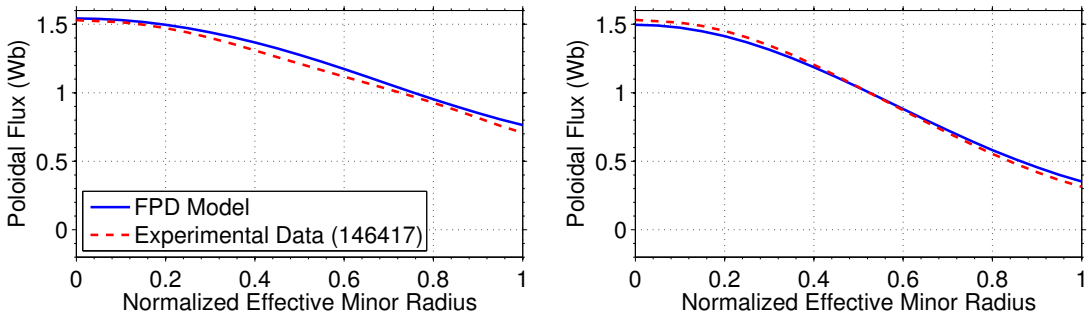

(a) $t = 1.0$ sec. (b) $t = 2.5$ sec.

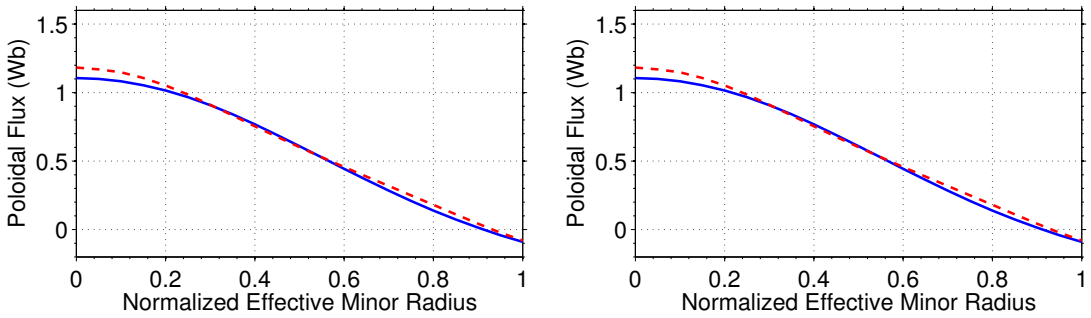

(c) $t = 4.0$ sec. (d) $t = 5.5$ sec.

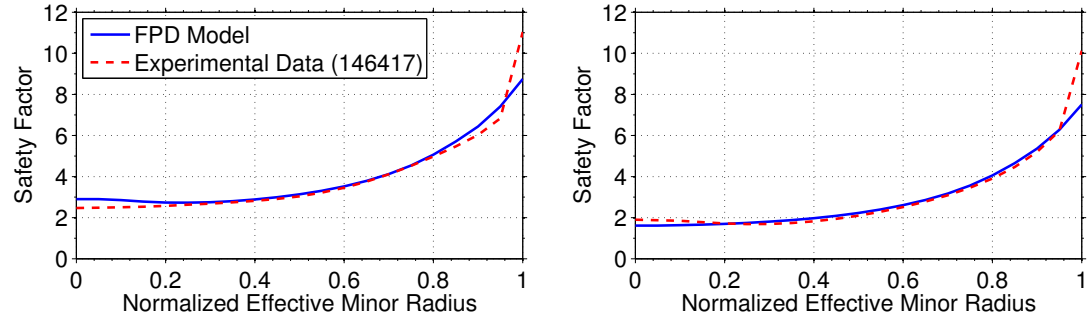

(e) $t = 1.0$ sec. (f) $t = 2.5$ sec.

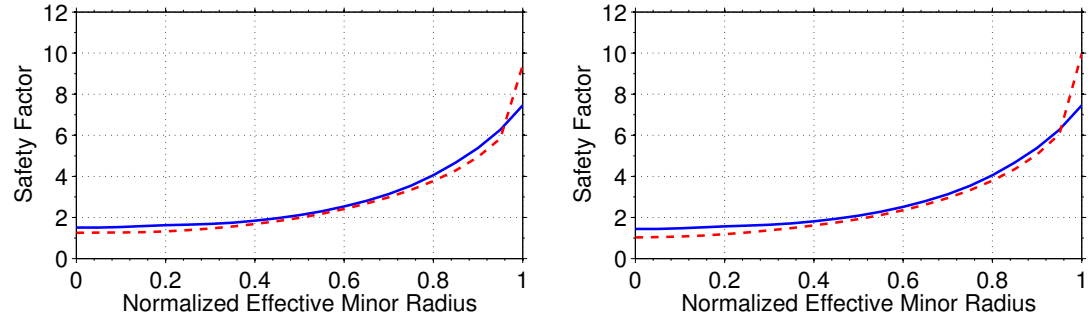

(g) $t = 4.0$ sec. (h) $t = 5.5$ sec.

Figure 6.5: Poloidal magnetic flux profile $\psi(\hat{\rho})$ (a)-(d) and safety factor profile $q(\hat{\rho})$ (e)-(h) at various time instances.

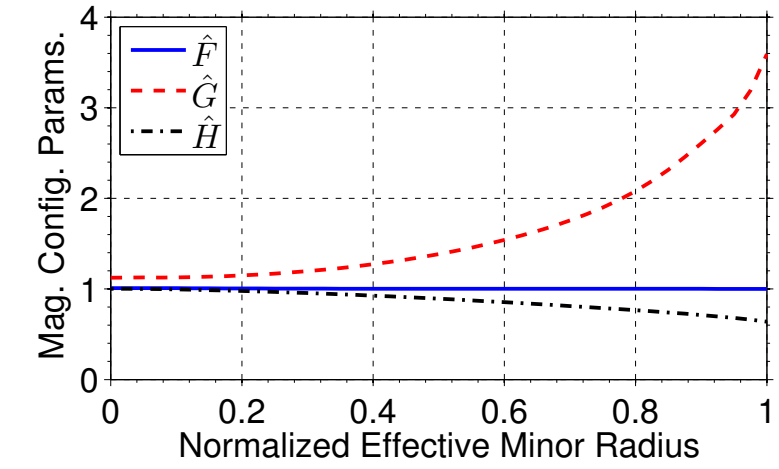
Mag. Config. Params.
$\hat{F}$
$\hat{G}$
$\hat{H}$
0
1
2
3
4
0
0.2
0.4
0.6
0.8
1
Normalized Effective Minor Radius

(a)

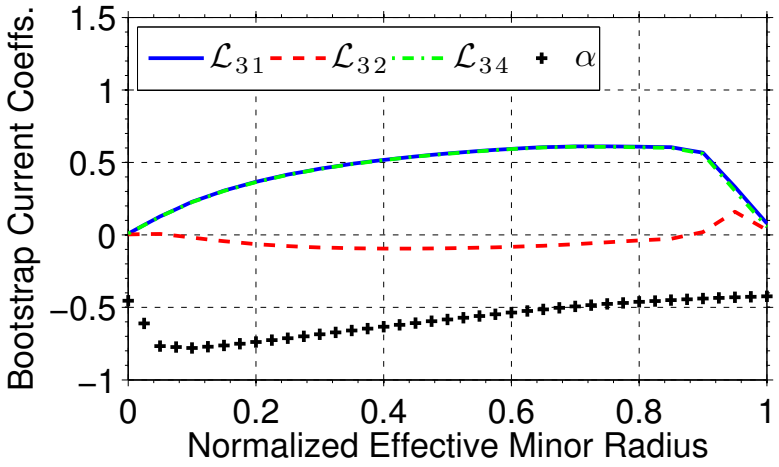
Bootstrap Current Coeffs.
$\mathcal{L}_{31}$
$\mathcal{L}_{32}$
$\mathcal{L}_{34}$
α
1.5
1
0.5
0
−0.5
−1
0
0.2
0.4
0.6
0.8
1
Normalized Effective Minor Radius

(b)

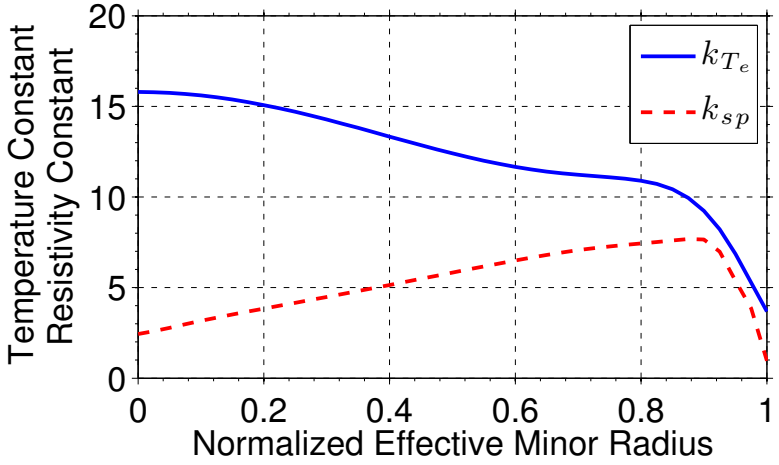
Temperature Constant
Resistivity Constant
k_{T_e}
k_{sp}
20
15
10
5
0
0
0.2
0.4
0.6
0.8
1
Normalized Effective Minor Radius

(c)

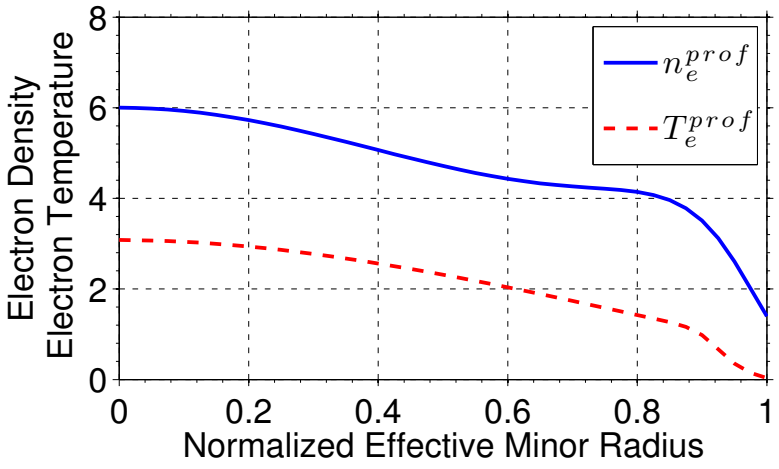
Electron Density
Electron Temperature
n_e^{prof}
T_e^{prof}
Normalized Effective Minor Radius

(d)

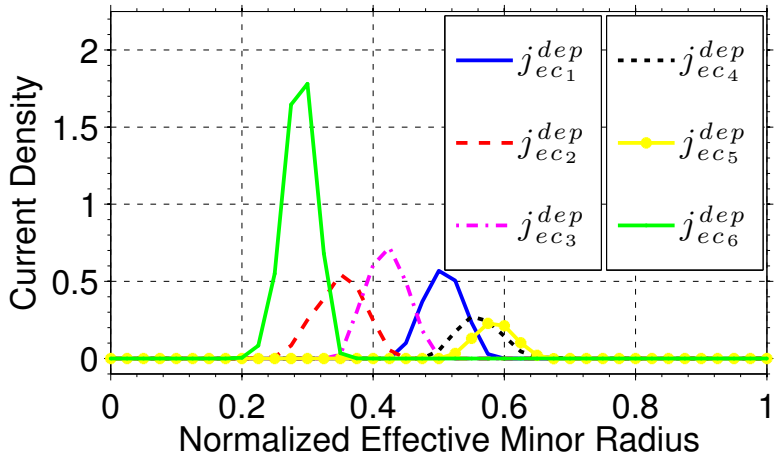
Current Density
$j_{ec_1}^{dep}$
$j_{ec_2}^{dep}$
$j_{ec_3}^{dep}$
$j_{ec_4}^{dep}$
$j_{ec_5}^{dep}$
$j_{ec_6}^{dep}$
Normalized Effective Minor Radius

(e)

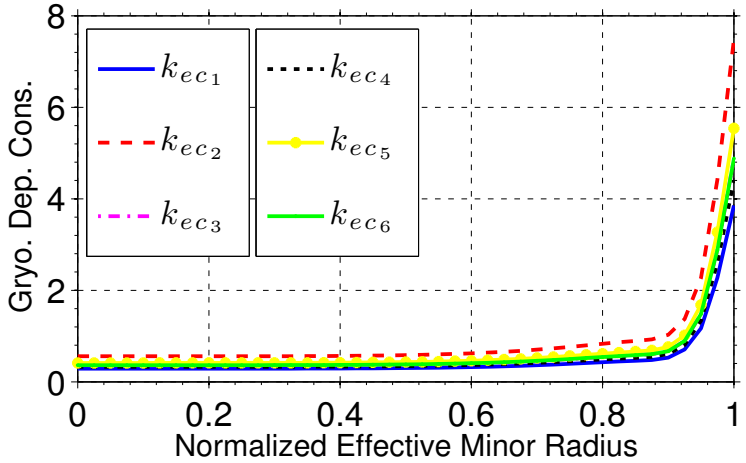
Gryo. Dep. Cons.
k_{ec_1}
k_{ec_2}
k_{ec_3}
k_{ec_4}
k_{ec_5}
k_{ec_6}
Normalized Effective Minor Radius

(f)

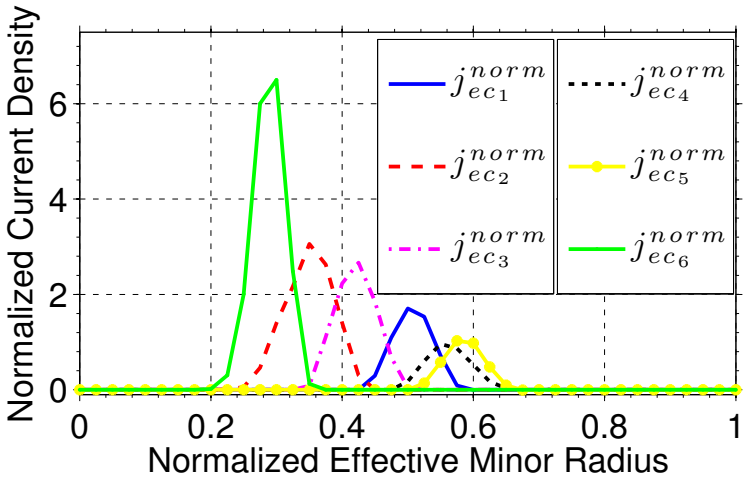
Normalized Current Density
Normalized Effective Minor Radius
$j_{ec_1}^{norm}$
$j_{ec_2}^{norm}$
$j_{ec_3}^{norm}$
$j_{ec_4}^{norm}$
$j_{ec_5}^{norm}$
$j_{ec_6}^{norm}$

(g)

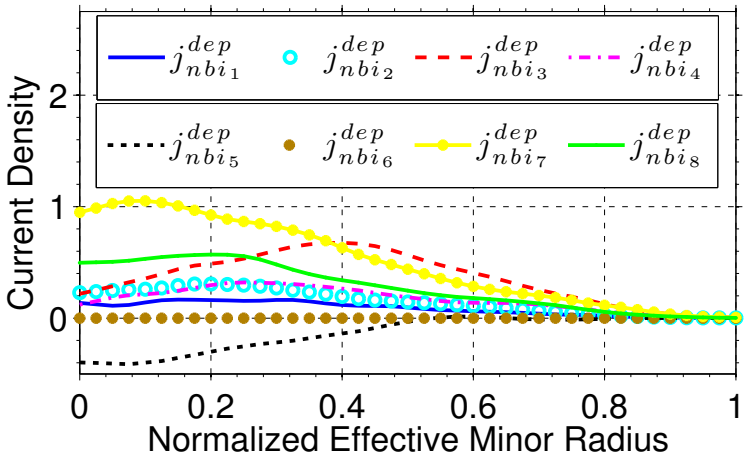
Current Density
Normalized Effective Minor Radius
$j_{nbi_1}^{dep}$
$j_{nbi_2}^{dep}$
$j_{nbi_3}^{dep}$
$j_{nbi_4}^{dep}$
$j_{nbi_5}^{dep}$
$j_{nbi_6}^{dep}$
$j_{nbi_7}^{dep}$
$j_{nbi_8}^{dep}$

(h)

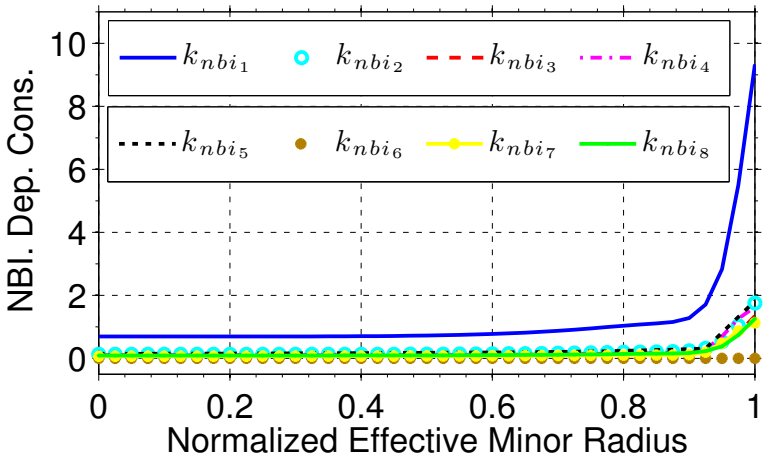
NBI. Dep. Cons.
Normalized Effective Minor Radius
k_{nbi_1}
k_{nbi_2}
k_{nbi_3}
k_{nbi_4}
k_{nbi_5}
k_{nbi_6}
k_{nbi_7}
k_{nbi_8}

(i)

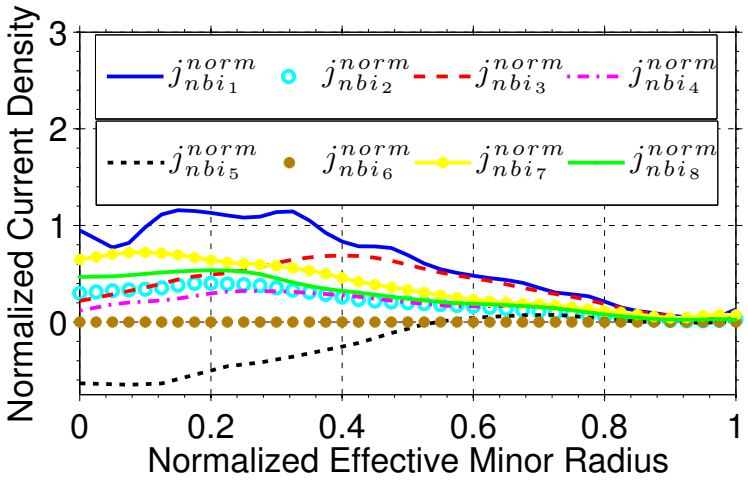

(j)

Figure 6.6: Off-axis Current Drive Scenarios: (a) Magnetic Configuration Parameters, (b) Bootstrap Current Coefficients, (c) Temperature Coefficient k_{T_e} ($10^9 m^{-3} A^{-1} W^{-1/2}$) & Resistivity Coefficient k_{sp} ($10^{-8} \Omega m keV^{3/2}$), (d) Electron Density Profile n_e^{prof} (m^{-3}) & Electron Temperature Profile T_e^{prof} (keV), (e) Reference Gyrotron Current Deposition Profiles $j_{ec_i}^{dep}$ ($10^5 Am^{-2}$), (f) Gyrotron Model Coefficients k_{ec_i} ($10^{14} m^{-3} keV^{-1} W^{-1}$), (g) Normalized Gyrotron Deposition Profile $j_{ec_i}^{norm}$ ($10^{18} Am^{-5} keV^{-1} W^{-1}$), (h) Reference NBI Current Deposition Profiles $j_{nbi_i}^{dep}$ ($10^5 Am^{-2}$), (i) NBI Model Coefficients k_{nbi_i} ($10^{14} m^{-3} keV^{-1} W^{-1}$), (j) Normalized NBI Deposition Profile $j_{nbi_i}^{norm}$ ($10^{18} Am^{-5} keV^{-1} W^{-1}$).

scenario that has energy and particle transport barriers near the plasma boundary. The parameters related to the magnetic configuration of the plasma equilibrium are shown in Figure 6.6 (a) and (b), the reference profiles for the various models are shown in Figure 6.6 (d), (e) and (h), the normalizing constants are shown in Figure 6.6 (c), (f) and (i), and the normalized auxiliary current deposition profiles are shown in Figure 6.6 (g) and (j). The other model constants are $B_{\phi,0}$=1.65 T, R_0=1.78 m, ρ_b=0.82 m, and Z_{eff}=1.49. Comparing with the on-axis current drive scenarios, the beam-line optical axes of 150L and 150R in the off-axis current drive scenarios are inclined up to 16.5° (shown in Figure 3.5), while the other beam-line optical axes are unchanged. The introduction of the off- axis beams provides more heating in the mid-radius of the tokamak. In Figure 6.6 (h) and (j), the peaks of $j_{nbi_3}^{dep}$ and $j_{nbi_4}^{dep}$ move

from $\hat{\rho} \approx 0.1$ to $\hat{\rho} \approx 0.4$.

The steady state gains of the off-axis first-principles-driven model for the ι profile are shown in Figure 6.7. In the figure, the steady state response $\Delta\bar{\iota}$ to unitary changes in the various inputs is plotted, where the dimensionless parameter Δu_n is given by 0.1, ΔP_{ec_i} and ΔP_{nbi_j} are given by 1 MW (co-injection is "+" and counter injection is "-") and ΔI_p is given by 0.1 MA, where $i \in \{1, 2, \cdots, 6\}$ and $j \in \{1, 2, \cdots, 8\}$. The plasma current I_p is the most capable actuator in adjusting the magnetic profile in absolute terms (shown in Figure 6.7 (a.1)). The steady state $\Delta\bar{\iota}$ response to the time evolution of the electron density u_n is shown in Figure 6.7 (a.2). The differences of the spatial injection positions of gyrotrons (shown in Figure 6.6 (e) and (g)) lead to the differences of the steady-state $\Delta\bar{\iota}$ response in Figure 6.7 (a.3)-(a.5) and (b1)-(b3). The co-injection and counter-injection beams affect the profile in different directions in agreement with prior experiments and on-axis model.

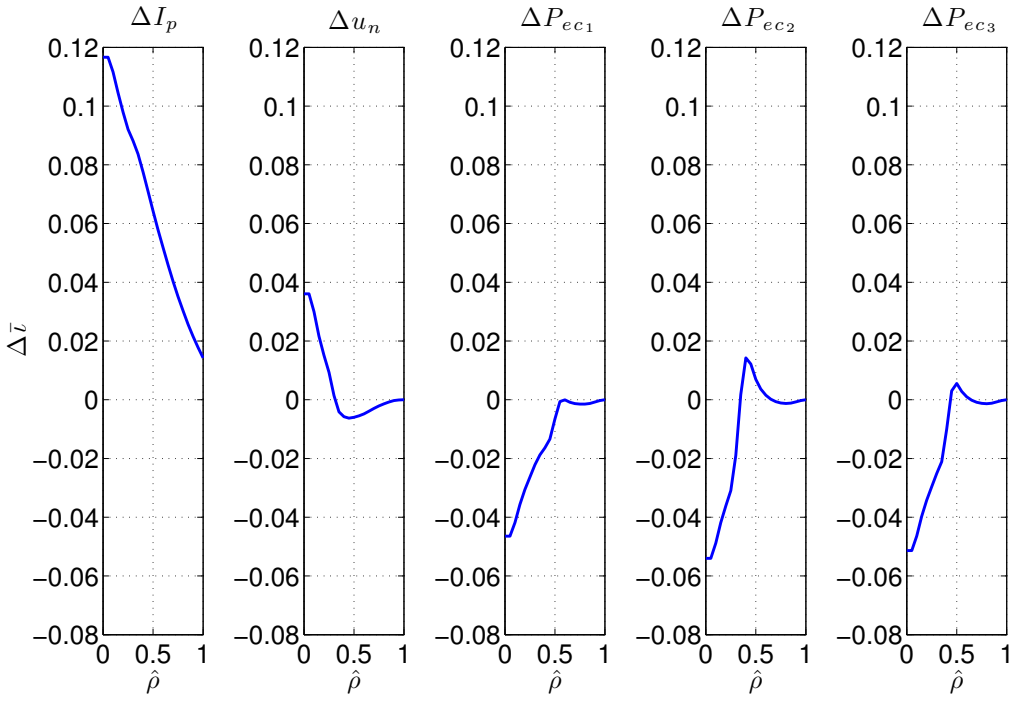

(a)

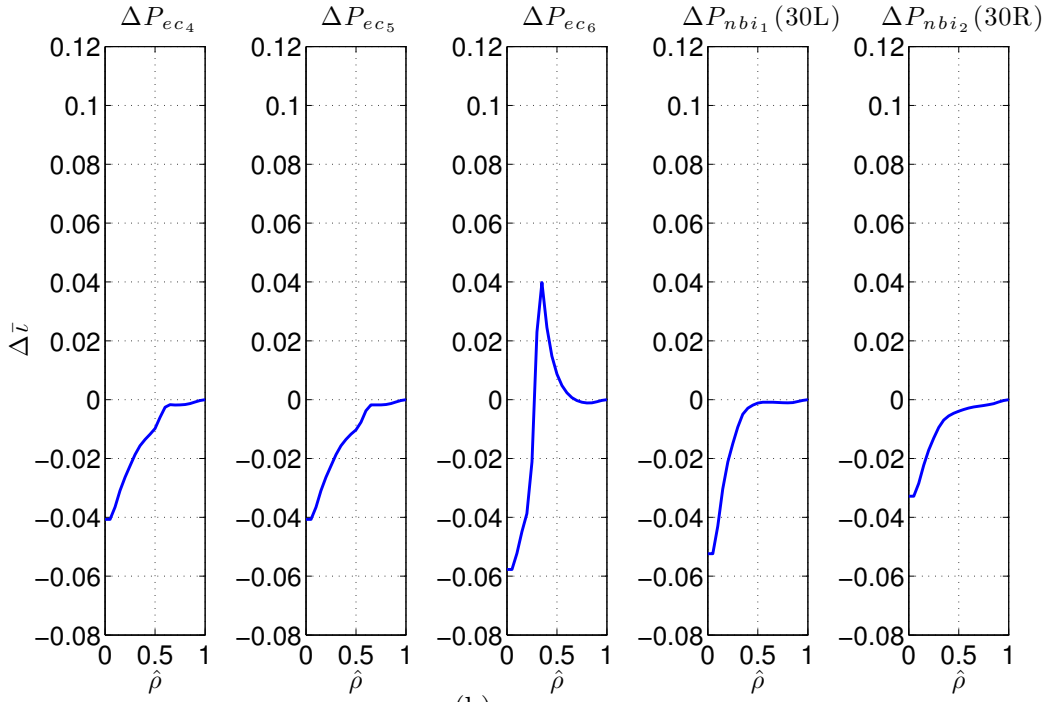

(b)

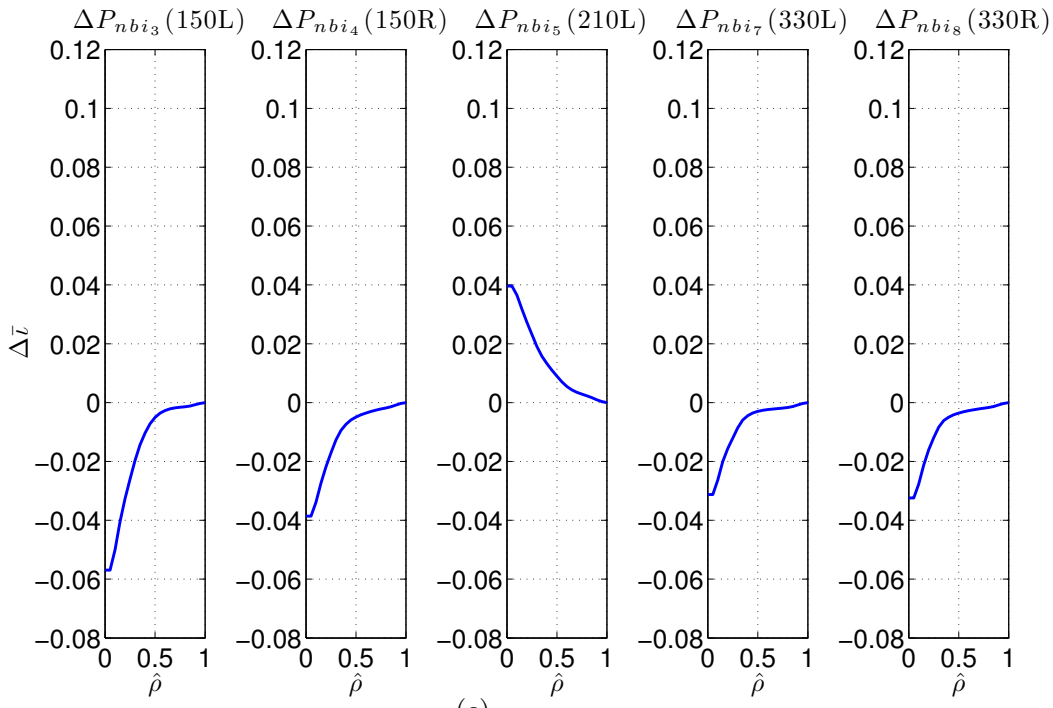

(c)

Figure 6.7: Steady state gains for the ι profile response for off-axis current drive scenarios. Note: the inputs are ΔP_{ec_i} (1 MW), ΔP_{nbi_j} (1 MW), Δu_n (0.1), and ΔI_p (0.1 MA), where $i \in \{1, 2, \cdots, 6\}$ and $j \in \{1, 2, \cdots, 8\}$.

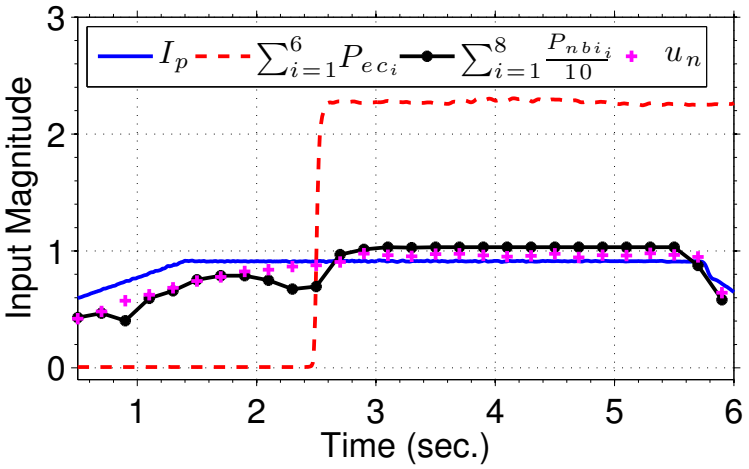

Figure 6.8: Control inputs applied during first-principles-driven model simulation and DIII-D shot #147394 (current in MA and power in MW).

6.6.1 Comparison between First-principles-driven Model Prediction and Experimental Data

We now describe a study that compares the evolution of the plasma parameters predicted by the first-principles-driven (FPD) model to the experimentally achieved plasma parameters in DIII-D off-axis shot #147394. The inputs (total plasma current I_p, total gyrotron launcher powers $\sum_{i=1}^{6} P_{ec_i}$, total neutral beam injection powers $\sum_{i=1}^{8} P_{nbi_i}$, and density regulation u_n) applied during both the simulation and the experiment are shown in Figure 6.8, time traces of ψ at various normalized effective minor radii are shown in Figure 6.9, and a comparison of the first-principles-driven model predicted and the experimentally achieved ψ and q profiles at various time instances is shown in Figure 6.10 (a)-(d) and Figure 6.10 (e)-(h), respectively. As shown in the figures, the trends of the first-principles-driven model predicted plasma parameters show good agreement with the experimental results in the off-axis current drive scenarios.

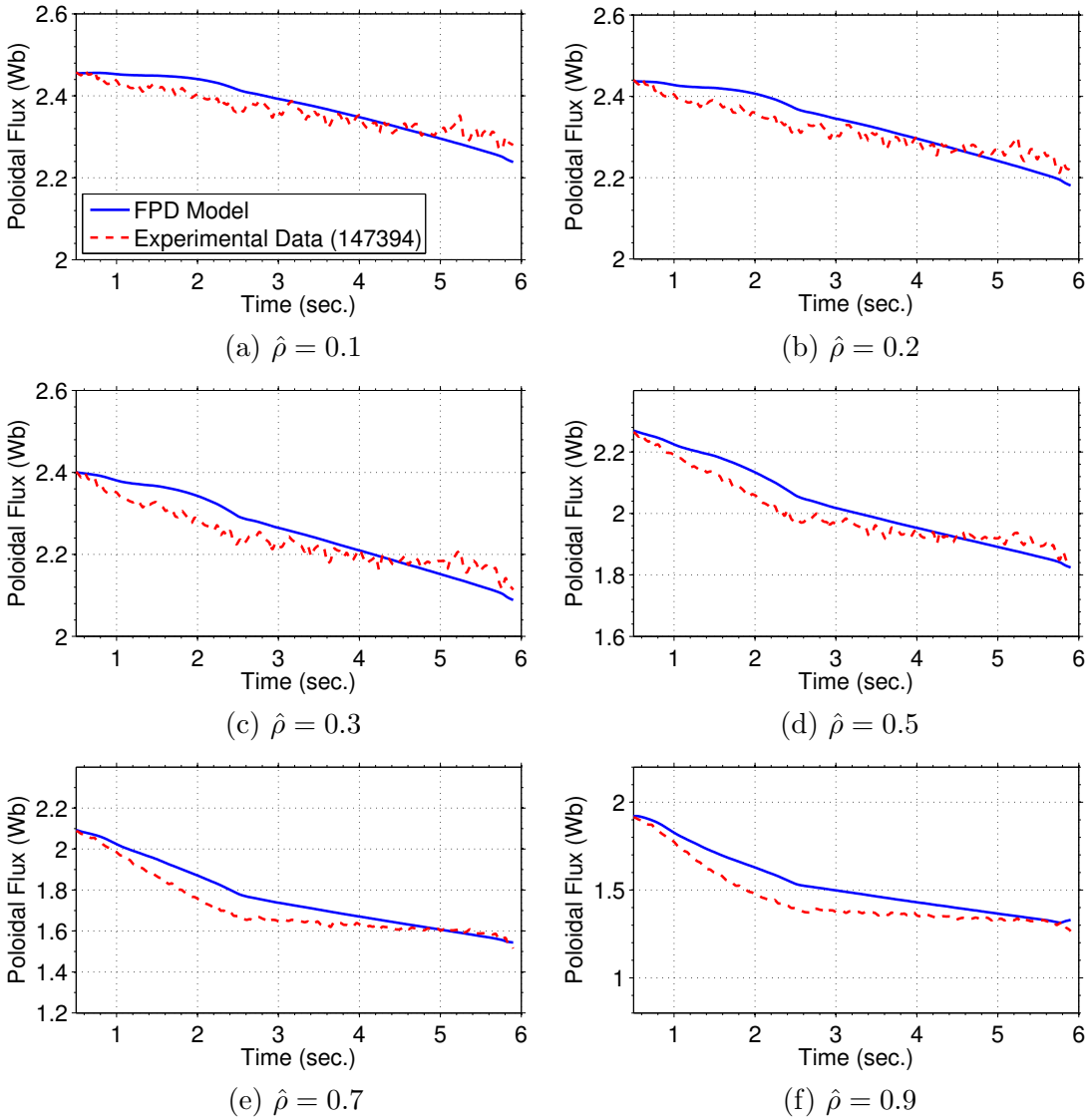

(a) $\hat{\rho} = 0.1$ (b) $\hat{\rho} = 0.2$

(c) $\hat{\rho} = 0.3$ (d) $\hat{\rho} = 0.5$

(e) $\hat{\rho} = 0.7$ (f) $\hat{\rho} = 0.9$

Figure 6.9: Time trace of poloidal magnetic flux ψ at various spatial locations. Note: first-principles-driven model (solid) and experimentally achieved (dash).

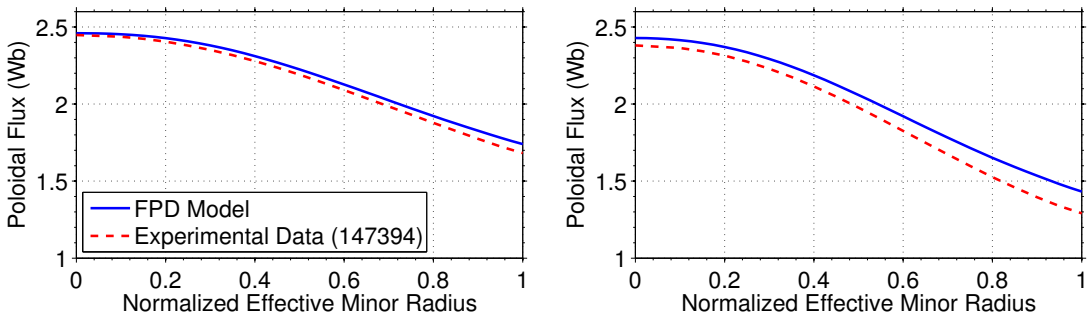

(a) $t = 1.0$ sec.

(b) $t = 2.5$ sec.

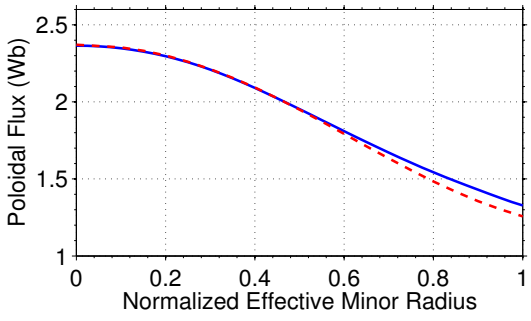

(c) $t = 4.0$ sec.

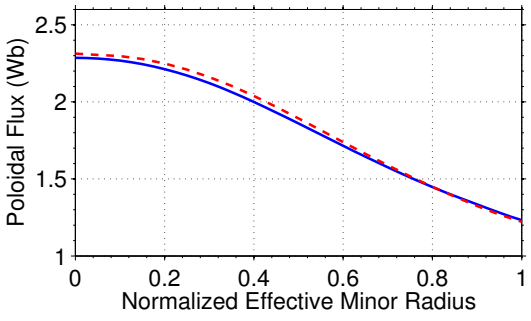

(d) $t = 5.5$ sec.

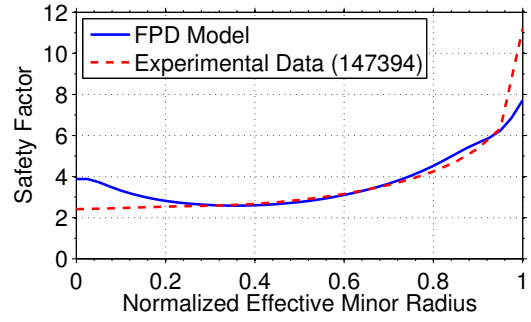

(e) $t = 1.0$ sec.

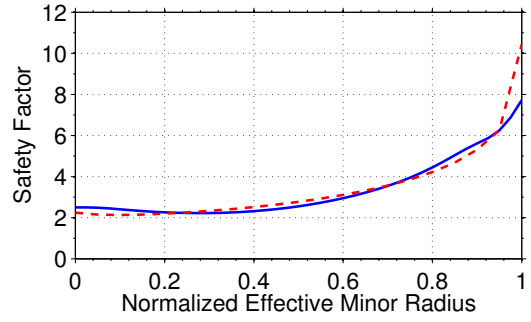

(f) $t = 2.5$ sec.

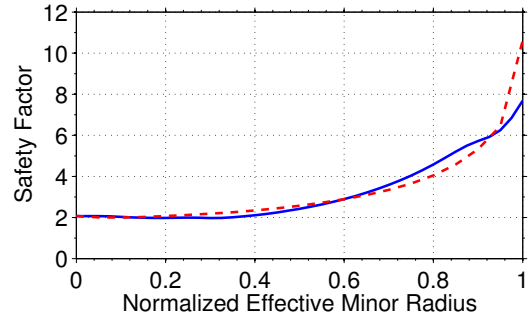

(g) $t = 4.0$ sec.

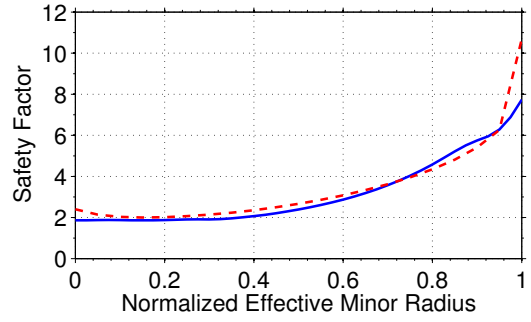

(h) $t = 5.5$ sec.

Figure 6.10: Poloidal magnetic flux profile $\psi(\hat{\rho})$ (a)-(d) and safety factor profile $q(\hat{\rho})$ (e)-(h) at various time instances.

6.7 Conclusion

The author develops a general simplified physics-based modeling approach to convert the first-principles physics model that describes the current profile evolution in the tokamak into a form suitable for control design, with emphasis on high performance operating scenarios. The first-principles-driven models' prediction capabilities are demonstrated by comparing the prediction to experimental data for DIII-D in the on-axis and off-axis current drive scenarios. It is important to note we are modeling-for-control, consequently, the model needs only to capture the dominant physics of the system dynamics as one of the main characteristics of feedback is the ability to deal with model uncertainties. The tailored models are employed to design feedback control algorithms to control the current profile evolution in H-mode scenarios in DIII-D [54], which will be discussed in the Chapter 7. Experimental testing of the designed controllers is part of our future work and will help assess the true requirements for model accuracy.

Chapter 7

First-principles-driven Control of the Rotational Transform Profile in High Performance Discharges in the DIII-D Tokamak

7.1 Introduction

In this chapter, we extend the previous work [48, 49, 50, 51] by developing first-principles-driven feedback controllers for current profile in high-confinement (H-mode) scenarios. Firstly, the governing infinite dimensional PDE (6.14) is approximated by a finite dimensional system of ordinary differential equations to facilitate the synthesis of a feedback controller by employing a truncated Taylor series expansion in space. While the state of the reduced-order model is linearized around a given feedforward operating trajectory, the control input nonlinearities are preserved through a nonlinear transformation, and a time-varying state-space representation of the deviation

dynamics is derived. Secondly, a singular value decomposition of the static gain matrix of the nominal plant model is employed to determine which linear combinations of the plant outputs we can effectively control. The mixed sensitivity H_∞ control method is applied to synthesize a closed-loop controller that minimizes the reference tracking error and rejects external disturbances with minimal control energy. Finally, the control performances of the first-principles-driven model-based controller and a previously designed data-driven model-based controller in Section 4.2 are compared. The first-principles-driven controller shows the potential for improving the closed-loop performance, especially near the center of the plasma.

This chapter is organized as follows. In Section 7.2, a first-principles-driven model for the plasma rotational transform ι profile evolution is presented. In Section 7.3, the PDE model is linearized around the feedforward trajectories of the system. Based on the linear model, the design of the plasma control algorithm is described. Closed-loop simulated and the comparison results are presented in Section 7.4. Section 7.5 states the conclusions.

7.2 Plasma Rotational Transform Profile Evolution Model

By combining the control-oriented models (6.3)-(6.9) with the magnetic diffusion equation (6.1), the desired first-principles-driven, control-oriented model of the poloidal magnetic flux profile evolution is obtained in (6.14). The rotational transform ι profile, defined as $\iota(\hat{\rho}, t) = -d\Psi/d\Phi$, is written as

$$\iota(\hat{\rho}, t) = -\frac{d\Psi}{d\Phi} = -\frac{2\pi \frac{\partial \psi}{\partial \hat{\rho}}}{\frac{\partial \Phi}{\partial \rho}\frac{\partial \rho}{\partial \hat{\rho}}} = -\frac{\theta}{B_{\phi,0}\rho_b^2 \hat{\rho}} \triangleq C_{FP}(\hat{\rho})\theta, \tag{7.1}$$

where $\theta(\hat{\rho},t) = \frac{\partial\psi}{\partial\hat{\rho}}(\hat{\rho},t)$ is the gradient of the poloidal flux profile. Therefore, we develop a model for θ, so we can control the ι profile evolution. Using the chain rule, (6.14) is expanded as

$$\frac{\partial\psi}{\partial t} = \frac{f_1 u_1}{\hat{\rho}}(\hat{\rho}\frac{\partial\psi}{\partial\hat{\rho}}\frac{dD_\psi}{d\hat{\rho}} + D_\psi\frac{\partial\psi}{\partial\hat{\rho}} + \hat{\rho}D_\psi\frac{\partial^2\psi}{\partial\hat{\rho}^2}) + \sum_{i=2}^{15} f_i u_i + (\frac{\partial\psi}{\partial\hat{\rho}})^{-1} f_{16} u_{16}. \qquad (7.2)$$

By differentiating (7.2) with respect to $\hat{\rho}$, the PDE governing the evolution of $\theta(\hat{\rho},t)$ is found to be

$$\frac{\partial\theta}{\partial t} = (h_{11}\frac{\partial^2\theta}{\partial\hat{\rho}^2} + h_{12}\frac{\partial\theta}{\partial\hat{\rho}} + h_{13}\theta)u_1(t) + \sum_{i=2}^{15}\frac{df_i}{d\hat{\rho}}u_i(t) + (\frac{1}{\theta}\frac{df_{16}}{d\hat{\rho}} - \frac{f_{16}}{\theta^2}\frac{\partial\theta}{\partial\hat{\rho}})u_{16}(t), \quad (7.3)$$

with boundary conditions

$$\theta(0,t) = 0, \qquad \theta(1,t) = -k_{17}u_{17}(t),$$

where $h_{11} = f_1 D_\psi$, $h_{12} = \frac{f_1 D_\psi}{\hat{\rho}} + f_1' D_\psi + 2f_1 D_\psi'$, and $h_{13} = f_1' D_\psi' + f_1 D_\psi'' + \frac{f_1' D_\psi}{\hat{\rho}} + \frac{f_1 D_\psi'}{\hat{\rho}} - \frac{f_1 D_\psi}{\hat{\rho}^2}$.

7.3 Control System Design

A general framework for real-time feedforward+feedback control of magnetic plasma profiles has been implemented in the DIII-D PCS [51]. The controller is implemented as a discrete-time state-space system with a sampling time of 20 ms. This sampling time is set based on the modulation of the motional Stark effect (MSE) beam used to obtain ι profile measurements in real-time. In this section, a multi-input-multi-output (MIMO) feedback controller based on the first-principles-driven model (7.1)-(7.3) is proposed for the regulation of the evolution of the ι profile on DIII- D.

7.3.1 Model Reduction and Linearization

The model (7.3) is discretized in space using a truncated Taylor series expansion to approximate the spatial derivatives to construct a reduced-order model suitable for control design. The non-dimensional domain of interest, $[0, 1]$, is represented as l nodes, and the spacing between the nodes, $\Delta\hat{\rho}$, is defined as $\Delta\hat{\rho} = 1/(l-1)$. Central finite difference spatial derivative approximations of $O(\Delta\hat{\rho}^2)$ are used in the interior node region, $2 \leq i \leq (l-1)$. The reduced-order discretized model is expressed as

$$\dot{X} = W(X, u), \tag{7.4}$$

where $X = [\theta_2, \theta_3, \cdots, \theta_{l-1}]^T$, $u = [u_1, u_2, \cdots, u_{17}]^T$, and W is a nonlinear function of the states and inputs. Let X_{FF}, u_{FF} and y_{FF} be the feedforward trajectories of the states, inputs and outputs, and these feedforward trajectories satisfy

$$\dot{X}_{FF} = W(X_{FF}, u_{FF}), \quad y_{FF} = C_{FP}X_{FF}. \tag{7.5}$$

By defining the perturbation variables $x = X - X_{FF}$ and $\Delta u = u - u_{FF}$, a linear model suitable for tracking control design can be obtained. Inserting the perturbation variables into (7.4) results in

$$\dot{X}_{FF} + \dot{x} = W|_{X_{FF},u_{FF}} + \frac{\partial W}{\partial X}|_{X_{FF},u_{FF}}x + \frac{\partial W}{\partial u}|_{X_{FF},u_{FF}}\Delta u + \cdots$$

Ignoring the higher order terms, a series of linear models are expressed as:

$$\dot{x} = \frac{\partial W}{\partial X}|_{X_{FF},u_{FF}}x + \frac{\partial W}{\partial u}|_{X_{FF},u_{FF}}\Delta u = A_{FP}(t)x + B_{FP}(t)\Delta u.$$

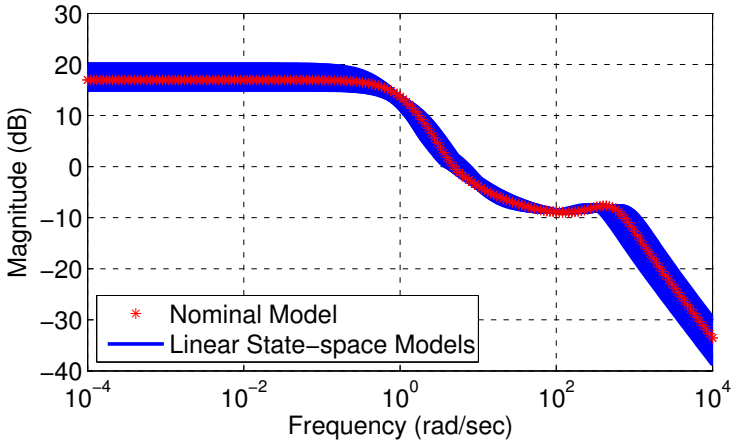

Figure 7.1: Frequency Study of First-principles-driven Plasma Models

By defining the outputs $\Delta y = y - y_{FF}$, we can obtain

$$y_{FF} + \Delta y = C_{FP}(X_{FF} + x).$$

Therefore, we obtain a linear time-variant, dynamic, state-space model, i.e.,

$$\dot{x} = A_{FP}(t)x + B_{FP}(t)\Delta u, \quad \Delta y = C_{FP}x. \tag{7.6}$$

A frequency study of the family of the state-space models (7.6), which compares the maximum singular values of the time-variant ι profile models, shows that the models do not have a large magnitude difference, as shown in Figure 7.1. Based on this frequency study, the model at 1.75 s is chosen as the nominal model, denoted as P_{FP_0} and expressed as

$$\dot{x} = A_{FP_0}x + B_{FP_0}\Delta u, \quad \Delta y = C_{FP_0}x. \tag{7.7}$$

The feedback controller is designed based on (7.7).

7.3.2 Singular Value Decomposition

Assuming a constant target $\Delta\bar{y}_{tar}$ and closed-loop stabilization, the system will reach steady state as $t \to \infty$. It is possible to define $\Delta\bar{y} = \lim_{t\to\infty} \Delta y(t)$, $\Delta\bar{u} = \lim_{t\to\infty} \Delta u(t)$, and $\bar{e} = \lim_{t\to\infty} e(t) = \Delta\bar{y}_{tar} - \Delta\bar{y}$. Therefore, the closed-loop system is specified by

$$\Delta\bar{y} = \bar{P}_{FP_0}\Delta\bar{u} = -C_{FP_0}A_{FP_0}^{-1}B_{FP_0}\Delta\bar{u}, \quad \Delta\bar{u} = \bar{\hat{K}}\bar{e},$$

where $P_{FP_0}(s)$ is the transfer function of (7.7) and $\bar{P}_{FP_0} = P_{FP_0}(0)$, and $\hat{K}(s)$ represents the transfer function of the to-be-designed controller and $\bar{\hat{K}} = \hat{K}(0)$.

In order to weight the control effort and tracking error, two positive definite weighting matrices $R \in \Re^{m\times m}$ and $Q \in \Re^{p\times p}$ are introduced to the system, where $p = l - 2$ is the number of outputs and m is the number of inputs. We then define the "weighted" steady-state transfer function, and its singular value decomposition (SVD) as $\tilde{P}_{FP_0} = Q^{1/2}\bar{P}_{FP_0}R^{-1/2} = USV^T$, where $S = \mathrm{diag}(\sigma_1, \sigma_2, \cdots, \sigma_m) \in \Re^{m\times m}$, $U \in \Re^{p\times m}$ ($U^TU = I$), and $V \in \Re^{m\times m}$ ($V^TV = VV^T = I$). By invoking the properties of the SVD, the matrix $Q^{-1/2}US$ defines a basis of the steady-state output values, and the matrix $R^{-1/2}V$ defines a basis of the steady-state input values. By defining $\Delta\bar{y}^* = S^{-1}U^TQ^{1/2}\Delta\bar{y}$, $\Delta\bar{y}^*_{tar} = S^{-1}U^TQ^{1/2}\Delta\bar{y}_{tar}$, and $\Delta\bar{u}^* = V^TR^{1/2}\Delta\bar{u}$, a square decoupled system is obtained:

$$\Delta\bar{y}^* = S^{-1}U^TQ^{1/2}\Delta\bar{y} = S^{-1}U^TQ^{1/2}Q^{-1/2}USV^TR^{1/2}\Delta\bar{u} = \Delta\bar{u}^*.$$

Substituting these expressions into the performance index $\bar{J} = \bar{e}Q\bar{e}^T$, the steady state cost function is obtained as:

$$\bar{J} = (\Delta\bar{y}^*_{tar} - \Delta\bar{y}^*)^TS^2(\Delta\bar{y}^*_{tar} - \Delta\bar{y}^*) = \sum_{i=1}^{m}\sigma_i^2(\Delta\bar{y}^*_{tar_i} - \Delta\bar{y}^*_i)^2.$$

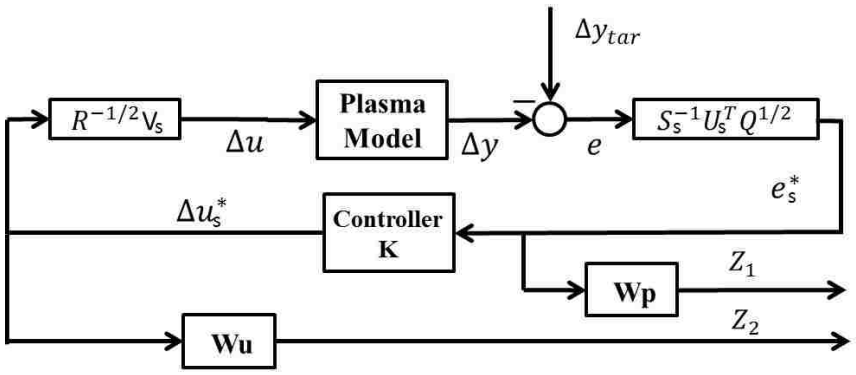

Figure 7.2: H_∞ Control Formulation

It is usually the case where $\sigma_1 > \cdots \sigma_k \gg \sigma_{k+1} > \cdots > \sigma_m > 0$. To avoid spending a lot of control effort for a marginal improvement of the cost function value, we partition the singular value set into significant singular values S_s and negligible singular values S_n. We can write $U = \begin{bmatrix} U_s & U_n \end{bmatrix}$, $V = \begin{bmatrix} V_s & V_n \end{bmatrix}$, $S = \text{diag}(S_s, \ S_n)$, and approximate the cost function $\bar{J}$ by

$$\bar{J}_s = \sum_{i=1}^{k} \sigma_i^2 (\Delta\bar{y}^*_{tar_i} - \Delta\bar{y}^*_i)^2 = (\Delta\bar{y}^*_{tar_s} - \Delta\bar{y}^*_s)^T S_s^2 (\Delta\bar{y}^*_{tar_s} - \Delta\bar{y}^*_s),$$

where $\Delta\bar{y}^*_{tar_s} = S_s^{-1}U_s^TQ^{1/2}\Delta\bar{y}_{tar}$, $\Delta\bar{y}^*_s = S_s^{-1}U_s^TQ^{1/2}\Delta\bar{y}$, $\bar{e}^*_s = \Delta\bar{y}^*_{tar_s} - \Delta\bar{y}^*_s$ and $\Delta\bar{u}^*_s = V_s^TR^{1/2}\Delta\bar{u}$. The matrix bases reduce to $Q^{-1/2}U_sS_s$ and $R^{-1/2}V_s$, and the decoupled system,

$$P_{FP_{DC}} = S_s^{-1}U_s^TQ^{1/2}P_{FP_0}R^{-1/2}V_s, \tag{7.8}$$

represents a one-to-one relationship between the inputs $\Delta\bar{u}^*_s$ and the outputs $\Delta\bar{y}^*_s$. More details of SVD can be found in Section 4.2.2.

7.3.3 Design of Mixed Sensitivity H_∞ Controller

The mixed sensitivity H_∞ technique is used to design the plasma ι profile controller, which can minimize the tracking error $e(t)$ while using as little feedback control ef-

fort as possible. The structure of the proposed controller is shown in Figure 7.2, where K is the feedback controller, Δu_d is the input disturbance, $Z_1 = W_p e_s^*$, $Z_2 = W_u \Delta u_s^*$, and W_p and W_u are two frequency-dependent weighting functions. The feedback system shown in Figure 7.2, is expressed in the conventional $P^* - K$ control framework. The generalized plant P^* is the transfer function from the input signals $[\Delta y_{tar_s}^{*T},\ \Delta u_s^{*T}]^T$ to the output signals $[Z_1^T,\ Z_2^T,\ e_s^{*T}]^T$, where $\Delta u_s^* = V_s^T R^{1/2} \Delta u$, $\Delta y_{tar_s}^* = S_s^{-1} U_s^T Q^{1/2} \Delta y_{tar}$, $\Delta y_s^* = S_s^{-1} U_s^T Q^{1/2} \Delta y$, and $e_s^* = \Delta y_{tar_s}^* - \Delta y_s^*$. The closed-loop transfer function is given by the lower linear fractional transformation (LFT), i.e.,

$$T_{zw} = F_l(P^*, K) = \begin{bmatrix} W_p M_s \\ W_u K M_s \end{bmatrix}, \tag{7.9}$$

where the sensitivity transfer function M_s is defined as $M_s = (I + P_{FP_{DC}} K)^{-1}$. Our purpose is to seek a controller $K(s)$ that stabilizes the system and minimizes the H_∞ norm of the transfer function T_{zw}, i.e.,

$$\min_{K(s)} \|T_{zw}(P^*, K)\|_\infty = \min_{K(s)} (\sup_\omega \bar{\sigma}[T_{zw}(P^*, K)(j\omega)]),$$

where $\bar{\sigma}$ represents the maximum singular value. This statement defines a mixed sensitivity H_∞ control problem, and the goal is to minimize both the tracking error ($W_p M_s$) and the control effort ($W_u K M_s$) at the same time. The weighting functions $W_p = \text{diag}\{W_{p_i}\}$ and $W_u = \text{diag}\{W_{u_i}\}$ are

$$W_{p_i}(s) = (\frac{s/\sqrt{M_{p_i}} + \omega_{p_i}}{s + \omega_{p_i}\sqrt{H_{p_i}}})^2, \quad W_{u_i}(s) = (\frac{s + \omega_{u_i}\sqrt{H_{u_i}}}{s/\sqrt{M_{u_i}} + \omega_{u_i}})^2,$$

where the coefficients M_{p_i}, ω_{p_i}, H_{p_i}, M_{u_i}, ω_{u_i}, and H_{u_i}, for $i = 1, 2, \cdots, k$, are design parameters in the H_∞ control synthesis. Finally, the overall plasma rotational

transform ι profile controller can be written as

$$\hat{K}(s) = \frac{\Delta U(s)}{E(s)} = R^{-1/2} V_s K(s) S_s^{-1} U_s^T Q^{1/2}, \tag{7.10}$$

where $\Delta U(s)$ and $E(s)$ denotes the Laplace transform of Δu and e respectively.

7.3.4 Nonlinear Transformation

The outputs of the feedforward+feedback controller now need to be converted to the physical actuator signals, I_p, P_{ec_i}, P_{nbi_j}, and u_n, and we employ the inverse nonlinear transformations of the control inputs of (7.3) to accomplish this. However, there are only eight beams in NBI, six gyrotrons in EC, plasma current I_p and density evolution parameter u_n, totalling sixteen independent actuators in DIII-D, but there are seventeen inputs in (7.3). Therefore, it is impossible to obtain a unique relationship between the u in (7.3) and physical actuator signals.

There are two different types of NBI beams in DIII-D: co-current and counter-current injection, which allows an important capability of mixed co-injection and counter-injection to heat the plasma without driving current. Based on this capability, a new variable, denoted as balanced-beam NBI power P_{BL}, is introduced in the model. The beam power P_{nbi_i} is therefore expressed as $P_{nbi_i} = P_{nbi_{i,CD}} + \gamma_{nbi_i} P_{BL}$, with $i \in \{1, 2, \cdots, 8\}$, where $P_{nbi_{i,CD}}$ is the portion of the total NBI power that drives current and γ_{nbi_i} is the fraction of balanced-beam power contributed by each beam. The objective is to determine the γ_{nbi_i} for each beam that minimizes the non-inductive current drive by P_{BL}. This defines a constrains linear optimal control problem,

$$\min_{\gamma_{nbi_i}} J_{BL}, \;\; \text{s.t.} \;\; \sum_{i=1}^{8} \gamma_{nbi_i} = 1, \tag{7.11}$$

where J_{BL} is a cost function, defined as

$$J_{BL} = \int_0^1 (\sum_{i=1}^{8} \hat{j}_{nbi_i}^{dep}(\hat{\rho})\gamma_{nbi_i} P_{BL})^2 d\hat{\rho}, \tag{7.12}$$

where $\hat{j}_{nbi_i}^{dep}$ is the normalized deposition profile, defined as $\hat{j}_{nbi_i}^{dep} = j_{nbi_i}^{dep}/P_{nbi_i}$. The parameter $j_{nbi_i}^{dep}$ is a reference deposition profile for the i^{th} beam of NBI.

The total power P_{tot} in DIII-D is expressed as $P_{tot} = P_{ohm} + \sum_{i=1}^{6} P_{ec_i} + \sum_{i=1}^{8} P_{nbi_i} - P_{rad}$. The ohmic power P_{ohm} and the radiated power P_{rad} are typically small, and can be ignored compared with the injected power from NBI and EC. Therefore, the total power P_{tot} is written as

$$P_{tot} \approx \sum_{i=1}^{6} P_{ec_i} + \sum_{i=1}^{8} P_{nbi_i} = \sum_{i=1}^{6} P_{ec_i} + \sum_{i=1}^{8} P_{nbi_{i,CD}} + P_{BL}.$$

The inverse nonlinear transformation between the inputs in (7.3) and the physical acturators are:

$$I_p = u_{17}, \quad P_{ec_i} = \frac{u_{i+1}u_{16}}{u_1^{2/3}}, \quad P_{nbi_{j,CD}} = \frac{u_{j+7}u_{16}}{u_1^{2/3}},$$

$$P_{BL} = (\frac{u_{16}}{u_1 u_{17}})^2 - \sum_{k=2}^{15} \frac{u_k u_{16}}{u_1^{2/3}}, \quad u_n = \frac{u_{16}}{u_1^{1/3}}, \tag{7.13}$$

where $u_l = u_{FF_l} + \Delta u_l$, $i \in \{1, 2, \cdots, 6\}$, $j \in \{1, 2, \cdots, 8\}$, and $l \in \{1, 2, \cdots, 17\}$.

7.3.5 Design of Anti-windup Compensator

At the moment of designing the H_∞ controller (7.10), the actuator saturations were not considered. As a result of saturation, the controller output does not drive the plant input and, as a consequence, the states of the controller may wind up because the plant does not respond as expected. An anti-windup compensator is needed to

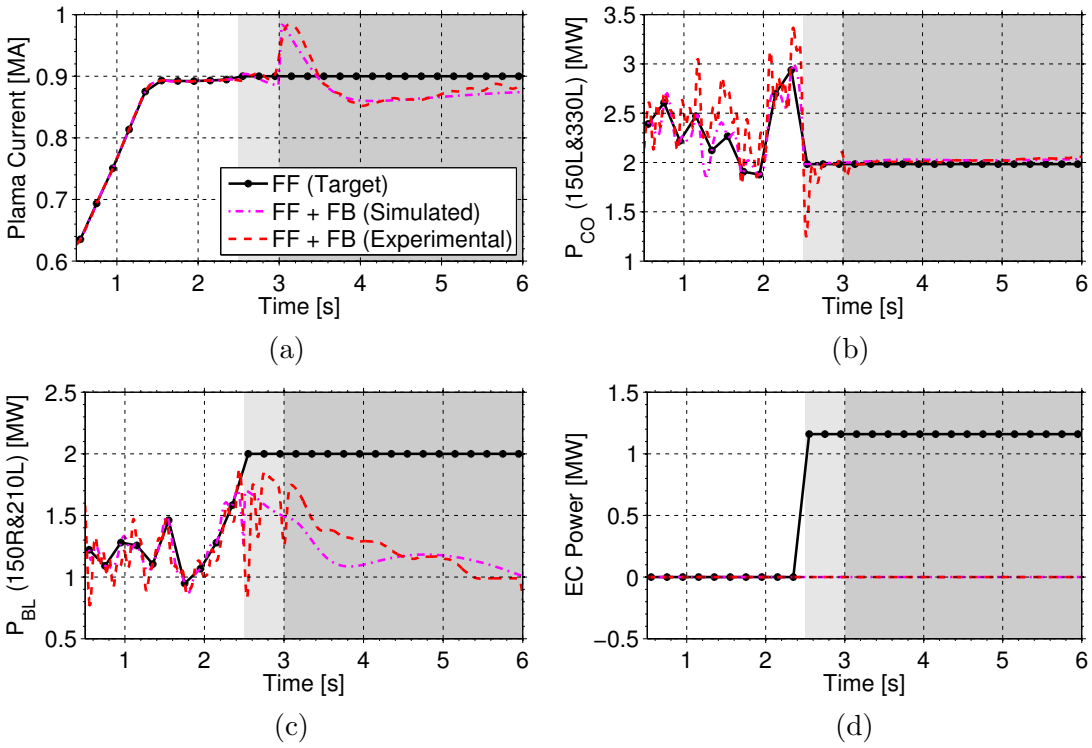

Figure 7.3: Rotational transform ι profile reference, closed-loop (data-driven model-based controller) simulated & experimental inputs (shot # 147704). Light-gray background: feedback on-disturbance off, dark-gray background: feedback on-disturbance on, white background: feedback off-disturbance off.

minimize the adverse effect of any control input saturation, and the ι profile controller in DIII-D is augmented with an anti-windup compensator. Details of the anti-windup compensation can be obtained from Section 4.2.5.

7.4 Closed-loop Simulations and Comparison

7.4.1 Model Verification

The objective in developing the simplified first-principles-driven model (6.14) is to capture the dominant physics that describe how the control actuators affect the plasma parameters, and hence the current profile evolution. Therefore, the actual

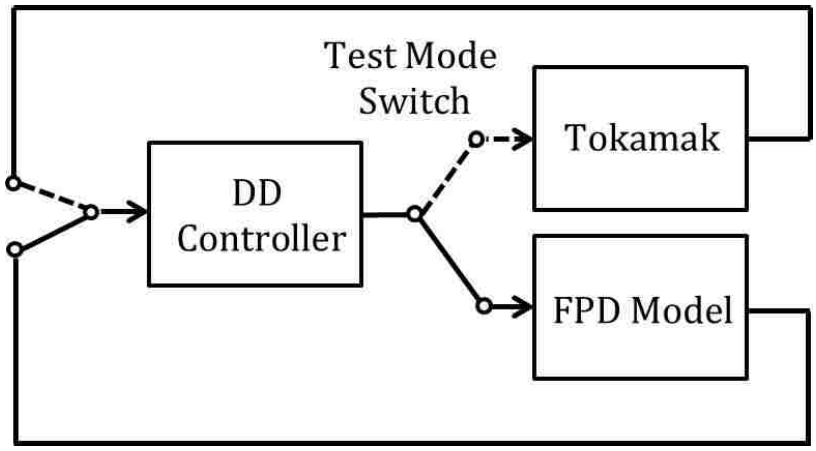

Figure 7.4: Model Verification Formulation.

controlled variable profile evolution in DIII-D may differ slightly from the evolution predicted by the PDE model (6.14). A model validation procedure was carried out by comparing the model prediction with experimental data. In Chapter 3, a data-driven model-based ι profile controller was designed for H-mode scenarios in DIII-D, and was tested experimentally (shot # 147704). Therefore a closed-loop simulation using the first-principles-driven (FPD) model and the experimentally tested data-driven (DD) controller is executed with the same conditions that were set in shot 147704. The model validation procedure is shown in Figure 7.4. We set the feedforward inputs (solid-dotted black lines in Figure 7.3), target ι profiles (solid-dotted black lines in Figure 7.5), and input disturbance ($\delta I_p = 0.1$ MA) equal to those utilized during the experiment. The feedback controller was active during the experiment in the interval $[t_i, t_f] = [2.5, 6]$, and this same time interval is chosen for the simulation study. The EC system and counter-injection beam (210R) were off during the experiment, so they are not used in the simulation. The actuators are the plasma current I_p, the co-current NBI power P_{CO}, distributed equally between the 150L and 330L beams, and the balanced-beam NBI power P_{BL}, distributed equally between the 150R and 210L beams, in both experiment and simulation. The simulated and experimental

closed-loop-controlled ι profile at $\hat{\rho} = [0.2,\ 0.4,\ 0.5,\ 0.6,\ 0.8,\ 0.9]$ are shown in Figure 7.5. The trends of all simulated inputs (Figure 7.3) and outputs (Figure 7.5) are very similar to those obtained in experiments, which suggests that the PDE model successfully captures the dominant physics of the ι profile response.

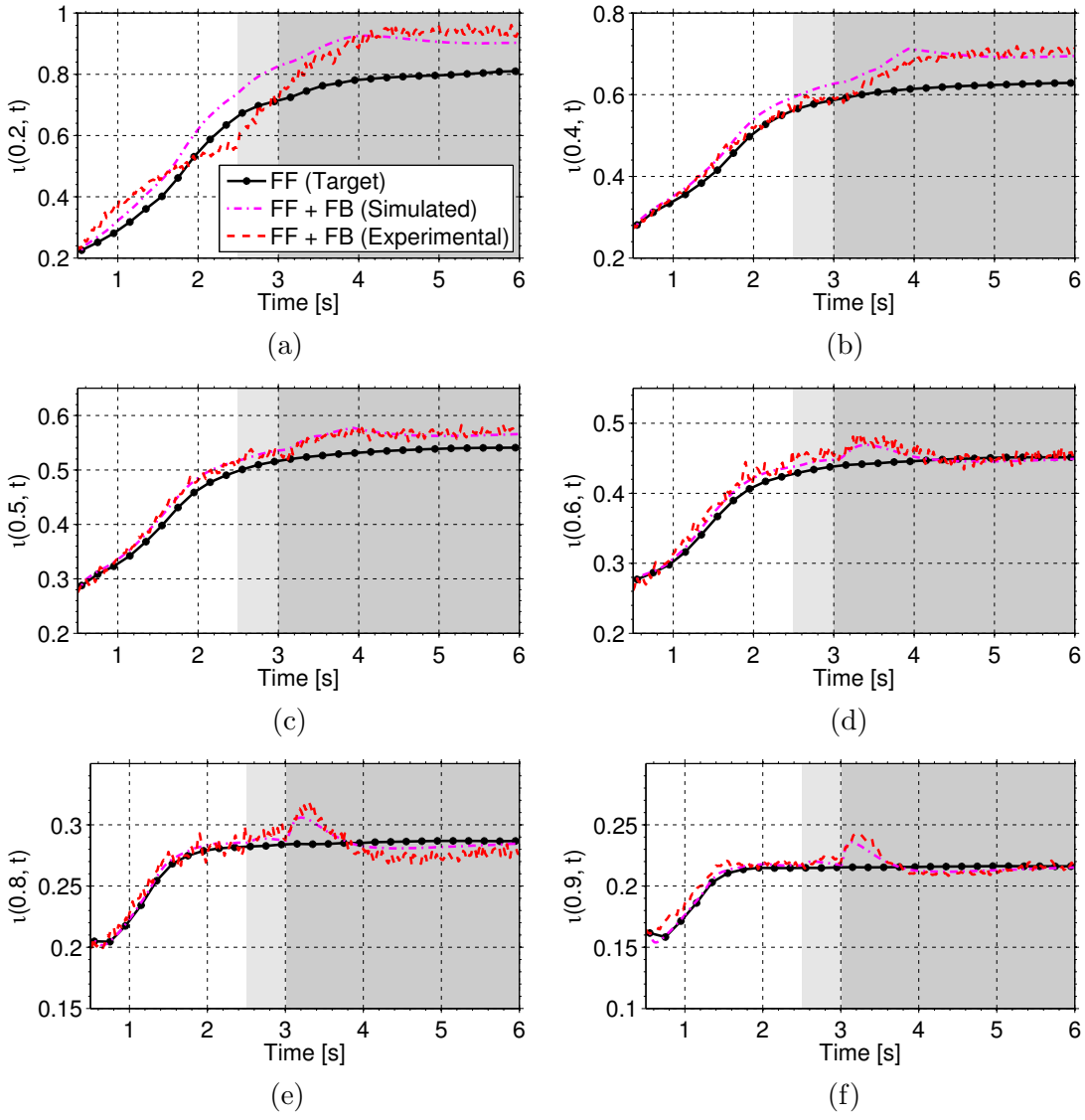

Figure 7.5: Rotational transform ι profile reference, closed-loop (data-driven model-based controller) simulated & experimental outputs (shot # 147704). Light-gray background: feedback on-disturbance off, dark-gray background: feedback on-disturbance on, white background: feedback off-disturbance off.

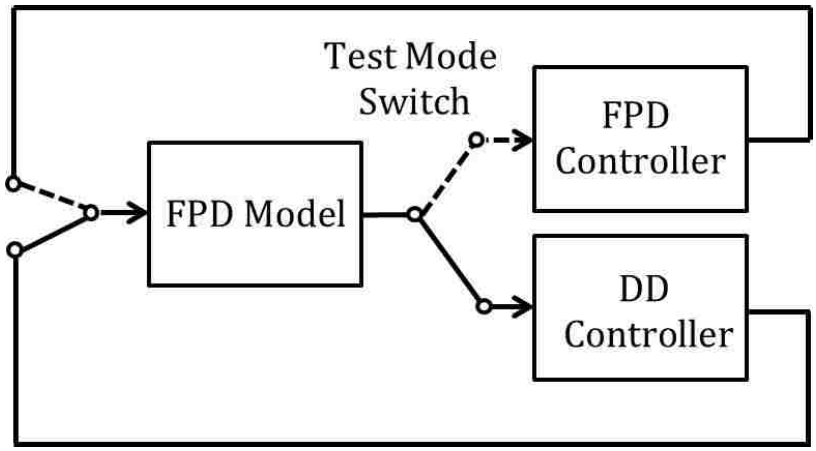

Figure 7.6: Control Performance Comparison.

7.4.2 Closed-loop Performance Comparison between First-principles-driven and Data-driven Model-based Controllers

Our previous ι profile controller in H-mode was based on the data-driven model (Chapter 3), which is only valid around the reference plasma state during the system identification experiment. The effectiveness of the data-driven model-based controllers may be limited when the plasma state moves away from the reference state. First-principles-driven modeling techniques allow for the derivation of models capturing the nonlinear response of the current profile to control actuation. The closed-loop simulation in this section is based on the first-principles-driven (FPD) magnetic diffusion equation (6.14), which represents the poloidal magnetic flux profile evolution during the discharge in DIII-D. The structure of the control performance comparison between the first-principles-driven (FPD) and data-driven (DD) model-based controllers is shown in Figure 7.6. The goal of the comparison is to demonstrate that the proposed controller is capable of regulating the system around a target ι profile even in the presence of multiple disturbances.

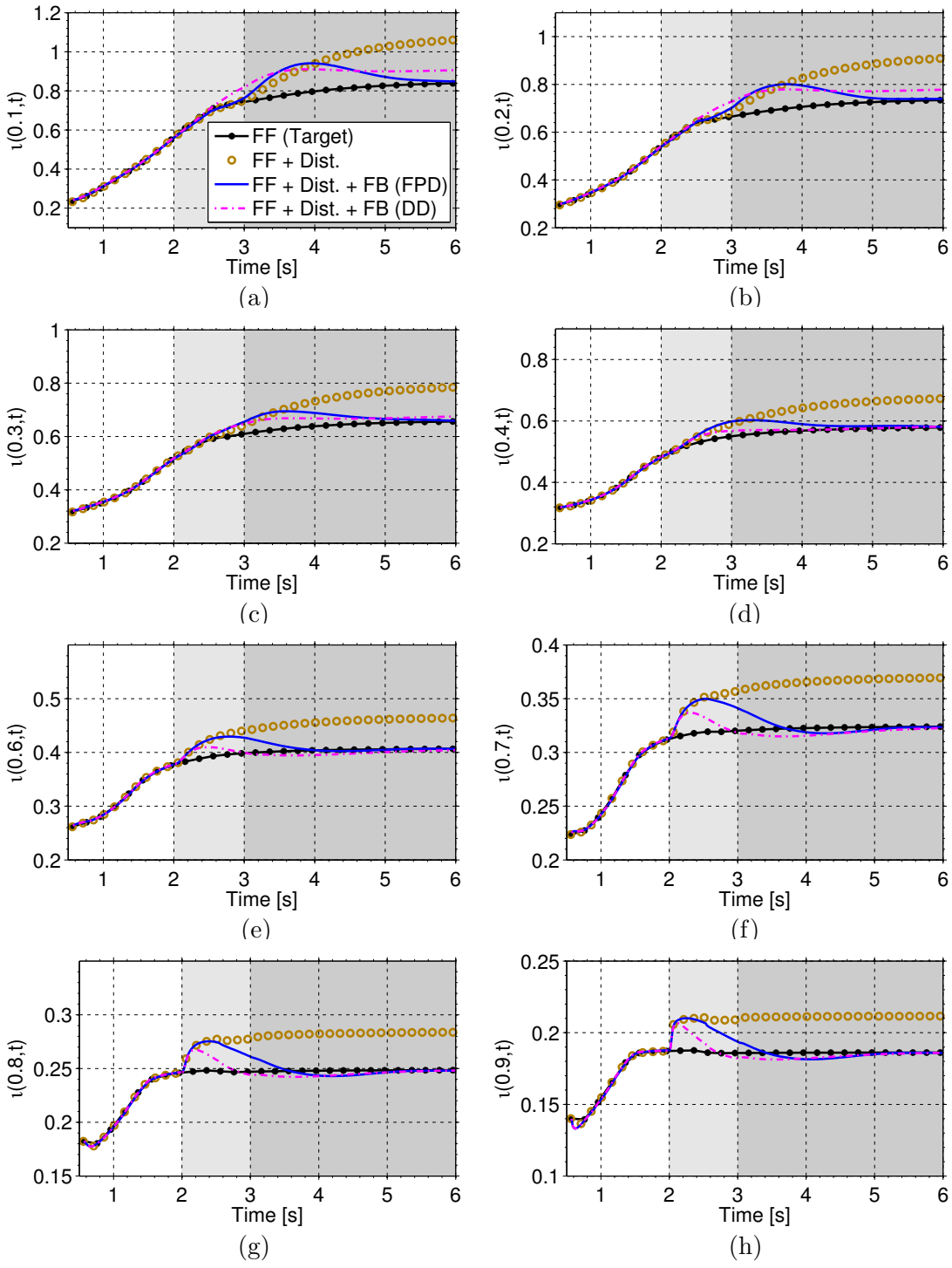

Figure 7.7: Simulated Outputs at $\hat{\rho} = 0.1,\ 0.2,\ 0.3,\ 0.4,\ 0.6,\ 0.7,\ 0.8,\ 0.9$. Light-gray background: feedback on - Disturbance I on, dark-gray background: feedback on - Disturbance II on, white background: feedback on - disturbance off.

Table 7.1: Input Disturbances (Units: MA & MW)

Dis.	ΔI_{p_d}	$\Delta P_{ec_{1_d}}$	$\Delta P_{ec_{2_d}}$	$\Delta P_{ec_{3_d}}$	$\Delta P_{ec_{4_d}}$	$\Delta P_{ec_{5_d}}$	$\Delta P_{ec_{6_d}}$	Δu_{n_d}
Δu_{d_1}	0.1	0	0	0	0	0	0	0
Δu_{d_2}	0.1	-0.1	-0.1	-0.25	-0.25	-0.1	-0.2	0

$\Delta P_{nbi_{1_d}}$	$\Delta P_{nbi_{2_d}}$	$\Delta P_{nbi_{3_d}}$	$\Delta P_{nbi_{4_d}}$	$\Delta P_{nbi_{5_d}}$	$\Delta P_{nbi_{6_d}}$	$\Delta P_{nbi_{7_d}}$	$\Delta P_{nbi_{8_d}}$
0	0	-0.25	-0.25	0	0	0	0
0	0	-0.25	-0.25	0	0	-0.25	-0.25

The reference plasma current, density evolution parameter, and heating and current drive (H&CD) powers come from a feedforward shot #146417, denoted as u_{FF}, and the ι profile resulting from these reference (feedforward) inputs, denoted as y_{FF}, are used as targets in the simulation, which are represented by black dotted lines in the figures in this section. Based on the present pulse capability of each gyrotron in the EC system, the EC power is turned on at $t = 2.5$ s. Two different disturbances $\Delta u_{d_i} = [\Delta I_{p_d},\ \Delta P_{ec_{j,d}},\ \Delta P_{nbi_{k,d}},\ \Delta u_{n_d}]$, shown in Table. 7.1, are introduced to the simulation, where $i \in \{1, 2\}$, $j \in \{1, \cdots, 6\}$, and $k \in \{1, \cdots, 8\}$. Disturbance I, Δu_{d_1}, representing a relatively large disturbance (0.1 MA) in I_p and small total disturbance (0.5 MW) in the NBI, is introduced at $t = 2$ s to test the regulating capability of the ι profile control. Disturbance II, Δu_{d_2}, representing a relatively large disturbance (0.1 MA) in I_p and large total disturbance (1 MW) in the NBI and EC, is introduced at $t = 3$ s to test ι profile control in different equilibrium. The start time of the control phase is moved backward from the current flat-top phase (2.5 s) to the current ramp-up phase (0.5 s). In order to compare control performances of the different controllers, we plot them in the same pictures (Figure 7.7-7.9).

The closed-loop-controlled ι profile (blue solid lines by the first-principles-driven (FPD) controller, and magenta dashed-dotted lines by the data-driven (DD) controller) at $\hat{\rho} = 0.1,\ 0.2,\ 0.3,\ 0.4,\ 0.5,\ 0.6,\ 0.7,\ 0.8,\ 0.9$ are shown in Figure 7.7. In

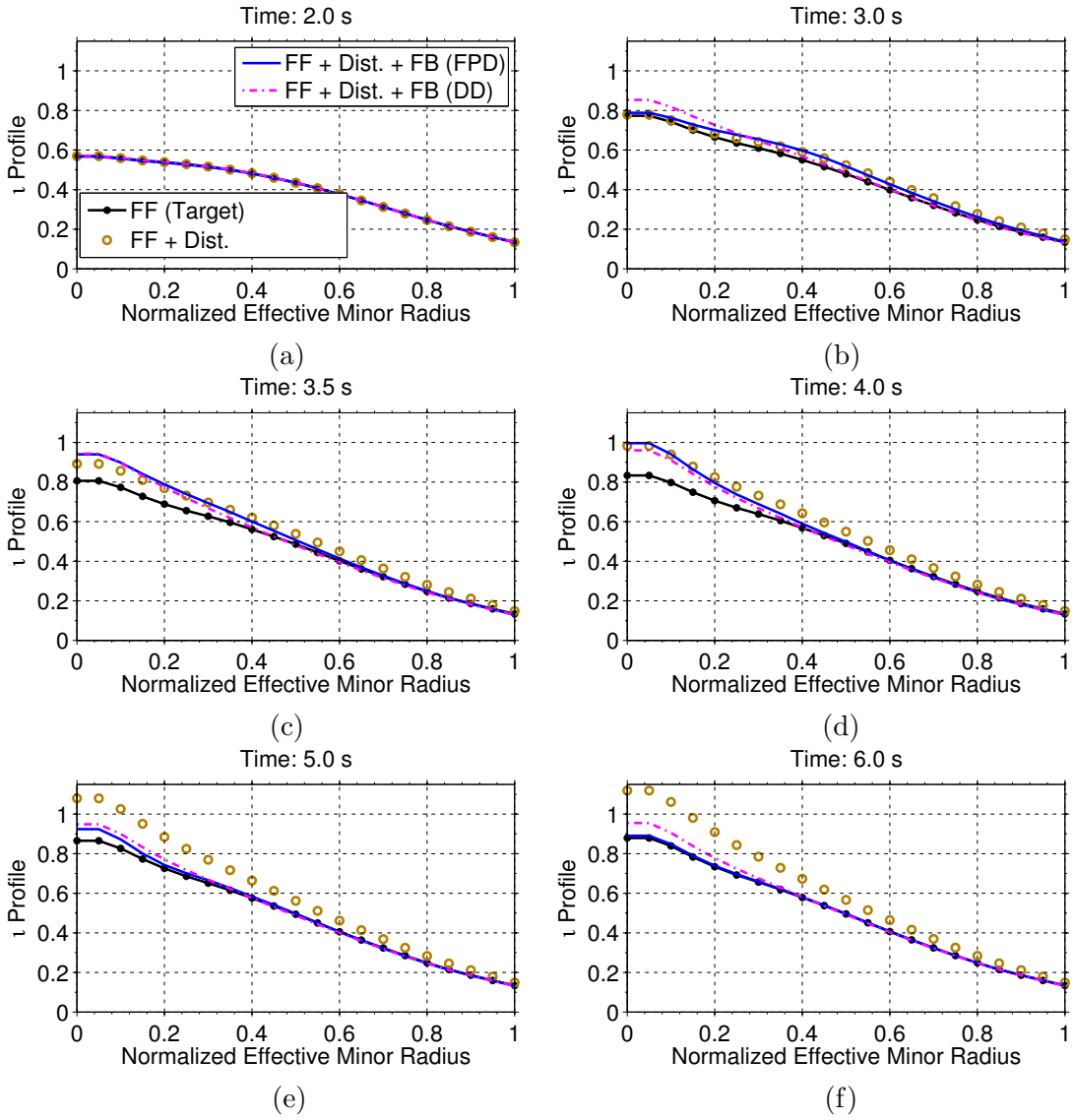

Figure 7.8: Closed-loop Simulated Plasma $\iota(\hat{\rho})$ profile at time $t = 2.0, 3.0, 3.5, 4.0, 5.0, 6.0$ seconds

addition, the feedforward (target) outputs (black solid-dotted lines) and feedforward with disturbances (brown circle lines) are shown in the same figure. In order to keep the outer profile tracking errors small, the plasma current disturbance is quickly rejected by the FPD and DD controllers after $t = 3$ s. There are nearly no tracking errors after $t = 4$ s for ι at $\hat{\rho} \geq 0.4$ as noted from Figure 7.7 (d)-(i). Note that the inner ι profile response is much slower than the boundary ι profile response, which is

due to the high temperature and slow diffusivity in the core relative to the boundary. This effect is explicitly taken into account at by including the temperature profile model in the FPD model. In the data-driven approach (Chapter 3), system identification technique assumes the limited bandwidth for the ι profile response, which may pose a risk to closed-loop performance due to the neglected dynamics. Comparing with the DD controller, the control performance of the FPD controller to the inner part of the ι profile ($\hat{\rho} \leq 0.2$) is improved, as shown in Figure 7.7 (a)-(b). A series of six plasma ι profiles at different times during the simulation are shown in Figure 7.8. The black solid-dotted lines denote the target profiles, and we see that with feedforward control only the target profile is not achieved in the presence of the disturbance (brown circle lines). Improved performance can be observed from the comparison with the controlled results by the FPD controller (blue solid lines) and the DD controller (magenta dashed-dotted lines).

The closed-loop outputs of the first-principles-driven (FPD) controller (blue solid lines) are compared with the closed-loop outputs of the data-driven (DD) controller (magenta dashed-dotted lines) in Figure 7.9. The two controllers reject the disturbance in the plasma current I_p quickly and drive the I_p around the constant reference (feedforward) value when the boundary ι profile reaches the target, as shown in Figure 7.9 (a). Beam and gyrotron powers, shown in Figure 7.9 (c)-(l), are weakly modulated by the DD model-based controller within the saturation limits, but strongly controlled by the FPD model-based controller. When the whole ι profile, especially the inner part of ι profile, reaches the target in the end of the simulation, H&CD powers are driven towards to their reference (feedforward) values by the FPD controller. After the disturbances especially with Δu_{d_2} are applied, the inputs of some gyrotrons and the 210L NBI reach saturation and activate the anti-windup compensator as shown in Figure 7.9 (d), (f), (g) and (k). The electron density is not

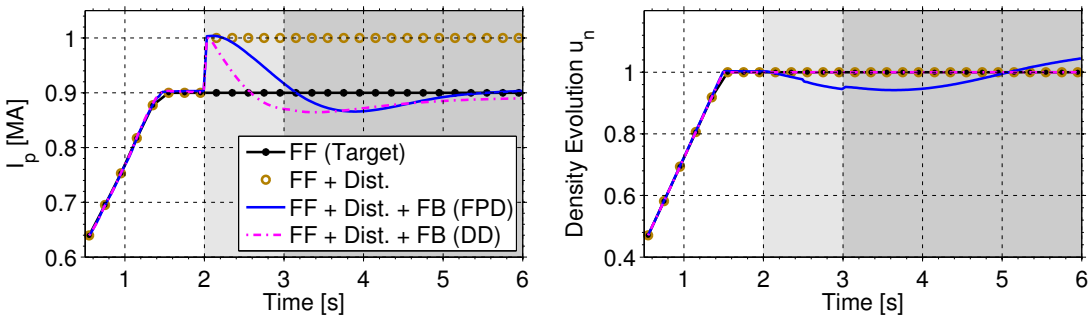
I_p [MA]
Time [s]
FF (Target)
FF + Dist.
FF + Dist. + FB (FPD)
FF + Dist. + FB (DD)

(a)

Density Evolution u_n
Time [s]

(b)

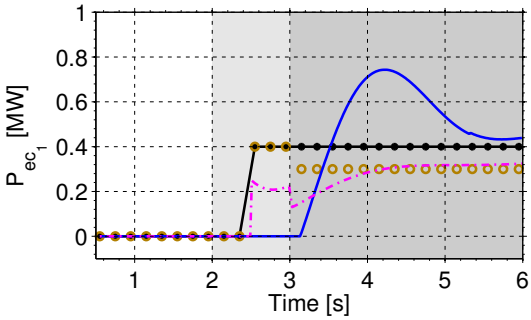
P_ec1 [MW]
Time [s]

(c)

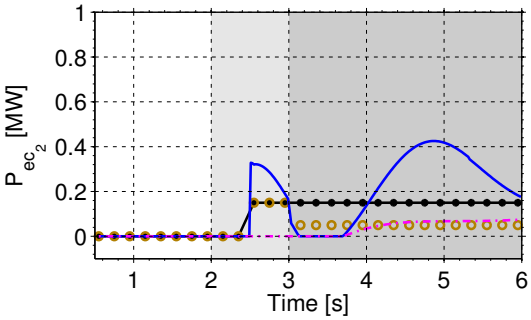
P_ec2 [MW]
Time [s]

(d)

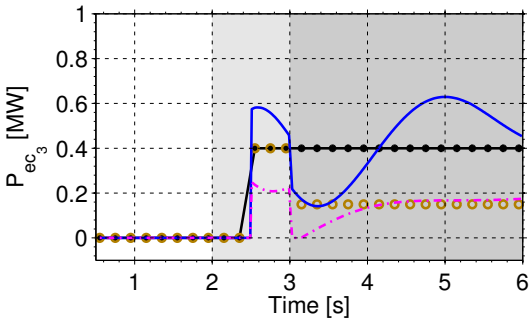
P_ec3 [MW]
Time [s]

(e)

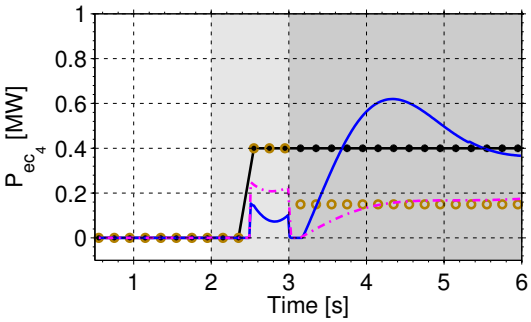
P_ec4 [MW]
Time [s]

(f)

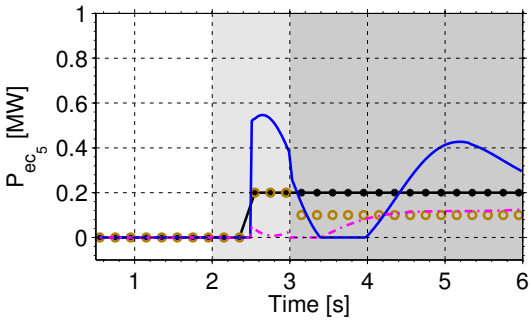
P_ec5 [MW]
Time [s]

(g)

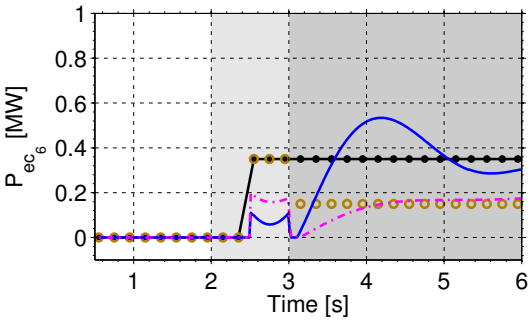
P_ec6 [MW]
Time [s]

(h)

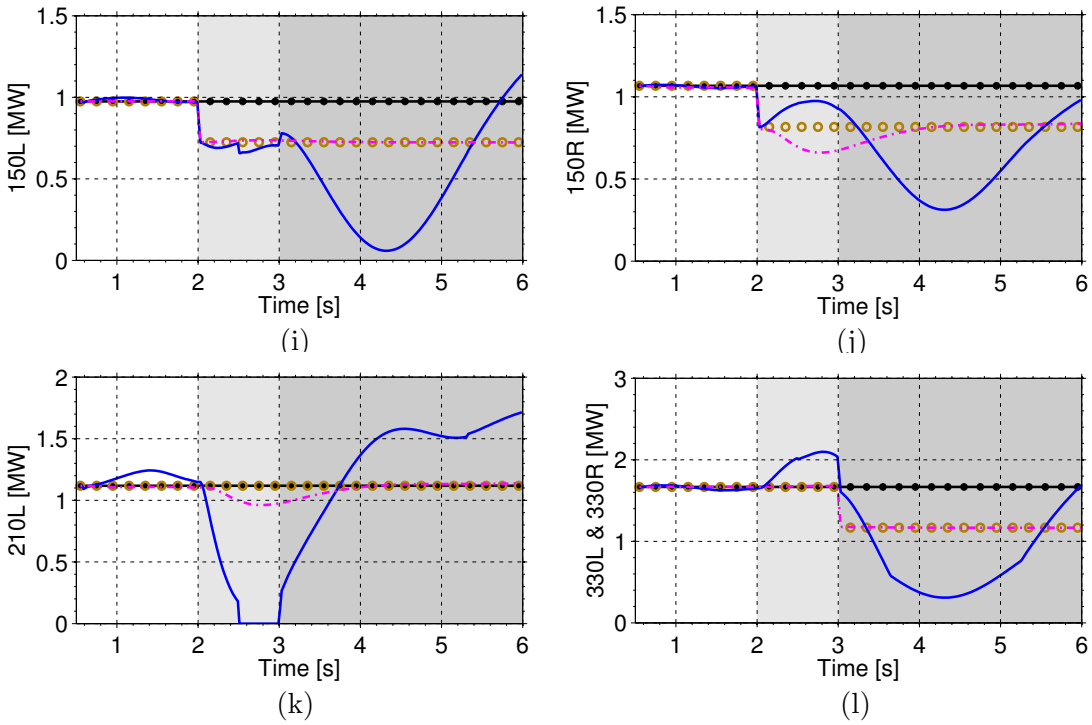

Figure 7.9: Rotational Transform ι Profile Closed-loop Simulated Inputs for Each Actuator: Reference (feedforward) inputs (black solid-dotted lines), feedforward inputs with disturbances (brown circle line), feedforward+feedback control by First-principles-driven (FPD) controller (blue solid lines), and feedforward+feedback control by Data-driven (DD) controller (magenta dashed-dotted lines). Light-gray background: feedback on - Disturbance I on, dark-gray background: feedback on - Disturbance II on, white background: feedback on - disturbance off.

controlled by the DD controller, so u_n is the same as the reference input. The FPD model includes the electron density model, which gives the new capability to control the density, as shown in Figure 7.9 (b). The central goal of current profile control is to regulate ι precisely in the inner part of plasma. Closed-loop simulated results by the first-principles-driven model-based controller in Figure 7.7 and Figure 7.8 show the control performance improvements in the inner part of the ι profile.

7.5 Conclusion

A first-principles-driven, model-based, multi-input-multi-output (MIMO), ι profile controller has been designed for the H-mode discharges in DIII-D. The control design is based on the control-oriented model. The feedback controller can regulate the system to the target, even in the presence of various disturbances. Singular value decomposition of the steady state transfer function is used to decouple the system and identify the most relevant control channels. The mixed sensitivity H_∞ technique is used to minimize the tracking error and to optimize control effort. The preliminary simulation results presented in this work show good progress towards current profile control in DIII-D. When compared with the control performance of a previous data-driven model-based current profile controller, the proposed first-principles-driven model-based H_∞ controller shows potential for improving control regulation in the inner part of the ι profile.

Chapter 8

Conclusion and Future Work

This dissertation work has focused on plasma current, position, shape and current density profile control in advanced tokamak operating scenarios. In this final chapter, we summarize our research work and briefly describe some areas that merit future research.

8.1 Contributions of Dissertation

The contributions of this dissertation are:

1. Model-based MIMO shape controllers were designed for NSTX. The design of the shape controller was based on linearized plasma response models in the current ramp-up phase and flat-top phase. The availability of independent current and position controllers transformed the shape control problem into an output tracking problem. Singular value decomposition of the steady state transfer function was used to decouple the system and identify the most relevant control channels, and the shape controllers were designed using this decoupled system. The DK-iteration technique, combining H_∞ synthesis and μ analysis,

was used to minimize the tracking error and optimize input effort. The proposed controllers were tested in simulations, and shows potential for expanding present experimental control capabilities.

2. A mixed-sensitivity H_∞, model-based ι profile and β_N controller for on-axis current drive scenarios was designed for DIII-D. The design was based on a two-timescale linear, data-driven, plasma-response model around a reference profile during the current flat-top phase in H-mode. The feedback controller can regulate the system to the target, which was close to the reference equilibrium, even in the presence of various disturbances. The feedback controller was then augmented with an anti-windup compensator, which keeps the given profile controller well-behaved in the presence of magnitude constraints in the actuators and leaves the nominal closed-loop unmodified when no saturation is present. The proposed controller represented one of the first profile controllers integrating magnetic and kinetic variables ever implemented and experimentally tested in DIII-D. Although limited in number and constrained by actuators problems, the preliminary experimental results show good progress towards routine current profile control in DIII-D.

3. A model-based robust ι profile and β_N controller for off-axis current drive scenarios was designed for DIII-D. Since the linear model was identified around a desired equilibrium in the current flat-top phase, an uncertainty was introduced to the identified model to partially account for the dynamic character of the plasma state equilibrium evolution in the current ramp-up phase. By using the DK-iteration technique, a robust controller was designed to stabilize this family of plasma models, which were reformulated into a nominal model with uncertainty. The proposed controller was tested in closed-loop PTRANSP

simulation, and then was experimentally tested in DIII-D. More experimental tests are needed to assess the appropriateness of using data-driven linear models for current profile control in off-axis current drive scenarios. The sensitivity of the static component of the controller to un-modeled or mis-modeled plasma response and its impact on performance need further analysis.

4. A physics-based control-oriented modeling approach to convert the first-principles physics model describing the current profile evolution in the tokamak into a form suitable for control design was developed, with emphasis on high performance operating scenarios. The PTRANSP simulation code was employed to tailored the model to on-axis and off-axis current drive scenarios, respectively. The first-principles-driven models' prediction capabilities were demonstrated by comparing the prediction to experimental data for DIII-D.

5. A mixed sensitivity H_∞, first-principles-driven, model-based, ι profile controller was designed for H-mode discharges in DIII-D. The feedback controller could regulate the system to the target, even in the presence of various disturbances in simulations. The preliminary simulation results presented show good progress towards current profile control in DIII-D. When compared with the control performance of a previous data-driven model-based current profile controller, the proposed first-principles-driven model-based controller shows potential for improving control regulation in the inner part of the ι profile. The proposed controller will be tested in the DIII-D 2013 experimental campaign.

8.2 Future Work

The construction of the ITER tokamak has raised awareness of the need of integrating different and sometimes competing controllers. So far, control efforts in tokamak

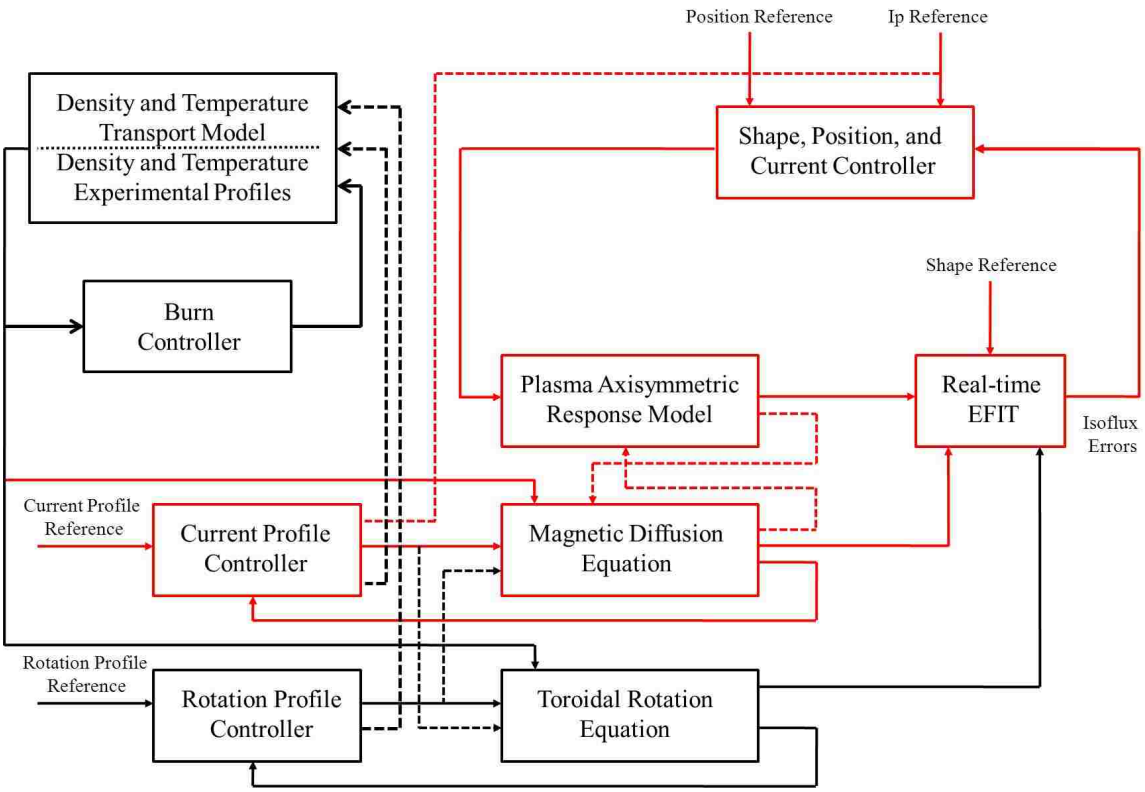

Figure 8.1: Integrated Control Configuration.

plasmas usually focused on individual and isolated objectives. However, this approach is sometimes unrealistic since different control objectives may be heavily coupled. This is the case of plasma shape and current profile control. For example, regulation of the total plasma current has been described above as a control output for the shape control problem (2.2) and at the same time as a control input for the current profile control problem (boundary control) (7.3). The neutral beams affect current profile control (6.8), and at the same time are inputs in the linearized axisymmetric plasma response models (2.1) used for shape control. In addition, the axisymmetric plasma response model (2.1) needed for shape control is obtained as a linearized response around a MHD equilibrium characterized by a specific current distribution or profile. Therefore, the MHD equilibrium is changed when the current profile is modified, and the axisymmetric plasma response models for shape control may need

to be updated in real time. For all these reasons, as shown in Figure 8.1 in red, we intend to consider an integrated approach to simultaneous control of plasma shape and current profile. Accomplished work is denoted by a red solid line, while future work is denoted by a red dashed line. For the simulation of the transport equations (current, density, temperature), it should be planned to integrate PTRANSP into MATLAB/SIMULINK.

The initial step toward integrating multiple individual controls in ITER is to integrate the multivariable model-based shape, vertical position, and current controller with the current density profile controller. The long term goal is to integrate this combined controller with control of rotation profile, density profile, pressure profile, and radial E-field, using feedback commands to actuators such as gas injectors, pumps, neutral beams, electromagnetic heating and current drives.

Bibliography

[1] A. Pironti and M. Walker, "Control of Tokamak Plasmas," *IEEE Control Systems Magazine*, vol. 25, no. 5, pp. 24–29, October 2005.

[2] J. Mandrekas and W. Stace, "Evaluation of Different Burn Control Methods for the International Thermonuclear Experimental Reactor," *13th IEEE Symp. on Fusion Eng.*, vol. 1, pp. 404–407, 1989.

[3] D. Anderson, T. Elevant, *et al.*, "Studies of Fusion Burn Control," *Fusion Tech.*, vol. 23, no. 1, pp. 5–41, 1993.

[4] T. Taylor *et al.*, "Physics of Advanced Tokamaks," *Plasma Physics and Controlled Fusion*, vol. 39, pp. B47–B73, 1997.

[5] J. Wesson, *Tokamaks*. Clarendon Press, Oxford, 2004.

[6] A. Pironti and M. Walker, "Fusion, Tokamaks, and Plasma Control," *IEEE Control Systems Magazine*, vol. 25, no. 5, pp. 30–43, October 2005.

[7] R. Buttery *et al.*, "Onset of Neoclassical Tearing Modes on JET," *Nuclear Fusion*, vol. 43, no. 2, pp. 69–83, 2003.

[8] R. LaHaye, "Neoclassical Tearing Modes and Their Control," *Physics of Plasmas*, vol. 13, no. 055501, 2006.

[9] F. Wagner *et al.*, "Recent Results of H-mode Studies on ASDEX," in *Proceeding of 13th Conference on Plasma Physics and Controlled Nuclear Fusion Research (IAEA)*, 1982, pp. 277–290.

[10] R. Hastie, "Sawtooth Instability in Tokamak Plasmas," *Astrophysics and Space Science*, vol. 256, pp. 177–204, 1997.

[11] Y. Mitrishkin and H. Kimura, "Plasma Vertical Speed Robust Control in Fusion Energy Advanced Tokamak," in *Proceeding of the 40th IEEE Conference on Decision and Control*, 2001.

[12] Y. Mitrishkin, V. Dokuka, *et al.*, "Plasma Magnetic Robust Control in Tokamak Reactor," in *Proceeding of the 45th IEEE Conference on Decision and Control*, 2006.

[13] D. Humphreys, M. Walker, *et al.*, "Initial Implementation of a Multivariable Plasma Shape and Position Controller on the DIII-D Tokamak," in *Proceeding of the 2000 IEEE International Conference on Control Applications*, 2000.

[14] M. Ariola, G. Ambrosino, *et al.*, "Design and Experimental Testing of a Robust Multivariable Controller on a Tokamak," *IEEE Transactions on Control Systems Technology*, vol. 10, no. 5, pp. 646–653, 2002.

[15] G. Ambrosino and R. Albanese, "Magnetic control of plasma current position and shape in Tokamaks," *IEEE Control Systems Magazine*, vol. 25, no. 5, pp. 76–92, 2005.

[16] G. Ambrosino *et al.*, "Design and Implementation of an Output Regulation Controller for the JET Tokamak," *IEEE Transactions on Control Systems Technology*, vol. 16, no. 6, pp. 1101–1111, 2008.

[17] Y. Mitrishkin, A. Korostelev, *et al.*, "Design and Modeling of ITER Plasma Magnetic Control System in Plasma Current Ramp-up Phase on DINA Code," in *Proceeding of the 49th IEEE Conference on Decision and Control*, 2009.

[18] J. Ferron *et al.*, "Real time equilibrium reconstruction for tokamak discharge control," *Nuclear Fusion*, vol. 38, pp. 1055–1066, 1998.

[19] D. Gates *et al.*, "Plasma shape control on the National Spherical Torus Experiment (NSTX) using real-time equilibrium reconstruction," *Nuclear Fusion*, vol. 46, pp. 17–23, 2006.

[20] W. Shi, M. Alsarheed, *et al.*, "Multivariable Model-based Shape Control for the National Spherical Torus Experiment (NSTX)," *Fusion Engineering and Design*, vol. 86, pp. 1107–1111, 2011.

[21] W. Shi, J. Barton, M. Alsarheed, and E. Schuster, "Multivariable multi-model-based magnetic control system for the current ramp-up phase in the national spherical torus experiment (nstx)," in *Decision and Control and European Control Conference (CDC-ECC), 2011 50th IEEE Conference on*, 2011, pp. 2632–2637.

[22] Y. Ou, T. Luce, E. Schuster, *et al.*, "Towards Model-based Current Profile Control at DIII-D," *Fusion Engineering and Design*, vol. 82, pp. 1153–1160, 2007.

[23] E. Witrant *et al.*, "A control-oriented model of the current profile in tokamak plasma," *Plasma Physics and Controlled Fusion*, vol. 49, pp. 1075–1105, 2007.

[24] F. Felici *et al.*, "Real-time physics-model-based simulation of the current density profile in tokamak plasmas," *Nuclear Fusion*, vol. 51, no. 083052, 2011.

[25] L. Ljung, *System Identification: Theory for the User*. New Jersey: Prentice Hall, 1999.

[26] W. Shi, W. Wehner, J. Barton, M. D. Boyer, E. Schuster, *et al.*, "Multivariable robust control of the plasma rotational transform profile for advanced tokamak scenarios in DIII-D," in *American Control Conference (ACC), 2012*, 2012, pp. 5037–5042.

[27] W. Shi, W. Wehner, J. Barton, M. Boyer, E. Schuster, *et al.*, "A two-time-scale model-based combined magnetic and kinetic control system for advanced tokamak scenarios on diii-d," in *Decision and Control (CDC), 2012 IEEE 51st Annual Conference on*, 2012, pp. 4347–4352.

[28] W. Shi, W. Wehner, J. Barton, *et al.*, "System Identification and Robust Control of the Plasma Rotational Transform Profile and Normalized Beta Dynamics for Advanced Tokamak Scenarios in DIII-D," *submitted to Nuclear Fusion*, 2012.

[29] W. Shi, W. Wehner, J. Barton, M. Boyer, E. Schuster, *et al.*, "PTRANSP Simulation and Experimental Test of a Robust Current Profile and β_N Controller for Off-axis Current Drive Scenarios in the DIII-D Tokamak," in *Proceeding of the 2013 American Control Conference*, 2013.

[30] D. Moreau *et al.*, "Real-time Control of the q-profile in JET for Steady State Advanced Tokamak Operation," *Nuclear Fusion*, vol. 43, pp. 870–882, 2003.

[31] D. Moreau, D. Mazon, *et al.*, "A Two Time Scale Dynamic Model Approach for Magnetic and Kinetic Profile Control in Advanced Tokamak Scenarios on JET," *Nuclear Fusion*, vol. 48, no. 106001, 2008.

[32] T. Wijnands, D. Houtte, G. Martin, X. Litaudon, and P. Froissard, "Feedback control of the current profile on Tore Supra," *Nuclear Fusion*, vol. 37, no. 6, p. 777, 1997.

[33] O. Barana, D. Mazon, L. Laborde, and F. Turco, "Feedback control of the lower hybrid power deposition profile on Tore Supra," *Plasma Physics and Controlled Fusion*, vol. 49, no. 7, p. 947, 2007. [Online]. Available: http://stacks.iop.org/0741-3335/49/i=7/a=001

[34] T. Suzuki, A. Isayama, S. Ide, T. Fujita, T. Oikawa, S. Sakata, M. Sueoka, H. Hosoyama, M. Seki, and J. Team, "Recent RF experiments and application of RF waves to real-time control of safety factor profile in JT-60U," *AIP Conference Proceedings*, vol. 787, no. 1, pp. 279–286, 2005. [Online]. Available: http://link.aip.org/link/?APC/787/279/1

[35] T. Suzuki, S. Ide, T. Oikawa, T. Fujita, M. Ishikawa, M. Seki, G. Matsunaga, T. Hatae, O. Naito, K. Hamamatsu, M. Sueoka, H. Hosoyama, M. Nakazatoand, and J. Team, "Off- axis current drive and real-time control of current profile in JT-60U," *Nuclear Fusion*, vol. 48, no. 4, p. 045002, 2008.

[36] J. Ferron *et al.*, "Feedback Control of the Safety Factor Profile Evolution during Formation of an Advanced Tokamak Discharge," *Nuclear Fusion*, vol. 46, no. 10, pp. L13–17, 2006.

[37] D. Moreau *et al.*, "Plasma Models for Real-time Control of Advanced Tokamak Scenarios," *Nuclear Fusion*, vol. 51, no. 063009, 2011.

[38] W. Wehner, W. Shi, E. Schuster, D. Moreau, *et al.*, "Optimal feedback control of the poloidal magnetic flux profile in the diii-d tokamak based on identified

plasma response models," in *American Control Conference (ACC), 2012*, 2012, pp. 5049–5054.

[39] W. Wehner, W. Shi, E. Schuster, *et al.*, "Identification and Control of Magneto-Kinetic Response During Advanced Tokamak Scenarios in DIII-D," in *Proceeding of the 2013 American Control Conference*, 2013.

[40] Y. Ou, C. Xu, E. Schuster, *et al.*, "Design and simulation of extremum-seeking open-loop optimal control of current profile in the DIII-D tokamak," *Plasma Physics and Controlled Fusion*, vol. 50, no. 115001, 2008.

[41] C. Xu, J. Dalessio, Y. Ou, E. Schuster, *et al.*, "Ramp-Up Phase Current Profile Control of Tokamak Plasmas via Nonlinear Programming," *IEEE Transactions on Plasma Science*, vol. 38, no. 2, pp. 163–173, 2010.

[42] F. Felici and O. Sauter, "Non-linear model-based optimization of actuator trajectories for tokamak plasma profile control," *Plasma Physics and Controlled Fusion*, vol. 54, no. 025002, 2012.

[43] Y. Ou, C. Xu, and E. Schuster, "Robust Control Design for the Poloidal Magnetic Flux Profile Evolution in the Presence of Model Uncertainties," *IEEE Transactions on Plasma Science*, vol. 38, no. 3, pp. 375–382, 2010, http://ieeexplore.ieee.org/stamp/stamp.jsp?arnumber=05404914.

[44] Y. Ou, C. Xu, E. Schuster, *et al.*, "Optimal Tracking Control of Current Profile in Tokamaks," *IEEE Transactions on Control Systems Technology*, vol. 19, no. 2, pp. 432–441, 2011.

[45] F. Bribiesca Argomedo, E. Witrant, C. Prieur, D. Georges, and S. Bremond, "Model-based control of the magnetic flux profile in a Tokamak plasma," in

Decision and Control (CDC), 2010 49th IEEE Conference on, 2010, pp. 6926–6931.

[46] O. Gaye, E. Moulay, S. Bremond, L. Autrique, R. Nouailletas, and Y. Orlov, "Sliding mode stabilization of the current profile in Tokamak plasmas," in *Decision and Control and European Control Conference (CDC-ECC), 2011 50th IEEE Conference on*, 2011, pp. 2638–2643.

[47] S. Kim and J. Lister, "A potentially robust plasma profile control approach for ITER using real-time estimation of linearized profile response models," *Nuclear Fusion*, vol. 52, p. 074002, 2012.

[48] J. Barton, M. D. Boyer, W. Shi, E. Schuster, *et al.*, "First-principles model-based robust control of the current profile evolution in the DIII-D tokamak," in *American Control Conference (ACC), 2012*, 2012, pp. 2134–2140.

[49] M. D. Boyer, J. Barton, E. Schuster, *et al.*, "Backstepping control of the plasma current profile in the DIII-D tokamak," in *American Control Conference (ACC), 2012*, 2012, pp. 2996–3001.

[50] M. Boyer, J. Barton, E. Schuster, *et al.*, "Current profile tracking for the DIII-D tokamak via LQI optimal control," in *Decision and Control (CDC), 2012 IEEE 51st Annual Conference on*, 2012, pp. 4341–4346.

[51] J. Barton, M. Boyer, W. Shi, E. Schuster, *et al.*, "Toroidal Current Profile Control During Low Confinement Mode Plasma Discharges in DIII-D via First-Principles-Driven Model-based Robust Control Synthesis," *Nuclear Fusion*, vol. 52, no. 123018, 2012.

[52] J. Barton, M. Boyer, *et al.*, "First-Principles Model-based Closed-loop Control of the Current Profile Dynamic Evolution on DIII-D," in *Proceeding of the 24th IAEA Fusion Energy Conference*, 2012.

[53] J. Barton, W. Shi, *et al.*, "Physics-based Control-oriented Modeling of the Current Density Profile Dynamics in High-performance Tokamak Plasmas," *submitted to the 52nd IEEE International Conference on Decision and Control*, 2013.

[54] W. Shi, J. Barton, *et al.*, "First-principles-driven Control of the Rotational Transform Profile in High Performance Discharges in the DIII-D Tokamak," *submitted to the 52nd IEEE International Conference on Decision and Control*, 2013.

[55] W. Wehner, C. Xu, E. Schuster, *et al.*, "Data-driven modeling and feedback tracking control of the toroidal rotation profile for advanced tokamak scenarios in DIII-D," in *Control Applications (CCA), 2011 IEEE International Conference on*, 2011, pp. 858–863.

[56] J. Freidberg, *Ideal Magnetohydrodynamics*. New York: Plenum Press, 1987.

[57] M. Walker and D. Humphreys, "Valid Coordinate Systems for Linearized Plasma Shape Response Models in Tokamaks," *Fusion Science and Technology*, vol. 50, no. 4, pp. 473–489, 2006.

[58] K. Astrom and B. Wittenmark, *Adaptive Control*. Dover Publications, Inc. Mineola, New York, 2008.

[59] A. Packard, "What News with μ: Structured Uncertainty in Multivariable Control," Ph.D. dissertation, UC Berkeley, 1988.

[60] H. Khalil, *Nonlinear Systems*, 3rd ed. New Jersey: Prentice Hall, 2001.

[61] M. Murakami *et al.*, "Off-axis neutral beam current drive for advanced scenario development in DIII-D," *Nuclear Fusion*, vol. 49, 2009.

[62] J. Lister, A. Portone, and Y. Gribov, "Plasma Control in ITER," *IEEE Control Systems Magazine*, vol. 26, no. 2, pp. 79–91, April 2006.

[63] S. Skogested and I. Postlethwaite, *Multivariable Feedback Control*. New York: John Wiley and Sons, Ltd, 2003.

[64] K. Zhou and J. C. Doyle, *Essentials of Robust Control*. New Jersey: Prentice Hall, 1997.

[65] E. Schuster, M. Krstic, M. Walker, and D. Humphreys, "Antiwindup scheme for plasma shape control with rate and magnitude actuation constraints in the DIII-D tokamak," in *Decision and Control, 2003. Proceedings. 42nd IEEE Conference on*, vol. 5, 2003, pp. 4634–4639 Vol.5.

[66] L. Zaccarian and A. R. Teel, *Modern Anti-windup Synthesis: Control Augmentation for Actuator Saturation*. New Jersey: Princeton University Press, 2004.

[67] E. Schuster, M. Walker, D. Humphreys, and M. Kristic, "Plasma Vertical Stabilization with Actuation Constraints in the DIII-D Tokamak," *Automatica*, vol. 41, pp. 1173–1179, 2005.

[68] R. Hawryluk, "An Empirical Approach to Tokamak Transport," in *Course on Physics of Plasma Close to Thermonuclear Conditions, Varenna, Italy*, 1979.

[69] M. Walker, "Emerging Applications in Tokamak Plasma Control," *IEEE Control Systems Magazine*, vol. 26, pp. 35–63, 2006.

[70] F. Hinton *et al.*, "Theory of plasma transport in toroidal confinement systems," *Rev. Mod. Phys.*, vol. 48, pp. 239–308, 1976.

[71] J. Blum, *Numerical Simulation and Optimal Control in Plasma Physics: With Application to Tokamaks*. Paris: John Wiley and Sons, Ltd, 1989.

[72] R. Prater, "Heating and Current Drive by Electron Cyclotron Waves," *Physics of Plasmas*, vol. 11, no. 5, pp. 2349–2376, 2004.

[73] O. Sauter *et al.*, "Neoclassical conductivity and bootstrap current formulas for general axisymmetric equilibria and arbitrary collisionality regime ," *Physics of Plasmas*, vol. 6, 1999.

Vita

Mr. Wenyu Shi was born on December 25, 1984 in Huainan City, Anhui Province, China. He obtained the Bachelor of Engineering Degree in Mechanical Engineering and Automation (Mechatronics) and the Second Bachelor of Science Degree in Mathematics and Applied Mathematics from Shanghai Jiao Tong University in 2007. After that, he started his graduate education in the Department of Mechanical Engineering and Mechanics at Lehigh University in 2007, and he received the degree of Master of Science in 2009. He began his Ph.D. program in the May 2009, working with Prof. Eugenio Schuster in the Laboratory for Control of Complex Physical Systems. Currently he is finishing the requirements for his Doctor of Philosophy Degree. Mr. Shi is a P.C. Rossin Doctoral Fellow in Mechanical Engineering at Lehigh University.

- **Publications**:

  I. Journal Papers:

  1. W. Shi, J.E. Barton, et al., "First-principles-driven Control of the Current Density Profile and Internal Energy in High Performance Discharges in DIII-D," in preparation.
  2. J.E. Barton, W. Shi, et al., "Physics-based First-principles-driven Control-oriented Modeling of the Plasma Current Profile and Stored Energy Evolutions in High Performance Tokamak Plasmas," in preparation.

3. W. Shi, W. Wehner, et al., "Closed-loop PTRANSP Simulation and Experimental Test of a Model-based Current Density Profile Controller for Advanced Tokamak Scenarios in DIII-D," in preparation.

4. W. Shi, W. Wehner, et al., "Data-driven modeling and robust control of the plasma rotational transform profile for advanced tokamak scenarios in DIII-D," submitted to *Nuclear Fusion*, 2012.

5. W. Shi, M. Alsarheed, E. Schuster, et al., "Multivariable model-based shape control for the National Spherical Torus Experiment (NSTX)," *Fusion Engineering and Design*, vol. 86, no. 6-8, pp. 1107-1111, 2011.

6. J.E. Barton, M.D. Boyer, W. Shi, E. Schuster, et al., "Toroidal current profile control during the ramp-up and early flat-top phases of low confinement mode plasma discharges in DIII-D via mixed-sensitivity H_∞ synthesis," *Nuclear Fusion*, Vol. 52, No. 123018 (24pp), 2012.

7. D. Moreau, $\cdots$, W. Shi, et al., "Integrated Magnetic and Kinetic Control of Advanced Tokamak Plasmas on DIII-D Based on Data-Driven Models," Accepted by *Nuclear Fusion*, 2013.

8. W. Shi and W. Guo, "The Analysis of the Manipulation Dexterity for 3R Open-chain Planar Robotic Linkage", *Journal of Shanghai Jiao Tong University*, vol. 43, pp. 143-147, 2009.

II. Refereed Conference Papers:

1. W. Shi, J.E. Barton, et al., "First-principles-driven Control of the Rotational Transform Profile in High Performance Discharges in the DIII-D Tokamak," submitted to the 52^{nd} *IEEE Conference on Decision and Control*, Florence, Italy, December 10 - 13, 2013.

2. J.E. Barton, W. Shi, et al., "Physics-based Control-oriented Modeling of the Current Density Profile Dynamics in High Performance Tokamak Plasmas," submitted to the 52^{nd} *IEEE Conference on Decision and Control*, Florence, Italy, December 10 - 13, 2013.

3. W. Shi, W. Wehner, et al., "PTRANSP Simulation and Experimental Test of a Robust Current Profile and β_N Controller for Off-axis Current Drive Scenarios in the DIII-D Tokamak," in Proceeding of the *2013 American Control Conference*, Washington DC, June 17 - 19, 2013.

4. W. Wehner, W. Shi, et al., "Identification and Control of Magneto-Kinetic Response During Advanced Tokamak Scenarios in DIII-D," in Proceeding of *2013 American Control Conference*, Washington DC, June 17 - 19, 2013.

5. W. Shi, W. Wehner, et al., "A Two-time-scale Model-based Combined Magnetic and Kinetic Control System for Advanced Tokamak Scenarios on DIII-D," in Proceeding of the 51^{st} *IEEE Conference on Decision and Control*, Maui, Hawaii, December 10 - 13, pp. 4347-4352, 2012.

6. J.E. Barton, M.D. Boyer, W. Shi, et al., "First-Principles Model-based Closed-loop Control of the Current Profile Dynamic Evolution on DIII-D," in Proceeding of the *24th IAEA Fusion Energy Conference*, San Diego, California, October 08 - 13, 2012.

7. D. Moreau, $\cdots$, W. Shi, et al., "Integrated Magnetic and Kinetic Control of Advanced Tokamak Scenarios Based on Data-Driven Models," in Proceeding of the *24th IAEA Fusion Energy Conference*, San Diego, California, October 08 - 13, 2012.

8. W. Shi, W. Wehner, et al., "Multivariable robust control of the plasma rotational transform profile for advanced tokamak scenarios in DIII-D," in

Proceeding of the *2012 American Control Conference*, Montréal, Canada, June 27 - 29, pp. 5037-5042, 2012.

9. W. Wehner, W. Shi, E. Schuster, et al., "Optimal feedback control of the poloidal magnetic flux profile in the DIII-D tokamak based on identified plasma response models," in Proceeding of the *2012 American Control Conference*, Montréal, Canada, June 27 - 29, pp. 5049-5054, 2012.

10. J.E. Barton, M.D. Boyer, W. Shi, E. Schuster et al., "First-Principles Model-based Robust Control of the Current Profile Evolution in the DIII-D Tokamak," in Proceeding of the *2012 American Control Conference*, Montréal, Canada, June 27 - 29, pp. 2134-2140, 2012.

11. W. Shi, J. Barton, M. Alsarheed and E. Schuster, "Multivariable multi-model-based magnetic control system for the current ramp-up phase in the National Spherical Torus Experiment (NSTX)," in Proceeding of the *50^{th} IEEE Conference on Decision and Control and European Control Conference*, Orlando, Florida, December 12 -15, pp. 2632-2637, 2011.

12. W. Shi and M. Chew, "Mathematical and Physical Analog Models of a Total Artificial Heart", in Proceeding of the *7th IEEE International Conference on Control and Automation*, December 09-11, Christchurch, New Zealand, pp. 637-642, 2009.

13. W. Shi and M. Chew, "Adaptive Control of a Total Artificial Heart – An Experimental Investigation", in Proceeding of the *7th IEEE International Conference on Control and Automation*, December 09-11, Christchurch, New Zealand, pp. 655-660, 2009.